Dipl.-Ing. Claudio Kotnig

Analysis and conceptual design of the cryogenic system of the Future Circular Collider

DISSERTATION

zur Erlangung des akademischen Grades

Doktor der technischen Wissenschaften

eingereicht an der

Technischen Universität Graz

Betreuer

Univ.-Prof. Dr.-Ing. habil. Günter Brenn

Institut für Strömungslehre und Wärmeübertragung

Graz, Juni 2018

EIDESSTATTLICHE ERKLÄRUNG

Ich erkläre an Eides statt, dass ich die vorliegende Arbeit selbstständig verfasst, andere als die angegebenen Quellen/Hilfsmittel nicht benutzt, und die den benutzten Quellen wörtlich und inhaltlich entnommenen Stellen als solche kenntlich gemacht habe. Das in TUGRAZonline hochgeladene Textdokument ist mit der vorliegenden Dissertation identisch.

04.06.2018

Datum

Unterschrift

Abstract

Particle colliders are today's most advanced tools to perform particle physics experiments and penetrate the mysteries of matter. The largest existing particle collider, the LHC, is about to reach its technical limits and the particle physics society has to decide which future machine will enable the successful research to gain new knowledge. One option is the superconducting Future Circular Collider (FCC), which would exceed the LHC's size and generated particle energies by far.

The enormous particle energies call for high magnetic fields, which only can be created reliably and economically by special superconducting materials at cryogenic temperature level. The intelligent design of the cryogenic distribution and discharge system to sustain the thermodynamic state of the superconducting electromagnets is the basis for an efficient and functional refrigeration and consequently for the physics experiments themselves.

Several requirements and constraints limit the technical possibilities and the cryogenic system has to be designed to accomplish all the demands imposed by the original purpose to perform particle physics experiments. In the present thesis the development of a conceptual design for the FCC cryogenic distribution and discharge system is presented.

Analytical and numerical methods are used to understand the cryogenic system's behaviour and to quantify the evolution and the magnitude of the thermodynamic state variables. The arrangement of the separately cooled units, the pipe diameters and the cryogen's initial states are varied and the different designs are exergetically analysed to obtain an indicatory value of the operational performance and costs. The respective capital costs and the availability as well as the compatibility with the optical lattice were taken into account to find a reliable and economic design meeting all requirements.

For the final design an overall electrical power consumption of about 220 MW for the steady-state in nominal operation was calculated with an exergetic efficiency of 20 %. The results show that the construction and operation of the cryogenic distribution and discharge system for the FCC for sure is an ambitious, but possible endeavour.

Kurzzusammenfassung

Teilchenbeschleuniger sind die derzeit fortgeschrittensten Werkzeuge zur Durchführung von Experimenten, um den Aufbau und das Verhalten von Materie zu erforschen. Der zur Zeit größte Teilchenbeschleuniger, der LHC, stößt bereits an seine technischen Grenzen und die Gemeinschaft der Teilchenphysiker muss entscheiden, mit welcher zukünftigen Maschine die besten Aussichten auf eine erfolgreiche Weiterführung der Experimente bestehen, um neues Wissen zu generieren und bestehendes zu vertiefen.

Eine Option ist die Konstruktion des Future Circular Collider (FCC), der den LHC in Größe und erzeugter Teilchenenergie bei Weitem überträfe. Die hohen notwendigen Teilchenenergien benötigen starke Magnetfelder, die nur mithilfe supraleitfähigem Materials bei sehr niedrigen Temperaturen erzeugt werden können, um die Beschleuniger zuverlässig und ökonomisch betreiben zu können. Ein sorgfältig durchdachtes System zur Verteilung und Rückführung des Kühlmittels, um den supraleitfähigen Zustand der Elektromagnete erhalten zu können, ist die Basis für ein effizientes und funktionierendes Kühlsystem und damit auch für die erfolgreiche Durchführung der physikalischen Experimente.

Die Entwicklung des Kühlsystems unterliegt jedoch strengen Anforderungen und Vorgaben, um den ursprünglichen Zweck der Beschleunigers zu ermöglichen: Die Durchführung von Experimenten. In der vorliegenden Dissertation werden die Entwicklung eines konzeptionellen Entwurfs des Tieftemperaturkühlsystems für den FCC und dessen exergetische Analyse beschrieben.

Analytische und numerische mathematische Methoden wurden angewendet, um das Verhalten des Kühlsystems qualitativ zu verstehen und um die Verläufe des thermodynamischen Zustands des Kühlmittels und die Größenordnung der Zustandsgrößen zu quantifizieren. Die Anordnung der separat gekühlten Einheiten, Rohrdurchmesser und der thermodynamische Zustand des zur Verfügung stehenden Kühlmittels wurden variiert und die sich daraus ergebenden unterschiedlichen Systeme exergetisch analysiert, um einen Indikator für die ökonomische Qualität und die Betriebskosten des Verteilungssystems zu erhalten. Die sich aus den Designs ergebenden Investionskosten, sowie eine Abschätzung der Fehleranfälligkeit und die Kompatibiltät mit der sich durch strahlenoptische Aspekte ergebenden Anordnung der Magnete flossen in den Entscheidungsprozess ein, um ein zuverlässiges und ökonomisches Kühlsystem zu entwickeln, das alle Voraussetzungen erfüllt.

Für den Betrieb des in dieser Arbeit vorgeschlagenen Designs ergibt sich unter Normalbedingungen im stationären Zustand eine notwendige elektrische Leistung von etwa 220 MW mit eine exergetischen Effizienz von 20 % für das gesamte System. Die Ergebisse zeigen, dass die Konstruktion und der Betrieb des Tieftemperaturkühlsystems für den FCC ein ehrgeiziges, aber durchaus realisierbares Unterfangen zu sein scheint.

Preamble

The present thesis was written in the framework of the Future Circular Collider Study at CERN in Geneva in cooperation with Graz University of Technology. The opportunity to participate in and contribute to a remarkable research project of this kind cannot be taken for granted. Herewith I would like to express my sincere gratitude to the M. Laurent Tavian and Univ.-Prof. Dr.-Ing. habil. Günter Brenn, who made the last three years possible.

I want to thank M. Laurent Tavian, long-standing head of the cryogenics group at CERN and now HiLumi Project Office Manager, for the profound insight he gave me into the field of cryogenics, the time spent for the impartation of his knowledge and his confidence in my work. Working for and with M. Laurent Tavian was an impressive experience and the optimal opportunity to develop as an engineer.

I want to thank Prof. Günter Brenn, head of the Institute of Fluid Mechanics and Heat Transfer at Graz University of Technology, for the fruitful discussions, the scientific guidance and for his help as an experienced academic researcher. Despite the distance of about 1000 km between Graz and Geneva, I always could rely on the support of Prof. Günter Brenn in scientific, administrative and personal matters.

I also would like to thank Dr. Dimitri Delikaris for the productive working atmosphere in the cryogenics group at CERN, Dr. Philippe Lebrun from CERN for his time and his know-how to improve and assess my work and Prof. Helfried Steiner from Graz University of Technology, who supported me with the numerical calculations.

Finally I want to thank my wife Helga for her patience and support especially during the last three years and my family, notably my parents, my sister and my grandfather, on whose support I always can count.

Graz, June 2018 Claudio Kotnig

Nomenclature

Table 1: List of Latin mathematical symbols

Symbol	Unit	Description
a	m/s	speed of sound
a	m^2/s	thermal diffusivity
A	m^2	area
$\dot{A}$	W	exergetic benefit
A_{GM}	$m\,s/kg$	Gorter-Mellink coefficient
$\hat{b}$	-	relative exergy loss
B	T	magnetic field strength
$\dot{B}$	W	exergy losses, anergy
Bi	-	Biot number
c	m/s	speed of light
c, c_p	$J/\left(kg\,K\right)$	specific heat capacity
c_{JT}	$K/\left(N\,m^2\right)$	Joule Thomson-coefficient
$\dot{C}$	W	exergy of transferred heat
d	m	slit height
d	m	(inner) diameter
D	m	(outer) diameter
e	C	particle charge
e	W	specific exergy of a fluid
e_a	W	specific external energy
E	J	energy
$\dot{E}$	W	exergy transported in a moving fluid
$\dot{E}$	W	external energy transported in a moving fluid
f	-	Darcy friction factor, Fanning friction factor
f_{Clean}	-	Cleanliness factor
f_k^{-1}	$W^{3.4}/\left(m^{5.8}K\right)$	thermal conductivity function
g	m/s^2	gravitational acceleration
h	$J/\left(kg\right)$	specific enthalpy
h	m	height
$\dot{H}$	W	enthalpy transported in a moving fluid
i, j	-	integer counting variables
I	A	electrical current
J	A/cm^2	current density

List of Latin mathematical symbols (continued)

Symbol	Unit	Description
k	$W/(m\,K)$	thermal conductivity
L	m	length
m	kg	mass
M	-	finite differences method factor
$\dot{m}$	kg/s	mass flow rate
n	-	number, amount
Nu	-	Nusselt number
p	$kg\,m/s$	momentum
p	N/m^2	pressure
P	W	power
P	m	perimeter
Pr	-	Prandtl number
$\dot{q}$	W/m	heat flux
$\dot{Q}$	W	heat
r, R	m	radius, curvature
R	$J/(kg\,K)$	specific gas constant
Re	-	Reynolds number
s	m	natural coordinate
s	$J/(kg\,K)$	specific entropy
S	K	source term
$\dot{S}$	W/K	entropy transported in a moving fluid
t	s	time
t	m	thickness
T	K	temperature
$\dot{U}$	W	inner energy transported in a moving fluid
u, v, w	m/s	velocity
$\dot{V}$	m^3/s	volume flow rate
$\dot{W}$	W	work power
$\dot{X}$	W	exergy effort
x, y, z	m	coordinates
$\hat{Z}$	m^{-3}	hydraulic impedance

Table 2: List of Greek mathematical symbols

Symbol	Unit	Description
α, β, φ	rad, %, $^{\circ}$	angle
β	-	ratio of particle velocity and speed of light
β	-	geometrical factor for the Hagen Poiseuille equation
γ	-	Lorentz factor
ϵ	m	absolute roughness

List of Greek mathematical symbols (continued)

Symbol	Unit	Description
ε	-	specific dimensionless exergy
ε	-	blank volume ratio
ϵ_C	-	Carnot factor for cooling
ζ	-	exergetic efficiency
Θ	-	temperature ratio
Θ	-	finite differences method time factor
η	-	dimensionless coordinate
η	-	efficiency
η_C	-	Carnot factor for heating
$\varkappa$	-	isentropic exponent
μ	$Pa\,s$	dynamic viscosity
μ	-	finite differences method geometrical factor
μ_0	H/m	permeability of free space
μ_r	-	relative permeability
ν	m^2/s	dynamic viscosity
ξ	-	Carnot efficiency
ξ	-	quality, vapour mass fraction
ρ	kg/m^3	density
τ	N/m^2	shear stress, normal stress
φ_q	-	heat distribution coefficient
ω	-	relaxation factor for the Gauss-Seidel method

Table 3: List of subscripts and abbreviations

Symbol	Description	Symbol	Description
0	initial state, rest state, basic	1Φ	single-phase
2Φ	two-phase	4.5	state at 4.5 K
I	inner cooling loop system	II	outer cooling loop system
a	ambient	ADI	Alternating Direction Implicit
Arc	arc	ax	axial
B	header B, boundary	$Bath$	static helium bath
BGS	beam gas scattering	BHX	bayonet heat exchanger
$Bore$	iron yoke bore(s)	BS	beam screen
BSU	beam screen unit	C	header C
cC	cold circulation	CC	cooling channel(s)
$chem$	chemical	Ch	cold mass channel(s)
Ci	circuits	$Circ$	circulator
CL	cooling loop, current lead(s)	CM	cold mass
CMU	cold mass unit	CN	Crank-Nicolson
Co	copper	$Coil$	coil
$cold$	cold	$Component$	component
$Cooled$	cooled	$Cooling$	cooling

List of subscripts and abbreviations (continued)

Symbol	Description	Symbol	Description
CP	cryoplant	$crit$	critical
D	header D, dry	Dry	dry
DP	dipole	E	header E
el	electrical	f	frictional
F	header F	FCC	Future Circular Collider
FDM	finite difference method	FP	feeder pipe
FVM	finite volume method	g	gravitational
GM	Gorter-Mellink	GS	Gauss-Seidel
h	hydraulic	H	Header
HC	half-cell	HT	heat transfer
HX	heat exchange(r)	iCh	inner beam screen chamber
IF	interface	in	inlet
IY, $Iron\,Yoke$	iron yoke	JT	Joule-Thomson
k	heat conduction	kin	kinetic
L	Landau	Lam	iron yoke lamination
LHS	left-hand side	lim	limit
Liq	liquid	LL	liquid level
m	momentum	Mag	magnet
max	maximal	MF	manifold
min	minimal	Mix	mixing, mixer
n	normalfluid	$NeHe$	Nelium
NTU	number of transfer units	out	outlet
P, $Pipe$	Pipe	PDE	Partial Differential Equation
PP	parallel pipe(s)	pot	potential
QRL	cryogenic distribution line	r	radial
R	relativistic state, return pipe, resistance	RC	re-cooling
red	reduced	Ref	refrigerant
RH	return header	RHS	light-hand side
s	superfluid, isentropic	$Sector$	sector
Sep	separator	SH	supply header
$Slits$	slits	$Source$	source
SR	Synchrotron Radiation	th	thermal
St	Steel	tot, Tot	total
TS	thermal shielding	$TT\Delta$	terminal temperature difference
$Valve$	valve	Vap	vapour
VL	boundary vapour-liquid	W, Wet	wetted
$wall$	wall	$warm$	wall
wC	warm circulation	$Weld$	weld, welding
Δp	pressure drop	λ	lambda state of helium
σ	radiation	φ	tangential
Φ	fluid phase		

Contents

1 Introduction

Today one of the most elaborate research projects is the exploration of the structure of matter - enormous experimental facilities are necessary to be able to gain knowledge at constantly smaller scales [1]. Existing particle colliders, above all the Large Hadron Collider (LHC), are about to reach their limits and following the European strategy in particle physics the European Organization of Nuclear Research (CERN) has performed international studies to design the next generation of particle colliders [2]. One study targets the conceptual design of a circular particle collider, named the Future Circular Collider (FCC).

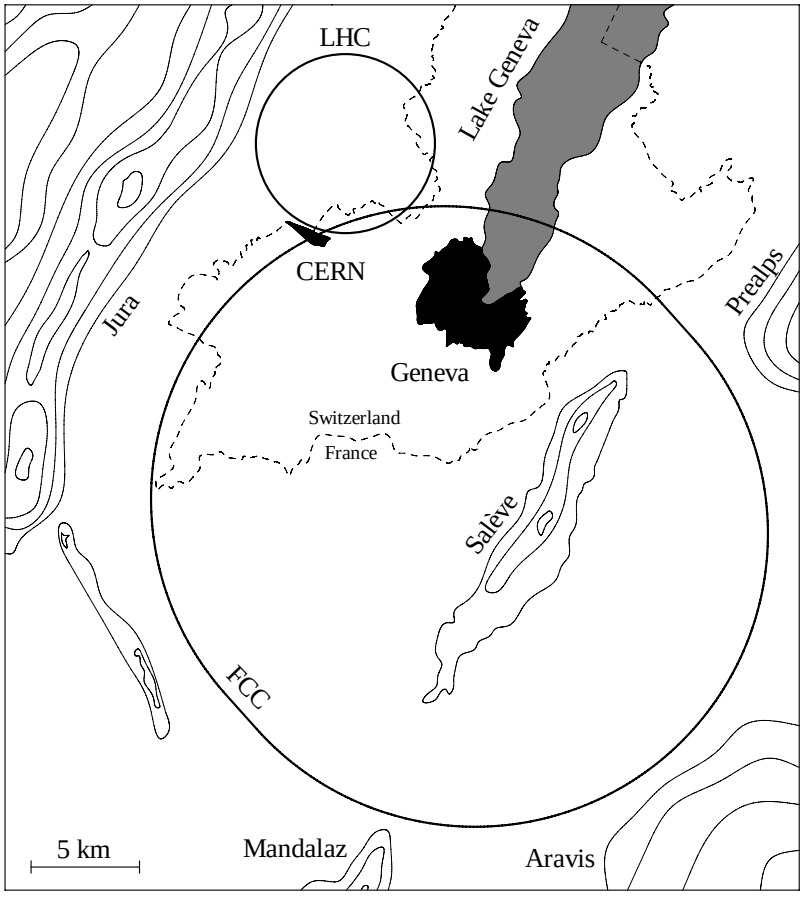

Figure 1.1: Schematic of the geographic location of the FCC and the LHC

The next indicatory step in the development of the FCC will be the European strategy meeting in 2019. Until then the conceptual design study of the entire construction of the FCC shall be

finalised and issued in the form of written reports. The tentative schedule of the FCC foresees the beginning of the experiments not before 2035. To understand how ambitious this goal is, figure 1.1 shows schematically the size and location of the FCC close to the Swiss city of Geneva. For comparison, the largest existing particle collider, the LHC, is also depicted in the illustration. It is located about 100 m below the surface and it is planned to position the FCC even deeper in a tunnel with a diameter of six meters and 100 km perimeter.

In a first step it is envisaged to use the tunnel and the infrastructure for installing a machine colliding electrons and positrons (FCC-ee). After the exploitation of knowledge in this configuration, the FCC-ee could be removed and substituted by different machinery to enable experiments with protons and ions - summarised as hadrons - and hence become the FCC-hh. From the cryogenic point of view, the FCC-hh is by far the more interesting and challenging version. All considerations, calculations and assumptions presented in this thesis are based on the requirements to operate the FCC as a hadron collider.

1.1 Particle Colliders

The question what matter consists of is as old as human culture. Even some ancient Greek philosophers, notably Democritus, assumed atoms - undividable small particles forming all matter. Also the idea of few different substances forming all matter was established and up to modern era the elements proposed by Aristotle served as a base for alchemists. Instead of the classification in the periodic table we know today, the basic materials were supposed to be earth, air, fire and water (held together by the fifth element: the quintessence). Each body is composed of the four different elements; the mixture yields shape and consistency. Investigations by chemists and physicists in the Age of the Enlightenment showed that both ideas of the ancient philosophers basically were correct. Today elements are defined as smallest units of matter distinguishable by chemical processes [3].

Measurements of the atomic weights showed that the elements differ by their mass (apart from isotopes) and with the discovery and study of radioactivity it could be proven that some elements emit particle radiation falsifying the idea of the "undividable" atoms as smallest bricks of matter. Depending on the type of radiation a radioactive body changes its elementary composition. The elements are therefore defined by the number and ratio of even smaller particles they consist of (protons, electrons and neutrons). In the early twentieth century scientists were able to get a first look on the internal structure of the atoms and based on the experiments the existence of an atomic nucleus carrying the major part of the atom's mass and the amazingly huge void space the nucleus is surrounded by was discovered [4].

With improved understanding of the composition and the structure, science strove to investigate the particles forming the atoms, but chemistry couldn't deliver the necessary tools to explore them. The mathematical models of theoretical physicists predicted several particles carrying mass, transferring forces (interactions) and even providing mass to other particles. To discover them, particles are accelerated and brought to collision. Due to the equivalency of mass and energy, a part of the particle energy is converted into mass, creating heavier particles, which then are investigated [5]. The machines designed for this task are particle accelerators or particle colliders. In accelerators the energy of charged particles is increased, which then are smashed against a resting mass, a so-called fixed target. Much higher collision energies become available for transformation, if particles are accelerated in opposed directions and brought to a head-on collision in particle colliders.

The age of particle accelerators began in the early 1930. In the first machines the charged particles were accelerated by an electrostatic field. The particle energies were limited by the maximal

voltage between the electrodes, which the particles could only pass once. The introduction of electrodynamic fields enabled to accelerate particles to much higher energies during repeated passages. In 1934 a so-called cyclotron was constructed by E. O. Lawrence and M. S. Livingston, in which charged particles were repeatedly accelerated by an alternating electric field, following a helical path in a magnetic field of constant strength. By applying adjustable magnetic fields, particles could be forced on a single curved trajectory to pass the same oscillating acceleration field again and again - the synchrotron, basis of all large circular accelerators and colliders existing today. In 1945 the first electron synchrotron was constructed by E. McMillan, seven years later, in 1952, the proton synchrotron followed under the lead of M. Oliphant [6].

Thenceforward machines were designed increasing in size and power to accelerate particles close to the speed of light to produce collisions at constantly rising energies to generate and detect new particles [7]. Until now the Large Hadron Collider (LHC) at CERN close to Geneva is by far the largest particle collider existing, its design foresees collisions of particles with a center-of-mass energy of 14 TeV. The design case is almost reached and the LHC approaches its physical and technical limits discovering "new physics". If the scientific community concludes that more essential knowledge can be gained by increasing the particle energy, the construction of an even larger particle collider could be the next step to penetrate the mysteries of matter. Several options are discussed and first concepts for new machines are about to be worked out in conceptual design studies at CERN, among others the Future Circular Collider (FCC).

1.1.1 Linear vs. Circular Colliders

The most obvious technique for producing head-on collisions is in two linear accelerators facing each other. To be able to bring them to collision, highly focussed and precisely aligned beams are required. Even with today's technology the major part of the accelerated particles passes the point of collision without interaction and has to be dumped. The amount of data gained during one experimental run is relatively small compared to the expended time.

In circular colliders the non-collided particles are led along a quasi-circular path and can be stored for several hours and used for multiple collision attempts in different interaction regions (experiments). Once the particles are accelerated only their energy losses during the circulation have to be compensated. The accelerated beams do not need to be as focussed as in a linear collider, but the residual particles after each attempt of collision have to be led on a curved path, deviated from their linear trajectory by (bending) magnets.

To increase the available energy during a collision the velocity of particles is increased, the necessary force to keep the particles on their designated path depends on their speed, their mass and the radius of curvature of their trajectory. Approaching to the speed of light c additionally supplied energy to the particles do not increase their velocity v accordingly, but yields a relativistic gain of mass. The diagram in figure 1.2 shows the measured mass m_R compared to the rest mass m_0 by an observer at rest with respect to the mass in an inertial frame [8].

$$\frac{v}{c} = \beta \tag{1.1}$$

$$\frac{m_R}{m_0} = \frac{1}{\sqrt{1-\beta^2}} = \gamma \tag{1.2}$$

The Lorentz factor γ also corresponds to the ratio of the relativistic mass-energy E_R and the rest mass-energy E_0.

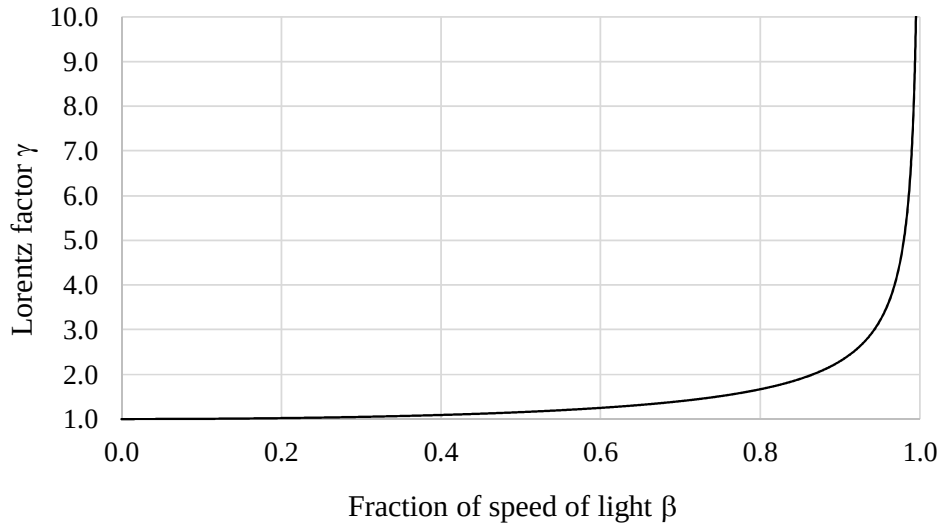

Figure 1.2: Lorentz factor γ vs. the ratio of velocity and speed of light β.

$$\gamma = \frac{E_R}{E_0} = \frac{E_{kin} + m_0\,c^2}{m_0\,c^2} = \frac{E_{kin}}{m_0\,c^2} + 1 \tag{1.3}$$

A desired energy increase during a collision is accompanied by a momentum increase of the circulated particles, where the relativistic momentum p_R can be calculated by dividing the energy by the speed of light. This simplified correlation illustrated in (1.4) only is valid for highly relativistic particles, whose rest-mass energy is negligible compared to the total energy.

$$p_R = \frac{E_R}{c} \tag{1.4}$$

The reluctance of the particles to follow a bent trajectory, the so-called magnetic rigidity, is the quotient of the momentum and the particle's charge e [1]. To force the particles on a curved path the product of the magnetic field B and the radius of curvature r equals the magnetic rigidity.

$$B\,r = \frac{p_R}{e} \tag{1.5}$$

The largest achievable centre-of-mass energy therefore is determined by the maximal possible magnetic field creatable and the smallest radius (i.e. the point of the highest curvature) of the particle collider. In general the magnetic fields are generated by electromagnets. Ferromagnetic iron alloys are used to increase the permeability of the magnetic circuits, which is described by Ampere's law.

$$\oint \vec{B} \cdot d\vec{s} = \mu_r\,\mu_0\,I \tag{1.6}$$

where μ_r denotes the relative permeability of iron, μ_0 denotes the permeability of free space and I denotes the current. (1.6) only applies for simplified cases, the qualitative statement though stays the same. It says, that the magnetic field strength depends on the electric current and the permeability of iron. Below a magnetic field strength of about 2 T the permeability of the used iron alloys is high and only small currents are necessary to create the magnetic field. If its strength exceeds 2 T, the iron saturates and its permeability decreases towards 1 and the electromagnet

seems to be operated in a vacuum. To obtain magnetic fields above 2 T, the necessary electrical current increases disproportionally large, calling for an accordingly low electrical resistance of the conductors to limit the electrical losses and the resistive heat to extract [9].

With development of refrigeration technologies in the end of the nineteenth century, the generation of constantly decreasing temperatures to liquefy all known gases was a research goal of physicists and engineers. During experiments with mercury at low temperature, the Dutch Nobel Laureate H. K. Onnes observed superconductivity - the phenomenon that metals conduct current loss-freely below a certain transition temperature [10]. With suitable superconducting material compositions large currents can create high magnetic fields with no generation of resistive heat. Albeit the three parameters - transition temperature T, magnetic field strength B and current density J - depend on and influence each other [11]. The diagram in figure 1.3 shows the qualitative correlation for three different superconducting materials.

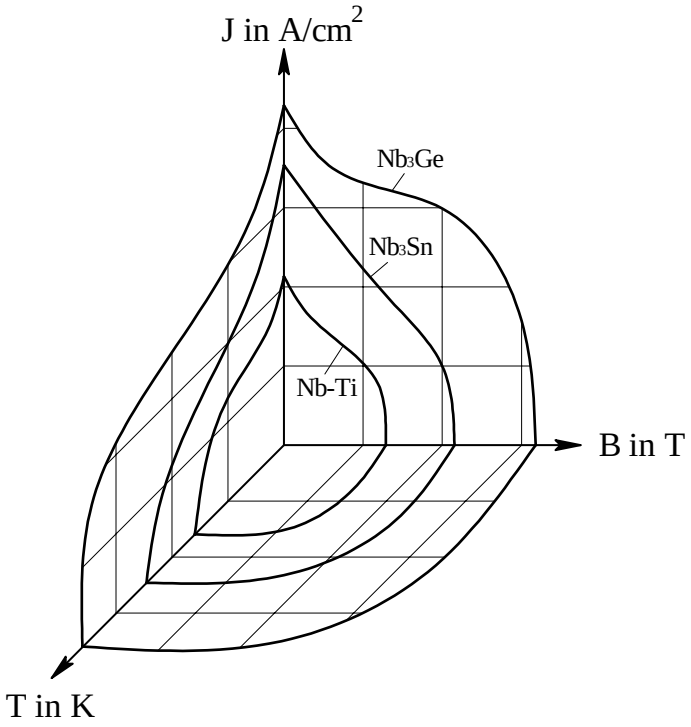

Figure 1.3: Qualitative correlation between transition temperature T, magnetic field strength B and current density J for three superconducting materials.

The combination of the scientific requirements and the used material determines the temperature limit of the superconducting magnets, which must not be exceeded to successfully run the circular particle collider.

1.1.2 Cryogenics in Circular Colliders

The main purpose of the refrigeration of a circular collider at cryogenic temperature level is the preservation of the superconducting state of the electromagnets. All the entering heat from ambiance and any heat generated by irreversible processes inside the machine has to be extracted at temperatures close to absolute zero. The major heat sources are listed and briefly explained below.

1. One main heat source are the heat leaks from the ambiance. Despite the sophisticated thermal insulation, heat always enters the machine due to the high temperature gradient and by passing non avoidable heat intercepts, for example connections to the cryogenic delivery system or connections for the electric supply.

2. Charged particles, deviated from their linear trajetory, emit synchrotron radiation at the power P_{SR} directly proportional to the particle energy E to the fourth power and inversly proportional to its rest mass m_0 to the fourth power and the radius of curvature r of the trajectory [12].

$$P_{SR} \propto \frac{E_R^4}{m_0^4 r} \tag{1.7}$$

   In circular hadron colliders before the LHC, the synchrotron radiation is a second order heat load due to the relatively small particle energies. The electron's rest mass is about 2000 times smaller than a proton's mass and therefore electron beams of the same energy emit a much higher amount of synchrotron radiation. As a consequence, limiting synchrotron radiation from electron beams requires a large radius of curvature, and hence, a small magnetic field, which can usually be attained with conventional, water-cooled magnets.

   However, the particle energies of the FCC-hh should reach up to 50 TeV (i.e. a centre-of-mass energy of 100 TeV) and the synchrotron radiation is the major heat load to be taken care of by the cryogenic system of the FCC [13].

3. When the synchrotron radiation hits the surrounding walls, photoelectrons can be produced. These negatively charged particles are accelerated towards the positively charged protons of the passing beam, hit the wall on the opposite side, and produce secondary electrons. The continuously increasing number of electrons due to an avalanche effect is called "electron cloud". Additionally, to pump energy from the circulating beams and dissipating it as heat on the wall of the beam chamber, electron clouds can develop beam instabilities leading to beam loss. The generation of electron clouds can be reduced or even entirely suppressed by a special coating and/or treatment of the walls which is planned to be installed in the FCC [14].

4. Although the hadron beams circulate in ultrahigh vacuum ($\approx 10^{-13}\ bar$), collisions of protons with residual gas molecules occur. This phenomenon is called beam-gas scattering and also leads to energy dissipation in the magnets [15].

5. The superconducting magnets are powered in series. At each end of a magnet, the superconducting cables have to be joined, by soldering or welding. Although of very low resistance, the joints are not superconducting and therefore subject to Joule dissipation [16].

The main task of the cryogenic system is the efficient and dependable provision and distribution of a suitable coolant at the necessary thermodynamic state. Whereas the efficiency in many cases can be increased by additional instrumentation and auxiliary equipment or highly sophisticated refrigeration systems, the reliability often suffers from an increased amount of technical components. Besides that, when constructing a machine of this size the capital costs for additional equipment become a non-negligible cost factor. A good compromise has to be found to design a reliable, efficient and affordable cryogenic distribution system.

2 Cryogenic distribution systems in large circular colliders

Large circular colliders are generally located underground. To reduce the size of the necessary caverns, cryogenic facilities are partly located above ground, and the necessary machinery to be put underground is minimized. Vertical shafts housing transfer lines for cryogen and electricity connect the facilities above ground with the facilities underground. A cryogenic distribution line, thermally well insulated and containing several headers, is installed parallel along the circular collider to supply and discharge cryogen via connections at periodic intervals.

The collider itself consists of straight sections and arcs. The straight sections contain the experiments (interaction regions), the RF cavities, the beam injection and dump facilities and other installations, some of which also need to be supplied with cryogens at low temperature. The requirements to the cryogen's state are specific and the necessary quantity is small. The major part of the delivered cryogen feeds the arcs, which contain the superconducting magnets to bend (dipoles) and focus (quadrupoles, sextopoles and other higher-order multipoles) the proton beams [17]. Figure 2.1 illustrates schematically the cryogenic system of a large circular collider.

The basic structure of the cryogenic distribution system of three existing circular colliders and the FCC design are presented. These machines reach beam energies from close to 1 TeV up to 50 TeV and require accordingly large cryogenic facilities. The original sketches are simplified and by no means exhaustive with emphasis on the cryogen distribution to the arcs.

The cooling duties for each type of equipment in the machine can be expressed in terms of temperature levels and corresponding heat loads. These parameters constrain the thermodynamic states of the cooling fluids. The main cryogenic consumers related to the arcs are listed below.

- **Cold Mass Cooling:** The cold mass includes all the masses forming the superconducting magnets, especially the coils, the collar and the iron yoke. The main purpose of the cold mass cooling is to keep the coil temperature below the requested temperature limit to guarantee the superconducting state. The required temperature level is the lowest.

- **Thermal Shielding:** To thermally shield the cold mass, part of the heat leaks from the ambiance are intercepted by a cryogen at intermediate temperature level. A well-chosen temperature level minimizes the refrigeration effort by compromising between the provision of the thermal shielding and the residual heat reaching the cold mass.

- **Current Lead Cooling:** The electric power to supply the magnets and create the necessary fields is produced at ambient temperature level. The conductors conveying the current into the cold masses from ambient temperature are so-called current leads.

- **Beam Screen Cooling:** A beam screen is a metal pipe integrated in the cold bore containing the proton beam. Among other functions (e.g. improving the vacuum quality), the beam screen works as a thermal barrier to protect the cold mass from beam-induced losses, in

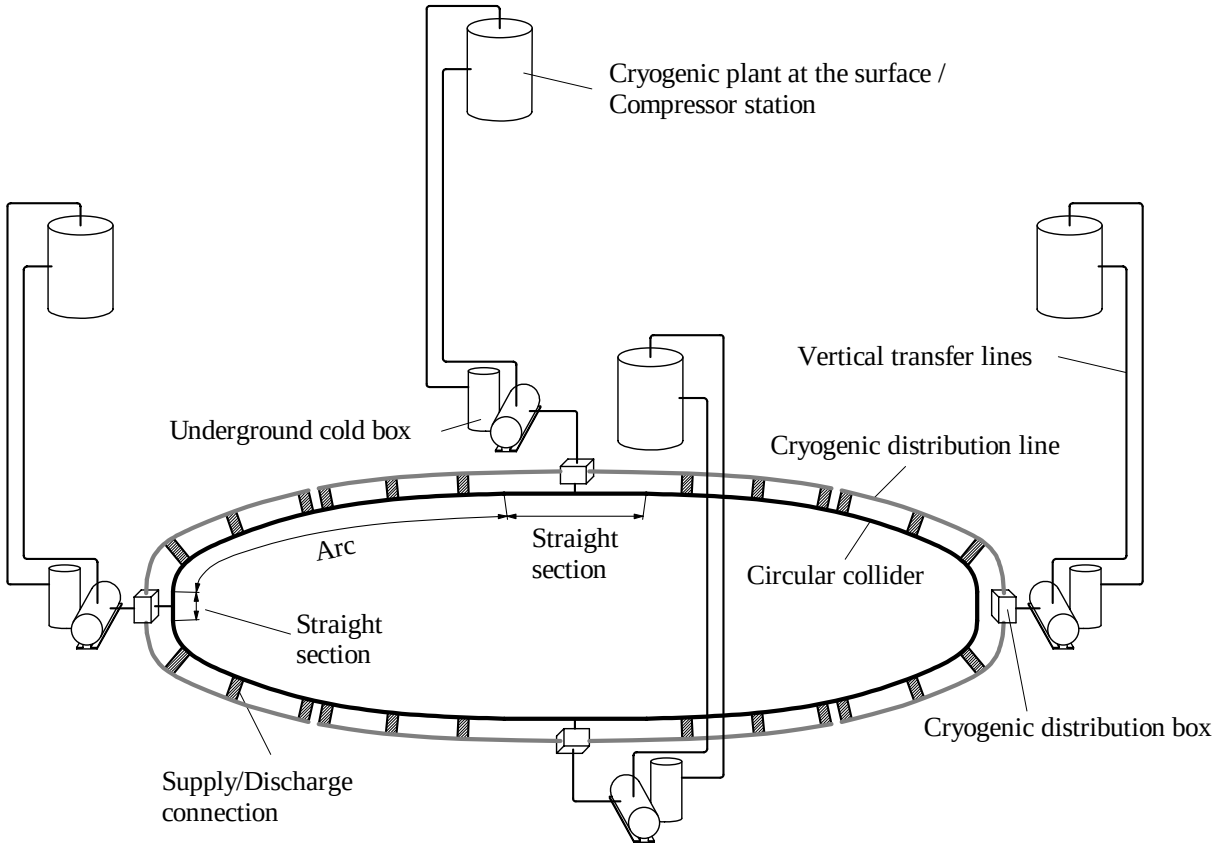

Figure 2.1: Structure of the cryogenic system of a large circular collider.

particular from the synchrotron radiation. The emitted photons are absorbed by the beam screen, and the generated heat is absorbed by a cryogen at higher temperature level than the cold mass, which reduces the thermodynamical impact on the refrigeration system. The LHC was the first machine equipped with a beam screen [18].

The arcs are supplied with cryogens of an appropriate state by a cryogenic distribution line (QRL) which is installed in parallel. The QRL houses different headers providing fresh and collecting the warmed up refrigerants. For the sake of presentability the naming convention was chosen based on the LHC system, where letters are assigned to distinguish the different headers by there task. The cryogen enters and leaves the collider at regularly installed Supply/Discharge connections.

- Header B: Low-pressure discharge pipe (pumping line)
- Header C: High-pressure supply pipe
- Header D: Quench line, low-pressure supply and high-pressure return
- Header E: Thermal shielding supply line
- Header F: Thermal shielding return line

We now discuss the properties of four circular colliders with an emphasis on their cryogenic system.

2.1 Tevatron

The circular collider Tevatron at FermiLab close to Chicago in the USA was initially operated as a particle accelerator with a fixed target and the first superconducting accelerator in the world. After reconstruction and upgrades, the Tevatron was operated as a collider from 1992 to 1995 and from 2001 to 2011. Protons and antiprotons (≈ 980 GeV) were brought to collision, yielding a centre-of-mass energy of almost 2 TeV.

Two different cryogens are used in the Tevatron - helium for the cold mass cooling and nitrogen for the thermal shielding. Each coolant is delivered by one large cryoplant via a cryogenic distribution line. Figure 2.2 schematically shows the designs of the cryogenic distribution line (left-hand side) and a dipole (right-hand side) [19] [20].

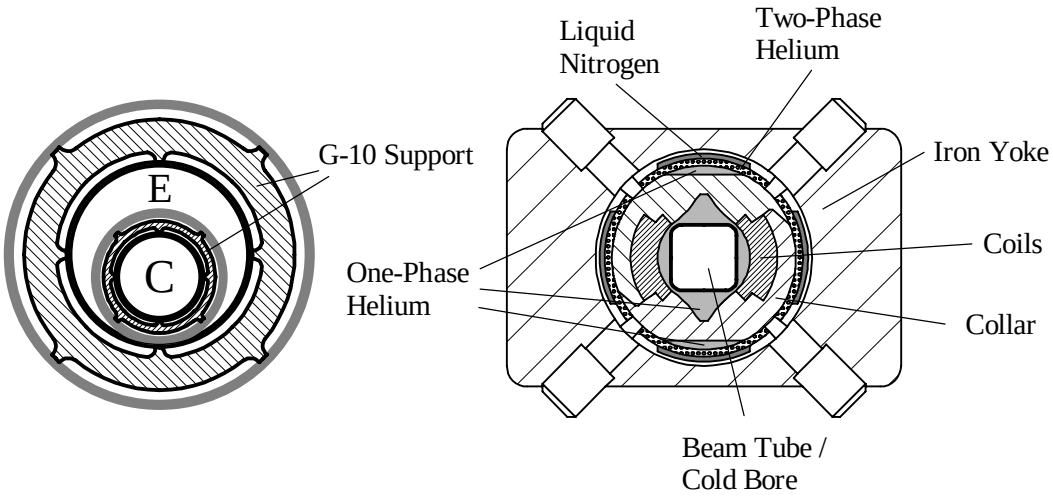

Figure 2.2: Schematics of the Tevatron cryogenic distribution line (left-hand side) and of a Tevatron dipole (right-hand side).

- **Cryogenic distribution line:** The smaller header C is supported by G-10, thermally insulated by superinsulation and vacuum and contained in a vacuum jacket which is included in the larger header E. Like that, the nitrogen supplied in header E also works as a thermal shield at intermediate temperature. Similarly, header E itself is also mounted using G-10 supports and thermally insulated by several layers of superinsulation and vacuum.
- **Cold mass:** The cold mass is cooled by forced circulation of supercritical helium at 4.5 to 4.6 K, continuously re-cooled by heat exchange with the returning two-phase helium flow. The supercritical helium passes the cold mass in three parallel channels: One annular channel around the cold bore, and two identical and symmetrically arranged channels at the top and the bottom of the collar. The two-phase flow and the nitrogen pass the magnets between the collar and the iron yoke.

In each sector, additionally one compressor station and four satellite refrigerators are installed. As illustrated in figure 2.3, Tevatron consists of six sectors named after the first letters in the Latin alphabet [21].

The magnet pattern of Tevatron is schematically illustrated in figure 2.4. Each of the six sectors consists of a straight section and seventeen beam-bending cells. One cell can be divided into two

half-cells which contain one quadrupole magnet and four dipole magnets in series. The total length of Tevatron amounts to about 6.5 km.

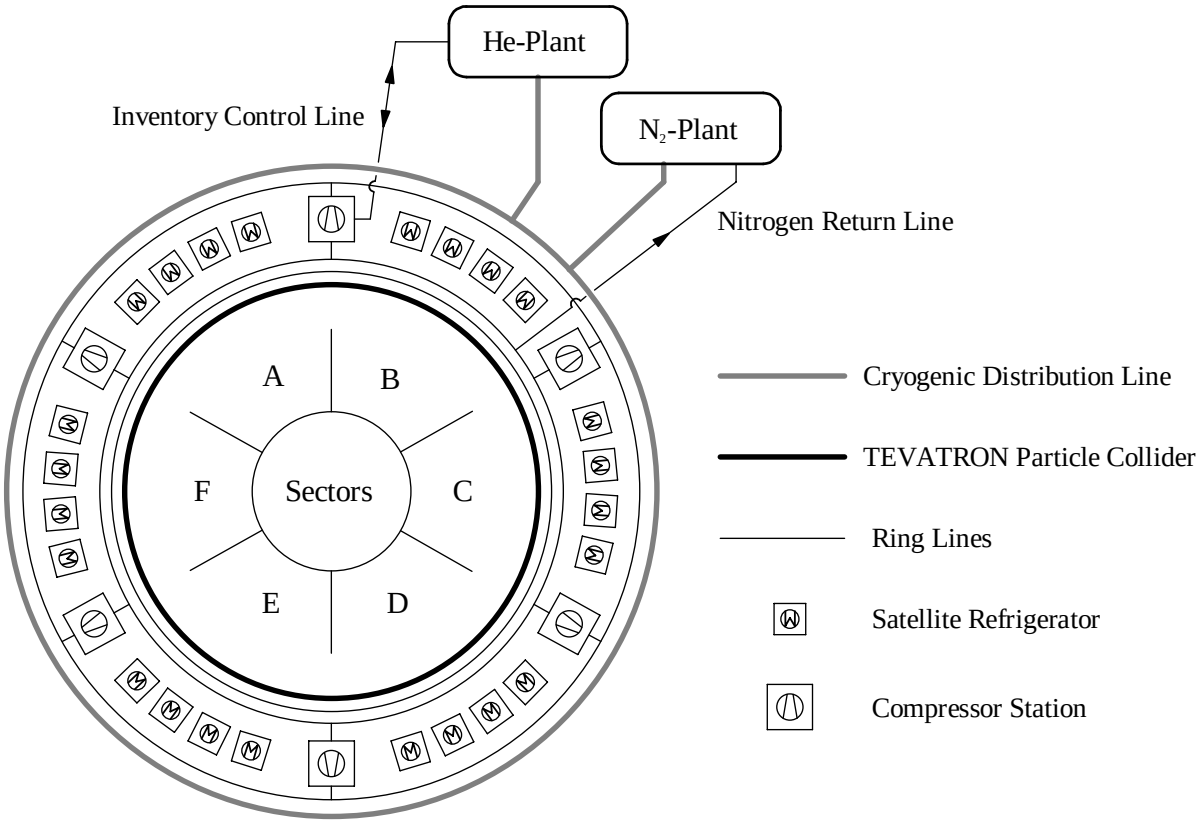

Figure 2.3: Schematic of the Tevatron circular collider and its basic cryogenic structure.

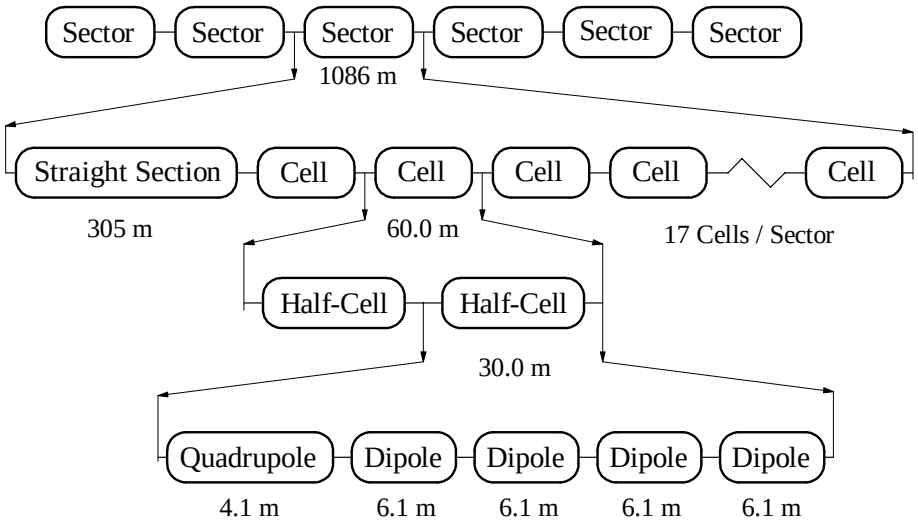

Figure 2.4: Structure of a Tevatron sector.

Figure 2.5 illustrates schematically the structure of one cryogenic sector. The cryoplants provide helium and nitrogen at different states (header C and header E) to the cryogenic distribution line. The satellite refrigerators are supplied in liquid helium by the central helium liquefier. In stand-by mode, the magnets can be cooled only by the nitrogen plant and the satellite refrigerators [22] [23].

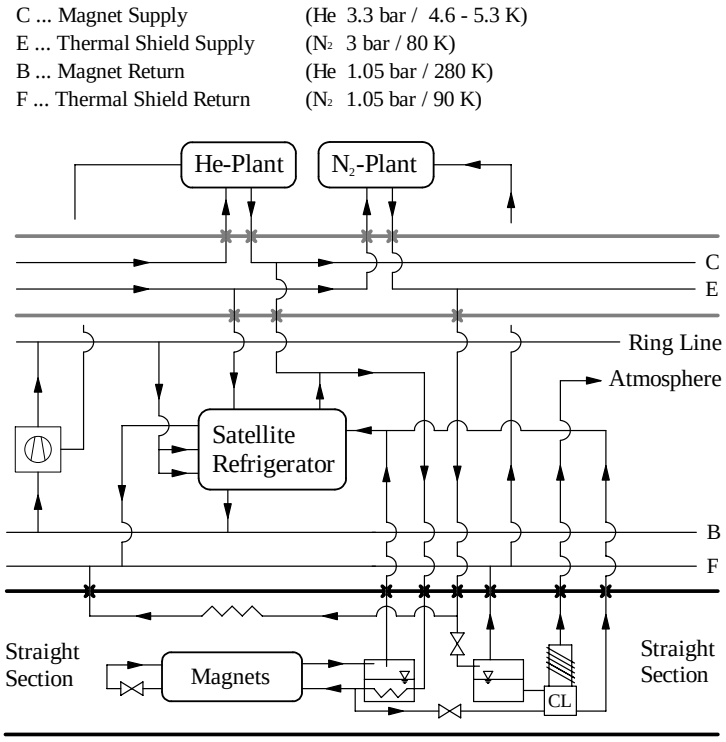

Figure 2.5: Schematic of the Tevatron cryogenic sector "B".

- **Cold Mass Cooling:** In nominal operation ("satellite mode"), helium at 3.3 bar and 5 K is mixed with helium exiting the satellite refrigerator. The total flow is cooled down in a heat exchanger by returning two-phase helium and then passes the magnets, extracting the heat load. At the sector's end, the warmed-up single-phase helium flow is expanded in a Joule-Thomson valve into the two-phase region and conveyed back through the magnets extracting heat and re-cooling the opposing single-phase helium flow. Any residual liquid helium at the sector inlet is vaporized in a separator with an integrated heat exchanger. The exiting helium vapour at a pressure of 1.2 bar is expanded in the satellite refrigerator and then discharged into the ring line B. The helium in line B is compressed by the compressor stations and conveyed to the helium plant and to the satellite refrigerators.

  In stand-by mode ("stand-alone mode"), the collider can be cooled only by the satellite refrigerators without operating helium plant. In this case, no cryogen is delivered by header C, but all the warmed-up helium is conveyed to the satellite refrigerators to be re-pressurized and re-cooled. The incoming helium flow is pre-cooled by a nitrogen flow coming from header E. A turbine generates additional cooling capacity by expanding a part of the helium flow. The pressurized and cooled helium then is conveyed along the same path as in the satellite mode.

Figure 2.6 illustrates the flow schemes in the two modes, where the not used lines and technical components are coloured in grey and the operating lines and technical components are coloured in black.

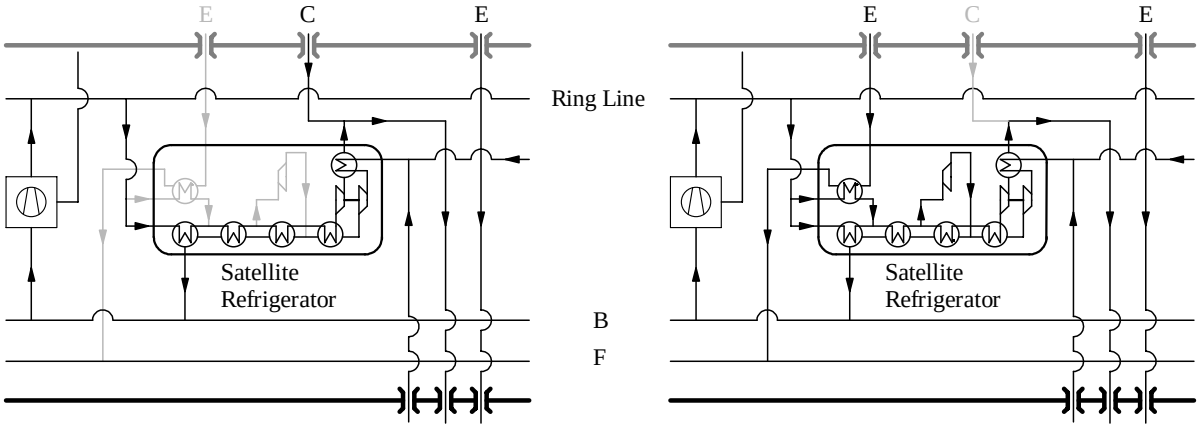

Figure 2.6: Satellite mode at high-load operation (left-hand side) and Stand-alone mode at low-load operation (right-hand side).

- **Thermal Shielding:** The nitrogen flow at 3 bar and 80 K passes the magnets heading to the sector end. After exiting the sector the warmed-up nitrogen flow is discharged to the ring line F and conveyed back to the nitrogen cryoplant.

- **Current Lead Cooling:** The current leads are cooled by both cryogens. The helium flow and the nitrogen flow are expanded into the two-phase region. The entire helium flow passes the lower (colder) part of the current leads, getting entirely vaporized, and is discharged to the satellite refrigerator. The nitrogen vapour is separated from the liquid and discharged to header F before the current leads are cooled. The liquid nitrogen then passes the upper (warmer) part of the current leads and extracts heat by getting vaporized at first and then by a temperature rise to ambient temperature level. The warmed-up nitrogen is released to the atmosphere [24].

2.2 HERA

The circular collider HERA at DESY in Hamburg was operated from 1992 to 2007. Protons ($\approx$ 920 GeV) and electrons ($\approx$ 27.5 GeV) were brought to collision, yielding a centre-of-mass energy of about 950 GeV. We only discuss here the proton ring which was superconducting.

Only helium was used as a coolant. Figure 2.7 shows schematics of the cryogenic distribution line (left-hand side) and a dipole (right-hand side) [25] [26].

- **Cryogenic distribution line:** The headers B, C and E are mounted using G-10 supports and thermally insulated by several layers of superinsulation and vacuum. The header F thermally shields the cryogenic distribution line and therefore is connected to the vacuum jacket.

- **Cold mass:** The cold mass is cooled by forced circulation of supercritical helium at 4.4 to 4.5 K, continuously re-cooled by heat exchange with the returning two-phase helium flow.

The supercritical helium passes the cold mass in three annular channels in parallel. One is located around the cold bore, between the beam tube and the coils, the other two are symmetrically arranged above and below the coils. The annular channel of the upper flow is formed by an integrated heat exchanger pipe holding the opposing two-phase helium flow. To achieve a symmetric magnetic field, the lower hole contains an aluminium filler, forming an identical channel for carrying the second single-phase flow. The thermal shielding pipe is mounted at a concentric jacket working as a heat intercept at intermediate temperature level.

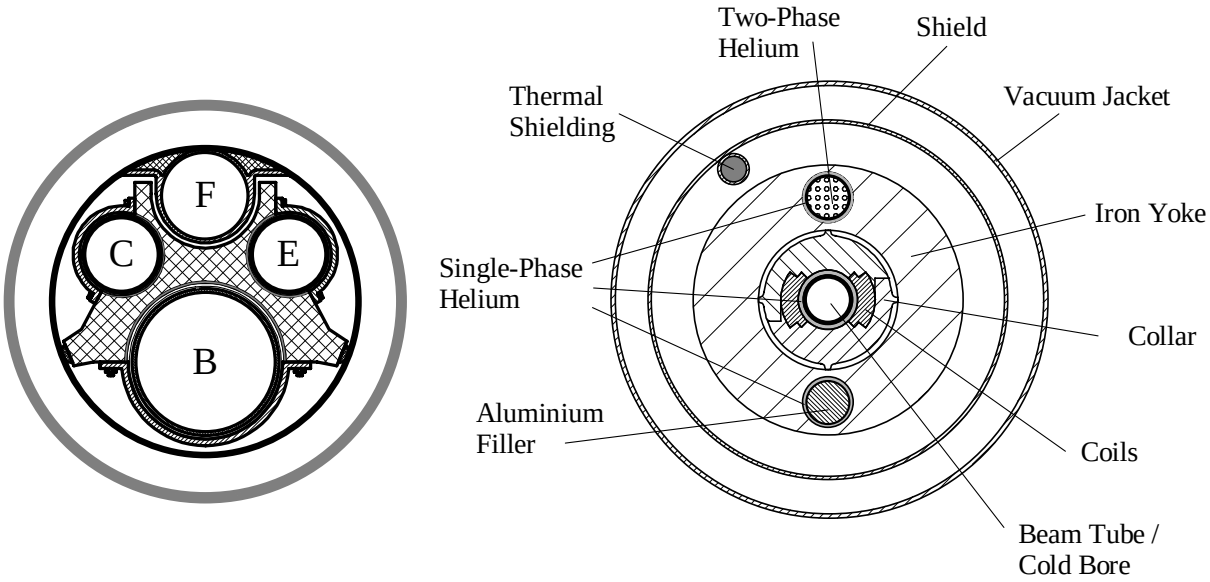

Figure 2.7: Schematics of the HERA cryogenic distribution line (left-hand side) and of a HERA dipole (right-hand side).

Three cryoplants, two of them are working in nominal mode and the third one is for redundancy in stand-by, located at the Western straight section provide the helium for the magnets and interaction points. The cryogenic distribution line is connected to the accelerator by feed boxes and middle boxes. Three room-temperature helium lines are installed parallel to the cryogenic distribution line. As illustrated in figure 2.8, HERA consists of eight sectors named after the cardinal points [27] [28].

The magnet pattern of HERA is schematically illustrated in figure 2.9. Each of the eight sectors consists of a half straight section and thirteen beam-bending cells. One cell can be divided into two half-cells which contain one quadrupole and two dipoles in series. The total perimeter of HERA amounts to about 6.3 km.

Figure 2.10 illustrates schematically the structure of two cryogenic sectors. The cryoplants provide helium at two different states (header C and header E) to the cryogenic distribution line.

- **Cold Mass Cooling:** Supercritical helium at 2.5 bar is cooled down to 4.4 K in a pre-cooler located in the feed boxes. The helium flow passes the magnets, heading to the middle box in which the warmed-up flow is expanded in a Joule-Thomson valve to the two-phase region. The returning two-phase helium re-cools the opposing single-phase flow by being vaporized. The exiting helium vapour is discharged into the header B and brought back to the cryoplants. Any residual liquid is collected in the pre-cooler.

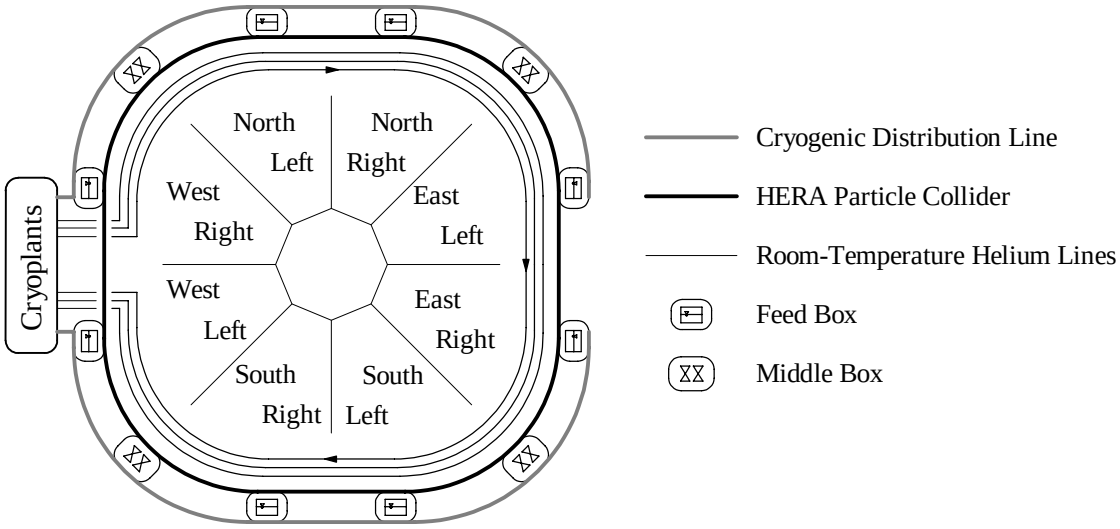

Figure 2.8: Schematic of the HERA circular collider and its basic cryogenic structure.

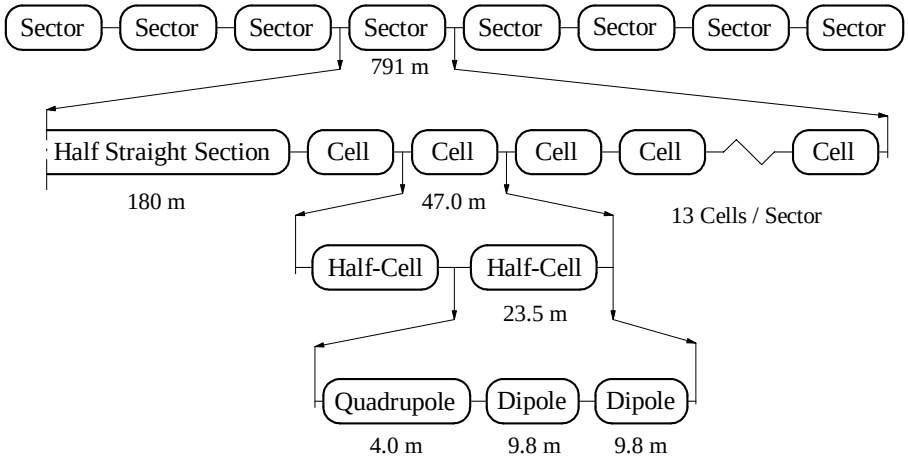

Figure 2.9: Structure of a HERA sector.

- **Thermal Shielding:** Helium at 18 bar and 40 K is distributed in the feed boxes to thermal shields and then passes the magnets, heading to the sector end. In the middle box, the warmed-up helium flow is discharged to the header F and conveyed back to the cryoplants.
- **Current Lead Cooling:** Supercritical helium at 4.4 K cools the current leads located in the feed boxes. The exiting warm helium gas at ambient temperature is discharged to one of the room-temperature ring lines and conveyed back to the cryoplants.

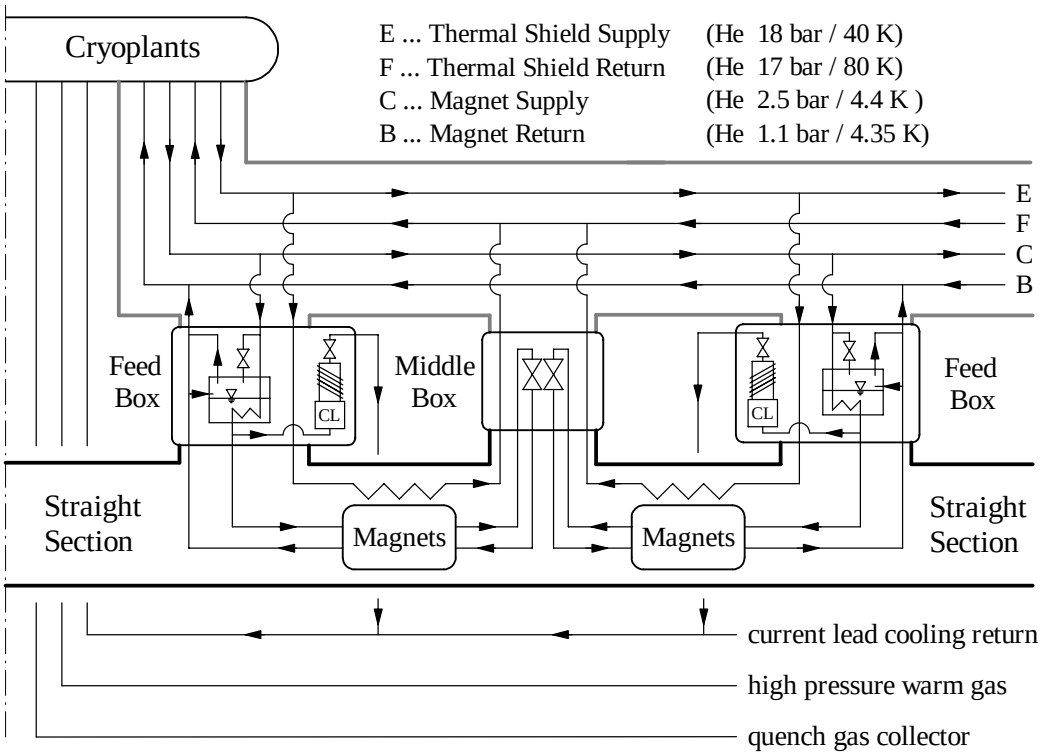

Figure 2.10: Schematic of the HERA cryogenic sectors "West Right" and "North Left".

2.3 Large Hadron Collider (LHC)

The circular collider LHC at CERN close to Geneva started its operation in 2008. After an incident and the subsequent repair works, the LHC was restarted in 2009, operating with half of the beam energy it was designed for (≈ 3.5 TeV per beam). This first run, in which the existence of the Higgs Boson was proven, lasted until 2013 before the LHC was stopped for two years to prepare the second run at design capacity. It was restarted in 2015 and now is in operation at beam energies of 6.5 TeV per beam, close to the expected value of 7 TeV.

The LHC superconducting magnets have twin apertures housing both circulating beams. The cold mass is immersed in a static superfluid helium bath, hydraulically disconnected from the circulated helium flows and continuously cooled by a HX tube in which a flow of two-phase helium extracts the heat. Figure 2.11 schematically shows the designs of the cryogenic distribution line installed parallel to the arc (left-hand side) and a dipole (right-hand side) [16].

- **Cryogenic distribution line:** The headers B, C and D are mounted using G-10 supports and thermally insulated by vacuum and layers of superinsulation. The surrounding shield is cooled by header F and also screened from heat leaks by superinsulation and vacuum [29].

- **Cold mass:** The entire cold mass is immersed in a static bath of superfluid helium at 1.9 K. Two-phase helium passes the heat exchanger tube ("bayonet heat exchanger"), extracting heat by getting vaporized. Two pipes are installed at the thermal shield, containing the helium flow delivered by header E. A solid connection to the support posts enables a high-temperature heat intercept. A second, low-temperature heat intercept of the support posts

is realized by the helium flow coming from header C. The beam screens located in the center of the two beam apertures are hydraulically connected in series with the low-temperature support post cooling flow.

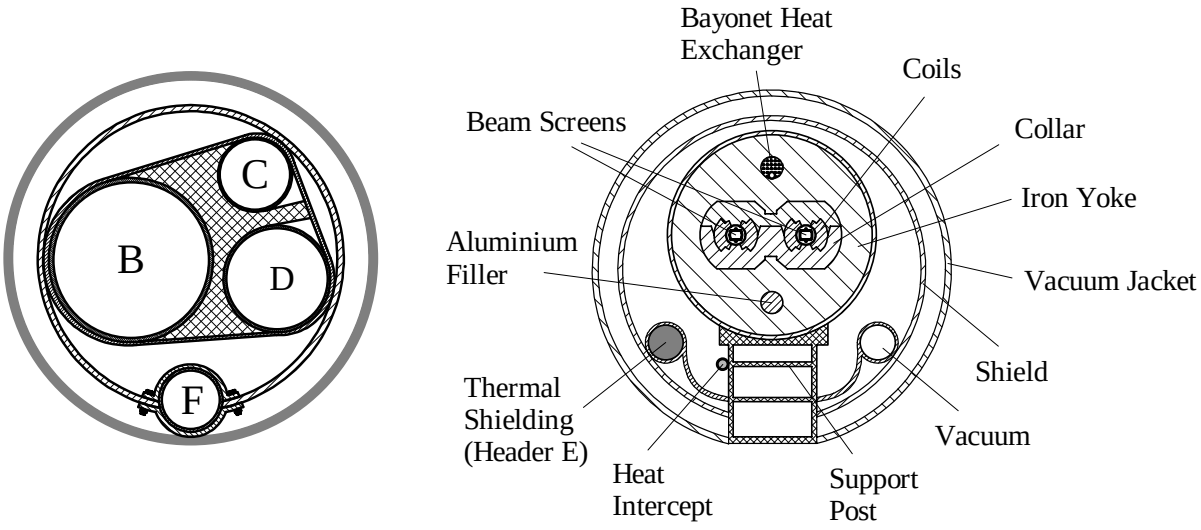

Figure 2.11: Schematics of the LHC cryogenic distribution line (left-hand side) and of an LHC dipole (right-hand side).

Experimental detectors, cavities and other necessary facilities to run the machine are distributed along eight straight sections, numbered consecutively from 1 to 8. The names of the cryogenic sectors (arcs) between two straight sections consist of the two numbers of the adjacent straight sections. Each cryogenic sector is supplied by one cryoplant (CP). The design foresaw the installation of always two cryoplants in the same location, as indicated in figure 2.12, to decrease the construction effort and for reasons of redundancy. This arrangement wasn't complied with for the sectors 12-23 in order to reuse the large cryoplant feeding the magnet test station [16].

Each LHC sector consists of one arc and two half straight sections. The cryogenic distribution line is installed parallel to the arcs and connected by so-called jumper connections every 107 m. The magnet pattern of the LHC for one sector is schematically illustrated in figure 2.13. Each (standard) cell can be divided into two half-cells - each half-cell of about 54 m length consists of one quadrupole and three dipoles in series. Figure 2.14 shows one arc subdivided into 23 cells, each of them connected to the cryogenic distribution line (QRL) by a jumper connection. The total perimeter of the LHC amounts to about 26.7 km.

The large room-temperature compressor stations and the major parts of the cryogenic facilities are located above ground. Vertical transfer lines housed in shafts are installed to transfer cryogen to and from the underground facilities. The final distribution and collection is done in a cavern which also contains a cold compressor station to compress helium vapour at very low pressure ($\approx$ 16 mbar) and then pump the compressed helium vapour ($\approx$ 1 bar) up to the cryoplant. Each cell is provided with helium by the two adjacent jumper connections - the cold mass cooling system of one entire cell is supplied by only one jumper connection, whereas the support post cooling and the beam screen cooling systems are supplied by the closer jumper connection, as schematically illustrated in figure 2.15 [16].

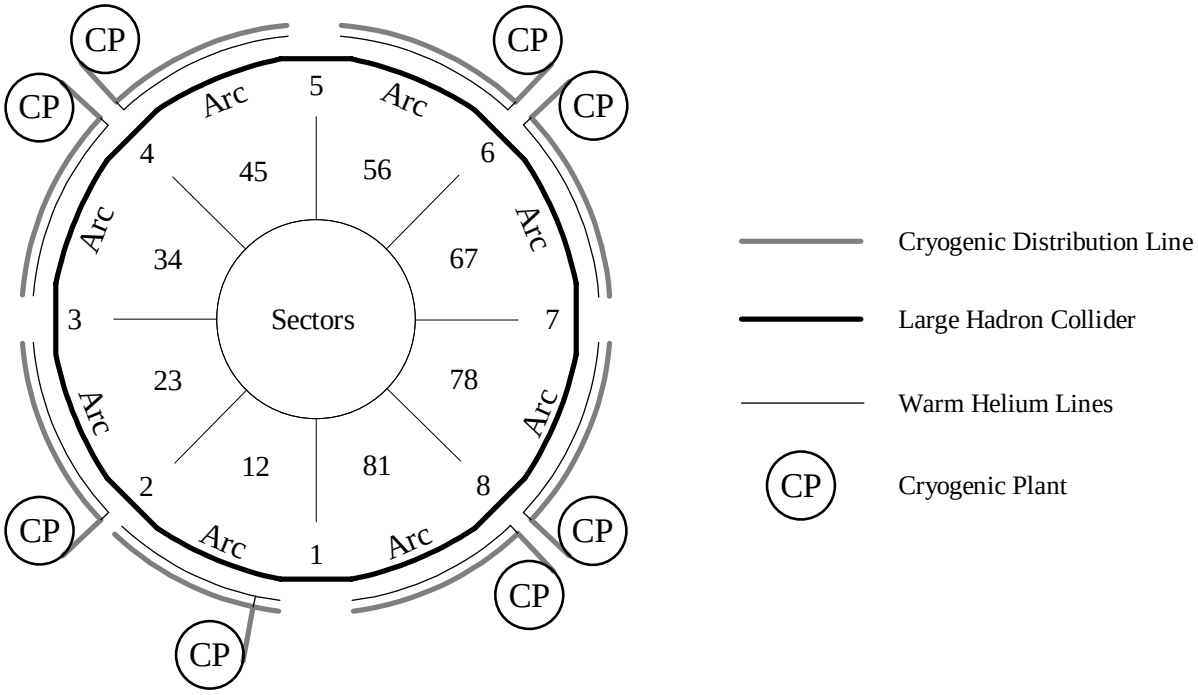

Figure 2.12: Schematic of the Large Hadron Collider and its basic cryogenic structure.

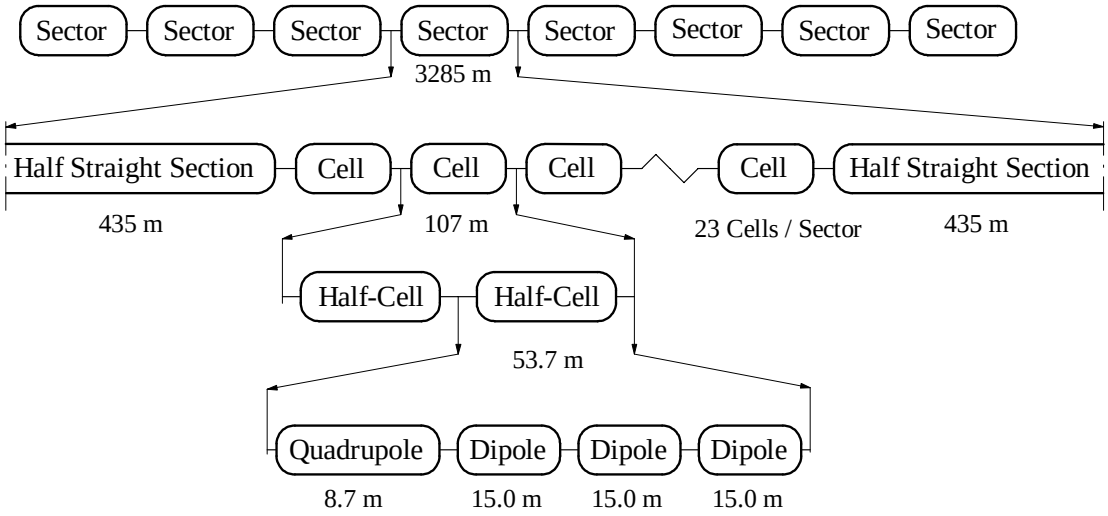

Figure 2.13: Structure of an LHC sector.

- **Cold Mass Cooling:** In each jumper connection, helium at 3 bar and 4.5 K from header C is delivered to one cell. After being cooled down by the returning helium vapour to about 2.2 K, it is expanded in a Joule-Thomson valve to the two-phase region, changing to the superfluid state. The two-phase flow passes the heat exchanger tube, extracting heat from the cold mass by being vaporized entirely. After leaving the cell, the helium vapour cools down the incoming helium flow and is then discharged into header B.

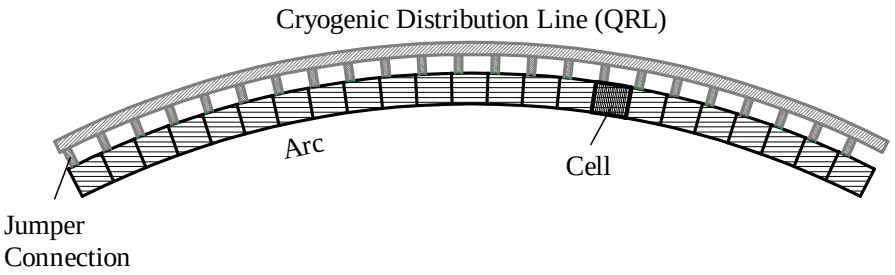

Figure 2.14: LHC arc, subdivided into 23 cells and its connection to the cryogenic distribution line (QRL).

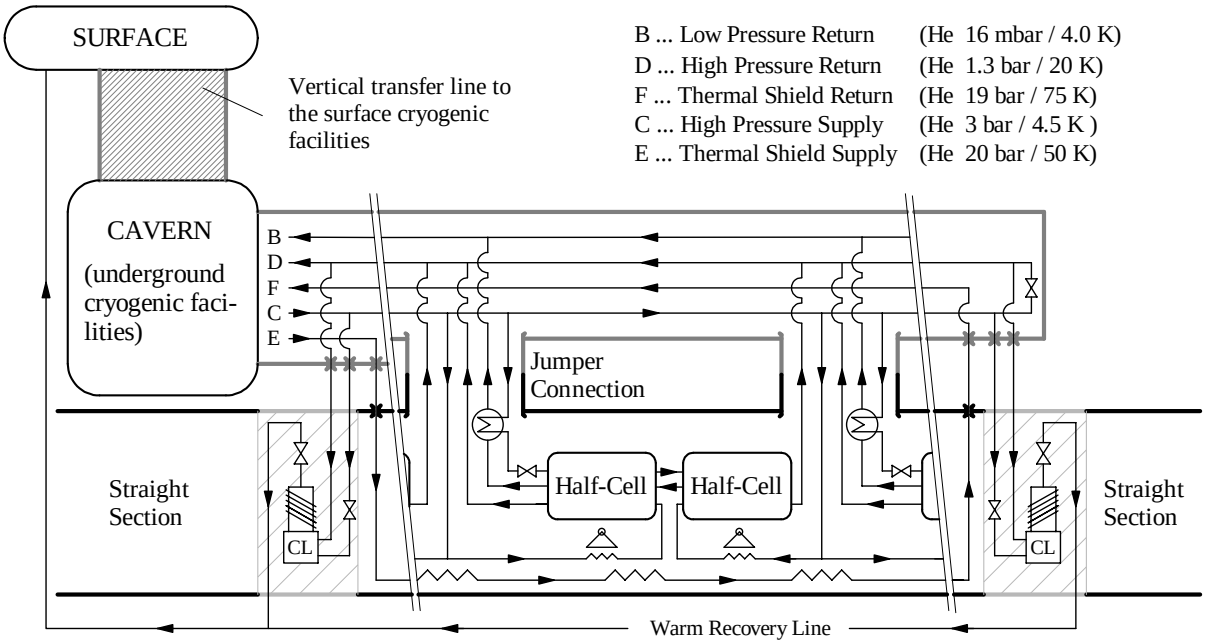

Figure 2.15: Schematic of the hydraulic scheme of an LHC cryogenic sector and the distribution system of a cell.

- **Thermal Shielding:** Close to the beginning of the arc, header E containing helium at 20 bar and 50 K leaves the cryogenic distribution line and enters the magnet vacuum jacket of the LHC. The helium flow thermally shields one entire arc before it is conveyed back to the cryogenic distribution line transitioning into the return header F.

  An additional helium flow from header C generates a second heat intercept at the support posts at about 4.6 K. After absorbing the heat leaks, the flow returns and is conveyed into the magnets to cool the beam screens.

- **Beam Screen Cooling:** The beam screens are cooled at a higher temperature level by the helium coming from the support post cooling (5 - 20 K). After extracting the heat load due to the beam induced losses, the helium flow is discharged into header D.

- **Current Lead Cooling:** The current leads are located close to the beginning and the end of an arc. A small helium flow from header C is expanded to the two-phase region (4.26 K and 1.3 bar) and then cools the lower (colder) part of the current leads by being vaporized.

A second helium flow from header D at 1.3 bar and 20 K is mixed with the vaporized helium ascending, and the total flow extracts the heat from the upper part of the current leads up to ambient temperature. The helium vapour then is discharged to the warm recovery line and returns to the surface cryoplants.

2.4 Future Circular Collider (FCC)

The approximate position of the FCC is shown in figure 1.1. This is the largest circular machine which can be installed in the Geneva basin, without entering neighbouring mountain formations with geology less suitable for tunnelling. The FCC project, as ambitious as it is, has reached its maximal size to be built close to CERN. The big advantage of this location is the existing infrastructure to operate the FCC. During the development of CERN, the constructed colliders increased gradually in size. The existing colliders are used to pre-accelerate the proton beams to insert them into the next-larger one. The LHC therefore, the presently largest existing particle collider, would work as a pre-accelerator for the FCC.

The successful design applied in the LHC to integrate both proton beams in one magnet was adopted for the FCC magnets as well as the cold mass cooling with two separated superfluid helium sources (the static pressurized bath and the two-phase flow in the bayonet heat exchanger). Figure 2.16 shows schematics of the cryogenic distribution line installed parallel to the arc (left-hand side) and an FCC dipole (right-hand side).

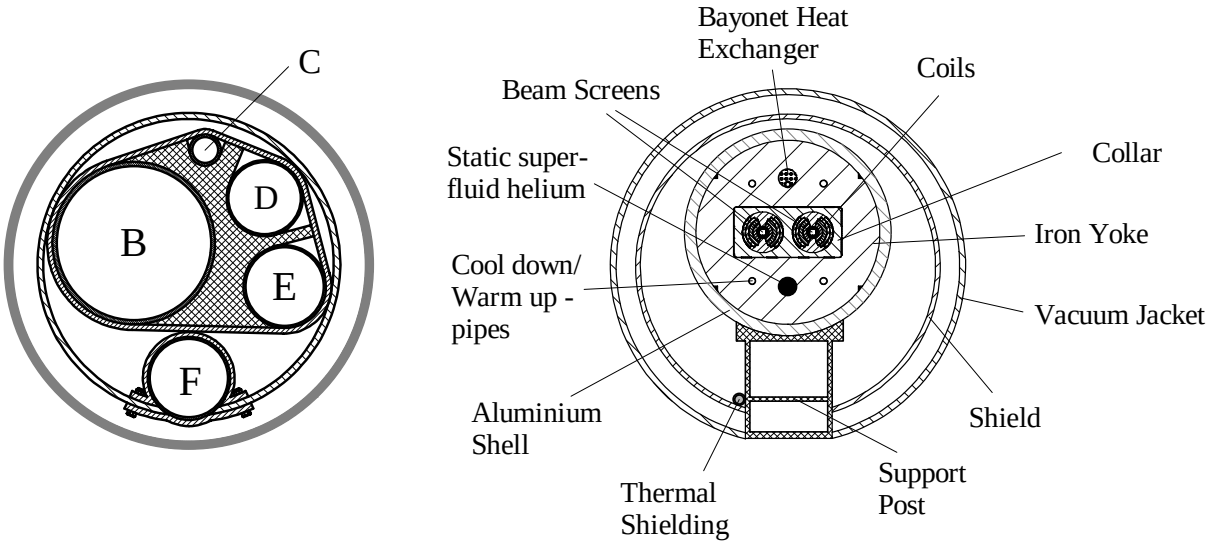

Figure 2.16: Schematics of the FCC cryogenic distribution line (left-hand side) and of an FCC dipole (right-hand side).

- **Cryogenic distribution line:** The FCC cryogenic distribution line houses all headers (B, C, D, E and F) along the entire arc's length, it is thermally shielded by header F. The final design does not exist yet. The illustration shown in figure 2.16 is a schematic drawing.

- **Cold mass:** The cold mass is immersed in a static bath of superfluid helium at 1.9 - 2 K. Two-phase helium passes the heat exchanger tube (the bayonet heat exchanger), extracting heat by getting vaporized. For the cool-down and warm-up, four hydraulically separated

pipes are used to protect the cold mass from high pressures. Since there is no longitudinal flow through the cold mass during cool-down and warm-up, there is no need to block the symmetric hole and it can be used for the heat conduction in the static helium bath. The thermal shielding pipe can be kept small due to the small mass flow rates. The contained flow cools the thermal shield and the support posts at 60 K. The beam screens located in the center of the two cold bores are hydraulically connected to the thermal shielding pipe in series. The final design of the FCC magnets does not exist yet. The illustration shown in figure 2.16 is a schematic drawing.

The FCC cryogenic layout is based on the LHC cryogenic system. The baseline foresees a ten-fold sectorization of the FCC cryogenic distribution system - eight long sectors with a length from 9.3 to 10.6 km each and four short sectors with a length of 5.8 km. Ten cryoplants in six locations provide the arcs with helium. The general structure of the cryogenic distribution system is illustrated in figure 2.17, where the naming of important locations follows the letters of the Latin alphabet in ascending order. Like in all the other presented concepts, different equipment is located in the straight sections (e.g. RF cavities, beam insertion/dump, experimental detectors, etc.). The special cryogenic requirements of these items are not dealt with in this thesis.

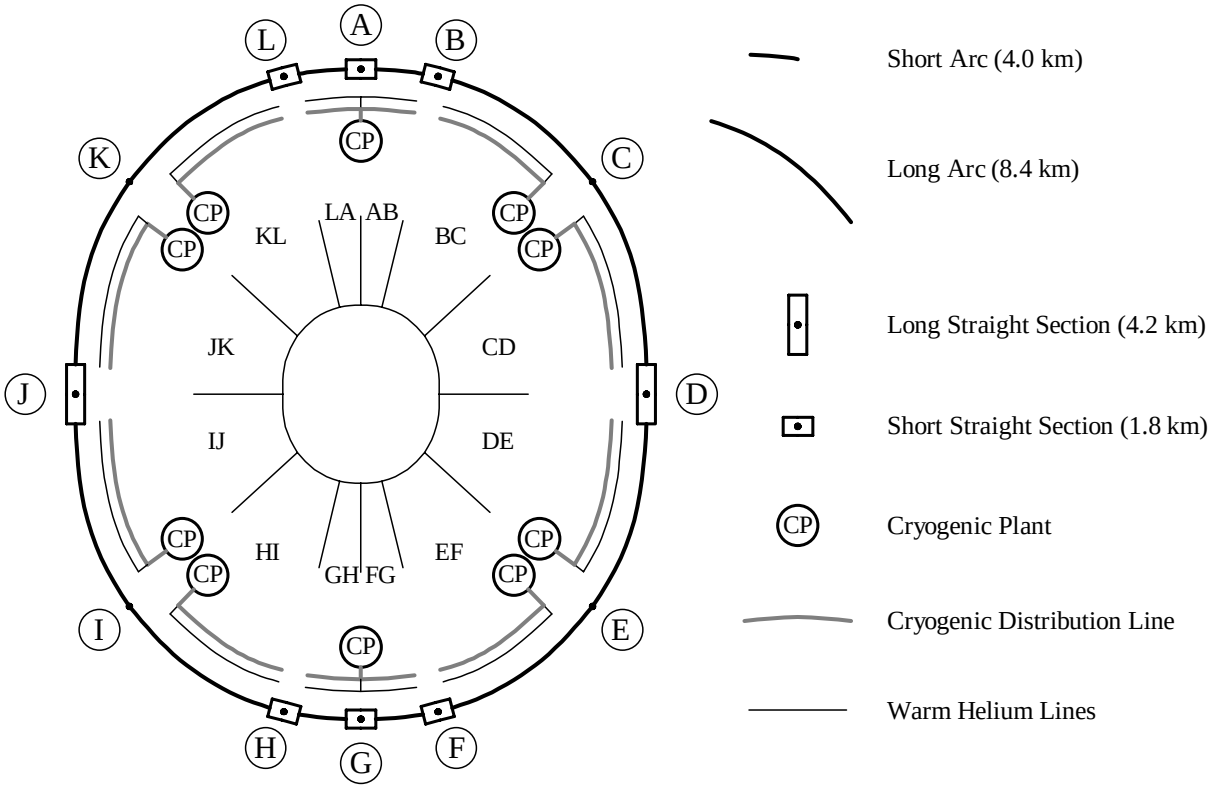

Figure 2.17: Schematic of the FCC cryogenic layout (Baseline).

For geotechnical reasons, the FCC is constructed with a slight slope reching 0.3 % with respect to a horizontal plane, which causes a maximal elevation difference of about ±25 m in the sectors C-D, D-E, I-J and J-K. The diagram in figure 2.18 illustrates the elevation of all the FCC sectors. The supplying cryoplant for each sector is assumed to be at the coordinates (0, 0), the abscissa shows the length of an arc in meters, the ordinate the corresponding elevation [30].

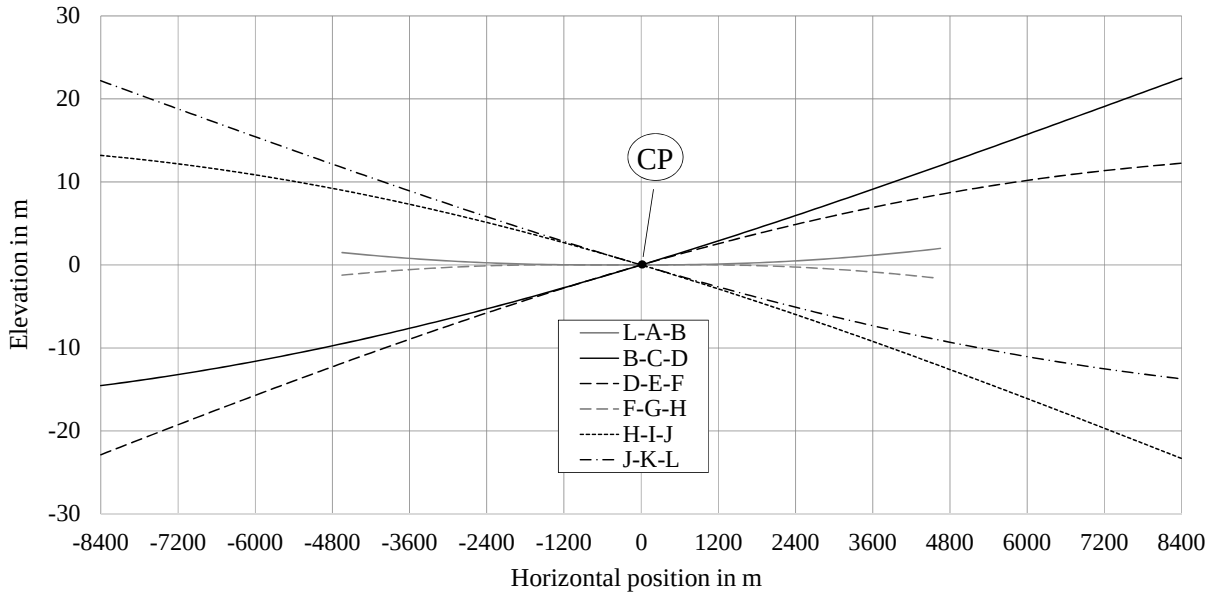

Figure 2.18: Elevation profiles of all the FCC sectors vs. the position along their lengths. In the diagram the supplying cryoplant is located at the coordinates (0, 0).

Due to the different sector lengths two different types of arcs (long arcs and short arcs) can be distinguished (see figure 2.19). Long arcs of 8.4 km of length are supplied by one cryoplant located at one of their ends, two short arcs are supplied in parallel by one cryoplant. The integration of two cryoplants at the same location saves effort for constructing the cavern as well as the vertical transfer lines to connect them to the surface facilities. Additionally, this arrangement permits a part-load redundancy - in case of failure of one cryoplant, the second one can take the refrigeration task to keep the arc at low temperature during repair works and/or maintenance. The provision of the cryogen along one entire long arc of course involves strong pressure losses and calls for larger pipe diameters to deliver and discharge the helium. Conversely, the design of a short arc cryogenic distribution saves operational costs at the redundancy's expense.

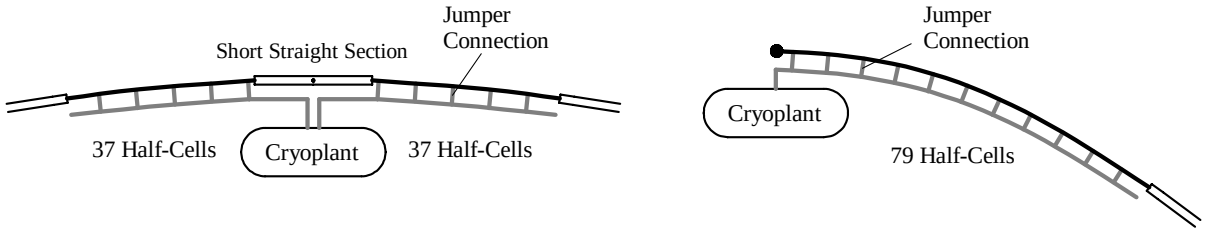

Figure 2.19: Two short arcs supplied by one cryoplant in parallel (left-hand side) and one long arc supplied by one cryoplant located at one arc's end (right-hand side).

As indicated in figure 2.19, one long arc contains 79 half-cells, one short arc 37. One half-cell has a length of about 107 m and consists of one quadrupole and six dipoles in series; each magnet has a length of 15 m. Each half-cell is connected to the cryogenic distribution line via a jumper connection, similar to the LHC. A schematic of the FCC half-cell is illustrated in figure 2.20.

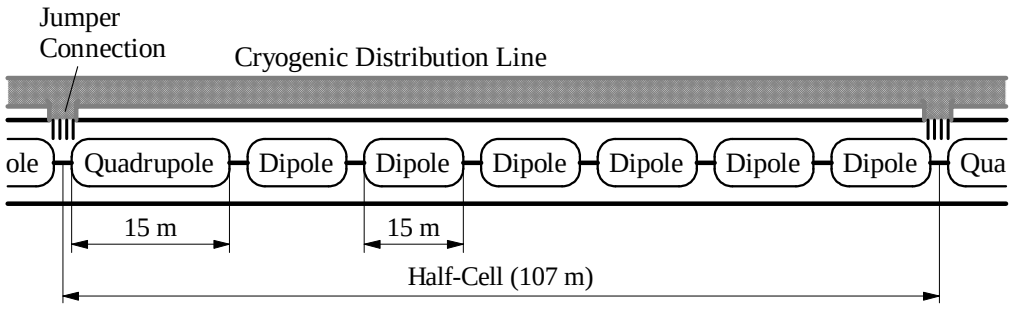

Figure 2.20: Schematic of an FCC half-cell and its connection to the cryogenic distribution line with jumper connections.

Figure 2.21 shows the recommended design of the underground cryogenic distribution system of the FCC. Explanations and details about the design and the decisions to find it are given in the following chapters of the thesis. All supply and return pipes meet in a cavern which is connected to the surface cryoplant by a vertical transfer line. The cavern also houses underground cryogenic facilities necessary for the dependable operation of the cold mass cooling cycle.

- **Cold Mass Cooling:** In each jumper connection, helium at 3 bar and 4.6 K from header C is delivered to one half-cell. After being cooled down by the returning helium vapour to 2.2 K, it is expanded in a Joule-Thomson valve to the two-phase region, changing to the superfluid state. The two-phase flow passes the heat exchanger tube extracting heat from the cold mass by being vaporized entirely. After leaving the half-cell the helium vapour cools down the incoming helium flow and is then discharged into header B.

- **Beam Screen Cooling:** Header E delivers helium at 50 bar and 40 K. In each jumper connection, a small helium flow is conveyed into the respective half-cell and cools the beam screens. The warmed-up helium ($\approx$ 60 K) then is conveyed to the thermal shielding pipe of the magnet vacuum jacket.

- **Thermal Shielding:** After having absorbed the heat load on the beam screen, the helium flow returns and thermally shields the magnet vacuum jacket of the same half-cell. The mass flow rate is controlled by a valve located in the jumper connection immediately before it is discharged into header F. The return header F thermally shields the cryogenic distribution line.

- **Current Lead Cooling:** The design up to now foresees a current lead cooling system almost identical to the LHC's one. The current leads are located close to the beginning and the end of an arc. A small helium flow from header C is expanded to the two-phase region (1.3 bar and 4.25 K) and then cools the lower (colder) part of the current leads by being vaporized. A second helium flow from header D (1.3 bar and 40 K) is mixed with the vaporized helium ascending, and the mixed flow extracts the heat from the upper part of the current leads up to ambient temperature. The helium vapour then is discharged to the warm recovery line and returns to the surface cryoplants.

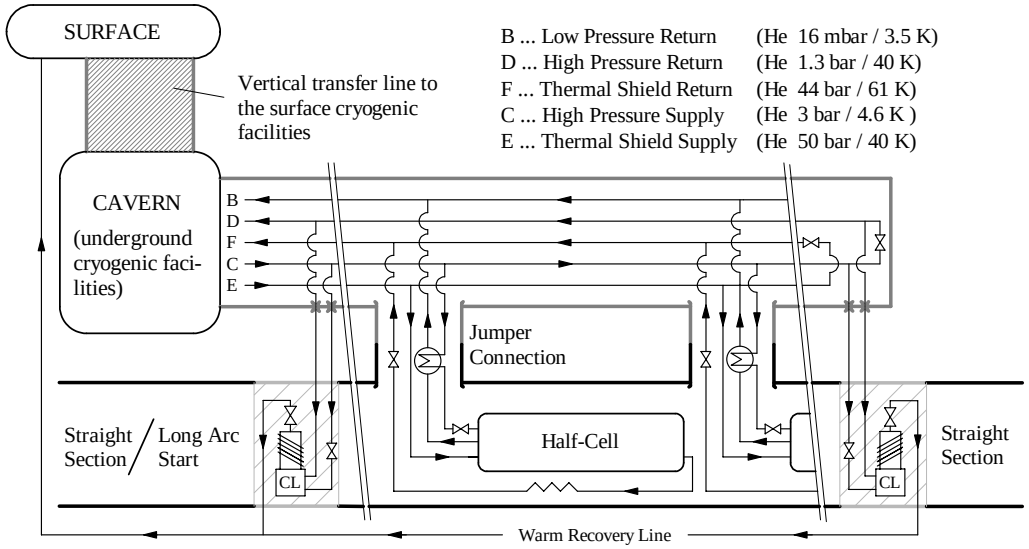

Figure 2.21: Schematic of the hydraulic scheme of an FCC cryogenic sector and the distribution system of a half-cell.

2.5 Comparison of key data of the presented circular colliders

Table 2.1 compares selected data for the requirements of the beam bending sections (arcs) of the three presented circular colliders to the expected values of the FCC [16] [28] [31] [32]. The main influence quantity for the design of the cryogenic distribution system are the heat load to be extracted and the corresponding temperature levels. The physically minimal necessary cooling powers without any losses were estimated - the comparison of these values alone shows the demands to the cryogenic facilities of the FCC. Although the LHC cryogenic system is about 20 times larger than the systems of the previous colliders, the dynamic heat loads in nominal operation are still lower than the static ones due to the introduction of the beam screen. Especially due to the large amount of synchrotron radiation emitted, this changes for the FCC and the dynamic heat loads will be a multiple of the static ones, placing new challenges to the transient operation of the FCC cryogenic system. The table below does not include the cooling of current leads.

Table 2.1: List of static and dynamic heat loads for the beam bending sections (arcs) of different circular colliders

Property	**HERA**	**TEVATRON**	**LHC**	**FCC**
Centre-of-mass energy	0.95 TeV	2 TeV	14 TeV	100 TeV
Circumference	6.3 km	6.5 km	27 km	100 km
Static heat loads (including distribution)	2.24 W/m @ 40 - 80 K	2.15 W/m @ 85 - 90 K	5.5 W/m @ 50 - 75 K	9.3 W/m @ 57 - 61 K
	0.17 W/m @ 4.4 K	0.14 W/m @ 4.6 K	0.085 W/m @ 4.6 - 20 K	–
	–	–	0.28 W/m @ 1.9 K	0.84 W/m @ 1.9 K
Dynamic heat loads	0.14 W/m @ 4.4 K	0.11 W/m @ 4.6 K	0.7 W/m @ 4.6 - 20 K	62.2 W/m @ 40 - 57 K
	–	–	0.15 W/m @ 1.9 K	0.8 W/m @ 1.9 K
Minimal required cooling power (Carnot)	0.19 MW	0.14 MW	2.88 MW	60.42 MW
Ratio of minimal required cooling powers to extract dynamic heat loads and to extract static heat loads	0.46	0.50	0.60	2.95

3 Basics of Cryogenic Refrigeration

The purpose of cryogenic refrigeration is the generation of very low temperatures (< 120 K). The applications range from the provision of some milliwatts at a temperature level of only a few millikelvins above absolute zero (e.g. measurement and analysis systems in outer space) to some kilowatts at higher temperature levels (e.g. cool-down of the LHC at CERN with nitrogen down to 80 K). The effort needed to provide the refrigerating capacity depends linearly on the heat load to be extracted from the facilities, machines and appliances and non-linearly on the required temperature level with respect to the ambient temperature. Figure 3.1 shows the minimal required power to extract 1 W of heat load depending on the desired temperature level for an assumed ambient temperature of 300 K ($\widehat{=}$ 26.85 °C). This is done with a reversible Carnot cycle, consequently the ratio represented by the ordinate on the diagram is called the Carnot factor. Real processes are less efficient due to irreversibilities.

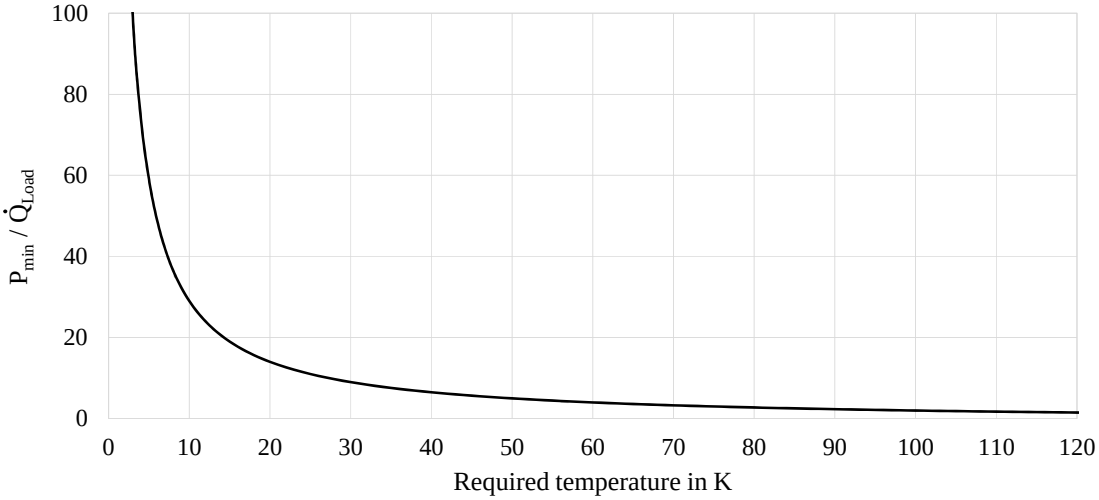

Figure 3.1: Minimal required power P_{min} in W to extract a heat load $\dot{Q}_{Load}$ of 1 W as a function of the required temperature level with an ambient temperature of 300 K.

At low temperatures, the necessary power effort increases strongly. Therefore, one major requirement of cryogenic engineering is to minimize the heat loads at the lowest temperature levels, e.g. by designing a good thermal insulation to protect the device against heat leaks from ambiance. The necessary refrigerating capacity can be additionally decreased by introducing thermal shields at different intermediate temperature levels to extract the major part of the heat leaks at higher temperatures. Another task is the minimization of irreversibilties due to the pressure losses in the cryogen flows. The necessary circulation/compression power increases with increasing pressure ratio and raises the heat to extract at cryogenic temperature level. The aim to minimize the pressure losses contradicts the requirement for smallest possible dimensions (e.g. pipe diameters) and to

use as few technical equipment as possible (e.g. number of valves) to decrease the capital costs and increase the reliability. Additionally, other design constraints can occur with respect to the application and the functionality. Cryogenics in the FCC is an ancillary installation and has to be subordinated to the requirements of the main components to fulfil their purpose (particle physics).

The structure and analysis of the cryoplants is not part of this thesis. For sake of completeness, however, some important thermodynamic cycles used in cryogenic engineering are briefly presented. Only a few substances can be used as coolants for low temperature applications, particularly due to the solidification of almost all substances close to absolute zero. For the ecological and economical assessment of the cryogenic distribution system, an exergy analysis presents itself, as the operational costs can be directly read from the resulting numbers. Some basic information regarding these three topics is summarised in this chapter.

3.1 Some thermodynamic cycles to generate very low temperatures

A thermodynamic cycle passed in the counter-clockwise direction in a T,s diagram represents a refrigeration process to extract heat at low temperature and release it at higher temperature [33]. In cryogenic engineering, many elaborate cooling schemes were developed, designed for the special requirements of the corresponding purpose. However, three basic refrigeration cycles are of particular significance for cryogenics as they provide a basis for most of the existing applications. They are briefly presented in this section [34].

3.1.1 Brayton cycle

The ideal Brayton cycle consists of two isobaric (④ → ① and ② → ③) and two adiabatic (① → ② and ③ → ④) changes of state, where the latter changes are isentropic if reversible. By applying work and passing the Brayton cycle counter-clockwise, temperatures below the ambiance's can be achieved. Figure 3.2 shows the basic set up of a Brayton machine and the corresponding thermodynamic cycle in the T,s diagram.

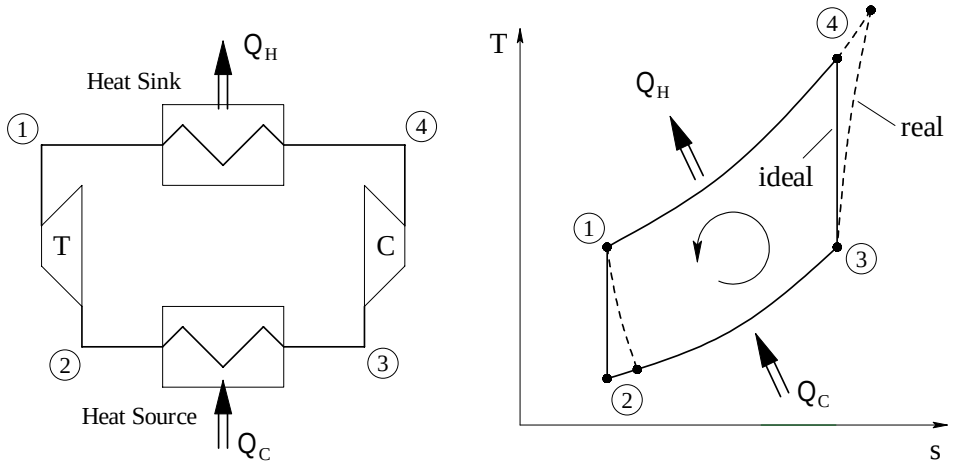

Figure 3.2: Technical arrangement of a Brayton cycle for refrigeration and process in the T,s diagram. The dashed lines indicate the real process.

3.1.2 Linde cycle

The ideal Linde cycle was developed for air liquefaction - it makes use of the temperature decrease during an isenthalpic expansion of gases below the inversion temperature (Joule-Thomson effect). To bring the gas to a temperature below inversion, it is first cooled down (① → ②) in a counterflow heat exchanger and then is expanded isenthalpically in the two-phase region (② → ③). The generated vapour fraction and any vaporized cryogen pass the heat exchanger absorbing heat from the counterflow (③ → ④). The gas flow then is para-isothermally compressed (④ → ①) and the cycle restarts. Figure 3.3 shows the basic set up of a Linde gas liquefaction arrangement and the corresponding thermodynamic cycle in the T,s diagram.

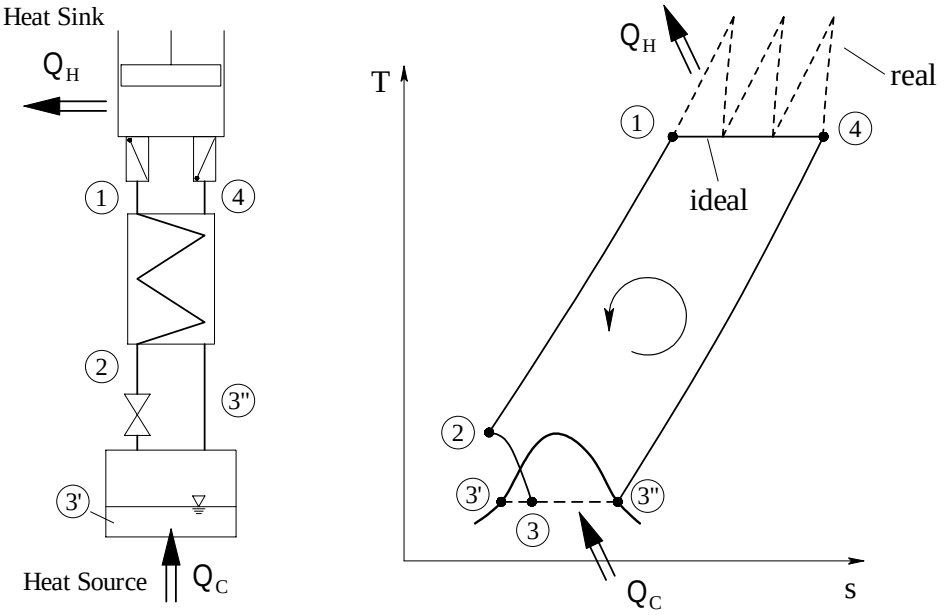

Figure 3.3: Technical arrangement of a Linde cycle for refrigeration and process in the T,s diagram. The dashed lines indicate the real process.

3.1.3 Claude cycle

The ideal Claude cycle combines the Linde cycle with intermediate Brayton stages and makes use of their cooling power to compensate for the temperature "pinch" in the heat exchangers resulting from the different specific heat capacities of the helium flows at different pressure levels. Its fundamental version is the basis for the common refrigeration processes to generate very low temperatures in cryogenic facilities of particle colliders. Figure 3.4 shows a Claude refrigerator with a single Brayton stage and the corresponding thermodynamic cycle in the T,s diagram. The number of intermediate Brayton stages can be increased for optimizing the cycle.

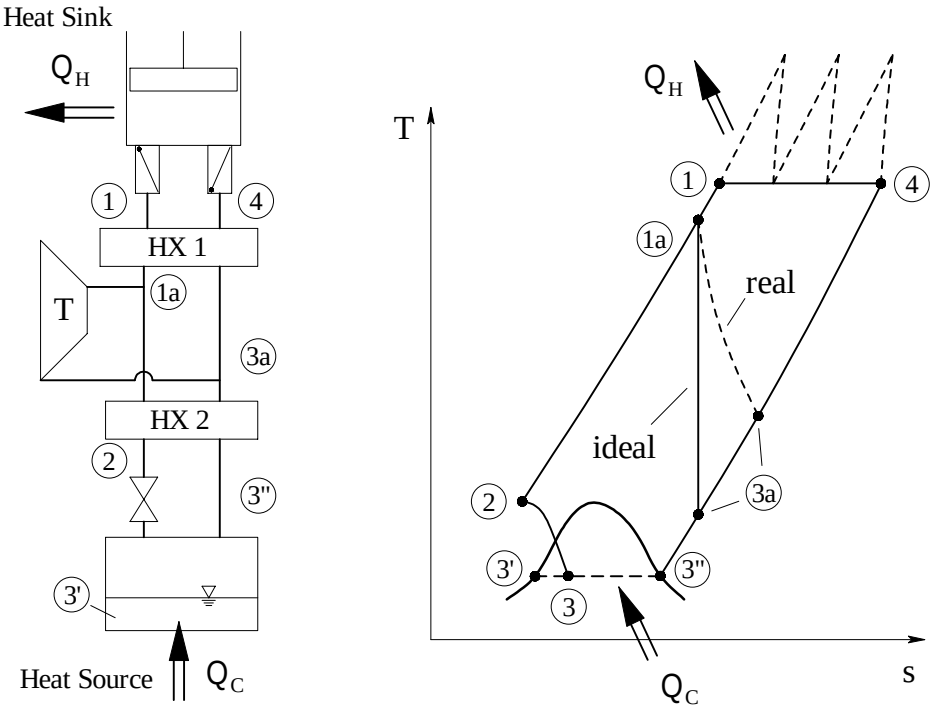

Figure 3.4: Technical arrangement of a Claude cycle for refrigeration with a single Brayton stage and process in the T,s diagram. The dashed lines indicate the real process.

3.2 Cryogens

The main requirement for coolants in cryogenic applications is a very low solidification point. Only a few substances, so-called cryogens, fulfil these demands. Table 3.1 lists the three most common cryogens for cooling applications in particle accelerators and a selection of important thermodynamic properties [33].

Table 3.1: Commonly used cryogens in particle accelerators

Name	**Triple point temperature in K**	**Triple point pressure in mbar**	**Critical temperature in K**	**Critical pressure in bar**
Helium*	2.17**	51**	5.20	2.29
Neon	24.6	433	44.41	27.22
Nitrogen	63.2	126	123.1	33.94

* Refers to He^4 with a mass number of 4; contrary to the much rarer He^3
** λ-Point values

3.2.1 Helium

Helium is an indispensable coolant for attaining temperature levels close to absolute zero, since it is the only substance which cannot be solidified below a pressure of 25 bar, therefore it has no triple

point. It shows unique properties tailor-made for its use in cryogenics. Figure 3.5 illustrates the phase diagram of He^4. The liquid phase is separated by the so-called λ-line in two regions: Above the λ-temperature, the liquid phase is called Helium I (He I) or normalfluid helium. Entering the superfluid region of Helium II (He II), the properties of the liquid helium change abruptly, showing remarkable qualities for cooling applications [36].

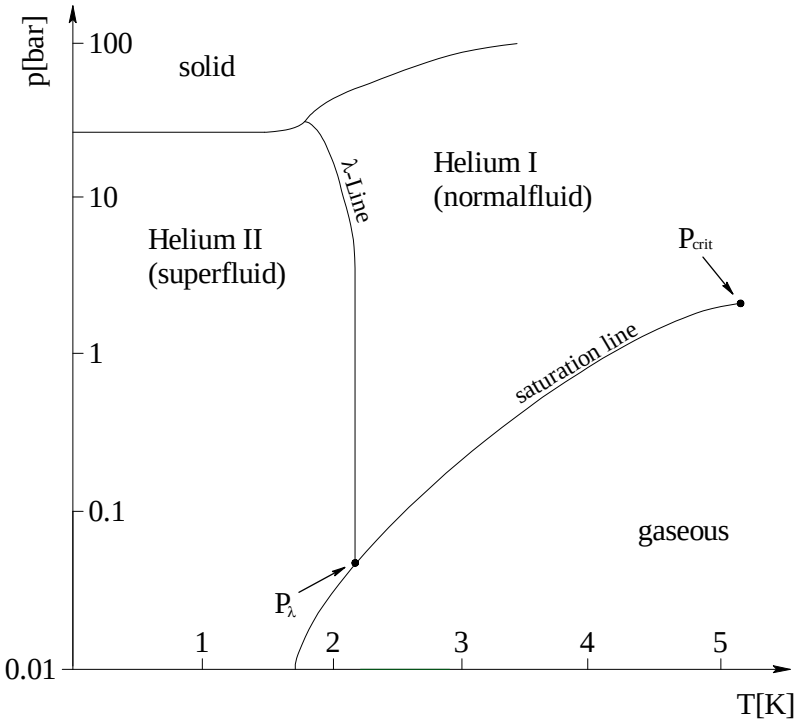

Figure 3.5: Phase diagram of helium (He^4).

3.2.1.1 Two-fluid model of superfluid helium

Above the λ-temperature, the experimentally determined dynamic viscosity of He I is almost constant. After the transition to He II, it decreases. The viscosity measurements at varying temperature yield different results, depending on the measurement method. By determining the flow velocity while passing capillaries with small diameters, a decrease of the viscosity by more than ten orders of magnitude compared to normalfluid helium was obtained. Interestingly enough, the flow viscosity increases with decreasing capillary diameter and constant pressure [35].

Another surprising behaviour of He II is called the thermomechanical effect. Two communicating vessels Ⓐ and Ⓑ filled with superfluid helium are connected with a small capillary. By increasing the pressure in, say, vessel Ⓐ, superfluid helium is pushed through the capillary and the liquid level in vessel Ⓑ rises. The mass flow, however, is accompanied by an opposed heat transfer, so that the helium temperature in vessel Ⓐ increases with respect to vessel Ⓑ. After removing the pressure difference, the system returns to its initial state [35].

These two phenomena can be described by using the phenomenological two-fluid model proposed by the Soviet physicist L. Landau based on ideas from the Hungarian physicist L. Tisza [37]. The basic idea is to model He II as a blend of a superfluid with a density of ρ_s and a normalfluid component with a density of ρ_n. The mass-ratio of the two components can be calculated using

the λ-point temperature ($T_\lambda = 2.17$ K) and density ($\rho_\lambda = 146.15$ kg/m^3). The diagram in figure 3.6 illustrates the composition of He II as a function of the temperature.

$$\rho = \rho_n + \rho_s \tag{3.1}$$

$$\rho_n = \rho_\lambda \left(\frac{T}{T_\lambda} \right)^{5.6} \quad for\ T \leq T_\lambda \tag{3.2}$$

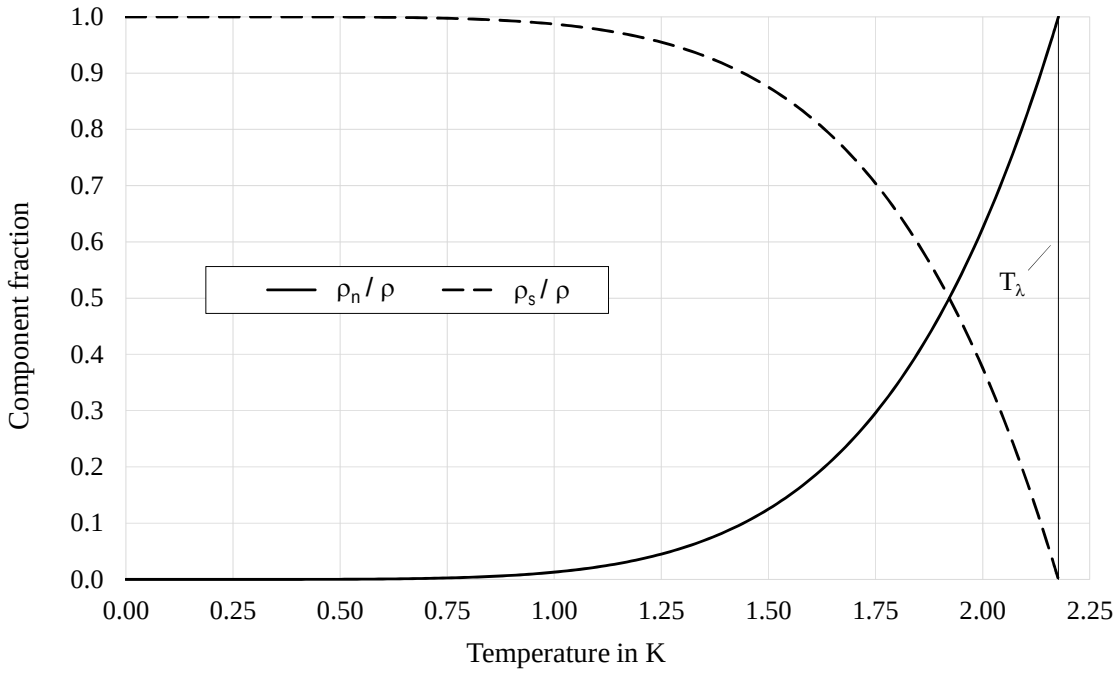

Figure 3.6: Composition of He II as a mixture of a superfluid component and of a normalfluid component vs. the temperature.

The superfluid component is assumed to have zero viscosity and zero entropy. With decreasing capillary diameter, the normalfluid component is blocked and (almost) only the superfluid component passes - therefore no flow resistance occurs. With the same argumentation, the thermomechanical effect can be clearly explained. With increased pressure in vessel Ⓐ, in particular the superfluid component is pushed into vessel Ⓑ and the mixture compositions in the two vessels change. According to (3.2) the temperatures vary.

3.2.1.2 Heat transfer in superfluid helium

By mentally reversing the thermomechanical effect, He II can be used to transport energy from a heat source to a heat sink. By absorbing heat, the superfluid helium component is transformed into normalfluid. The entropy carrying normalfluid component flows to the heat sink, driven by a pressure difference generated by the different mixture compositions. At the heat sink, the entropy of the normalfluid component is removed, turning it into superfluid again. The correlation between pressure difference, temperature difference and exchanged heat ($\widehat{=}$ transported entropy) was derived by H. London [35]. Figure 3.7 illustrates schematically the heat transfer due to the reversed thermomechanical effect.

$$\frac{\Delta p}{\Delta T} = \rho\, s \tag{3.3}$$

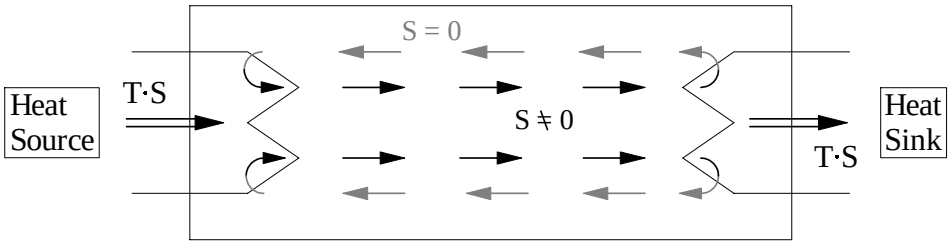

Figure 3.7: Opposing helium flows in Landau's two-fluid model. Only the normalfluid component (black) carries entropy, the superfluid component's (grey) entropy and viscosity are zero.

In a closed vessel the net helium flow is zero and the heat is transferred by internal convection [38]. If the heat flux to transport is low (i.e. low velocities) and the flow channel is narrow, the opposing helium flows are laminar, resulting in a linear correlation between the temperature gradient and the transferred heat. By exceeding a critical heat flux, and subsequently a critical velocity, the helium flows enter the turbulent regime, impeding each other and the correlation between the transferred heat and the temperature gradient becomes non-linear [39] [40]. The steady-state heat transport problem can be solved analytically and the temperature gradient can be expressed as a function of the helium component velocities. Substituting the velocities using mass consistency yields (3.4) [41].

$$\frac{dT}{dz} = \underbrace{-\frac{\beta\,\mu_n}{d^2\,(\rho\,s)^2\,T}\,\dot{q}}_{Landau\ regime} \quad \underbrace{-\frac{A_{GM}\,\rho_n}{\rho_s^3\,s^4\,T^3}\,\dot{q}^m}_{Gorter-Mellink\ regime} \tag{3.4}$$

The first term on the RHS of (3.4) is named after Landau and describes the heat transfer in the laminar flow regime. β denotes a geometrical factor of the channels derived from the Hagen-Poisseuille equation for laminar flow, μ_n denotes the dynamic viscosity of the normalfluid component and d denotes the hydraulic diameter or slit height of the flow cross section [35]. The second term on the RHS of (3.4) is named after C. J. Gorter and J. H. Mellink and describes the heat transfer in the turbulent case [42]. The Gorter-Mellink coefficient A_{GM} summarises the influence of several state variables and therefore itself is a state variable. The temperature gradient generated is not linearly dependent on the heat flux, the exponent m, according to the theory, takes a value of 3.

Due to the similarity of (3.4) and Fourier's law, it has become established to call the heat transfer in He II a heat conduction and an apparent (or effective) thermal conductivity was introduced to describe the heat transport driven by the internal convection. Consequently, the inverse of the fraction in front of the heat flux in (3.4) is called the thermal conductivity function f_k^{-1} [41].

$$\frac{1}{f_k} = \frac{\rho_s^3\,s^4\,T^3}{A_{GM}\,\rho_n} \tag{3.5}$$

However, measurements performed during experiments yielded values of the exponent m and the thermal conductivity function f_k^{-1} different from the theory's predictions. The best experimental

fit for the exponent m was determined to be 3.4 - the corresponding thermal conductivity function can be retrieved by an approximation formula or in tabulated form [43]. Figure 3.8 shows the thermal conductivity of He II as a function of the temperature predicted by the theory (solid line) and calculated with two mathematical fits, which yield the experimentally obtained thermal conductivity function as a function of the temperature. The dashed line represents the more accurate equation generated by a tenth order polynomial and a pressure correction term ($p = 1.3\ bar$) [41]. The dash-dotted line represents the results of an approximation equation (3.6) to obtain the thermal conductivity in the desired temperature range (1.8 K – 2.0 K), where the temperature T enters the formula in kelvin. The thermal conductivity shows a maximum close to a temperature of 1.9 K. For this reason, among others, cryogenic applications using superfluid helium are designed to operate close to this temperature.

$$\frac{1}{f_k} = 825\left\{1 - cos\left[6.05\ sin\left(2.1\left(T_\lambda - T\right)\right)\right]\right\} \cdot 10^{11.6} \quad \text{in} \quad \frac{W^{3.4}}{m^{5.8}\,K} \tag{3.6}$$

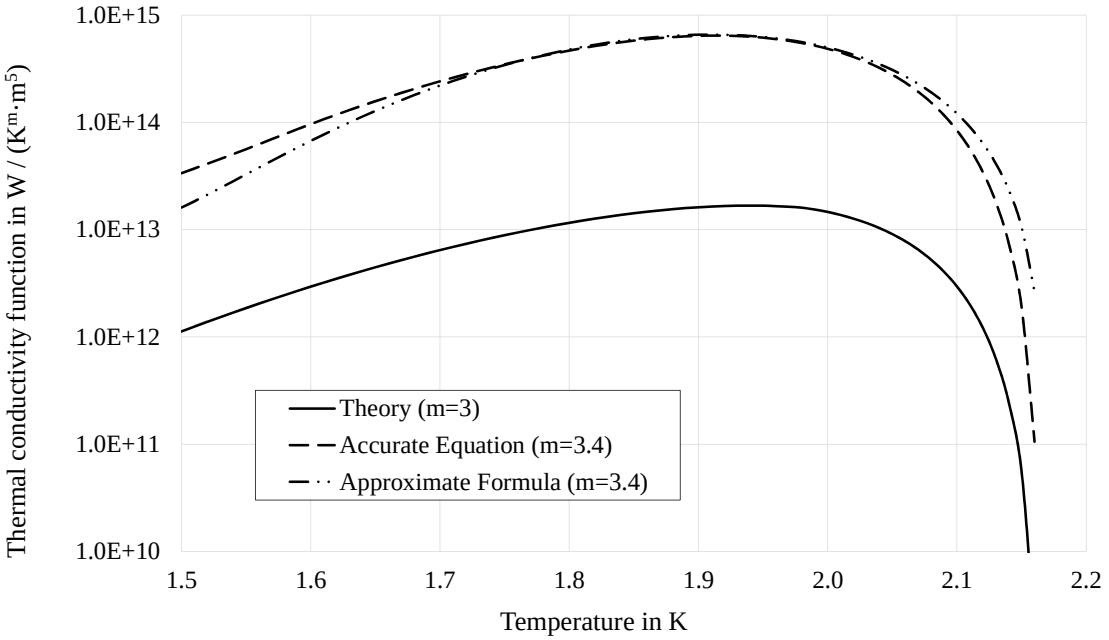

Figure 3.8: Values of the thermal conductivity function $1/f_k$ of superfluid helium as a function of temperature for a pressure of 1.3 bar, predicted by the theory (solid line) and obtained by empirically found formulas (dashed line and dash-dotted line).

3.2.2 Neon

Solidification below the triple point at 24.6 K does not allow the use of neon close to absolute zero. There are some other cooling applications at higher temperature level for which neon could be a possible coolant. Main advantage compared to helium is its high density, and as a result, the lower mass flow rates and pressure losses. Drawbacks of neon are price and availability, as well as the lack of experience in large facilities like the FCC. Cooling of the FCC beam screens with neon could be envisaged. The main concern though was a risk of possible solidification during an interruption of flow consectutive to a power cut due to the low temperature level and the large heat capacity of

the magnets. Therefore it was decided against the large-scale use of neon in the FCC beam screens. However, the refrigeration cycle re-cooling the warmed-up helium of the beam screen loop uses a blend of helium and neon [44].

3.2.3 Nitrogen

Nitrogen can be cheaply harvested from the air with air liquefaction and seperation facilities. Due to its high triple point temperature it cannot be used as a cryogen during nominal operation of the FCC. The baseline of the FCC design foresees the cool-down and warm-up procedures performed with the beam screen cooling refrigeration unit. In case, during the conceptual design phase, the impossibilty of using these facilities for the transient operation becomes apparent, the cool-down of the entire cold mass down to 80 K could be designed to be realized with a nitrogen cycle [45].

3.3 Exergy and Anergy

Etymologically, the greek word $\varepsilon\nu\varepsilon\rho\gamma\varepsilon\iota\alpha$ (energeia) means "an inner ability to have some effect" [46]. The first law of thermodynamics states, that energy cannot be generated or destroyed, but only transported or transformed. It does not exclude any conversions of one form of energy to any other. The second law of thermodynamic states, that not all forms of energy can be entirely converted into other forms. To account for the different convertibility of energy, it is divided into a convertible part (exergy) and a non-convertible part (anergy).

$$Energy = Exergy + Anergy \tag{3.7}$$

Exergy first was introduced by the French physicist L. G. Gouy in his groundbreaking paper "Sur l énergie utilisable" as "Useful Energy" [47]. Soon the concept of useful energy was taken up, expanded and generalized by other scientists, e.g. by the Slovene chemical engineer Z. Rant, who invented the terms "Exergy" and "Anergy" [48]. Due to elegance and the importance of exergetic considerations, today almost every book about thermodynamics dedicates a chapter to this topic.

Several forms of energy are pure exergy, e.g. electrical energy and mechanical work. The inner energy of a fluid is not entirely convertible and any entropy generation in an irreversible process corresponds to a transformation of exergy into anergy. The exergy flow $\dot{C}$ contained in an energy flow exchanged by a temperature difference (heat $\dot{Q}$) depends on its state relative to the ambiance (subscript a). $\dot{C}$ is calculated by multiplying the transferred heat with the Carnot factor η_C or its negative value ϵ_C.

The ideal thermodynamic cycle to maximize the exergy harvest $\dot{X}_{max}$ or minimize the exergy effort $\dot{X}_{min}$ can be achieved by passing a Carnot process [50]. In case of a clockwise cycle ($T > T_a$), heat is supplied and partly transformed into mechanical work - $\dot{C}$ corresponds to the maximal work to extract from the cycle. In case of a counter-clockwise passed cycle ($T < T_a$), mechanical work is supplied to extract heat - $\dot{C}$ corresponds to the minimal necessary work required for the refrigeration task. For the entire thesis an ambient temperature T_a of 300 K was assumed. The diagram in figure 3.9 illustrates the Carnot factor for cooling (ϵ_C) and heating (η_C).

$$\dot{X}_{max} = \dot{C} = \dot{Q} \underbrace{\left(1 - \frac{T_a}{T}\right)}_{\eta_C} \quad for\ T > T_a \tag{3.8}$$

$$\dot{X}_{min} = \dot{C} = \left| -\dot{Q} \underbrace{\left(\frac{T_a}{T} - 1 \right)}_{\epsilon_C} \right| \quad for\ T < T_a \tag{3.9}$$

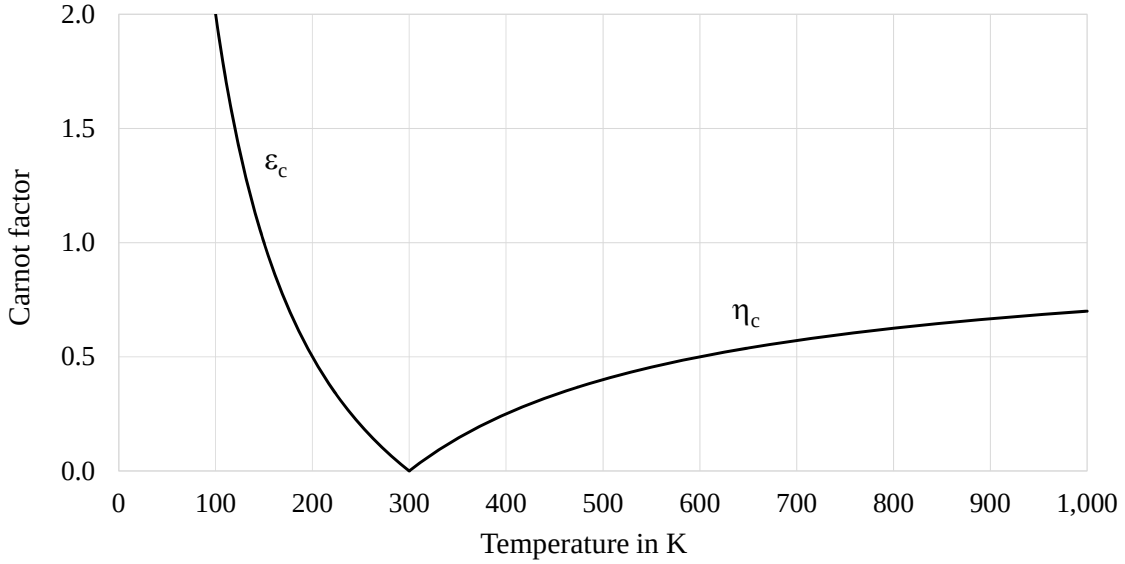

Figure 3.9: Carnot factor for cooling ϵ_C and for heating η_C vs. the temperature in K for an ambient temperature of 300 K.

The change of the sign in (3.9) indicates that the exergy and the energy flows point in different directions. That means that exergy is supplied to the cooled body by extracting heat from it. Thermodynamically speaking, the task of a cryogen in a refrigeration process is to transport exergy and deliver it to the objects to cool. To obtain the actual exergetic effort used in a refrigeration process, the exergy flow transported in a cryogen must be calculated. In an open system operating in steady-state, the enthalpy offers itself to describe the processes in the system.

The specific exergy e of a mass flow rate $\dot{m}$ corresponds to the exergy of the enthalpy calculated with the specific enthalpy h and the specific entropy s of the cryogen's state. Any kinetic and potential energy $e_{kin} + e_{pot}$ is pure exergy, but can be neglected within the considered system boundaries of the discussed applications, as well as any chemical exergy e_{chem} contained in the cryogen.

$$\dot{E} = \dot{m}\, e = \dot{m} \left[h - h_a - T_a \left(s - s_a \right) + \underbrace{e_{kin} + e_{pot}}_{small} + \cancel{e_{chem}} \right] \approx \dot{m} \left[h - h_a - T_a \left(s - s_a \right) \right] \tag{3.10}$$

3.3.1 Exergetic valuation of refrigeration applications

The advantage of analysing a thermodynamic system exergetically (compared to an energetic analysis) is the inherent distinction between convertible and non-convertible forms of energy (exergy and anergy). In real applications, the exergy to run a refrigeration cycle always exceeds the physically minimal exergy effort due to irreversible processes. The delivered exergy is partly transformed

into anergy, i.e. exergy is lost. To assess the quality of the cryogenic system and its components, two dimensionless values are used. The Carnot efficiency ξ is defined as the ratio of the physically minimal exergy to run a refrigeration process (determined by the Carnot factor) and the expended exergy effort $\dot{X}$ [34]. It compares the real process management with the ideal Carnot process, the reciprocal value of the Carnot efficiency directly shows the extra costs for the operation of the cryogenic system compared to the physically minimum.

$$\xi = \frac{\dot{X}_{min}}{\dot{X}} \tag{3.11}$$

The exergetic efficiency ζ of a process is defined as the ratio of the exergy outcome $\dot{X}_{out}$ and the exergy input $\dot{X}_{in}$. The difference corresponds to the produced anergy, hence the sum of all n occurring exergy losses $\sum_{i=1}^{n} \dot{B}_i$.

$$\zeta = \frac{\dot{X}_{out}}{\dot{X}_{in}} = \frac{\dot{X}_{in} - \sum_{i=1}^{n} \dot{B}_i}{\dot{X}_{in}} = 1 - \frac{\sum_{i=1}^{n} \dot{B}_i}{\dot{X}_{in}} \tag{3.12}$$

The exergetic efficiency can be used to describe the quality of single technical components (e.g. heat exchangers), where the entering and exiting exergy is defined unambiguously in most cases. The scope of a cooling process could be to conserve food or enable particle physics and the exergy outcome cannot be expressed in numbers. Therefore an exergetic benefit $\dot{A}$ of the refrigeration process based on its technical purpose has to be defined to be able to quantify and compare it. Keeping the temperature of an object below a determined limit T_{lim} is the (technical) benefit of a cooling application. The physically minimal effort to achieve this goal seems to be a reasonable choice.

$$\zeta = \frac{\dot{A}}{\dot{X}_{in}} \stackrel{!}{=} \frac{\dot{X}_{min}}{\dot{X}} \tag{3.13}$$

By defining the exergetic benefit as the minimal necessary exergy effort, the exergetic efficiency and the Carnot efficiency of a cryogenic application are identical.

3.3.1.1 Provision and consumption of exergy

The total exergetic effort to run a refrigeration cycle can either be delivered entirely by the cryoplant ("Black Box" design) or can be the combination of exergy delivered by a cryoplant via a heat exchanger and the electrical power of a circuit-internal compressor/pump ("Integrated Circulator" design). The two principles are illustrated in figure 3.10. Considering the distribution cycle only (System I), the total necessary (net) exergy $\dot{X}_{tot}$ in the first case corresponds to the difference of the exergy flows entering and leaving the system boundary (3.14). In the latter case, the circulation power has to be added (3.15).

$$\dot{X}_{tot} = \dot{X}_{CP} = \dot{m}\,(e_{in} - e_{out}) \tag{3.14}$$

$$\dot{X}_{tot} = P_{Circ} + \dot{X}_{CP} = P_{Circ} + \dot{m}\,(e_{in} - e_{out}) \tag{3.15}$$

$$\zeta_I = \frac{\dot{X}_{min}}{\dot{X}_{tot}} = \frac{\dot{A}}{\dot{X}_{tot}} \tag{3.16}$$

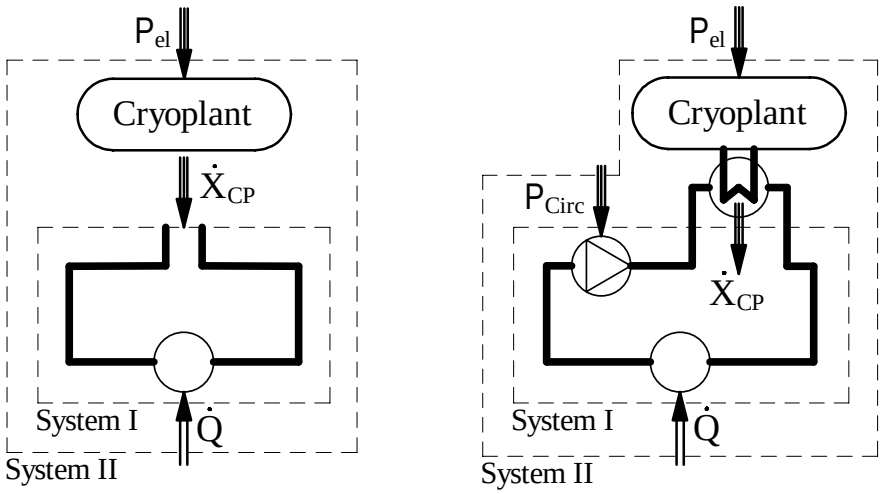

Figure 3.10: Schematic of the "Black Box" design (left-hand side) and schematic of the "Integrated Circulator" design (right-hand side).

The ratio of the exergy delivered by the cryoplant $\dot{X}_{CP}$ and the electric power P_{el} consumed by the plant yields the exergetic efficiency of the cryoplant ζ_{CP}. By combining the exergetic efficiencies of the distribution system (System I) and of the cryoplant, the exergetic efficiency of the entire cryogenic facility ζ_{II} can be calculated (corresponding to the definition of System II).

$$\zeta_{CP} = \frac{\dot{X}_{CP}}{P_{el}} \tag{3.17}$$

$$\zeta_{II} = \zeta_{CP}\,\zeta_I \frac{\dot{X}_{CP}}{\dot{X}_{CP} + P_{Circ}} \tag{3.18}$$

Cryoplants of different size and operating temperatures could be compared by their exergetic efficiency and the exergy they deliver. However, due to the extraordinary importance of helium and its application at a (saturation) temperature of 4.5 K, it has become established to express the exergy to be provided by a cryoplant $\dot{X}_{CP}$ as an equivalent to the heat extraction $\dot{Q}_{4.5}$ at a temperature of 4.5 K [53].

$$\dot{X}_{CP} = \frac{\dot{X}_{min}}{\zeta_I} = \frac{\sum \dot{Q}_i\,\epsilon_C(T_i)}{\zeta_I} = \dot{Q}_{4.5}\,\epsilon_C(T{=}4.5\,K) \tag{3.19}$$

$$\dot{Q}_{4.5} = \frac{\sum \dot{Q}_i\,\epsilon_C(T_i)}{\zeta_I\,\epsilon_C(T{=}4.5\,K)} = \frac{\dot{X}_{CP}}{\epsilon_C(T{=}4.5\,K)} \tag{3.20}$$

In a Carnot process the minimal exergy necessary at ambient temperature (300 K) to extract a heat load of 1 W at 4.5 K is given by the Carnot factor ϵ_C (corresponds to about 66 W/W as shown in the diagram illustrated in figure 3.1). The necessary electric power divided by the equivalent heat yields a value to compare the exergetic consumption and performance of different cryoplants.

$$\frac{P_{el}}{\dot{Q}_{4.5}} > \epsilon_C(T{=}4.5\,K) \approx 66\ \frac{\text{W of electrical power}}{\text{W of heat to extract @ 4.5 K}} \tag{3.21}$$

The definition of the system under observation and its boundaries is elementary to analyse the exergetic performance correctly. Focus of this thesis is the analysis of the distribution system

(corresponding to the System I in figure 3.10). The analysis of the cryoplants is not included. However, Carnot efficiencies of the cryoplants are assumed based on estimation or experience to be able to "translate" the results into electrical power consumption and operational costs. For more information, references are made to reports of TU Dresden, CEA Grenoble and CERN [44] [51] [52].

3.3.2 Exergy losses

Due to irreversible changes of state, exergy is not conserved, but partly transformed into anergy (exergy losses). To improve the performance of a refrigeration process, the exergy losses must be matched accordingly to their sources. The cryogen flow in a non-adiabatic pipe of length Δz shall be considered. The difference of the incoming and outgoing exergy flows corresponds to the sum of the exergy losses due to frictional pressure drop $\dot{B}_{\Delta p}$ and any entering or exiting exergy flows $\dot{C}$ due to heat transfer as indicated in figure 3.11.

$$\dot{E}_{in} - \dot{E}_{out} = \dot{B}_{\Delta p} + \dot{C} \tag{3.22}$$

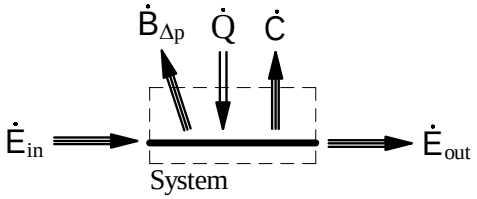

Figure 3.11: Exergy balance of a mass flow passing a heated pipe.

3.3.2.1 Exergy losses by pressure drop

The exergy difference in (3.22) can be substituted by the thermomechanical exergy defined in (3.10) and using the total enthalpy difference $\Delta\dot{H}$ and entropy difference $\Delta\dot{S}$.

$$\underbrace{\dot{E}_{in} - \dot{E}_{out}}_{\Delta\dot{E}} = \dot{B}_{\Delta p} + \dot{C} = \underbrace{\dot{H}_{in} - \dot{H}_{out}}_{\Delta\dot{H}} - T_a \underbrace{\left(\dot{S}_{in} - \dot{S}_{out}\right)}_{\Delta\dot{S}} \tag{3.23}$$

Equation (3.24) below shows the first law of thermodynamics for an open system. Only the steady state operation is taken into account, therefore the RHS of (3.24) equals zero. The transport of external exergy with entering and exiting mass flows is negligible. No work $\dot{W}$ is extracted and (3.24) can be rewritten as (3.25).

$$\underbrace{\dot{W}}_{Work} + \underbrace{\dot{Q}}_{Heat} + \underbrace{\sum_{i=1}^{n} \dot{m}_i \left(h_i + e_{a\,i}\right)}_{Enthalpy\,+\,external\,energy} = \underbrace{\dot{U} + \dot{E}_a}_{Internal\,+\,external\,energy} \tag{3.24}$$

$$\underbrace{\dot{Q}}_{Heat} + \underbrace{\sum_{i=1}^{n} \dot{m}_i\, h_i}_{\Delta\dot{H}} = 0 \tag{3.25}$$

The enthalpy transport equals the transferred heat. Using the defining equation for the enthalpy (3.26), the transferred heat $\dot{Q}$ can be substituted, yielding (3.27).

$$\Delta\dot{H} = \dot{m}\left(\int T\,ds + \int \frac{dp}{\rho}\right) \tag{3.26}$$

$$-\Delta\dot{H} = \underbrace{\int d\dot{Q}}_{\dot{Q}} = -\dot{m}\left(\int T\,ds + \int \frac{dp}{\rho}\right) \tag{3.27}$$

From (3.27) the entropy flux difference can be expressed explicitly (3.28). Substituting $\Delta\dot{S}$ of (3.23) with the RHS of (3.28) and rearranging yields (3.29).

$$\underbrace{-\dot{m}\int ds}_{-\Delta\dot{S}} = \dot{m}\int \frac{dp}{\rho T} + \int \frac{d\dot{Q}}{T} \tag{3.28}$$

$$\dot{B}_{\Delta p} + \dot{C} = \underbrace{\dot{m}T_a\int \frac{dp}{\rho T}}_{\dot{B}_{\Delta p}} + \underbrace{\int\left(\frac{T_a}{T} - 1\right)d\dot{Q}}_{\dot{C}} \tag{3.29}$$

The exergy decrease $\dot{C}$ due to the heat absorption corresponds to the second term on the RHS of (3.29), the first term expresses the exergy loss due to the pressure drop. A closer look reveals the dependency of the pressure drop exergy losses on the temperature level at which they are generated.

By applying numerical methods for the approximate calculation of integrals (e.g. a Riemann Sum), the integrands in (3.29) can be extracted from the integrals and then the integrals can be substituted.

$$\dot{B}_{\Delta p} + \dot{C} = \underbrace{\frac{\dot{m}}{\overline{\rho}}\frac{T_a}{\overline{T}}\Delta p}_{\dot{B}_{\Delta p}} + \underbrace{\left(\frac{T_a}{\overline{T}} - 1\right)\dot{Q}}_{\dot{C}} \tag{3.30}$$

In the cryogenic domain helium cannot be assumed to behave like an ideal gas. However, to demonstrate the general correlations of the exergy of the enthalpy as a function of temperature and pressure, it is derived based on an ideal gas. The enthalpy difference and the entropy difference can be substituted by the corresponding temperature differences and pressure ratios. By dividing e by the product of the ambient temperature and the specific gas constant, RT_a, the dimensionless specific exergy ε of the enthalpy can be calculated [50]. After rearranging (3.31) to (3.33) the necessary pressure ratio p/p_a to obtain a certain (dimensionless) specific exergy is found as a function of the temperature ratio T/T_a.

$$\varepsilon = \frac{e}{RT_a} = \underbrace{c_p\frac{T - T_a}{RT_a}}_{\Delta h} - T_a\underbrace{\frac{c_p ln\,(T/T_a) - R ln\,(p/p_a)}{RT_a}}_{\Delta s} \tag{3.31}$$

$$\varepsilon = \underbrace{\frac{c_p}{R}}_{\frac{\varkappa}{\varkappa-1}}\left(\frac{T}{T_a} - 1 - ln\frac{T}{T_a}\right) + ln\frac{p}{p_a} \tag{3.32}$$

$$\frac{p}{p_a} = exp\left[\varepsilon - \frac{\varkappa}{\varkappa - 1}\left(\frac{T}{T_a} - 1 - ln\frac{T}{T_a}\right)\right] \tag{3.33}$$

Figure 3.12 shows the diagram generated from (3.33). From (3.33) follows that the dimensionless exergy at ambient temperature and ambient pressure is 0. With changing temperature of the ideal gas, the same exergy values are reached even at lower pressure ratios. Keeping the temperature ratio constant, the exergy increases with increasing pressure ratio. All the isolines ("isexergies") show maxima at ambient temperature. At these maxima also the horizontal distances between these isolines are maximal. The same pressure change/drop therefore influences the specific exergy less, if the temperature is close to ambient temperature.

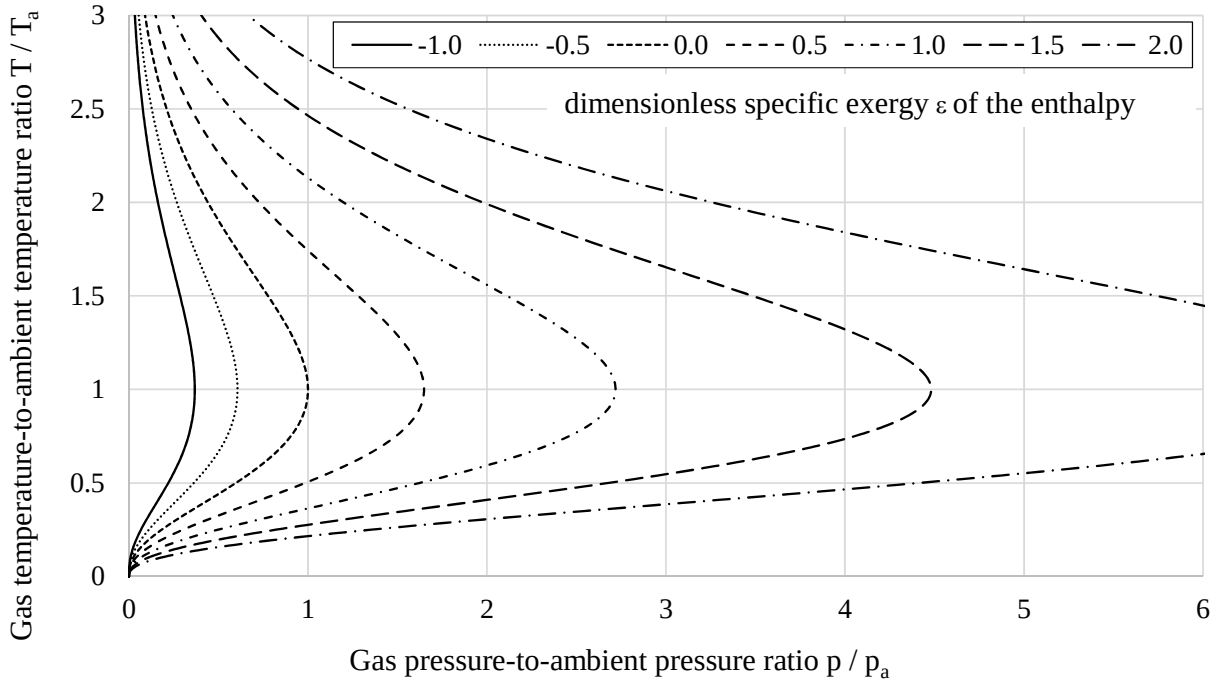

Figure 3.12: Specific exergy isolines $T/T_a = f(p/p_a)$ for the enthalpy of an ideal gas.

3.3.2.2 Exergy losses by heat transfer

In a perfectly insulated cooling application the entire heat released by the cooled material must be absorbed by the cooling material (first law of thermodynamics). The physical need for a temperature difference ΔT_Q to transfer heat (second law of thermodynamics) causes a difference between the exergy released by the cooling material $\dot{C}_{Cooling}$ and the exergy received by the cooled material $\dot{C}_{Cooled}$. The difference between $\dot{C}_{Cooling}$ and $\dot{C}_{Cooled}$ is the heat transfer exergy loss $\dot{B}_{HT}$. Figure 3.13 shows schematically the exergy flows of a body cooled by a cryogen and the corresponding internal heat and exergy fluxes causing the heat transfer exergy losses.

$$\dot{C}_{Cooled} = \dot{Q}\left(\frac{T_a}{T_{Cooled}} - 1\right) \tag{3.34}$$

$$\dot{C}_{Cooling} = \dot{Q}\left(\frac{T_a}{T_{Cooling}} - 1\right) \tag{3.35}$$

$$\dot{B}_{HT} = \dot{C}_{Cooling} - \dot{C}_{Cooled} = \dot{Q}T_a\left(\frac{1}{T_{Cooling}} - \frac{1}{T_{Cooled}}\right) \tag{3.36}$$

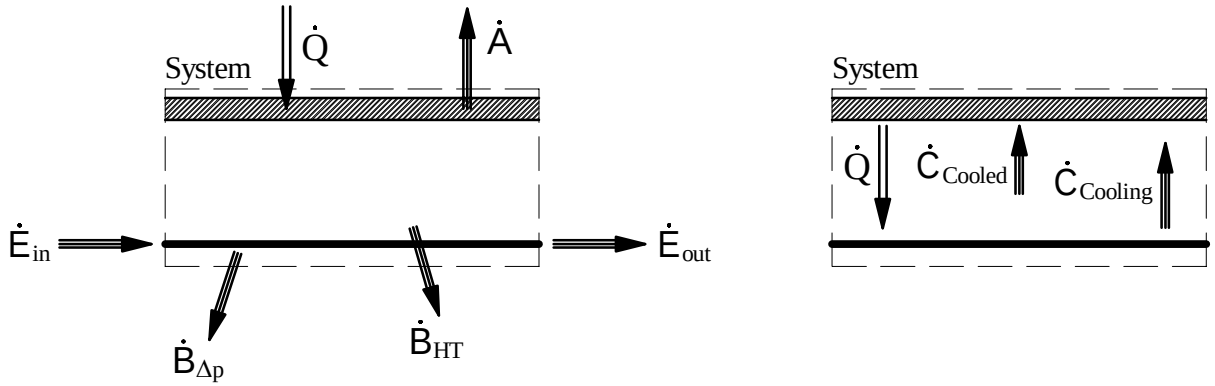

Figure 3.13: Exergy and heat fluxes across the system boundaries (left-hand side) and within the system boundaries (right-hand side) of a body cooled by a cryogen carrying pipe.

In steady-state operation, no changes of temperature or transferred heat occur in time, albeit in large systems they cannot be assumed to be constant over the entire length of the cooling loop L_{CL}. To obtain the total heat transfer loss, all the local exergy losses have to be summed up over the entire length.

$$\int d\dot{B}_{HT} = T_a \int_0^{L_{CL}} \left(\frac{1}{T_{Cooling}(z)} - \frac{1}{T_{Cooling}(z) + \Delta T_Q(z)}\right) \dot{q}(z)\, dz \tag{3.37}$$

The complex influences of the variables on each other, including the temperature dependent material properties, enable an analytical solution in simplified cases only. The heat transfer losses were calculated numerically, where the thermodynamic state of the cryogen passing Δz was kept constant.

Exergy losses $\dot{B}_{lim}$ due to a lower temperature than the necessary temperature limit are also calculated with (3.36). The actual material temperature T_{Cooled} and the upper temperature T_{lim} have to be used.

$$\dot{B}_{lim} = \dot{Q}T_a\left(\frac{1}{T_{Cooled}} - \frac{1}{T_{lim}}\right) \tag{3.38}$$

3.3.2.3 Exergy losses in process equipment

Most of the technical components used are compactly constructed and the transit time of the working fluid inside them is low, so that they can be treated as adiabatic. The sum of all the generated exergy losses in these components consists of pressure drop, heat transfer and mixing exergy losses. Generally, the assignment of the entire loss to the corresponding physical causes is not of primary interest, and therefore the anergy production due to each effect is not calculated. The component exergy loss can be calculated by summing up the exergies of all entering and exiting

cryogen mass flows. Figure 3.14 shows the exergy balances for selected technical components. The system boundaries are assumed to be adiabatic.

$$\dot{B}_{Component} = \sum \Delta \dot{E}_{in} - \sum \Delta \dot{E}_{out} \tag{3.39}$$

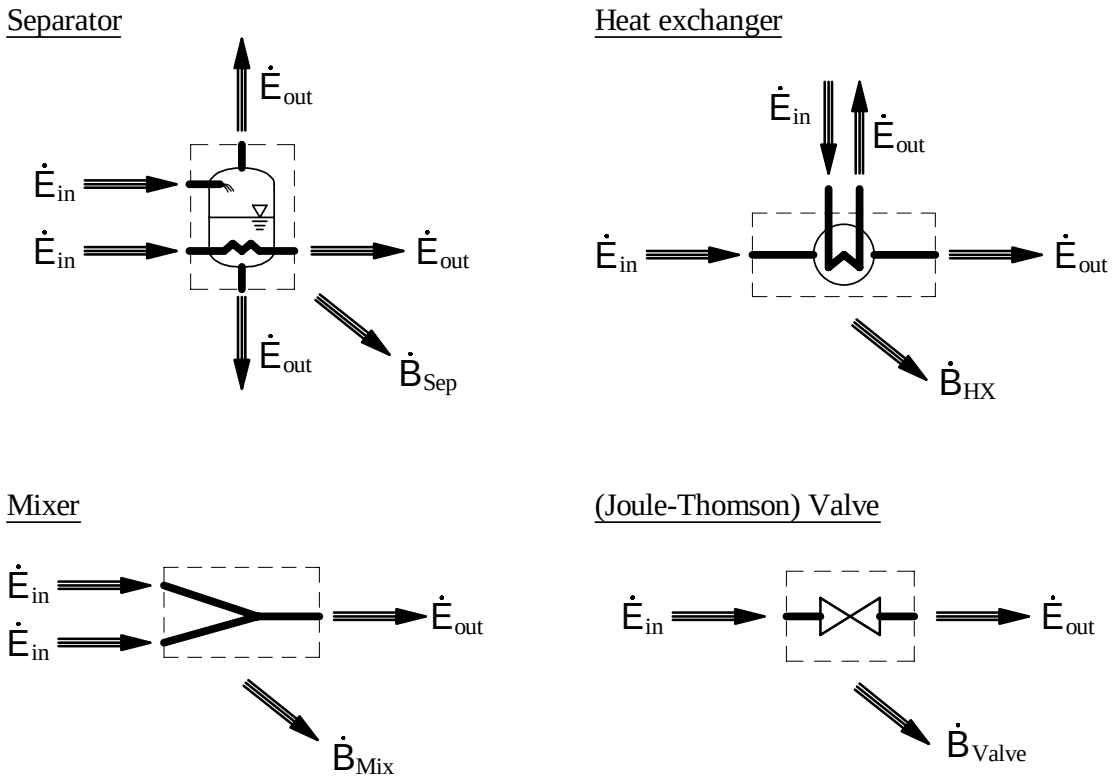

Figure 3.14: Exergy balances of technical components and processes.

3.3.2.4 Exergy losses in circulators and compressors

Any circulator in the cooling loop is driven by electric energy, hence by a pure exergy effort $\dot{X}_{Circ}$. Irreversible processes in the energy transformation in the circulator converts part of the exergy input into anergy $\dot{B}_{Circ}$. This exergy loss can be calculated by the difference of the entering and exiting exergy flows and the required circulation power. Figure 3.15 shows the exergy balance for a cryogen flow (re-)pressurised by a circulator.

$$\dot{B}_{Circ} = P_{Circ} - \left(\dot{E}_{out} - \dot{E}_{in}\right) = -\dot{m} T_a \left(s_{out} - s_{in}\right) \tag{3.40}$$

The necessary circulation power P_{Circ} of cryogenic gas circulators can be obtained by considering the isentropic efficiency η_s, usually specified by the manufacturer. It is defined as the ratio of the isentropic enthalpy difference and the real enthalpy difference of the necessary pressure rise.

$$\dot{X}_{Circ} = P_{Circ} = \dot{m} \left(h_{out} - h_{in}\right)_{real} \tag{3.41}$$

$$\eta_s = \frac{\left(h_{out} - h_{in}\right)_{isentropic}}{\left(h_{out} - h_{in}\right)_{real}} \tag{3.42}$$

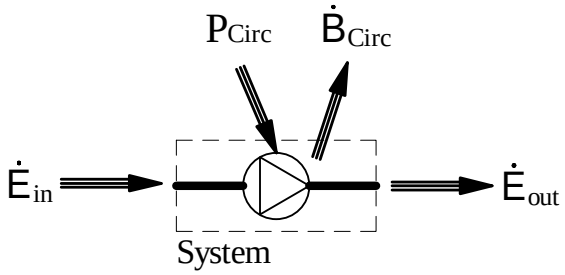

Figure 3.15: Exergy balance of a circulator.

4 Cold Mass Cooling

The main purpose of the cold mass cooling system is to keep the coil temperature below the transition temperature to guarantee the coils' superconducting state. The choice of the cold mass temperature level determines the structure and the working principle of the cryogenic system. The major part of the existing colliders is operated at about 4 K (compared to 1.9 K in the LHC). The higher temperature generally entails technical advantages regarding the cryogenic plants including their availability, the investment costs and the operational costs (as graphically shown in figure 3.1). However, the choice of a cold mass temperature around 4 K is accompanied by an increased necessary amount of (very expensive) superconducting material and a degradation of the vacuum quality [54]. Additionally, a system working at 4 K cannot take advantage of the properties of superfluid helium.

The advantages of a cold mass cooling system operating below the λ-temperature outweigh the disadvantages and it was decided to design an LHC-like cold mass refrigeration. Nevertheless, the possibility of a cold mass design operated at 4 K also was considered and should still be kept in mind as an option.

4.1 Heat Load

Four different heat sources are taken into account [55]:

- Beam gas scattering (dynamic: $\dot{q} = 0 \div 0.45$ W/m)
- Resistive heating in the coil splices (dynamic: $\dot{q} = 0 \div 0.3$ W/m)
- Heat transfer through the cold bore (semi-dynamic: $\dot{q} = 0.12 \div 0.2$ W/m)
- Heat transfer from the ambiance (static: $\dot{q} = 0.43$ W/m)

Depending on the operational mode of the FCC, the contributions of the different heat sources vary. The dynamic heat loads in nominal operation, as well as the static heat loads depicted in figure 4.1, were estimated based on the experience made with the LHC and on preliminary calculations performed by the STI group (**S**ources, **T**argets and **I**nteractions) of the EN-Department at CERN [56]. The installed refrigeration capacity was determined to be capable of handling 1.75 times the heating power received in nominal operation for isolated cold mass units (CMU). Four operational modes are investigated [57]. The assumed axial heat load distributions on one lattice half-cell ($L_{HC} = 107$ m) are illustrated in figure 4.1.

1. Stand-By Mode (only static heat leaks: $\dot{q} = 0.55$ W/m)
2. Low Energy Operation (static heat leaks and resistive heating: $\dot{q} = 0.85$ W/m)
3. Nominal Operation ($\dot{q} = 1.38$ W/m)
4. Installed Capacity ($\dot{q} = 2.44$ W/m)

The heat load on the cold mass is not distributed uniformly over the entire cross section. Except the static heat leaks, the heat loads appear mainly in or close to the coils.

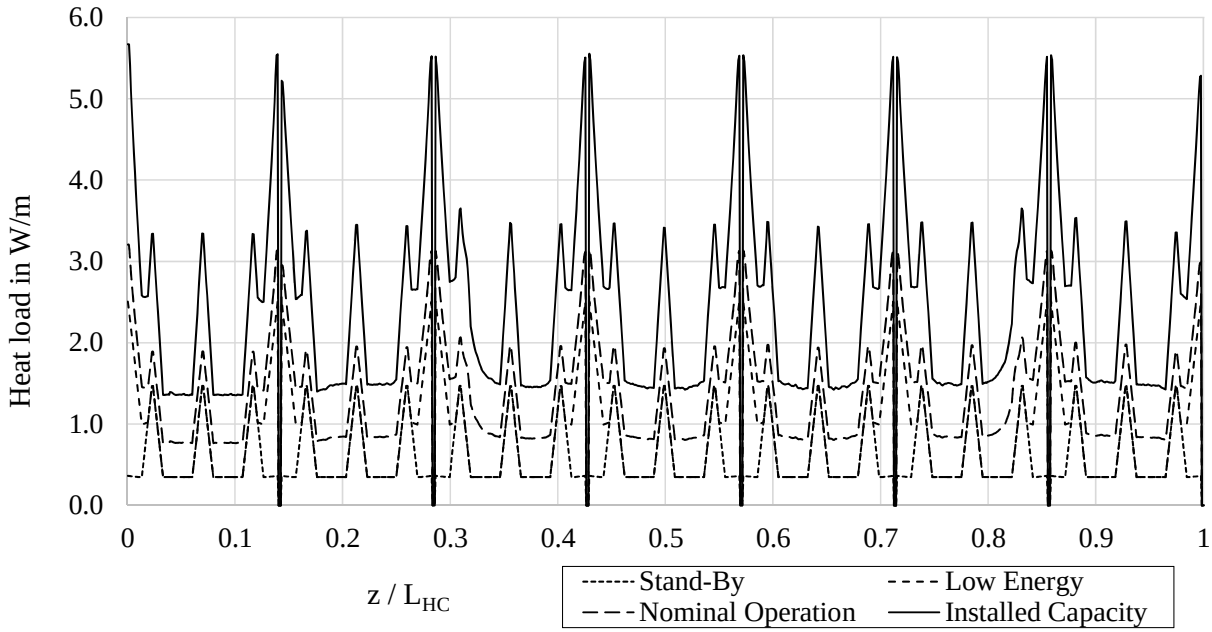

Figure 4.1: Assumed heat load distribution along the length of one half-cell for four different operational modes.

4.2 Total vaporization condition

The cold mass temperature must be kept in a very small range, calling for minimal helium temperature changes during the refrigeration process in the magnets. The temperature of a (azeotropic) coolant in the two-phase regime is independent of the heat absorption, but the helium mass flow rate $\dot{m}_{CMU}$ delivered must correspond to the heat load on the (parallel) cooled CMU, hence also to its length L_{CMU}.

$$\dot{q}\, L_{CMU} = \dot{m}_{CMU} \left(h'' - h_{JT}\right) \tag{4.1}$$

h'' denotes the specific enthalpy of the saturated helium vapour, h_{JT} denotes the specific enthalpy in the Joule-Thomson valve and $\dot{q}$ denotes the average heat load in W/m. One parallel cooled CMU must consist of an integer number of half-cells ($\widehat{=}$ 7 magnets in a series (= 107 m)), where n_{HC} denotes the number of half-cells per parallel cooled CMU and L_{HC} denotes the length of a half-cell.

$$\dot{m}_{CMU} = \frac{\dot{q}\, L_{HC}\, n_{HC}}{h'' - h_{JT}} \tag{4.2}$$

In case the delivered helium mass flow rate is too low, the cold mass temperature increases. In case the helium mass flow rate is too high, vaporization of the liquid helium in excess generates exergetic losses.

4.3 Basic exergetic considerations

Considering the total vaporization condition and a "black box" perspective of a parallel cooled CMU, very basic exergetic considerations can be derived. The exergetic effort $\dot{X}_{CMU}$ to drive the

cold mass cooling system corresponds to the difference of the exergy flow $\dot{E}_C$ entering from the supply header C and the exergy flow $\dot{E}_B$ exiting into the return header B. The minimal exergetic effort $\dot{A}_{CMU}$ only depends on the coil temperature limit T_{lim} and the heat load $\dot{q}\,L_{CMU}$ to extract.

$$\dot{X}_{CMU} = \dot{E}_C - \dot{E}_B = \dot{m}_{CMU}\,\Delta e_{CB} \tag{4.3}$$

$$\dot{A}_{CMU} = \dot{q}\,L_{CMU}\left(\frac{T_a}{T_{lim}} - 1\right) \tag{4.4}$$

$$\zeta = \frac{\dot{A}_{CMU}}{\dot{X}_{CMU}} = \frac{h'' - h_{JT}}{\Delta e_{CB}}\left(\frac{T_a}{T_{lim}} - 1\right) \quad \rightarrow \quad \zeta \propto \frac{h'' - h_{JT}}{\Delta e_{CB}} \tag{4.5}$$

where Δe_{CB} denotes the difference in specific exergy between the supplied helium by header C and the discharged helium in header B. The coil temperature limit, the specific enthalpy of the saturated vapour, the state of the supplied helium and the ambient temperature cannot or can only hardly be changed. The efficiency depends primarily on the specific exergy of the exiting helium flow, which is mainly a function of its pressure. Apart from reducing the pressure losses to their reasonable minimum, the driving temperature difference to enable a sufficient heat transfer must also be kept as small as possible.

4.4 Cold Mass Design

The generation of a suitable magnetic field to bend and focus the hadron beams requires an elaborate functional interaction of all parts of the cold mass. Centrepieces of the FCC cold mass are the two cold bores containing the beams and the beam screens. The superconducting coils are arranged symmetrically around the two cold bores. To impede movements due to the high magnetic forces, a high-strength stainless steel collar compresses the single coil cables and keeps them in place. The collar is embedded in the ferromagnetic iron yoke, which enforces and homogenizes the magnetic field and limits the stray magnetic field. The design of the iron yoke plays a crucial role and cannot readily be changed for cryogenic purposes. The cryogenic design therefore has to manage with as little space as possible. The iron yoke is contained in an aluminium shell. Figure 4.2 illustrates the preliminary design of an FCC dipole cold mass, adapted for the baseline cooling concept with superfluid helium.

The cold mass must be designed symmetrically with respect to the horizontal and the vertical mid-planes to obtain a symmetrical magnetic field. All the voids of the cold mass are filled with pressurized liquid superfluid helium (coloured black in figure 4.2).

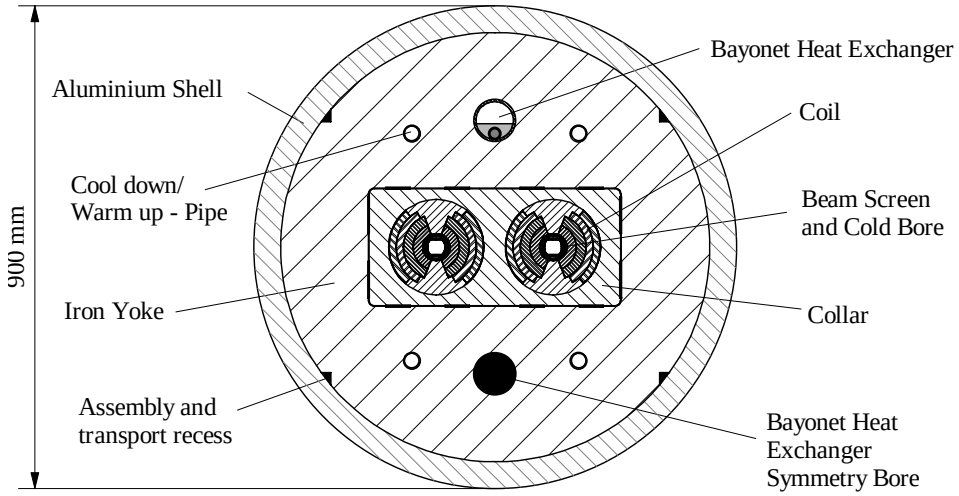

Figure 4.2: Schematic of the FCC dipole cold mass design for the superfluid helium cooling application.

4.4.1 Superconducting Coils

The final design of the superconducting coils is not determined yet. Three principal concepts are still investigated and under development:

1. Block Coil Design [58]
2. CosΘ Design [59]
3. Common Coil Design [60]

Independent of the final design choice, the basic structure of the coils is similar. The superconducting cable is made of a composite of copper and Nb_3Sn in different ratios, depending on the position of the cables. Each cable is electrically insulated and kept in position by copper wedges (CosΘ Design), the different coils are separated by titanium pole pieces. Several cables are combined to assembly units and separated from each other by additional layers of electrically insulating synthetics (Kapton and G-11). Figure 4.3 shows a schematic of an FCC CosΘ Design dipole coil. The inner diameter of the coils without the cold bore has a width of 48 mm. In case of the cooling with superfluid helium, the outer diamater is 165 mm, the thickness of the insulators was determined to be 0.5 mm for the layers in the inside of the coils and 1 mm around the coils. The necessary amount of superconducting material, and therefore the size of the coils, increases with the temperature level of the cold mass cooling. For a maximal coil temperature of 4 K (normalfluid helium cooling), an increase of the outer diameter to 178 mm was assumed.

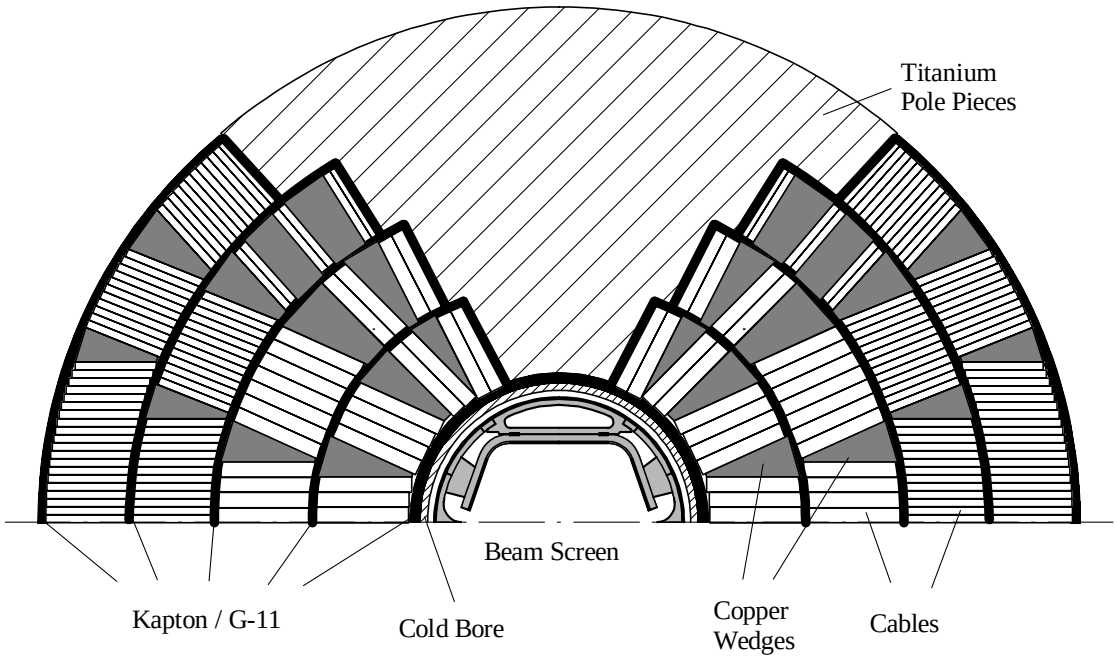

Figure 4.3: Schematic of an FCC CosΘ Design dipole coil.

4.5 Cold Mass cooling with superfluid helium

The cold mass cooling (CMC) with He II is a well-established concept, applied successfully for years in the LHC [62]. On the basis of the schematic in figure 4.4, the general concept shall briefly be explained: Single-phase normalfluid helium (approximately 4.6 K and 3 bar) is supplied by header C, cooled down in a counterflow heat exchanger, and is expanded in a Joule-Thomson valve into the two-phase region. In steady-state operation the separator is dried out, it only works as a buffer in transient modes, when the cryogen is not entirely vaporized in the bayonet heat exchanger [63]. The He II two-phase flow is conveyed to the bayonet heat exchanger's end by a smaller feeder pipe integrated in the bayonet heat exchanger. To avoid exergy losses, liquid entrainment in the returning two-phase helium must be reduced by keeping the flow in the (smooth) stratified flow regime. The liquid He II phase is vaporized, extracting heat from the cold mass. The entirely vaporized flow exits the bayonet heat exchanger, passes the dry separator and the heat exchanger, cooling down the incoming helium flow. Then it is discharged into the return header B to be conveyed back to the cold compressor station.

The space between the laminations, the assembly and transport recesses and the bayonet heat exchanger symmetry bore (in the further text summarized as "blank volume") is filled with static pressurized (1.3 bar) superfluid helium. The heat transfer from the coils to the bayonet heat exchanger is enabled by the high thermal conductivity of He II.

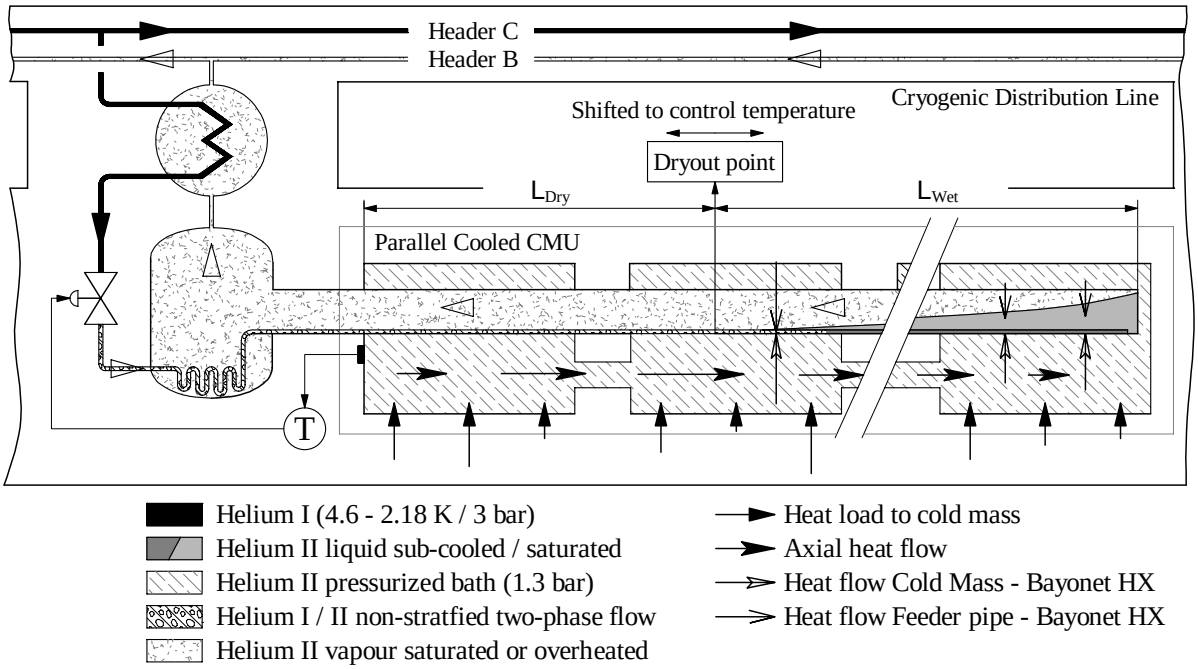

Figure 4.4: Hydraulic scheme of the cold mass cooling with superfluid helium.

4.5.1 Controlling and transient operation

The liquid phase of the stratified flow in the heat exchanger pipe moves at very low velocity (in the order of tens of cm per second). A control strategy based on the measurement of the liquid level in the separator is not possible due to the large delay times of the system's response. To avoid liquid helium losses, the separator must be dried out during steady-state operation, as indicated in figure 4.4. Therefore, part of the bayonet heat exchanger is dried out (L_{Dry}), only the section at the parallel cooled CMU's end is partially wetted (L_{Wet}).

To control the helium flow, the temperature of the pressurized helium bath is measured. If it exceeds a determined setpoint temperature, the Joule-Thomson valve opens, the mass flow rate increases and the dry section shortens. If, on the other hand, the temperature falls below the setpoint, the Joule-Thomson valve closes, the helium mass flow rate decreases, and the dry section becomes longer.

Only during unexpected transients (controlling issue, resistive transition of the superconducting coils (quench), ...), the dry length can vanish, and an overflow partly fills the separator with liquid helium [61]. This buffered amount is slowly vaporized during the following phase of steady-state operation by cooling down the incoming two-phase flow.

4.5.2 Bayonet Heat Exchanger

Figure 4.5 illustrates the cross section of the bayonet heat exchanger with the integrated feeder pipe.

The relative velocity between the liquid and vapour determines the flow pattern of the two-phase flow [64]. The He II two-phase flow in the bayonet heat exchanger should be kept in the stratified flow regime to avoid liquid entrainment by wrested droplets and subsequently the generation of helium mist transported in the vapour phase. The helium mist indeed improves the heat tranfer

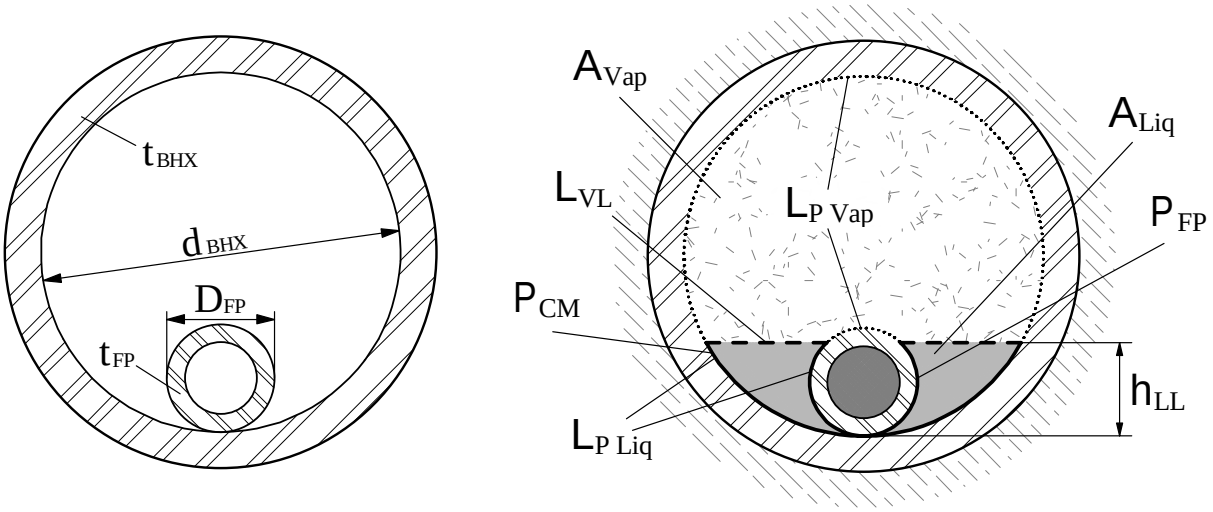

Figure 4.5: General used symbols to describe the bayonet heat exchanger geometry (left-hand side) and surfaces and perimeters for the pressure drop calculation of bayonet heat exchanger stratified flow and perimeters contributing to the radial heat transfer between stratified flow and the static helium bath and the stratified flow and the feeder pipe flow (right-hand side).

by impinging partly on the inner surface of the copper pipe, but discharged, non-vaporized helium droplets into return header B generate an exergy loss, which must be avoided [65]. To keep the helium flow in the stratified regime with little liquid entrainment, the relative velocity must be kept low, which can be achieved by a sufficiently large bayonet heat exchanger diameter. Vapour velocities up to 5 m/s ($= v_{lim}$) are possible to suppress the generation of mist in the vapour phase [67][66]. A first criterion for the minimal diameter can be set.

$$v_{Vap} = \frac{\dot{q}\, L_{CMU}}{(A_{BHX} - A_{FP})\, \rho_{Vap}\, (h'' - h_{JT})} \leq v_{lim} \tag{4.6}$$

$$d_{BHX} \geq \frac{2}{\sqrt{\pi}} \sqrt{\frac{\dot{q}\, L_{CMU}}{v_{lim}\, \rho_{Vap}\, (h'' - h_{JT})} + A_{FP}} \tag{4.7}$$

A second design constraint limits the maximal pressure (i.e. temperature) drop Δp_{lim}, which is shown in (4.8) and whose derivation, neglecting the feeder pipe, can be found in Appendix A [63]. By rearranging, another constraint for the minimal diameter can be obtained.

$$\Delta p_{lim} \geq \frac{f}{2\, \rho_{Vap}\, (d_{BHX} - D_{FP})\, \left[0.25\, \pi\, \left(d_{BHX}^2 - D_{FP}^2\right)\right]^2} \frac{\dot{q}^2\, L_{CMU}^3}{3\, (h'' - h')^2} \frac{1 - \xi_0^3}{(1 - \xi_0)^3} \tag{4.8}$$

$$d_{BHX} \geq \left[\frac{8\, f}{3\, \pi^2\, \Delta p_{lim}\, \rho_{Vap}} \frac{\dot{q}^2\, L_{CMU}^3}{(h'' - h')^2} \frac{1 - \xi_0^3}{(1 - \xi_0)^3}\right]^{1/5} \tag{4.9}$$

where f denotes the Darcy friction factor and ξ_0 denotes the vapour mass fraction of the stratified flow at the parallel cooled CMU's end, if there is no heat transferred from the feeder pipe flow to the stratified flow.

In both cases, the parallel cooled CMU length is the restricting factor. To reduce the space needed for the bayonet heat exchanger in the cold mass and save iron for the magnetic performance, the parallel cooled length must be kept short.

4.5.2.1 Quasi one-dimensional stratified flow

The bayonet heat exchanger geometry prompts to treat the stratified flow as a one-dimensional problem. The one-dimensional modelling equations to perform a numerical simulation are derived from the three-dimensional Navier-Stokes equations, describing the mass, momentum and energy balances for each of the two phases. The complete derivations can be found in Appendix B [68]. Figure 4.6 graphically shows the effects taken into account to model the stratified flow in the bayonet heat exchanger.

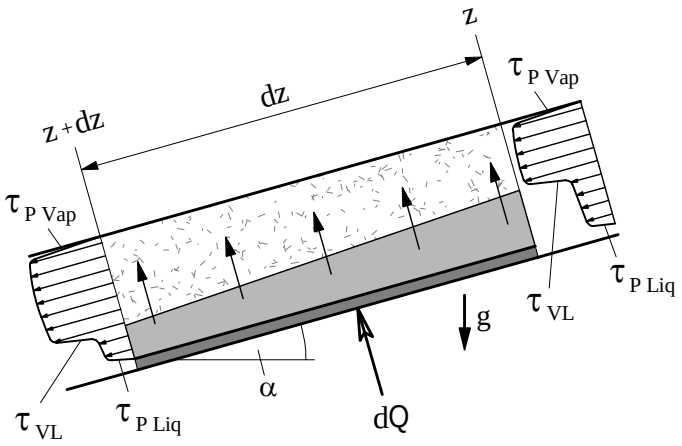

Figure 4.6: Stratified flow in the bayonet heat exchanger.

Mass (4.10), momentum (4.11) and energy (4.20) balance equations were solved for each phase, where only the steady-state operation was considered. The subscript Φ denotes the phases Liq and Vap.

Mass The generated vapour mass due to vaporization is the product of the total helium flow rate $\dot{m}_{CMU}$ and the change of the vapour mass fraction $d\xi$. The mass balance reads

$$\frac{d}{dz}\left(A_\Phi \, \rho_\Phi \, w_\Phi\right) = \pm \dot{m}_{CMU} \, \frac{d\xi}{dz} \tag{4.10}$$

The plus sign indicates the equation for the vapour phase, the minus sign for the liquid phase. w denotes the average velocity in the flow cross section and ρ the average density of the corresponding phase.

Momentum If any slope angle α occurs, the cryogen passes the half-cell in the descending direction. The pressure of the two-phase flow is assumed to be constant over the entire flow cross section. The quasi one-dimensional momentum balance of phase Φ reads

$$\underbrace{\dot{m}_\Phi \frac{dw_\Phi}{dz}}_{Change\ of\ momentum} = \underbrace{-A_\Phi \frac{dp}{dz}}_{Pressure\ forces} \underbrace{\mp \tau_{VL} L_{VL} - \tau_{P\Phi} L_{P\Phi}}_{Friction\ forces} + \underbrace{g \, \rho_\Phi \, A_\Phi \, sin\ \alpha}_{Weight} - \underbrace{\dot{m}_{CMU} \frac{d\xi}{dz} \Delta w_{VL}}_{Vaporization} \tag{4.11}$$

$$\Delta w_{VL} = 0 \qquad \ldots \text{for the liquid phase}$$
$$\Delta w_{VL} = w_{Vap} - w_{Liq} \qquad \ldots \text{for the vapour phase}$$

A denotes the cross sectional area, L_P denotes the part of a pipe's perimeter wetted by the corresponding phase, L_{VL} denotes the length of the interface between the two phases and τ the corresponding shear stresses. In the wall friction terms, the plus sign corresponds to the liquid phase, the minus sign to the vapour phase. The shear stresses between the pipe wall and the fluids were calculated with the Fanning friction factor $f_{P\Phi}$ derived by the formula of Churchill, the interfacial Fanning friction factor f_{VL} was calculated according to Andritsos and Hanratty [69].

$$\tau_{P\Phi} = f_{P\Phi} \frac{\rho_\Phi w_\Phi^2}{2} \tag{4.12}$$

$$\tau_{VL} = f_{VL} \frac{\rho_{Vap} \left(w_{Vap} - w_{Liq}\right)^2}{2} \tag{4.13}$$

where

$$f_{P\Phi} = \left[\left(\frac{8}{Re} \right)^{12} + (A+B)^{-1.5} \right]^{1/12} \tag{4.14}$$

with

$$A = \left\{ 2.457 ln \left[\left(\left(\frac{7}{Re}^{0.9} + 0.27 \frac{\epsilon}{d_h} \right)^{-1} \right) \right] \right\}^{16} \tag{4.15}$$

$$B = \left(\frac{37530}{Re} \right)^{16} \tag{4.16}$$

and

$$f_{VL} = f_{PVap} \qquad \ldots for\ w_{SVap} \leq w_{S0} \tag{4.17}$$
$$f_{VL} = f_{PVap} \left[1 + 15 \sqrt{\frac{h_{LL}}{d_{BHX}}} \left(\frac{w_{SVap}}{w_{S0}} - 1 \right) \right] \qquad \ldots for\ w_{SVap} > w_{S0} \tag{4.18}$$

with

$$w_{S0} = 5 \sqrt{\frac{\rho_a}{\rho_{Vap}}} \tag{4.19}$$

ϵ denotes the absolute roughness of the pipe wall, d_h the hydraulic diameter of the bayonet heat exchanger, w_{SVap} the superficial velocity of the vapour phase and ρ_a the helium density at ambient condition.

Thermal Energy In the energy balance, the longitudinal heat conduction was neglected. Radial heat transfer from the cold mass and from the feeder pipe flow to the stratified flow was accounted for. $(h'' - h')$ denotes the latent heat of vaporization of the helium, $\dot{q}_{CM}$ and $\dot{q}_{FP}$ denote the heat fluxes transferred to the stratified flow from the cold mass and the feeder pipe in W/m^2. The liquid and the vapour were assumed to be in thermodynamic equilibrium.

$$\dot{m}_{CMU} \left(h'' - h'\right) d\xi = \left(\dot{q}_{CM} P_{CM} + \dot{q}_{FP} P_{FP}\right) dz \tag{4.20}$$

For solving these equations, it was assumed that the longitudinal pressure drop in the two phases is identical [70]. All geometric parameters can be expressed as functions of the height of the liquid level h_{LL} in the bayonet heat exchanger.

4.5.2.2 Feeder pipe flow

The helium flow in the feeder pipe was modelled as homogeneous, if it was in the two-phase regime [41]. After exiting the Joule-Thomson valve, the helium flow enters the feeder pipe as a two-phase flow. Due to the higher pressure, the feeder pipe flow temperature is higher than the stratified flow temperature. Therefore the heat flux $\dot{q}_{FP}$ is transferred from the feeder pipe flow to the stratified flow. For temperatures below the λ-temperature, the thermal resistivity between the liquid helium and the copper pipe wall is mainly driven by the Kapitza resistance [72]. Three thermal resistivities in series were taken into account [71]:

1. The Kapitza resistance between the liquid phase of the stratified flow and the outer wall of the feeder pipe
2. The thermal resistivity of the feeder pipe copper wall
3. The thermal resistance between the inner feeder pipe wall and the feeder pipe flow, where
   - the Kapitza resistance was calculated, if the feeder pipe flow temperature was below the λ-temperature and
   - the heat transfer coefficient derived from a Nusselt function obtained by the Gnielinski correlation (4.21) was calculated, if the temperature exceeded the λ temperature [73].

$$Nu = \frac{(f/8)\,(Re - 1000)\,Pr}{1 + 12.7\sqrt{f/8}\left(Pr^{2/3} - 1\right)} \tag{4.21}$$

The wetted perimeter P_{FP} of the outer surface of the feeder pipe was taken to calculate the contributing area for the heat transfer (see figure 4.5). The thermal conductivity of the copper k_{Co} was assumed to be constant (88 W/(m·K)).

$$\dot{q}_{FP} = \frac{T_{FP} - T_{BHX}}{1/h_{out}\left(T{=}T_{BHX}\right) + t_{FP}/k_{Co} + 1/h_{in}\left(T{=}T_{FP}\right)} \tag{4.22}$$

A decreased vapour quality of the stratified flow generates less pressure drop. By improving the heat transfer from the feeder pipe flow to the stratified flow, more energy can be thermally bypassed decreasing the average vapour mass fraction of the stratified flow after the dryout point. Therefore a low thermal resistance between the stratified flow and the feeder pipe flow is advantageous. By enabling a good heat transfer, the feeder pipe flow is liquefied entirely on its way to the parallel cooled CMU's end. After total liquefaction of the feeder pipe flow, the feeder pipe flow temperature is similar to the stratified flow temperature, since the temperature of the latter depends only on its pressure.

Figure 4.7 illustrates the thermal processes in the bayonet heat exchanger. After exiting the Joule-Thomson valve, the temperature of the feeder pipe flow exceeds the temperature of the helium vapour in the outer pipe of the bayonet heat exchanger. Along the dry section, the heat transferred is low. Starting from the dryout point, the heat transferred from the feeder pipe flow to the stratified flow increases, until the feeder pipe flow is entirely liquefied. In the single-phase regime the temperature is not firmly connected to the pressure and the heat transfer causes an assimilation of the feeder pipe flow temperature to the stratified flow temperature, which is determined by the pressure. The temperature difference becomes small and therefore the transferred heat is low. The direction, in which the heat is transferred, depends on the pressure drop in the two flows, since the Joule-Thomson coefficient of the sub-cooled single-phase feeder pipe flow is negative.

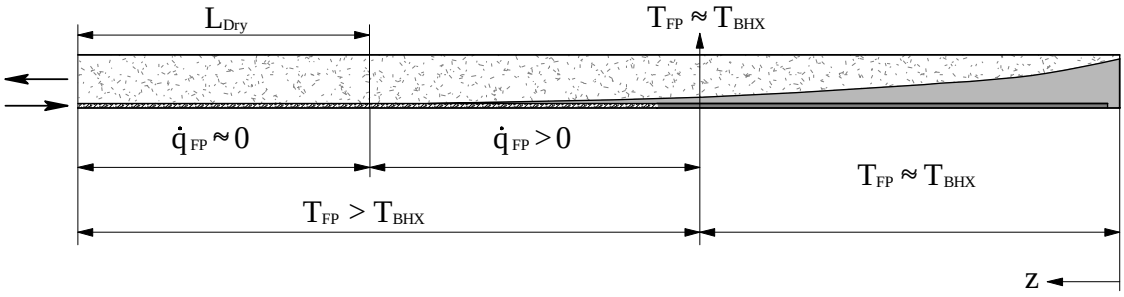

Figure 4.7: Heat exchange between the feeder pipe flow and the stratified flow.

4.5.2.2.1 Reversed heat flux

The temperature variation along the axial coordinate z, which is defined positive in the flow direction of the stratified flow, consists of the pressure dependency of the temperature and the generated pressure drop.

$$\frac{dT}{dz} = \frac{dT}{dp}\frac{dp}{dz} \tag{4.23}$$

$$\left(\frac{dT}{dz}\right)_{FP} = \underbrace{\frac{dT}{dp}}_{c_{JT}} \left(\frac{dp}{dz}\right)_{FP} \tag{4.24}$$

$$\left(\frac{dT}{dz}\right)_{BHX} = \left(\frac{dT}{dp}\right)_{2\Phi} \left(\frac{dp}{dz}\right)_{BHX} \tag{4.25}$$

The diagram in figure 4.8 shows the absolute value of the Joule-Thomson coefficient c_{JT} for three different temperatures in the liquid state and the correlation between temperature and pressure in the two-phase region $(dT/dp)_{2\Phi}$ vs. the pressure.

Starting at the point of equal temperature and proceeding mentally in negative z-direction, the pressure of the feeder pipe flow decreases and the pressure of the stratified flow increases. The two pressure gradients cause a temperature increase in each flow towards to the bayonet heat exchanger's end. Due to the negative Joule-Thomson coefficient of the single-phase feeder pipe flow, a pressure drop causes a temperature increase. The pressure profiles in the two pipes therefore

define the direction, in which heat is transferred. The temperature of the two-phase stratified flow is determined by the pressure, therefore any pressure related temperature difference is equalized by a heat flux to approach the feeder pipe flow temperature to the stratified flow temperature.

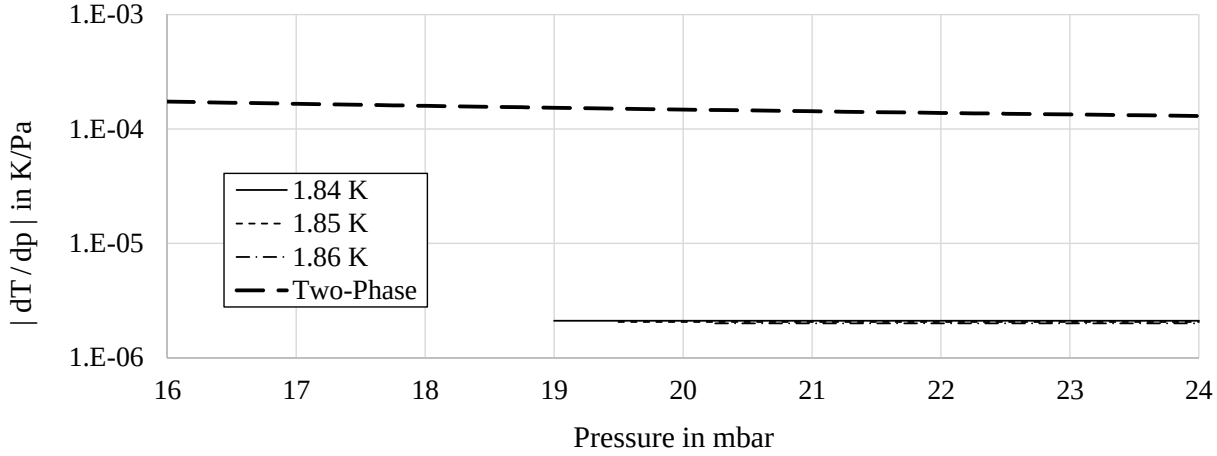

Figure 4.8: Joule-Thomson coefficient of sub-cooled helium for three different temperatures (thin lines) and correlation of temperature and pressure in the two-phase region (bold dashed line) vs. the pressure. The Joule-Thomson coefficient c_{JT} ($= dT/dp$) of the sub-cooled single-phase helium has a negative sign.

- Close to the point of equal temperature, the vapour phase occupies almost the entire pipe volume. The high volumetric flow causes high pressure drops an facilitates a reversed heat flux, pointing from the stratified flow to the feeder pipe flow.
- Close to the bayonet heat exchanger end the vapour mass fraction is low and subsequently the generated pressure drop is reduced. Therefore the heat flux tends to point from the feeder pipe flow to the stratified flow.

The feeder pipe flow is a high-density single-phase flow, the density of the stratified flow varies with its vapour mass fraction. Now we compare the two extreme cases for an entirely vaporized helium flow in the outer pipe of the bayonet heat exchanger ($\xi = 1$) and for an entirely liquid helium flow in the outer pipe of the bayonet heat exchanger ($\xi = 0$). The first case represents approximately the conditions at the point of equal temperature, the latter represents approximately the conditions at the bayonet heat exchanger's end.

Expressing the pressure gradients with the Darcy-Weisbach equation and dividing one by the other yields (4.26). The negative sign at the RHS of (4.26) originates from the opposing flow directions of the helium flows in the feeder pipe and in the outer pipe of the bayonet heat exchanger.

$$\frac{dp_{FP}}{dp_{BHX}} = -\frac{d_{BHX}\,A_{BHX}^2}{d_{FP}\,A_{FP}^2}\,\frac{\rho_{BHX}}{\rho_{FP}}\,\frac{f_{FP}}{f_{BHX}}\,\frac{2\,dz\,\dot{m}_{FP}^2}{2\,dz\,\dot{m}_{BHX}^2} \tag{4.26}$$

The diagram in figure 4.9 shows solutions of (4.26) for a saturated liquid helium flow ($\xi = 0$) in the outer pipe of the bayonet heat exchanger and for a saturated gaseous helium flow ($\xi = 1$) in the outer pipe of the bayonet heat exchanger for different saturation temperatures vs. the feeder pipe inner diameter. The Darcy friction factor was obtained with the formula of Swamee-Jain.

$$f = 0.25 \left[log_{10} \left(\frac{\epsilon}{3.7\, d_h} + \frac{5.74}{Re^{0.9}} \right) \right]^{-2} \tag{4.27}$$

Table 4.1: Reversed heat flux data

Input Value	**Symbol**	**Value**	**Unit**
Inner diameter of outer bayonet heat exchanger pipe	d_{BHX}	mm	83.1
Thickness of the feeder pipe wall	t_{FP}	1	mm
Absolute roughness of any pipe	ϵ	15	μm
Mass flow rate	$\dot{m}$	7.3	g/s

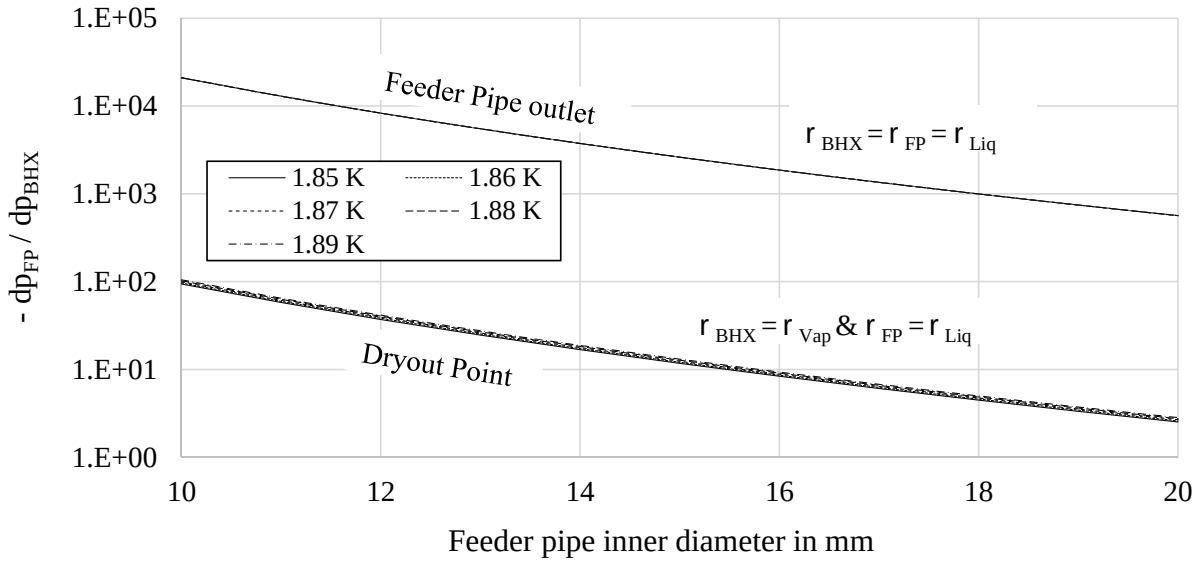

Figure 4.9: Pressure drop ratio for liquid helium flows in the feeder pipe and the outer pipe of the bayonet heat exchanger (labelled "Feeder Pipe outlet") and for a liquid helium flow in the feeder pipe and the helium vapour flow in the outer pipe of the bayonet heat exchanger (labelled "Dryout Point").

The temperature dependency on the pressure for the two-phase region is about two orders of magnitude higher than the Joule-Thomson coefficient of the single-phase helium (see diagram in figure 4.8). A pressure drop ratio lower than 10^2 causes a reversion of the heat flux. For feeder pipe diameters large enough, a reversed heat flux pointing from the stratified flow to the feeder pipe flow occurs between two points of equal temperature as schematically illustrated in figure 4.10.

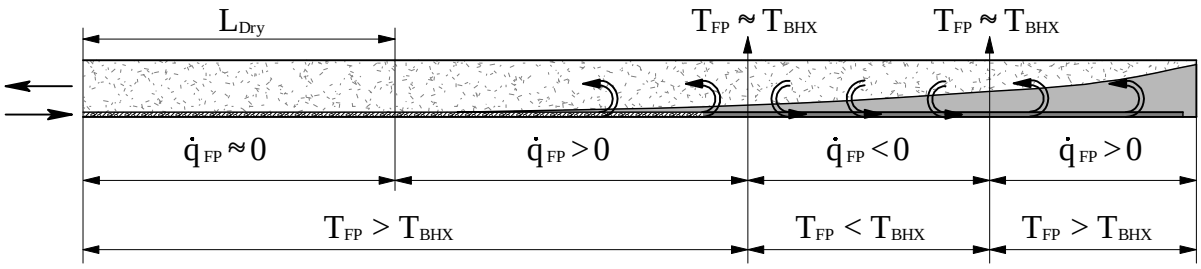

Figure 4.10: Reversed heat flux between two points of equal temperature.

4.5.2.2.2 Helium state at the feeder pipe outlet

The feeder pipe flow exits the feeder pipe in a sub-cooled state. The outlet pressure drop shifts the helium into the two-phase regime, otherwise the sub-cooled state of the feeder pipe flow cannot be reached. Numerical calculations have been performed to verify this statement, but it now should be proven with a reductio ad absurdum. We start with the assumption that the helium is still a sub-cooled single-phase fluid after having left the feeder pipe.

1. The outlet pressure drop lowers the helium pressure, the change of state corresponds to an isenthalpic process. Due to the negative Joule-Thomson coefficient, the temperature increases.

2. Due to the temperature rise, heat will be transferred to the feeder pipe flow. Therefore the feeder pipe flow's specific enthalpy must decrease in the counterflow direction. As long as the flow is sub-cooled, the temperature of the helium in the outer pipe of the bayonet heat exchanger increases, when heat is extracted from the cold mass. After entering the two-phase region, the temperature decreases corresponding to the pressure drop.

3. The feeder pipe flow temperature is lower than the temperature of the helium flow in the outer pipe of the bayonet heat exchanger and receives heat. The specific enthalpy decreases continuously in the counterflow direction and the thermodynamic state at the Joule-Thomson valve cannot be reached.

4. To reverse the heat flux, the temperature of the stratified flow must be lower than the temperature of the feeder pipe flow, which can be arranged by high pressure losses in the stratified flow. Pressure losses in the stratified flow must be avoided, however, to increase the cooling scheme's efficiency. An efficient design with a large bayonet heat exchanger, therefore cannot generate the necessary pressure losses to reverse the heat flux.

The feeder pipe flow in the sub-cooled state will release the helium flow into the two-phase region entering the bayonet heat exchanger. Depending on the geometry, the outlet pressure drop of the feeder pipe flow varies. The temperature at the feeder pipe outlet was assumed to be equal to the one of the stratified flow and the helium states can be achieved unambiguously for a given outlet pressure drop.

Figure 4.11 left shows the impossibility of a sub-cooled bayonet heat exchanger pipe flow for an efficient cold mass cooling system by illustrating the theoretical evolution in a small section of the p,h diagram. At the right-hand side, the determination of the helium states at the parallel cooled CMU's end to fulfil the enthalpy condition and the temperature condition is shown for three different outlet pressure drops in a small section of the p,h diagram.

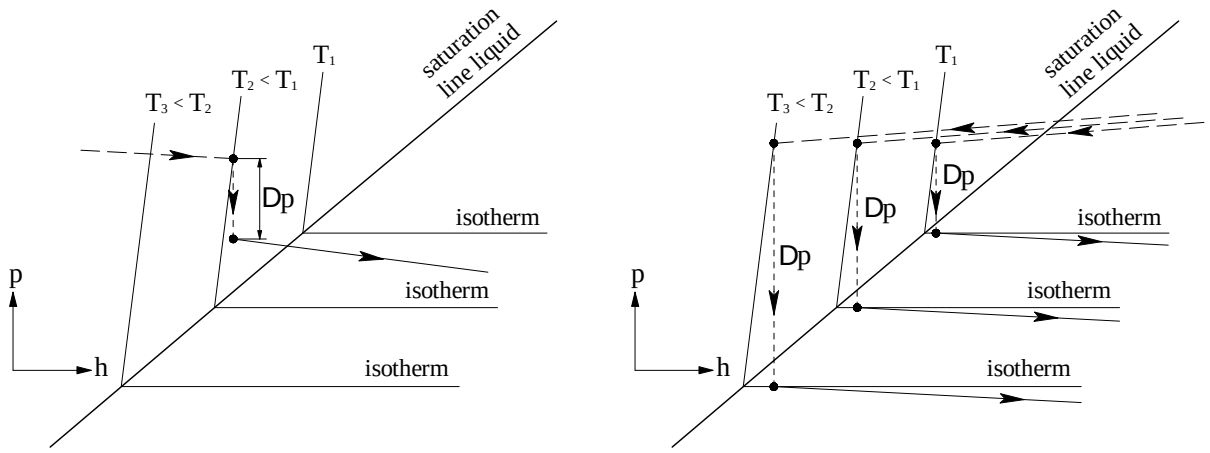

Figure 4.11: Impossibility of the feeder pipe flow (long dashed line) to reach the initial condition at the Joule-Thomson valve outlet with the heat exchanger pipe flow (solid line) starting as a sub-cooled single-phase liquid (left-hand side) and three different outlet pressure drops at the feeder pipe outlet for three different saturation temperatures (right-hand side).

4.5.3 Pressurised static bath of He II

For dependable operation of the cold mass cooling system in a steady-state mode, a minimal dry length of 20 % of the parallel cooled CMU length was determined. The major part of the heat load along the dry section of the cold mass has to be conducted axially to the wetted section by the static helium bath. To enable a sufficient axial heat transfer, channels containing the pressurized He II (free area) have to be integrated into the cold mass. Figure 4.12 schematically shows the structure of the cold mass containing axial channels for heat conduction.

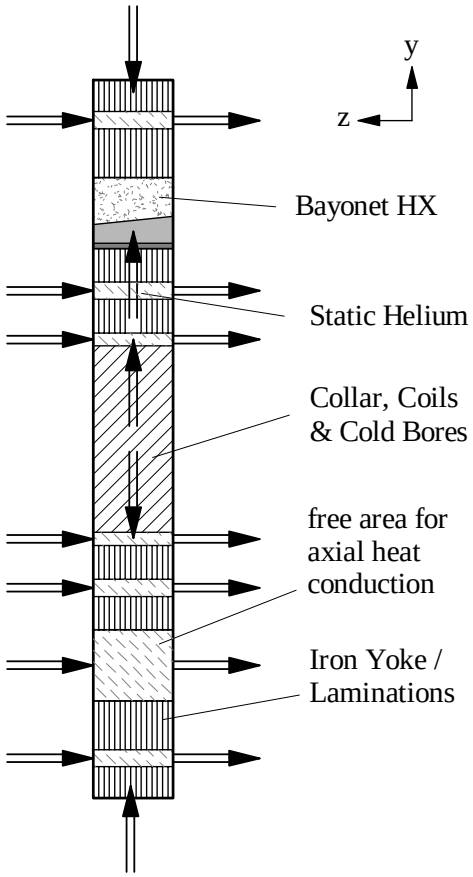

Figure 4.12: Cold mass slice with schematically indicated heat fluxes. The symmetry bore, the transport and assembly recesses and additionally designed channels create a free cross section area in the iron yoke, containing helium to conduct the absorbed heat load axially (compare with figure 4.2). The arrows schematically represent the heat fluxes.

4.5.3.1 Radial heat transfer

The heat load on the cold mass has to be conducted radially to the bayonet heat exchanger. A non negligible fraction of the heat has to pass the coils themselves.

Coils A numerical simulation based on the finite volume method with the open source program "OpenFOAM" was performed. A simplified coil geometry based on the CosΘ-design for an FCC dipole was modelled. The coils were assumed to consist of a heterogeneous Nb_3Sn-Copper composite, where the two inner rings had a copper fraction of 66 % and the two outer rings had a copper fraction of 50 %. The heat load distribution of the beam gas scattering was estimated based on the results allocated by the STI group (**S**ources, **T**argets and **I**nteractions) of the EN-Department at CERN. Figure 4.13 illustrates qualitatively the assumed distribution of the heat load due to the beam gas scattering ($\dot{Q}_{BGS}$) on one coil. The angles $\beta_1 - \beta_4$ mark four different paths for which the temperatures are plotted in the diagram in figure 4.14.

A 2D-simulation was performed for several slices with different heat loads. The temperature dependency of the thermal conductivity of the materials were taken into account, the surrounding helium bath was assumed to have a constant temperature of 1.9 K. Between the outermost materials, Kapton and aluminium, and the superfluid helium a Kapitza resistance was calculated [74][75]. The temperature difference between the highest temperature of the coil and the helium bath temperature was in the range of 50 mK for the cold mass cross section, which receives the highest heat load due to beam gas scattering. Figure 4.14 shows the radial temperature profiles of the cold mass cross section with the highest impact due to beam gas scattering for four different angles (β_1 - β_4),

as indicated in figure 4.13. For all subsequent considerations, the heat transfer within the coils is neglected and the temperature of the static helium bath is used as a limiting factor, bearing in mind an additional thermal resistance creating a driving temperature difference in the order of 50 mK.

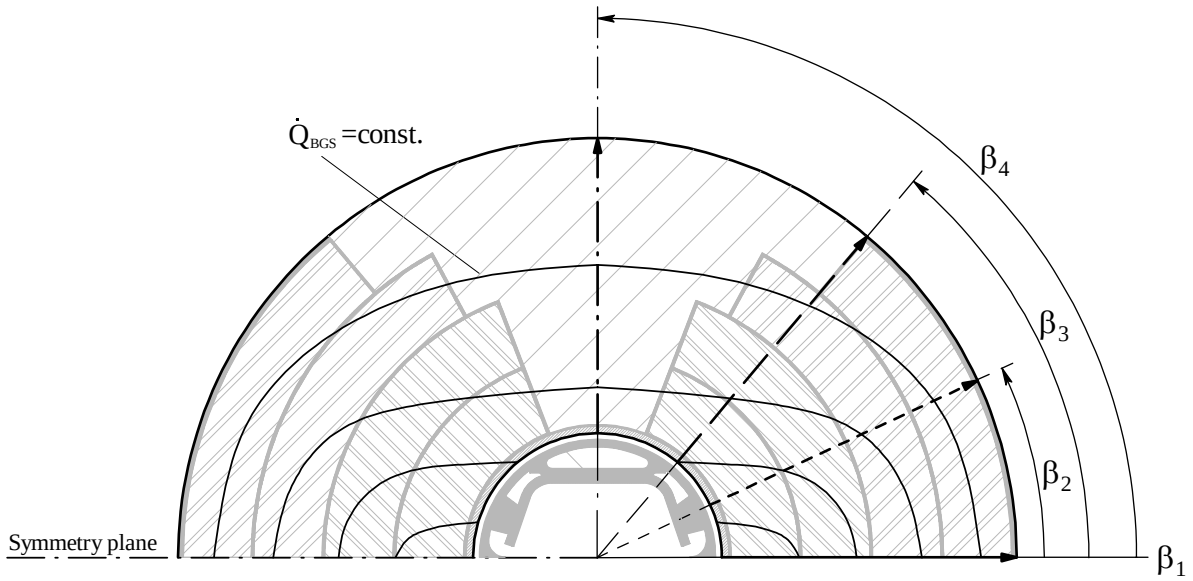

Figure 4.13: Qualitative heat distribution due to beam gas scattering and four angles for which the radial temperature profiles are shown in figure 4.14.

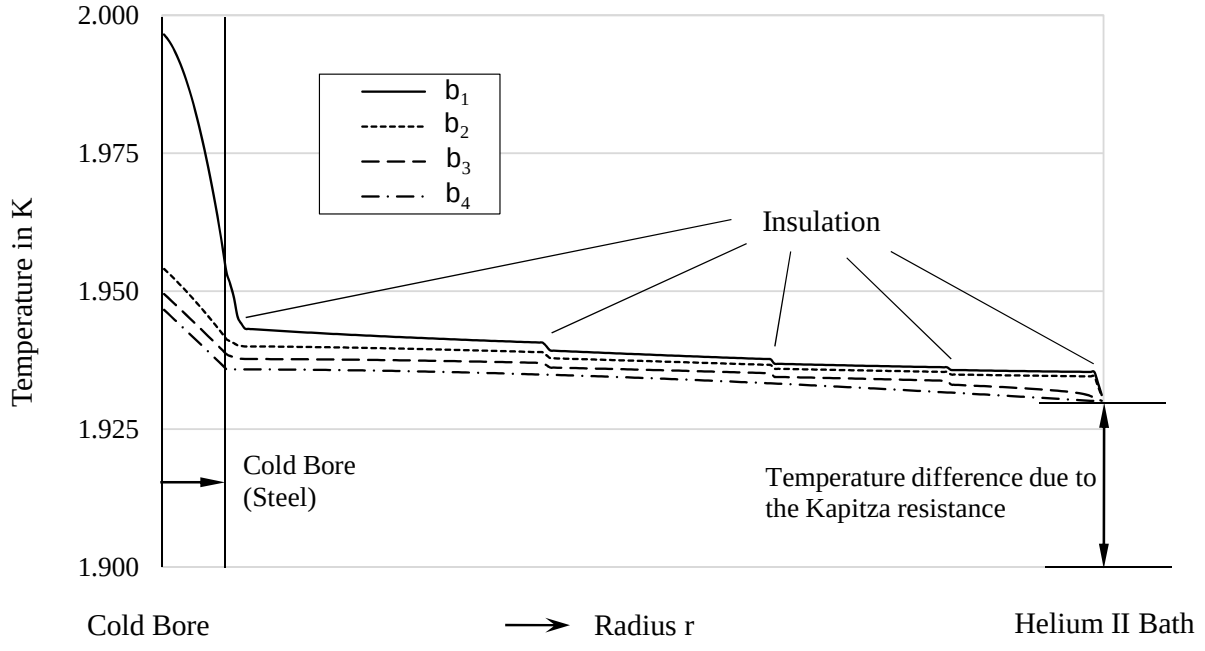

Figure 4.14: Radial temperature profiles in the coil at the cross section with maximal heat load due to beam gas scattering along four different paths.

Iron Yoke The iron yoke consists of stacked laminations of thickness t_{Lam} of 6 mm, as schematically shown in figure 4.15. The drawing on the left side corresponds to the depiction of a magnet's "slice" of the length Δz as illustrated in figure 4.12. The thickness t_{Lam} of a lamination and the distance d_{Lam} between two laminations are illustrated exaggerated for the sake of understanding. Based on the magnet design of the LHC, the blank volume ε_{CM} between the laminations is assumed to be 2 %. The average distance d_{Lam} between two laminations can be estimated as

$$d_{Lam} \approx t_{Lam}\,\varepsilon_{CM} = 120\ \mu m. \tag{4.28}$$

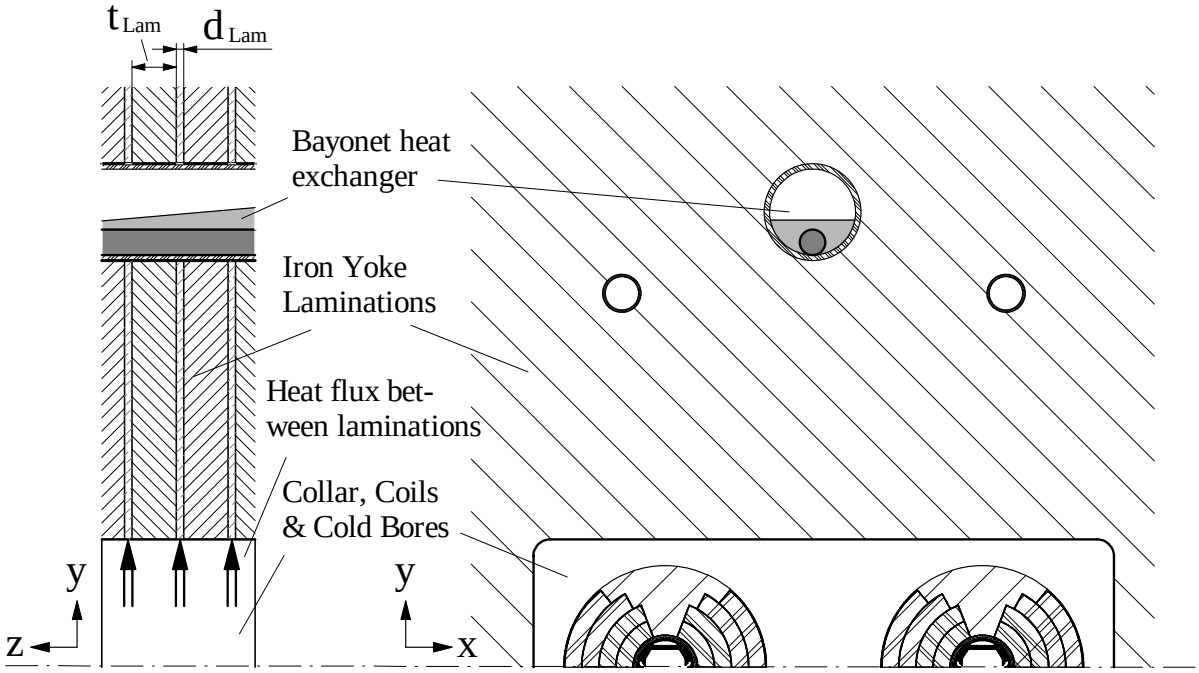

Figure 4.15: Schematic of the radial heat transfer between the iron yoke laminations illustrated in the y,z-plane (left-hand side) and the x,y-plane (right-hand side).

The order of magnitude of the generated temperature difference to transfer the heat between the iron yoke laminations was estimated with an analytical approach. In a first case, only the diameter of the bayonet heat exchanger is assumed to be the area contributing to transfer the entire heat. In second case, the heat sink and the heat source are modelled as concentric cylinder jackets. The real values should be ranged between these two extreme cases. The geometric assumptions of the two cases are illustrated in figure 4.16. Since a small necessary driving temperature difference is advantageous for the cold mass cooling system, the first case is referred to as "pessimistic" case and second case is referred to as "optimistic" case.

The driving temperature difference to transfer the heat between two laminations can be calculated with (3.4). The derivation of the Landau regime term is based on the equation of Hagen and Poiseuille for laminar flows, the geometry factor β depends on the shape of the channel [35]. The velocity profile of a flow between two plates with the distance d_{Lam} is calculated with (4.29). The geometric definitions are illustrated in figure 4.17. Since the distance between two laminations is about four to five orders of magnitude smaller than the width of the flow channel, the velocity profile of the flow over the channel width can be assumed to be constant.

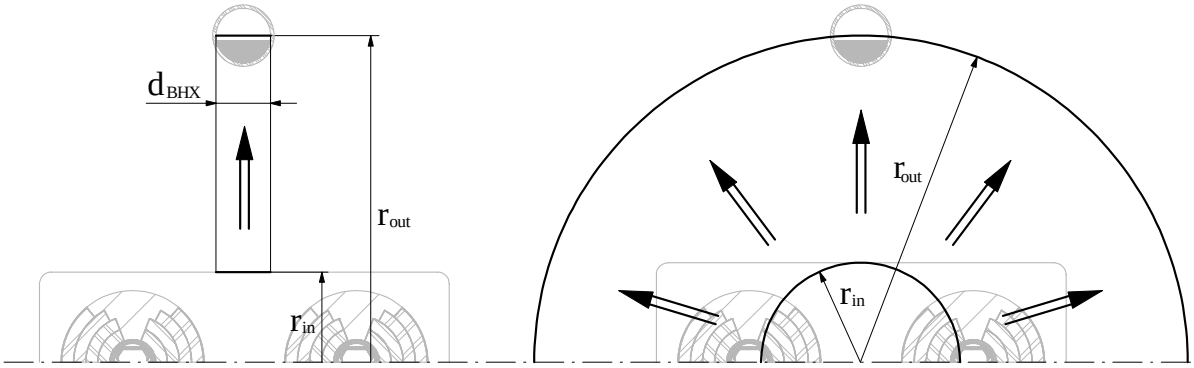

Figure 4.16: Pessimistic assumption of the contributing area to transfer the heat between the iron yoke laminations (left-hand side)and optimistic assumption of the area contributing to transfer the heat between the iron yoke laminations (right-hand side).

$$\frac{du_r}{d\eta} = \frac{\eta}{\mu}\frac{dp}{dr} \quad \rightarrow \quad \int,\ u_{wall} = 0 \quad \rightarrow \quad u_r\left(r,\eta\right) = \frac{\eta^2 - \left(d_{Lam}^2/4\right)}{2\mu}\frac{dp}{dr} \tag{4.29}$$

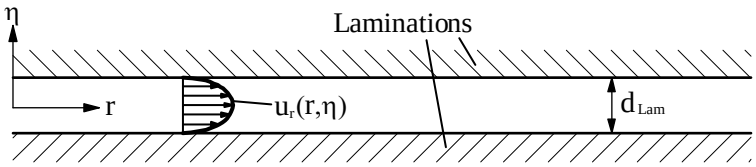

Figure 4.17: Laminar velocity profile in the slit between two iron yoke laminations.

The analytical derivation of the temperature difference with constant helium properties for the two cases is shown in parallel. The left column below contains the equations for the pessimistic case, the right column for the optimistic case. The heat $\dot{Q}$ transferred can be obtained by (4.30) [35].

$$\dot{Q} = \rho \dot{V} T s \tag{4.30}$$

Using the London equation (3.3), the pressure difference can be substituted to obtain the temperature gradient generated by the Landau Term dT_L/dr. The contribution of the Gorter-Mellink term dT_{GM}/dr can be calculated with the second term of the RHS of (3.4).

Pessimistic Case:

$$\dot{V} = 2\, d_{BHX} \int_0^{\frac{d_{Lam}}{2}} u_r\left(\eta\right)\, d\eta \tag{4.31}$$

$$\dot{V} = -\frac{d_{BHX}\, d_{Lam}^3}{12\,\mu}\frac{dp}{dr} \tag{4.32}$$

Optimistic Case:

$$\dot{V} = 4\,\pi\, r \int_0^{\frac{d_{Lam}}{2}} u_r\left(r,\eta\right)\, d\eta \tag{4.36}$$

$$\dot{V} = -\frac{\pi\, r\, d_{Lam}^3}{6\,\mu}\frac{dp}{dr} \tag{4.37}$$

$$\dot{Q} = \rho \dot{V} T s = -\frac{d_{BHX}\, d_{Lam}^3\, T\, \rho\, s}{12\,\mu} \frac{dp}{dr} \quad (4.33)$$

$$\frac{dT_L}{dr} = \underbrace{-12}_{\beta} \frac{\dot{Q}\,\mu}{d_{BHX}\,(\rho\, s)^2\, T\, d_{Lam}^3} \quad (4.34)$$

$$\frac{dT_{GM}}{dr} = -\underbrace{\frac{A_{GM}\,\rho_n}{\rho_s^3\, s^4\, T^3}}_{f_k} \left(\frac{\dot{Q}}{D_{BHX}\, d_{Lam}}\right)^3 \quad (4.35)$$

$$\dot{Q} = rho \dot{V} T \;\; s = -\frac{\pi\, r\, d_{Lam}^3\, T\, \rho\, s}{6\,\mu} \frac{dp}{dr} \quad (4.38)$$

$$\frac{dT_L}{dr} = \underbrace{-\frac{6}{\pi}}_{\beta} \frac{\dot{Q}\,\mu}{r\,(\rho s)^2\, T\, d_{Lam}^3} \quad (4.39)$$

$$\frac{dT_{GM}}{dr} = -\underbrace{\frac{A_{GM}\,\rho_n}{\rho_s^3\, s^4\, T^3}}_{f_k} \left(\frac{\dot{Q}}{2\, r\, \pi\, d_{Lam}}\right)^3 \quad (4.40)$$

The symbols ΔT_L and ΔT_{GM} represent the contributions of the Landau term and the Goerter-Mellink term to the total temperature difference ΔT between heat source and heat sink.

$$\Delta T = \int_{r_{in}}^{r_{out}} \left(\frac{dT_L}{dr} + \frac{dT_{GM}}{dr}\right) dr = \Delta T_L + \Delta T_{GM} \quad (4.41)$$

$$\Delta T_L = \frac{\beta\,\mu\,\dot{Q}}{d_{BHX}\,(\rho\, s)^2\, T\, d_{Lam}^3}\,(r_{out} - r_{in}) \quad (4.42)$$

$$\Delta T_{GM} = \frac{f_k\, \dot{Q}^3}{d_{BHX}^3\, d_{Lam}^3}\,(r_{out} - r_{in}) \quad (4.43)$$

$$\Delta T_L = \frac{\beta\,\mu\,\dot{Q}}{(\rho\, s)^2\, T\, d_{Lam}^3}\, ln\frac{r_{out}}{r_{in}} \quad (4.44)$$

$$\Delta T_{GM} = \frac{f_k\, \dot{Q}^3}{4\,\pi^3\, d_{Lam}^3} \left(\frac{1}{r_{in}^2} - \frac{1}{r_{out}^2}\right) \quad (4.45)$$

$$\Theta_{Lam} = \frac{\Delta T_L}{\Delta T_{GM}} \quad (4.46)$$

$\Theta_{Lam} >> 1$	$\rightarrow$	Landau term is driving force
$\Theta_{Lam} \approx 1$	$\rightarrow$	The two terms contribute similarly
$\Theta_{Lam} << 1$	$\rightarrow$	Gorter-Mellink term is driving force

The diagram in figure 4.18 shows the temperature difference ΔT and the ratio Θ_{Lam} vs. the transferred heat for different slit heights d_{Lam} between the laminations based on the pessimistic assumptions and optimistic assumptions.

One meter of cold mass consists of more than 166 laminations, hence the heat is transferred in 166 slits in parallel. The cryogenic system is designed to handle an average heat load of 2.44 W/m ($\widehat{=}$ 0.015 W/slit). Even in the pessimistic case, this heat transfer generates a temperature difference in the order of tenths of millikelvins, the Landau term is the driving force of the heat transfer. The temperature of the iron yoke can confidently assumed to be dependent only on the axial coordinate z.

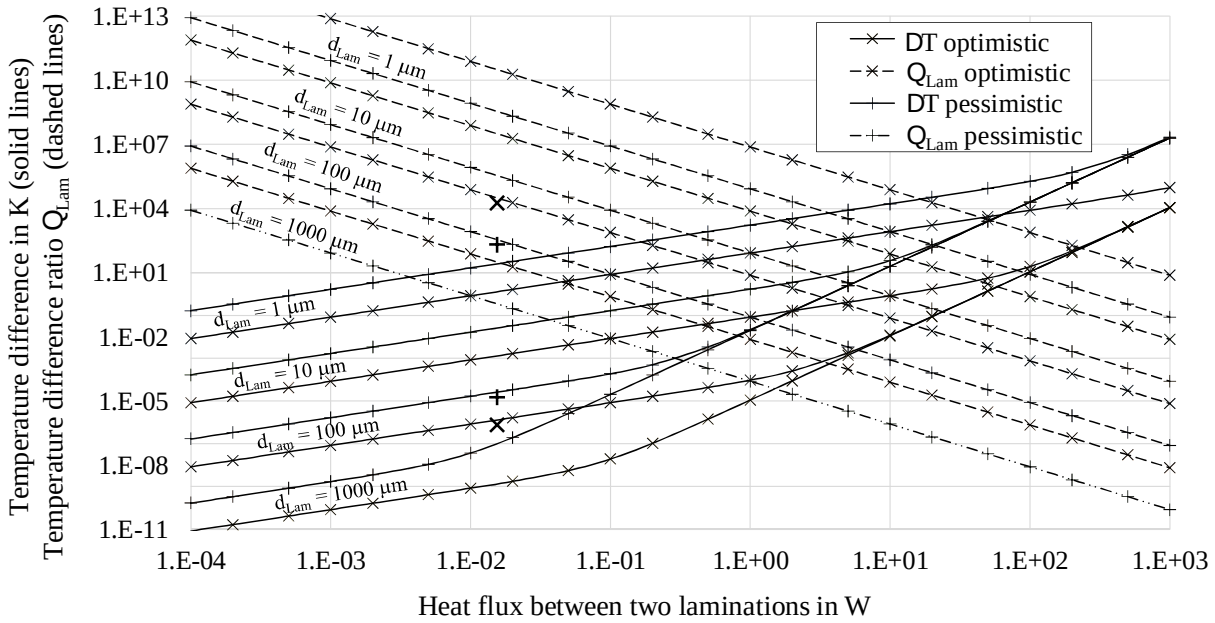

Figure 4.18: Temperature difference (solid lines) and Θ_{Lam} (dashed lines) vs. transferred heat flow between two laminations for different slit heights ($T_{Bath} = 1.9$ K, $p_{Bath} = 1.3$ bar, $r_{in} = 0.2$ m and $r_{out} = 0.4$ m). The lines marked with crosses correspond to the optimistic case, the lines marked with pluses to the pessimistic case (see figure 4.16). The large crosses and pluses mark the results for the assumed slit height (120 μm) and heat flux (0.015 W/slit) for the FCC cold mass.

Bayonet heat exchanger Heat is transferred from the iron yoke to the helium flow in the bayonet heat exchanger. As discussed in the previous section, the iron yoke temperature T_{IY}, by good estimation, can be assumed to be uniform in the entire cold mass cross section. The same statement applies for the temperature T_{BHX} of the stratified helium flow in the outer pipe of the bayonet heat exchanger. Figure 4.19 illustrates schematically the heat flux in the bayonet heat exchanger copper pipe.

Figure 4.19: Heat flux in one half of the bayonet heat exchanger. Due the much higher thermal resistance of the dry perimeter, part of the heat is tangentially conducted to the wetted inner surface along the copper pipe.

R_{BHX} ... radius of the bayonet heat exchanger

φ_{LL} ... angle defined by the liquid level in the bayonet heat exchanger

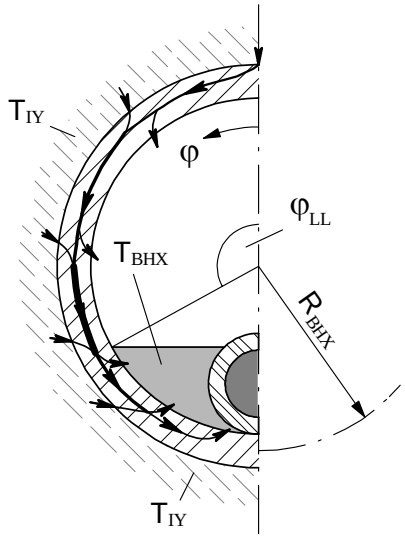

Between the copper pipe and the He II a Kapitza conductance is crucial for the radial heat transfer. For temperature differences much smaller than the absolute temperature ($\Delta T << T$) of the helium, Van Sciver proposes a simple formula to calculate the heat transfer coefficients (h_{IY} for the heat transfer between the static helium bath and the bayonet heat exchanger copper pipe and h_{Wet} for the heat transfer between liquid phase of the stratified flow and the bayonet heat exchanger copper pipe) [41].

$$h = (400 + 500\, f_{clean})\, T^3 \tag{4.47}$$

where h is obtained in $W/\left(m^2K\right)$, T is obtained in K and the non-dimensional factor f_{clean} describes the cleanliness of the copper surface with values between 0 (dirty) and 1 (clean). The results presented in this subsection were calculated with a cleanliness factor of 1, for technical surfaces the cleanliness factor has to be reduced accordingly. The heat transfer coefficient between the vapour phase and inner pipe wall is two orders of magnitude smaller than the Kapitza conductance, even for an entirely vaporized helium flow after the dryout point.

Only in immediate vicinity of the dryout point and thereafter the heat flux transferred to the helium flow passing the dry surface becomes notable compared to the total transferred heat flux as illustrated in the diagrams in the figures 4.23 and 4.25. Hence, for the entire bayonet heat exchanger length the heat transfer coefficient between the helium vapour and the pipe wall was assumed to be 30 $W/\left(m^2K\right)$, which corresponds to an average value for the dry section. However, after the dryout point, heat can only be transferred to the helium flow through the dry pipe wall.

The derivation of the equations to calculate the heat flux and the temperature profile in the bayonet heat exchanger pipe is illustrated in the Appendix C. Two different approaches were chosen and the results were compared.

Negligible radial thermal resistance in the copper pipe wall The diagrams in the figures 4.20 – 4.23 are created with data calculated neglecting the radial thermal resistance of the copper pipe wall as illustrated in the first subsection of Appendix C. The tangential temperature and heat flux profiles in the copper pipe wall are depicted. The most interesting result can be gathered from the graphs in figure 4.23. They show the transferred heat from the cold mass to the stratified flow depending on the liquid level for different driving temperature differences. The bold lines, which match almost exactly for each investigated driving temperature difference, represent the ratio of the heat entering the copper pipe from the iron yoke (i.e. at the outer pipe surface) at the pipe sections $\varphi < \varphi_{LL}$ and $\varphi > \varphi_{LL}$.

Infinite tangential thermal resistance in the copper pipe wall The diagrams in the figures 4.24 and 4.25 are created with data calculated neglecting the tangential heat transfer in the copper pipe wall as illustrated in the second subsection of Appendix C. The almost linear evolution of the temperature vs. the pipe radius insinuates that the situation is comparable with an heat transition through a non-curved wall. Also, the small temperature difference between the inner and the outer surface of the copper pipe justifies the assumption of a radially constant temperature profile, as made in the calculation with negligible radial thermal resistance in the copper pipe wall. The diagram in figure 4.25 shows the total transferred heat from the cold mass to the stratified flow depending on the liquid level and its distribution to the wetted and the dry perimeter for the two approaches.

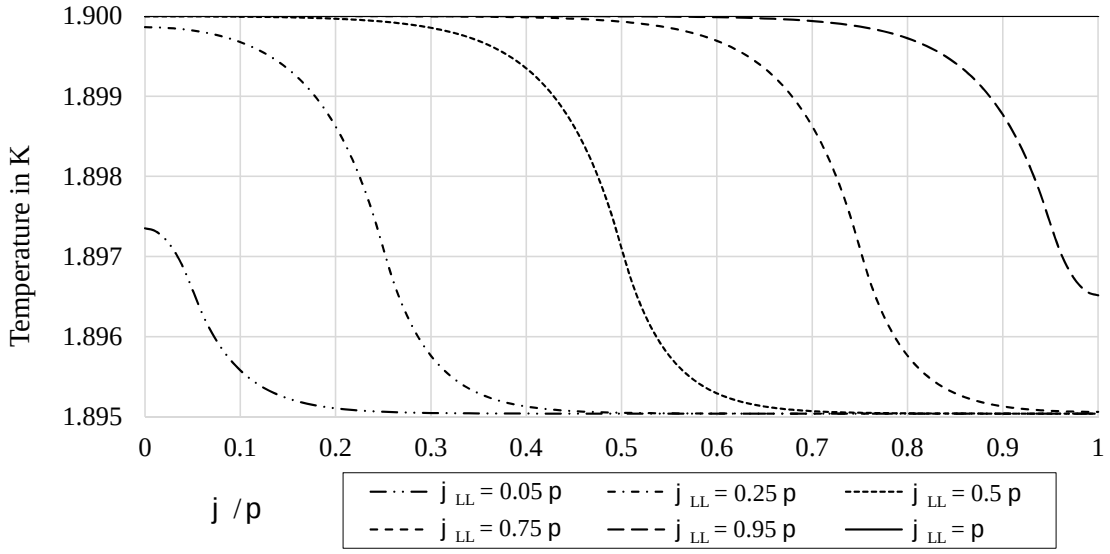

Figure 4.20: Tangential temperature profiles in one half of the bayonet heat exchanger copper pipe at R_{BHX} vs. the coordinate φ/π for different liquid levels (expressed by the angle φ_{LL}) and an iron yoke temperature T_{IY} of 1.9 K and a stratified flow temperature T_{BHX} of 1.89 K. The lowest temperature occurring corresponds approximately to the average temperature of the stratified flow and the cold mass ($\approx$ 1.895 K).

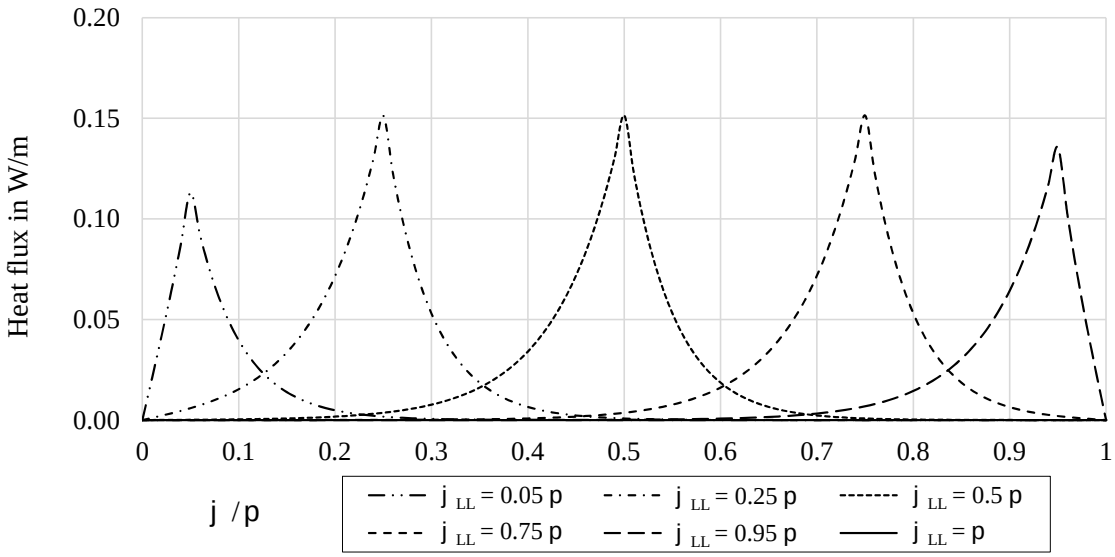

Figure 4.21: Tangential heat flux profile in one half of the bayonet heat exchanger copper pipe vs. the coordinate φ/π for different liquid levels (expressed by the angle φ_{LL}) and an iron yoke temperature T_{IY} of 1.9 K and a stratified flow temperature T_{BHX} of 1.89 K.

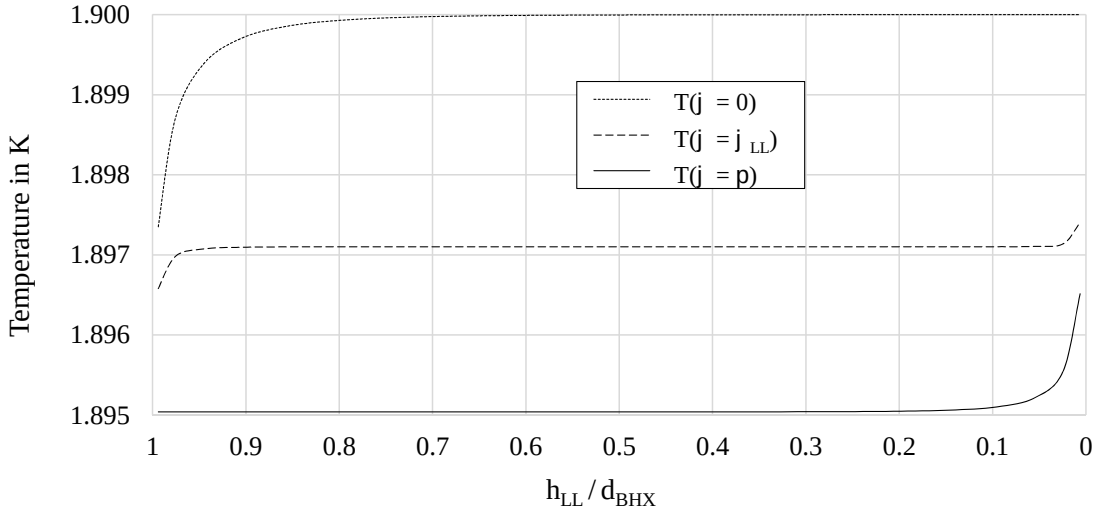

Figure 4.22: Temperature of the bayonet heat exchanger copper pipe at the positions $\varphi = 0$, $\varphi = \varphi_{LL}$ and $\varphi = \pi$ vs. the liquid level h_{LL} (divided by the inner diameter of the bayonet heat exchanger d_{BHX}) for an iron yoke temperature T_{IY} of 1.9 K and a stratified flow temperature T_{BHX} of 1.89 K.

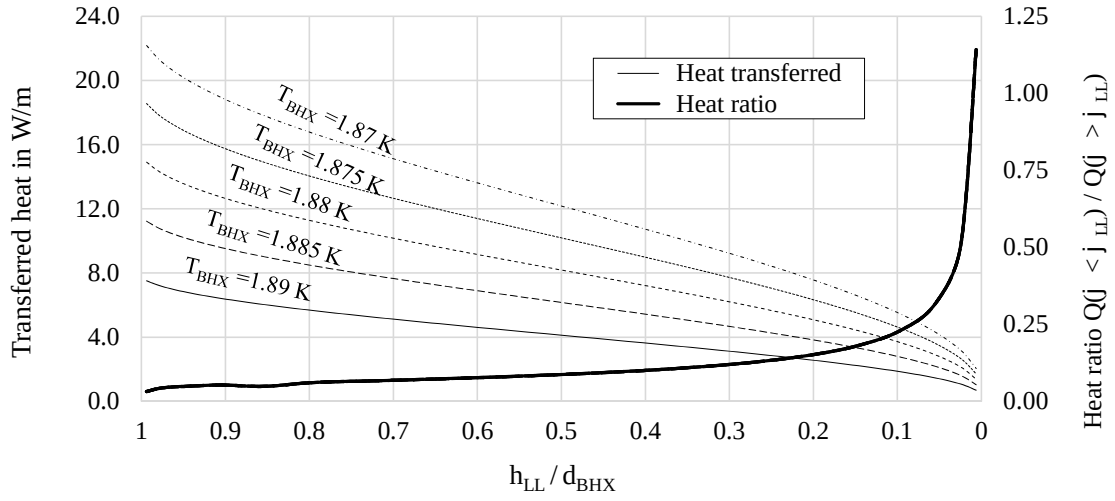

Figure 4.23: Total transferred heat in W/m from the cold mass to the bayonet heat exchanger (thin lines) and ratio of the heat at the outer surface of the copper pipe for the pipe sections $\varphi < \varphi_{LL}$ and $\varphi > \varphi_{LL}$ (bold lines) vs. the liquid level h_{LL} (divided by the inner diameter of the bayonet heat exchanger d_{BHX}) for an iron yoke temperature T_{IY} of 1.9 K and five different stratified flow temperatures T_{BHX}.

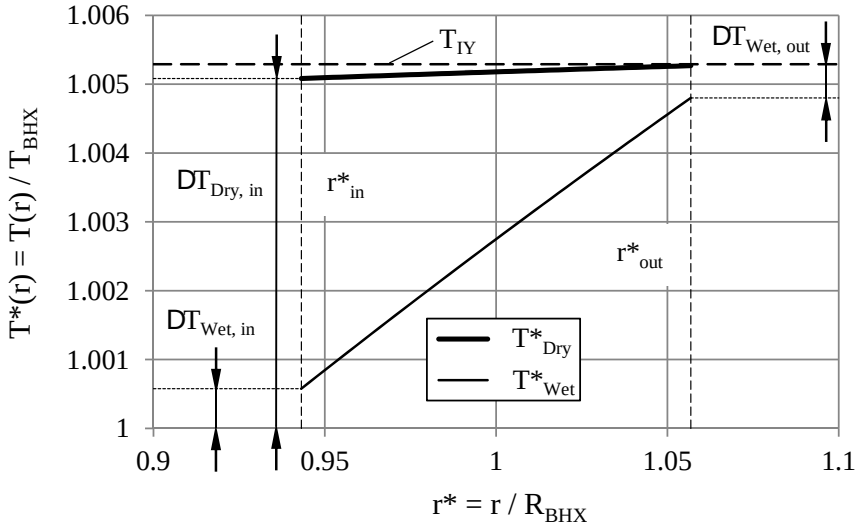

Figure 4.24: Radial, dimensionless temperature profile in the copper pipe wall vs. the dimensionless radius for a liquid helium flow (thin line) and a helium vapour flow (bold line). At the outside the driving temperature difference in the liquid case is larger than in the vapour case, since the heat transfer numbers are identical, but the transferred heat is smaller in the vapour case. At the inside the driving temperature difference for the liquid case is much smaller than for the vapour case, due to the significant difference of the heat transfer numbers.

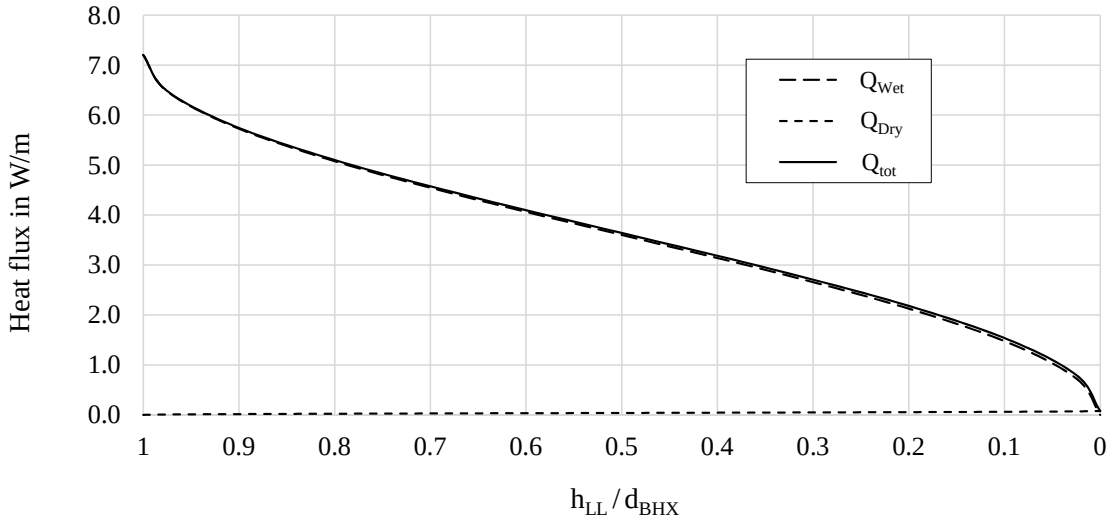

Figure 4.25: Radial heat transfer through the copper pipe wall vs. the liquid level h_{LL} (divided by the inner diameter of the bayonet heat exchanger d_{BHX}) for a helium temperature $T_{BHX} = 1.89\,K$. The long-dashed line corresponds to the heat transfer at the wetted surface, the short-dashed line corresponds to the heat transfer at the dry surface and the solid line line corresponds to their sum.

By comparing the total transferred heat calculated by the different approaches as shown in the diagram in figure 4.26, the heat flux profiles can be recognized as almost identical. Therefore it is assumed that both simplified mathematical approaches can be used to calculate the heat transfer and a two-dimensional calculation of the copper pipe wall's temperature field can be omitted. Assuming the possibility of tangential heat conduction, more heat can be extracted by the pipe section defined by an angle $\varphi > \varphi_{LL}$, which also can be seen by the higher heat ratio (grey lines in the diagram in figure 4.26). The good accordance of the results of the two calculations causes to assume that they are a sufficient approximation of the given situation.

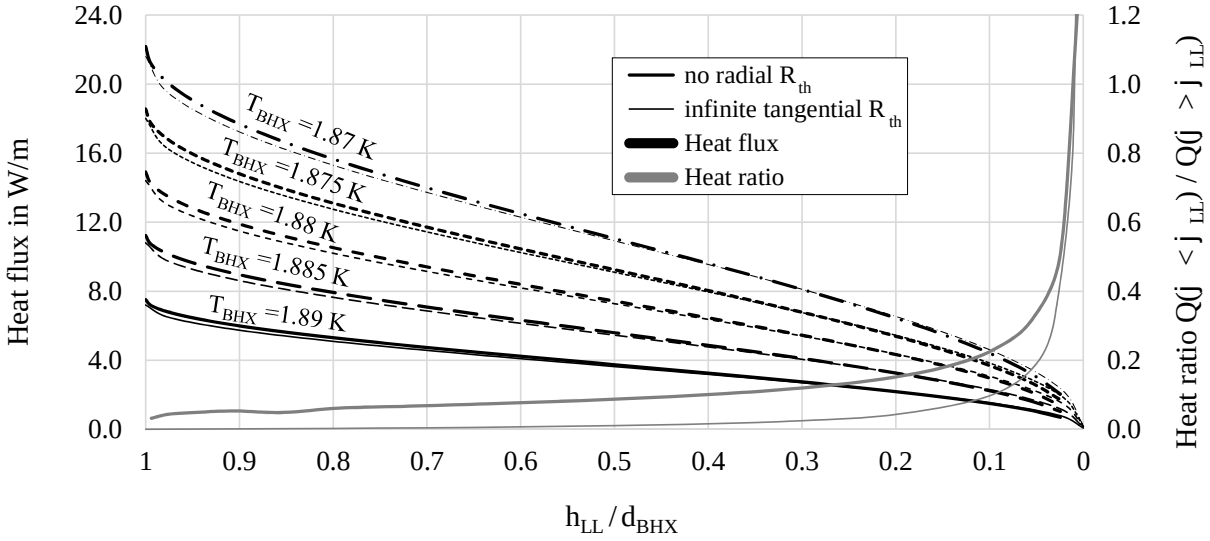

Figure 4.26: Comparison of the results gained by the two different approaches of the total transferred heat (black) and the ratio of the heat transferred at the outer surface of the copper pipe for the pipe sections $\varphi < \varphi_{LL}$ and $\varphi > \varphi_{LL}$ (grey) vs. the liquid level h_{LL} (divided by the inner diameter of the bayonet heat exchanger d_{BHX}) for different helium temperatures. The results for the negligible radial thermal resistance are represented with the bold lines, the results for the infinite tangential resistance with the thin lines.

4.5.3.2 Axial heat transfer

The axial heat transfer to extract the heat load on the cold mass along the dry section is enabled by the static helium in the free cross section area of the iron yoke. Due to the high heat fluxes and the wide channels, the contribution of the Landau term is much smaller than the contribution of the Gorter-Mellink term and can be neglected.

$$\frac{dT}{dz} = -\underbrace{\frac{\beta\mu}{d^2\,(\rho s)^2\,T}\dot{q}}_{<10^{-9}\ K/m} - \underbrace{\frac{A_{GM}\rho_n}{\rho_s^3 s^4 T^3}\dot{q}^m}_{>10^{-7}\ K/m} \tag{4.48}$$

4.5.3.3 Analytical estimation of the total temperature difference

To investigate the basic temperature evolution in a CMU, the total temperature difference ΔT_{tot} between the warmest point of the helium bath and the stratified flow at the parallel cooled CMU's

end is calculated analytically. The total temperature difference consists of the axial temperature difference along the dry section ΔT_{Dry}, the axial temperature difference along the wetted section ΔT_{Wet} and the radial temperature difference between the static helium bath and the stratified flow at the bayonet heat exchanger's end ΔT_{CM-Bay}.

$$\Delta T_{tot} = \Delta T_{Dry} + \Delta T_{Wet} + \Delta T_{CM-BHX} \tag{4.49}$$

Simplifications are assumed for the following considerations (see figure 4.27):

- The heat load $\dot{q}_{Source}$ is consistently distributed to the entire half-cell length
- The extracted heat by the bayonet heat exchanger $\dot{q}_{BHX}$ is consistently distributed to the entire wetted length L_{Wet} of the bayonet heat exchanger - no heat is transferred, when the bayonet heat exchanger is dried out
- In the second term on the RHS of (4.48) (Gorter-Mellink regime) an exponent m of 3 is used according to the prediction of the theory
- The thermal conductivity function f_k^{-1} is constant
- The free cross section area for the axial heat transfer A_{CM} is constant

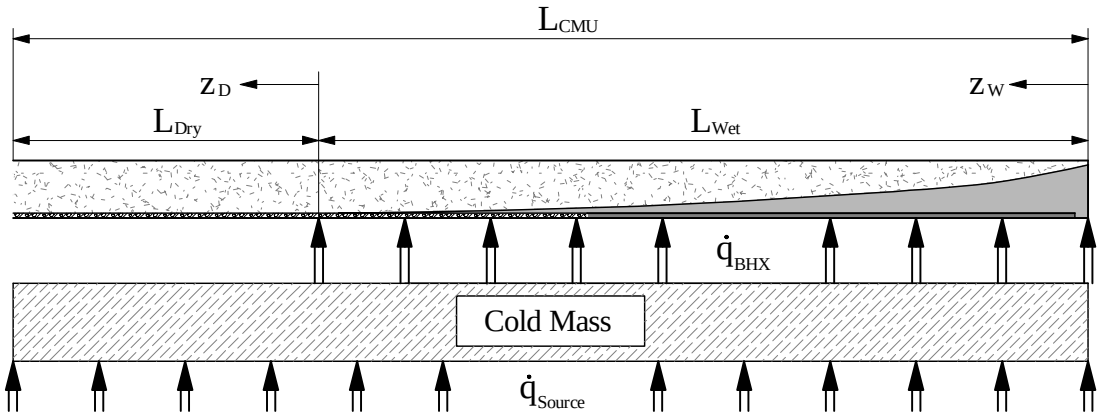

Figure 4.27: Thermal and geometrical assumptions for the derivation of the total temperature difference.

The axial temperature differences can be calculated according to (4.50) and (4.51).

$$\Delta T_{Dry} = \int d\Delta T_{Dry} = \int_0^{L_{Dry}} \overbrace{\left(\frac{\dot{q}_{Source}\, z_D}{A_{CM}}\right)^3}^{\dot{q}^3(z)} f_k \, dz_D = \frac{\dot{q}_{Source}^3 f_k L_{Dry}^4}{4 A_{CM}^3} \tag{4.50}$$

$$\begin{aligned} \Delta T_{Wet} &= \int d\Delta T_{Wet} = \int_0^{L_{Wet}} \frac{\left[\dot{q}_{Source} L_{Dry} + (\dot{q}_{Source} - \dot{q}_{BHX})\, z_W\right]^3 f_k}{A_{CM}^3} dz_W = \\ &= \frac{f_k}{4 A_{CM}^3} \frac{1}{\dot{q}_{Source} - \dot{q}_{BHX}} \left[\dot{q}_{Source} L_{Dry} + (\dot{q}_{Source} - \dot{q}_{BHX})\, z_W\right]^4 \Big|_0^{L_{Wet}} = \\ = \frac{f_k}{4 A_{CM}^3} &\frac{1}{\dot{q}_{Source} - \dot{q}_{BHX}} \left\{\left[\dot{q}_{Source} L_{Dry} + (\dot{q}_{Source} - \dot{q}_{BHX})\, L_{Wet}\right]^4 - \left(\dot{q}_{Source} L_{Dry}\right)^4\right\} \end{aligned} \tag{4.51}$$

The heat extracted by the bayonet heat exchanger equals the heat load on the cold mass. The wetted length can be substituted by the difference of the parallel cooled CMU's length and the dry length.

$$\left.\begin{aligned} \dot{q}_{BHX}\, L_{Wet} &= \dot{q}_{Source}\, L_{CMU} \\ L_{Wet} &= L_{CMU} - L_{Dry} \end{aligned}\right\} \dot{q}_{BHX} = \dot{q}_{Source}\, \frac{L_{CMU}}{L_{CMU} - L_{Dry}} \tag{4.52}$$

$$\Delta T_{Wet} = \frac{f_k}{4\, A_{CM}^3} \dot{q}_{Source}^3\, L_{Dry}^3\, (L_{CMU} - L_{Dry}) \tag{4.53}$$

$$\Delta T_{Dry} + \Delta T_{Wet} = \underbrace{\frac{\dot{q}_{Source}^3\, f_k\, L_{CMU}}{4\, A_{CM}^3}}_{=C_{ax}} L_{Dry}^3 =: \Delta T_{Tot} \tag{4.54}$$

The radial temperature difference at the bayonet heat exchanger's end increases with the heat flux to transfer to the stratified flow $\dot{q}_{BHX}$ - it can be kept small, if the heat is transferred over a preferably long wetted length. Its minimum $(\Delta T_{CM-BHX})_{min}$ is reached, if the dry length is zero and $\dot{q}_{Source} = \dot{q}_{BHX}$. Based on this consideration, the necessary radial temperature difference can be estimated with (4.55), yielding the total temperature difference as a function of L_{Dry}.

$$\Delta T_{CM-BHX} = (\Delta T_{CM-BHX})_{min} \left(\frac{L_{CMU}}{L_{CMU} - L_{Dry}} \right) \tag{4.55}$$

$$\Delta T_{Tot} = C_{ax}\, L_{Dry}^3 + (\Delta T_{CM-BHX})_{min} \left(\frac{L_{CMU}}{L_{CMU} - L_{Dry}} \right) \tag{4.56}$$

$$\underbrace{\frac{\Delta T_{Tot}}{(\Delta T_{CM-BHX})_{min}}}_{\Theta_{Tot}} = \underbrace{\frac{C_{ax}}{(\Delta T_{CM-BHX})_{min}}}_{\Theta_{ax}} L_{Dry}^3 + \frac{L_{CMU}}{L_{CMU} - L_{Dry}} \tag{4.57}$$

The smallest possible total temperature difference is achieved, when the dry section length vanishes. The diagram in figure 4.28 illustrates graphically the dependency of the total temperature difference ratio Θ_{Tot} on L_{Dry} for different values of Θ_{ax}, which is a measure for the ratio of the thermal resistivities in axial and radial direction.

The curves shown in the diagram in figure 4.28 at first have a convex shape and, after a strong increase of the slope, become concave. If the axial thermal resistance can be kept low, the point of the strong of the slope can be shifted to longer dry sections causing a lower temperature difference Θ_{Tot}. With increasing length of a parallel cooled CMU, the thermal resistance has to be decreased accordingly. The main parameter, which can be varied, is the free cross sectional area in the iron yoke.

The dry length cannot be reduced to zero for reasons of the dependable controlling, as elucidated in section 4.5.1. The axial temperature profile along the parallel cooled CMU can be calculated analytically using two equations for the wetted section length and the dry section length (as indicated in figure 4.27).

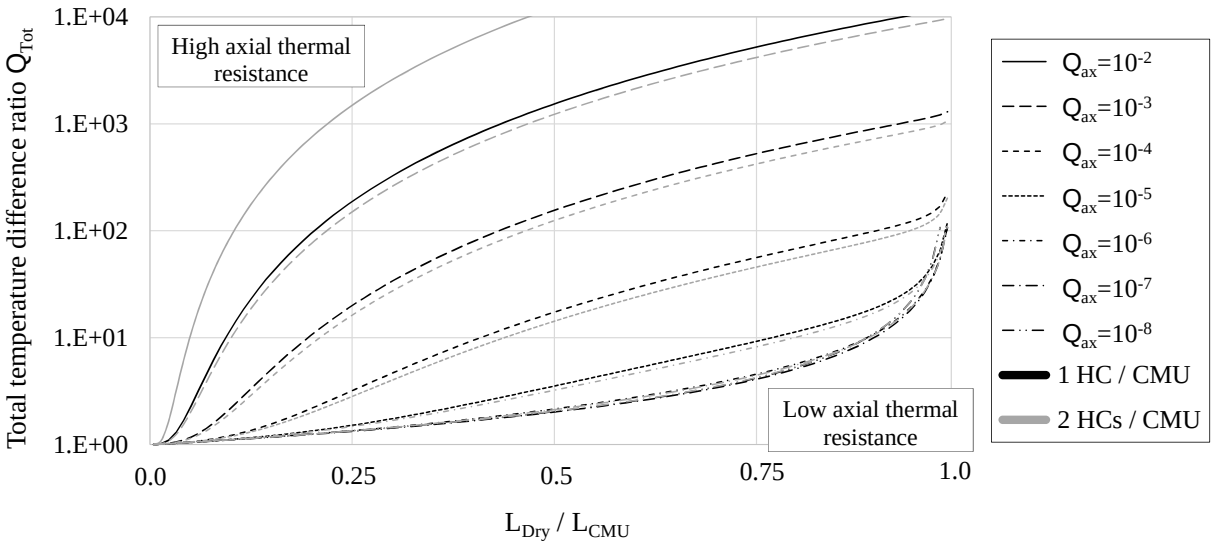

Figure 4.28: Total temperature difference ratio Θ_{Tot} vs. L_{Dry}/L_{CMU} for different thermal resistivity ratios Θ_{ax} and two different parallel cooled CMU lengths (1 half-cell in series (thin lines) and two half-cells in series (bold lines)).

- Wetted section length (L_{Wet}) for the axial coordinate $0 \leq z_W \leq L_{Wet}$:

$$\Delta T_{Wet}(z_W) = \Delta T_{CM-BHX} - \frac{f_k}{4\,A_{CM}^3} \frac{\left[\dot{q}_{Source}\,L_{Dry} + (\dot{q}_{Source} - \dot{q}_{BHX})\,z_W\right]^4}{\dot{q}_{Source} - \dot{q}_{BHX}} \tag{4.58}$$

- Dry section length (L_{Dry}) for the axial coordinate $0 \leq z_D \leq L_{Dry}$:

$$\Delta T_{Dry}(z_D) = \Delta T_{Wet}(z_W = L_{Wet}) + \frac{\dot{q}_{Source}^3\,f_k}{4\,A_{CM}^3}\left[L_{Dry}^4 - (L_{Dry} - z_D)^4\right] \tag{4.59}$$

Figure 4.29 shows the axial temperature profile of the cold mass for different lengths of the dry section (solid lines) calculated section-wise with (4.58) and (4.59). The dots on the curves are located at the inflection points, which also mark the dryout points. The temperature of the static helium bath at the dryout point shows a maximum for dry lengths of 80 – 90 % of the parallel cooled CMU length (to compare with the dashed curve in figure 4.29).

By increasing the free cross section area in the iron yoke linearly with the parallel cooled CMU's length, the temperature difference can theoretically be kept at the same level to obtain the same dry section length. However, long parallel cooled CMUs need less technical components and auxiliary equipment, but they call for large bayonet heat exchangers and a large free cross section area in the iron yoke. To minimize the necessary space for cryogenics in the cold mass, the parallel cooled CMUs must be kept short.

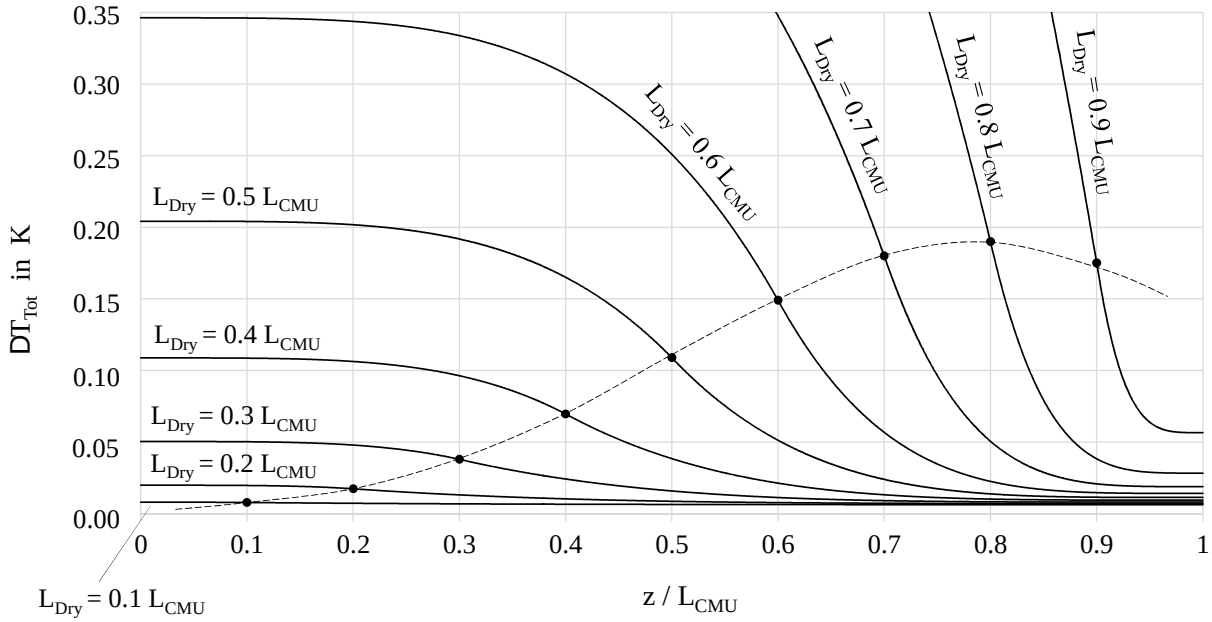

Figure 4.29: Total temperature difference for different dry sections (solid lines) and temperature of the static helium bath at the dryout point (dashed line) vs. the axial coordinate z/L_{CMU} ($A_{CM} = 156\ cm^2$, $f_k = 1.5 \cdot 10^{-13}\ m^5\,K\,W^{-3}$, $L_{CMU} = L_{HC}$, $\dot{q}_{Source} = 1.38\ W/m$, $(\Delta T_{CM-BHX})_{min} = 0.01\ K$).

4.5.4 Parallel cooled cold mass units (CMUs)

The FCC cold masses are cooled in parallel. Each parallel CMU consists of an integer number of half-cells. The parallel CMU is supplied by header C, and the vaporized helium is discharged into header B. An increase of the CMU length reduces the necessary amount of cryogenic equipment, but raises the space needed in the cold mass for cryogenic purposes. To guarantee dependable controlling, the minimal dry length was determined to be 20 % of the parallel cooled CMU's length [80]. This requirement was chosen for the nominal heat load case. At reduced heat load, the dry length can extend to a larger fraction of the total one.

4.5.4.1 Numerical simulation of a parallel cooled CMU

The basic structure of a parallel cooled CMU is illustrated in figure 4.4. The cold mass and the integrated components have been discussed in the previous sections. The treatment of the other technical components are now briefly explained.

- **Heat Exchanger:** The heat exchanger at the parallel cooled CMU's inlet works as a thermal bypass, transferring heat from the incoming high pressure helium flow to the exiting helium vapour. The lower specific enthalpy of the high pressure flow entering the Joule-Thomson valve h_{JT} causes a reduction of the vapour mass fraction after the isenthalpic expansion. No pressure drop for the high-pressure side was taken into account and the outlet temperature was set to be 2.18 K, hence close above the λ-temperature. Experiences with the LHC cold mass cooling system show that it is not possible to achieve a lower temperature than the λ-temperature, due to the transition to superfluid helium causing parasitic heat conduction from the warm end to the cold end of the heat exchanger's high-pressure side. The pressure

drop of the helium vapour passing the low-pressure side was set to be 1 mbar at maximal mass flow rate for the installed capacity, following the technical components used in the LHC, and is less for smaller helium mass flow rates ($\propto \dot{m}_{CMU}^2/\rho$) [81]. Energy consistency yields the temperature of the exiting helium flow of the low-pressure side. The terminal temperature difference of the heat exchanger therefore is an output value of the calculation.

- **Joule-Thomson valve:** The inlet condition is determined, the expansion in the Joule-Thomson valve is assumed to be isenthalpic. The outlet pressure and vapour mass fraction follow from the calculated pressure drop in the feeder pipe.

- **Separator:** In steady-state operation the separator is dry. No pressure drops were taken into account.

Table 4.2: Cold mass cooling with superfluid helium: Basic data

Input Value	**Symbol**	**Value**	**Unit**
Ambient temperature	T_a	300	K
Ambient pressure	p_a	1.013	bar
Temperature header C	T_C	4.6	K
Pressure header C	p_C	2.8	bar
Absolute roughness of any pipe	k	15	μm
Wall thickness heat exchanger pipe	t_{BHX}	5	mm
Cleanliness factor bayonet heat exchanger inside	$f_{clean\ BHX\ in}$	0.5	-
Cleanliness factor bayonet heat exchanger outside	$f_{clean\ BHX\ out}$	0.8	-
Wall thickness feeder pipe	t_{FP}	1	mm
Cleanliness factor feeder pipe each surface	$f_{clean\ FP}$	0.5	-
Inner diameter feeder pipe	d_{FP}	15	mm
Thermal conductivity of copper	$t_{HX\ Pipe}$	88	W/(m·K)
Minimal dry length	$L_{Dry\ min}$	$0.2\,L_{CMU}$	m
Maximal vapour velocity in the bayonet heat exchanger (at the dryout point)	$v_{Vap\ max}$	5	m/s
Helium temperature Joule-Thomson valve inlet	$T_{JT\ in}$	2.18	K
Maximal slope of the FCC machine	α	0.3	%

The helium properties were taken from the library 'HePak' (Cryodata Inc.). The maximal slope of the FCC is expected to be ±0.3 %, and the cryogenic distribution system is designed to have a descending stratified flow in each parallel cooled CMU, independent of its location.

The feeder pipe flow was modelled as a homogeneous flow, if it was in the two-phase regime [76]. The viscosity of the gas-liquid mixture was calculated with the correlation of McAdams (4.60) [82].

$$\mu = \left(\frac{\xi}{\mu_{Vap}} + \frac{1-\xi}{\mu_{Liq}} \right)^{-1} \tag{4.60}$$

The Darcy friction factor to calculate the pressure drop in the single-phase regime was obtained with the explicit formula of Swamee-Jain (4.27) [83].

4.5.4.2 Hydraulic design of a parallel cooled CMU

A single parallel cooled CMU must be designed to operate dependably at the installed capacity. The diameter of the bayonet heat exchanger, the free cross sectional area in the iron yoke and the length of a parallel cooled CMU (i.e. the number of half-cells it consists of) are the design parameters of interest.

Diameter of the bayonet heat exchanger The maximal helium vapour velocity in the outer pipe of the bayonet heat exchanger determines the diameter of the bayonet heat exchanger. The minimal inner diameter as a function of the saturation temperature of the stratified flow can be estimated with (4.7) as graphically illustrated in the diagram in figure 4.30. The lower pressure limit for the helium vapour flow in the bayonet heat exchanger is 16 mbar (as discussed in section 4.5.5). For a parallel cooled CMU corresponding to one half-cell, this yields a inner bayonet heat exchanger diameter of more than 80 mm to keep the vapour velocity below its limit and the value was set to be 83 mm. For parallel cooled CMUs consisting of more than one half-cell in series, the diameters can be scaled with a factor $\sqrt{2}$.

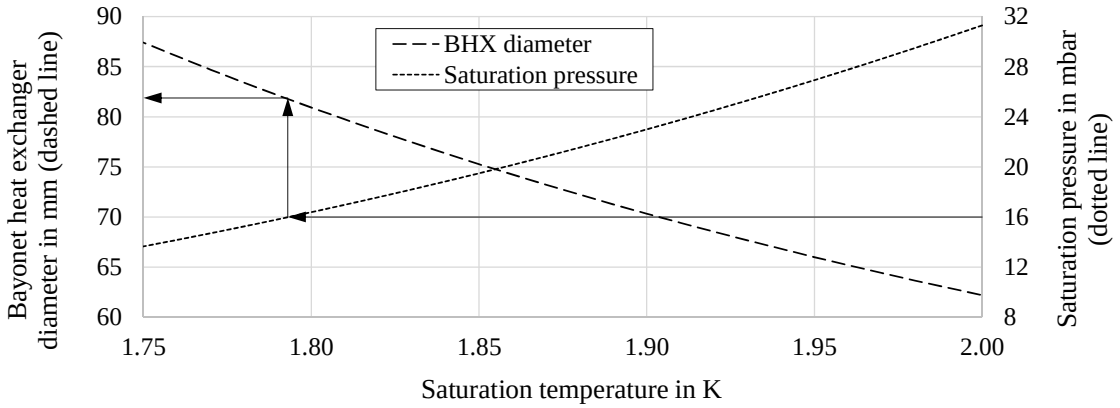

Figure 4.30: Minimal inner bayonet heat exchanger diameter for a parallel cooled CMU of one half-cell length (dashed line) and saturation pressure (dotted line) vs. saturation temperature of the stratified flow. For a minimal bayonet heat exchanger outlet pressure of 16 mbar a diameter of slightly above 80 mm is needed.

Cross sectional free area for axial heat conduction Figure 4.31 shows the required free area in the cold mass for a sufficient axial heat conduction, depending on the difference between the maximal bath temperature $T_{Bath\,max}$ and the feeder pipe outlet temperature $T_{FP\,out}$ for three cold mass temperature levels, with and without slope and operating at the installed capacity and a parallel cooled CMU length corresponding to one half-cell length. The half-cells located in inclined sectors provide the critical design parameters for the cold mass cooling system. The effect of the cold mass temperature on the required free area is of secondary order compared to the influence of the available temperature range.

The already available free cross section area in the cold mass, due to the actual design, amounts to about 156 cm^2. For a parallel cooled CMU of one half-cell length, this area results in a temperature difference between the feeder pipe outlet and the maximal bath temperature of slightly more than 50 mK, which is similar to the LHC's value (see diagram in figure 4.31).

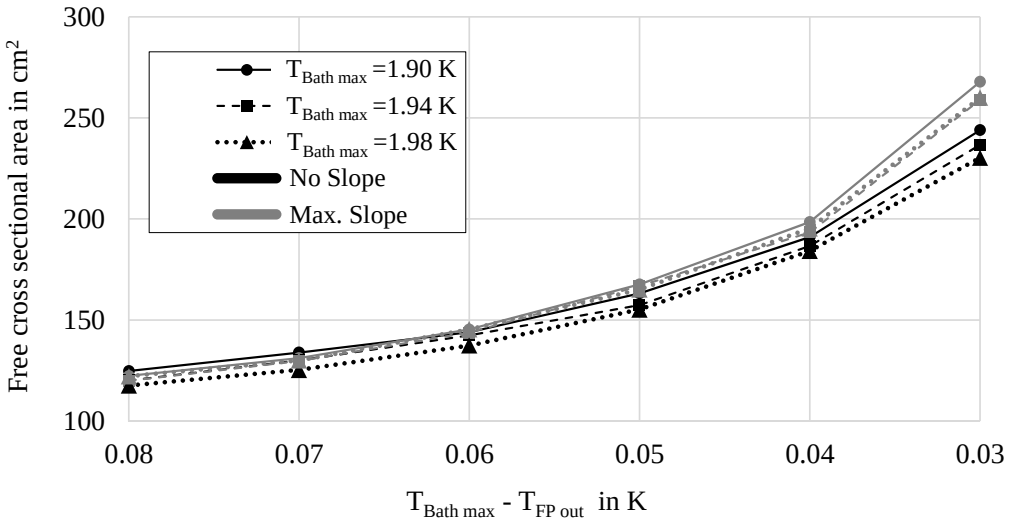

Figure 4.31: Required free cross sectional area vs. the difference between the maximal bath temperature $T_{Bath\,max}$ and the feeder pipe outlet temperature $T_{FP\,out}$ out for three different temperature levels, with and without slope, operating at the installed capacity for a parallel cooled CMU length corresponding to one half-cell.

The diagrams in figure 4.32 illustrate the temperature and heat flux profiles in a parallel cooled CMU with a length corresponding to one half-cell for a free cross sectional area of 156 cm^2. ① marks the dryout point, where also the inflection points of the temperature profiles of the helium bath and the maximal axial heat flux occur. At the parallel cooled CMU's end, the heat flux extracted from the cold mass is high due to the large wetted perimeter of the bayonet heat exchanger (②). With decreasing liquid level and increasing cold mass temperature, the heat flux profile shows a convex shape with a local minimum (③). Close to the dryout point, the driving temperature difference increases, causing a high heat transfer before it suddenly decreases strongly due to the total vaporization of the helium (④). The heat flux entering from the feeder pipe is large, corresponding to the high driving temperature difference - after passing a short distance, the feeder pipe flow is liquefied entirely, and the temperature approaches to the stratified flow temperature (⑤). The temperature of the entirely vaporized helium flow in the outer pipe of the bayonet heat exchanger increases due to the heat extracted from the warmer feeder pipe flow. When exeeding the static helium bath temperature, heat is transferred to the cold mass (⑥), which is represented by a negative heat flux in the diagram below in figure 4.32. The peaks in the heat load profile are caused by the increased electrical resistance of the joined superconducting cables to form a loop and by the heat entering the cold mass through the support posts.

Length of a parallel cooled CMU To obtain a comparable helium bath temperature and saturation temperature in the bayonet heat exchanger for longer parallel cooled CMUs, the free area and the bayonet heat exchanger area must be scaled linearly with the length of the parallel cooled CMU. The diagram in figure 4.33 shows the necessary space for cryogenic purposes in the iron yoke for different parallel cooled CMU lengths.

With each additional half-cell cooled in a series, about 7.5 % of the iron yoke area must be sacrificed for cryogenic applications, if the temperature difference $T_{Bath\,max} - T_{FP\,out}$ shall be kept

in the order of 50 mK. An increase of the temperature difference does not entail a sufficient reduction of the necessary space in the iron yoke to justify the accompanying loss of efficiency, due to the lower refrigeration temperature. A small free area also reduces the permanent helium inventory and therefore decreases the investment costs for the helium itself and the necessary storage and buffer infrastructure. After consideration of the advantages and disadvantages of the different lengths of the parallel cooled CMUs, it was determined to correspond to the length of one half-cell.

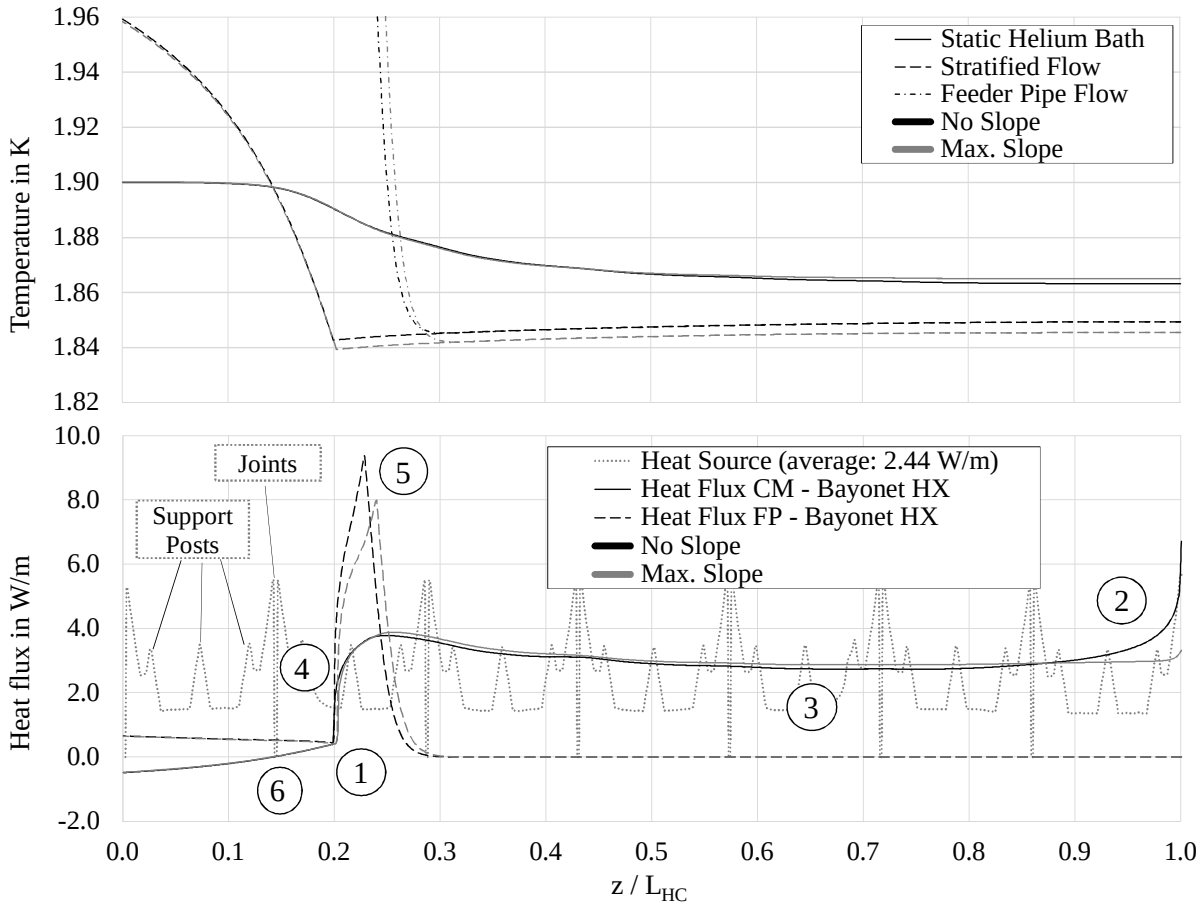

Figure 4.32: Temperature profiles for the static helium bath, the stratified flow and the feeder pipe flow (top) and heat flux from the static helium bath to the bayonet heat exchanger, from the feeder pipe flow to the bayonet heat exchanger, and the heat load (bottom) vs. the axial coordinate $z/L_{CMU}\,(=L_{HC})$ with and without slope, a maximal bath temperature of 1.9 K, a free iron yoke cross sectional area A_{CM} of 156 cm^2 and operating at the installed capacity.

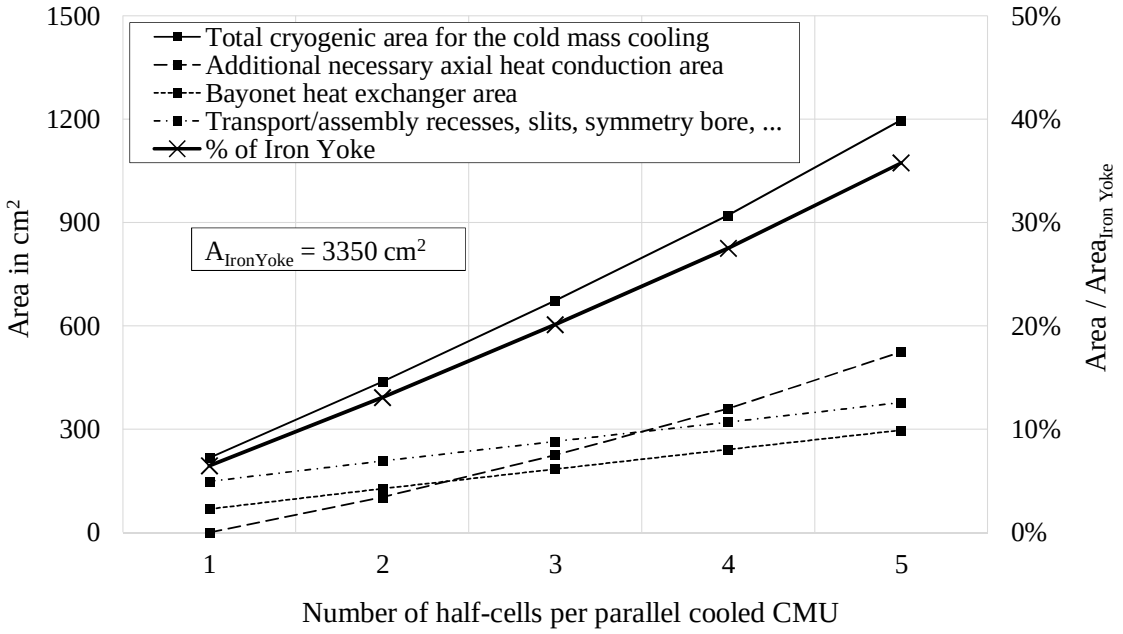

Figure 4.33: Necessary transverse space and its distribution for cryogenic purposes in the iron yoke in cm^2 (thin lines) and the resulting fraction of the entire iron yoke cross section area (bold lines) vs. length of a parallel cooled CMU. The results pertain for a temperature difference $T_{Bath\,max} - T_{FP\,out}$ of 55 mK corresponding to a free area of 156 cm^2 for one half-cell per parallel cooled CMU.

4.5.4.3 Exergetic analysis of one parallel cooled CMU

Figure 4.34 shows an exergy flow diagram of one parallel cooled CMU. The entire exergy loss consists of

- the heat transfer losses in the heat exchanger $\dot{B}_{HX}$,
- the pressure drop losses in the Joule-Thomson valve $\dot{B}_{JT}$,
- the pressure drop losses in the feeder $\dot{B}_{\Delta p\,FP}$,
- the heat transfer losses between the feeder pipe flow and the stratified flow $\dot{B}_{HT\,FP-BHX}$,
- the pressure drop losses of the stratified flow $\dot{B}_{\Delta p\,BHX}$,
- the heat transfer losses between the cold mass and the bayonet heat exchanger $\dot{B}_{HT\,CM-BHX}$,
- the heat transfer losses in the cold mass due to axial conduction $\dot{B}_{HT\,ax}$ and
- the (virtual) heat transfer losses in the cold mass due to undercutting the necessary temperature limit $\dot{B}_{lim}$.

The diagram in figure 4.35 shows the distribution of the relative exergy losses $\hat{b}_i$ (bars) for one half-cell operated at the installed capacity. The sum of the relative exergy losses and the exergetic efficiency yield 100 %, hence the exergetic efficiency can easily be calculated by subtracting the sum of the relative losses from 100 %. The solid black line represents the exergy consumption of the parallel cooled CMU without taking into account any losses of the distribution system and the cryoplants.

$$\hat{b}_i = \frac{\dot{B}_i}{\dot{B}_{tot}} \, (1 - \zeta) \tag{4.61}$$

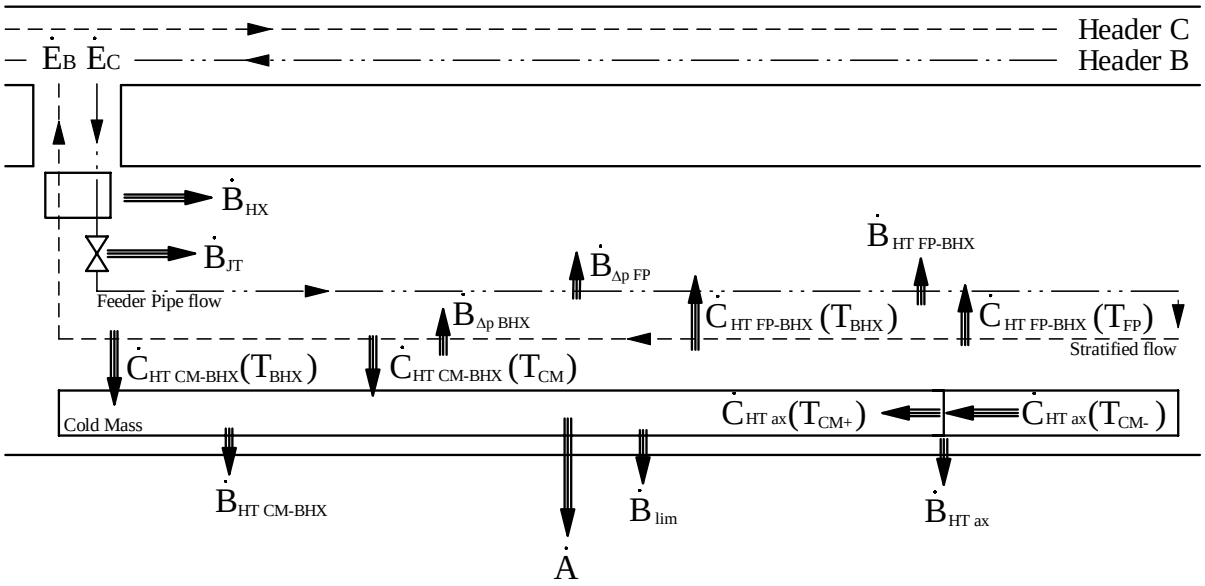

Figure 4.34: Exergy flow diagram of a parallel cooled CMU.

Heat exchanger The lowest bar (chequered pattern) represents the exergy loss of the heat exchanger. Although the heat exchanger loss is one of the major parts, the overall efficiency decreases without heat exchanger. Its performance is limited by reaching the λ-temperature at the high-pressure side, therefore the loss cannot be decreased. The losses could increase though, if the real terminal temperature difference is higher than the calculated minimum (which is about 0.3 K).

Joule-Thomson valve, feeder pipe and heat transfer stratified flow - feeder pipe flow The second bar (brick pattern) represents the exergy loss due to the pressure drop in the Joule-Thomson valve and in the feeder pipe. The third, black bar represents the exergy loss due to the heat transfer from the feeder pipe flow to the stratified flow. For a given saturation temperature of the stratified flow, the state of the helium at the feeder pipe outlet is determined and independent of the geometry of the feeder pipe by good approximation. The transferred heat from the feeder pipe flow to the stratified flow is therefore set and independent of the feeder pipe flow temperature.

The change of the exergy of helium between the Joule-Thomson valve inlet and feeder pipe outlet must correspond to the sum of the received exergy from the stratified flow, the exergy losses due to the isenthalpic expansion in the Joule-Thomson valve and the pressure drop in the feeder pipe.

$$\Delta e_{JT+FP} = h_{JT\ in} - h_{FP\ out} - T_a\ (s_{JT\ in} - s_{FP\ out}) \tag{4.62}$$

$$\dot{m}_{CMU}\,\Delta e_{JT+FP} + \underbrace{\dot{Q}_{FP}\left(\frac{T_a}{T_{FP}} - 1\right)}_{\dot{C}_{HT\ FP-BHX}(T_{FP})} - \dot{B}_{\Delta p\ FP} - \dot{B}_{JT} = 0 \tag{4.63}$$

With decreasing feeder pipe diameter, a larger part of the total pressure drop will be generated in the feeder pipe and the helium leaves the Joule-Thomson valve at higher pressure and temperature.

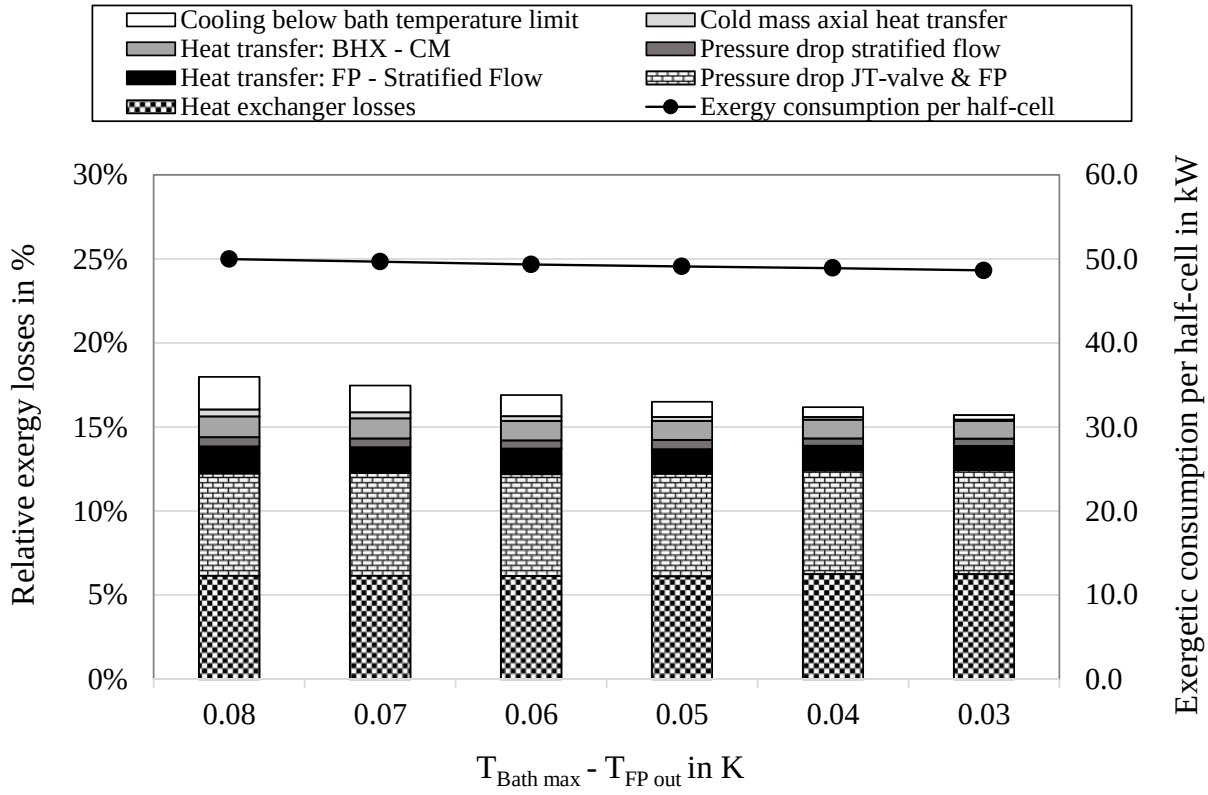

Figure 4.35: Relative exergy losses (bars) corresponding to the primary ordinate and exergy consumption per parallel cooled CMU ($\widehat{=}L_{HC}$) in kW (black line) corresponding to the secondary ordinate vs. the difference between the maximal bath temperature $T_{Bath\,max}$ and the feeder pipe outlet temperature $T_{FP\,out}$ for one half-cell operated at the installed capacity, maximal slope, a maximal bath temperature of 1.9 K and a free area A_{CM} of 156 cm^2.

The exergy flow, which the feeder pipe flow receives from the stratified flow, decreases due to the higher temperature of the feeder pipe flow. To fulfil (4.63) the pressure drop exergy losses must decrease (although the overall pressure drop does not change).

The temperature of the stratified flow can be assumed to be constant compared to the feeder pipe temperature. The exergy flow released by the stratified flow $\dot{C}_{HT\,FP-BHX}\,(T_{BHX})$ therefore also is constant.

$$\dot{m}_{CMU}\,\Delta e_{JT+FP} + \dot{C}_{HT\,FP-BHX}\,(T_{BHX}) = const. = \dot{B}_{HT\,FP-BHX} + \dot{B}_{\Delta p\,FP} + \dot{B}_{JT} \qquad (4.64)$$

For a given saturation temperature of the stratified flow and total liquefaction of the feeder pipe flow, the exergy losses $\dot{B}_{HT\,FP-BHX}$, $\dot{B}_{\Delta p\,FP}$ and $\dot{B}_{JT}$ are determined and cannot be changed.

The major part of the total exergy loss of this cooling principle is determined and the range of exergetic improvement is limited to the much smaller fraction of the residual losses.

Pressure drop in the stratified flow The fourth (dark grey) bar represents the exergy losses due to the pressure drop in the stratified flow. These losses already are very low, theoretically they

could be decreased even more, if the bayonet heat exchanger is enlarged (at the cost of the quality of the magnetic field). Another possibility is the improvement of the heat transfer from the feeder pipe flow to the stratified flow to keep the vapour mass fraction of the stratified flow small as long as possible.

Heat transfer static helium bath - stratified flow The fifth (medium grey) bar represents the exergy losses due to the heat transfer from the cold mass to the stratified flow. Since the Kapitza resistances cannot be changed, the thermal conductivity of the used copper and the thickness of the copper pipe wall are the only variables. During a quench, the pressure of the static helium bath can rise up to twenty bar. To withstand the pressure forces and avoid buckling, the right alloy must be combined with a sufficient wall thickness, therefore neither the material nor the thickness can be chosen freely.

Axial heat transfer in the static helium bath The sixth (light grey) bar represents the exergy losses due to the axial heat transfer in the static helium bath. Also these losses are diminishingly small. By decreasing the minimal dry section, the losses could be markedly reduced. Increasing the free area in the iron yoke does not have a large effect, but would impair the magnetic field quality.

Cooling below the bath temperature limit The topmost bar (white) represents the exergy losses due to the refrigeration below the necessary temperature limit. The large influence of the saturation pressure of the stratified flow is obvious. Also these losses could be reduced by increasing the free area in the iron yoke or decreasing the length of the dry section.

The minimal dry length and the free area are determined for different technical reasons. An improvement of the exergetic efficiency under these circumstances does not justify the necessary technical effort. However, the possible gain of this cooling concept is limited to about three percentage points. The exergetic efficiencies reached are already very close to the technically possible.

4.5.5 Sector distribution and discharge system

One FCC long cryogenic sector consists of 79 half-cells ($\approx$ 8400 m) cooled in parallel. The temperature of the last half-cell and the pressure evolution in the return header B dictate the operation temperature of all the previous half-cells. The pressure of the helium vapour exiting the parallel cooled half-cells is in the order of 15 to 30 mbar. To avoid choking of the return header B, its diameter must be chosen accordingly large. Figure 4.36 schematically illustrates the structures of two inclined sectors with negative and positive slope.

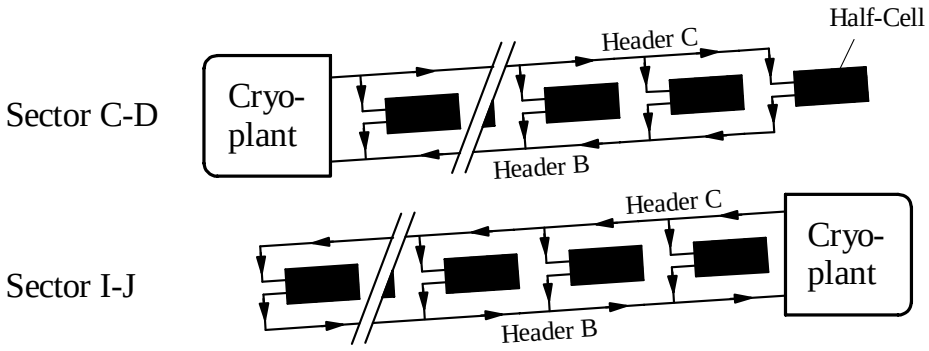

Figure 4.36: Schematic of the two inclined sectors C-D and I-J with positive and negative slopes.

4.5.5.1 Influence of the FCC slope on the distribution system

Based on the preliminary elevation profile illustrated in figure 2.18, the sectors C-D (positive slope) and I-J (negative slope) show the largest altitude difference between the respective sector end and the cryoplant. Lower pressure limits for the helium flows were determined.

Header C: 2.5 bar minimal helium pressure, to keep the flow in the single-phase state
Header B: 15 mbar minimal (cold compressor) suction pressure for dependable and efficient cold compressor operation

1. **Negative Slope**

   - **Header B:** The discharge pressure (header B pressure) of the last half-cell is maximal. When returning, friction and increasing gravitational potential decreases the pressure of the helium vapour and therefore the temperature levels of the previous half-cells. The minimal dry length condition is critical in the last half-cell at the sector's end. This scenario is crucial for the header B design to keep the static helium bath temperature of all half-cells below the necessary limit.
   - **Header C:** Close to the cold compressor station, the frictional pressure drop is partly compensated by the decrease of altitude. Due to branching helium mass, the header C mass flow rate decreases and the pressure increases. The point of minimal pressure is located close to the cold compressor station, which has to deliver helium at a pressure slightly higher than the lower pressure limit.

2. **Positive Slope**

   - **Header B:** The mass flow in header B at the end of a sector is very low and the gain in pressure, due to the decreasing altitude, is larger, than the frictional losses. Therefore, the dry section of the last half-cell must be longer, than the limit to fulfil the condition in all previous half-cells. With increasing mass flow rate on its way to the cold compressor station, the frictional pressure drops outweigh and the pressure decreases.
   - **Header C:** The lowest pressure in header C is at the inlet of the last half-cell. The cryoplant has to deliver helium at a clearly higher pressure level to avoid undercutting the lower limit of 2.5 bar.

The critical design case of the cold mass cryogenic distribution system is an ascending vapour flow returning to the cryoplant (negative slope), since the frictional and gravitational pressure losses sum up. Independent of the slope, the half-cells are fed at the lower point to have the stratified flow in the bayonet heat exchangers flowing downwards. One half-cell of 107 m can have a altitude difference of about 60 cm between the two ends.

4.5.5.2 Numerical simulation of a cold mass cooling sector system

The helium properties were taken from the library 'HePak' (Cryodata Inc.). Additional presumed values and numbers and boundary conditions are listed in table 4.3 and complete or replace the values given in table 4.2.

Table 4.3: Cold mass cooling with superfluid helium: Sector cooling

Input Value	**Symbol**	**Value**	**Unit**
Temperature header C cryoplant outlet	$T_{C\,in}$	4.6	K
Lower pressure limit header C	$p_{C\,min}$	2.5	bar
Diameter header C	d_C	80	mm
Lower pressure limit header B	$p_{B\,min}$	15	mbar
Heat load on header B	$\dot{q}_B$	0.24	W/m

The Darcy friction factor to calculate the pressure drop in the single-phase fluids was obtained with the explicit formula of Swamee-Jain [83]. Due to the large diameter of the header B, a constant heat load of about 2000 W per long sector was assumed.

4.5.5.3 Helium vapour discharge system

The diagram in figure 4.37 shows the static bath temperature of the last half-cell as a function of the diameter of the header B for a suction pressure of 15 mbar operating at the nominal capacity.

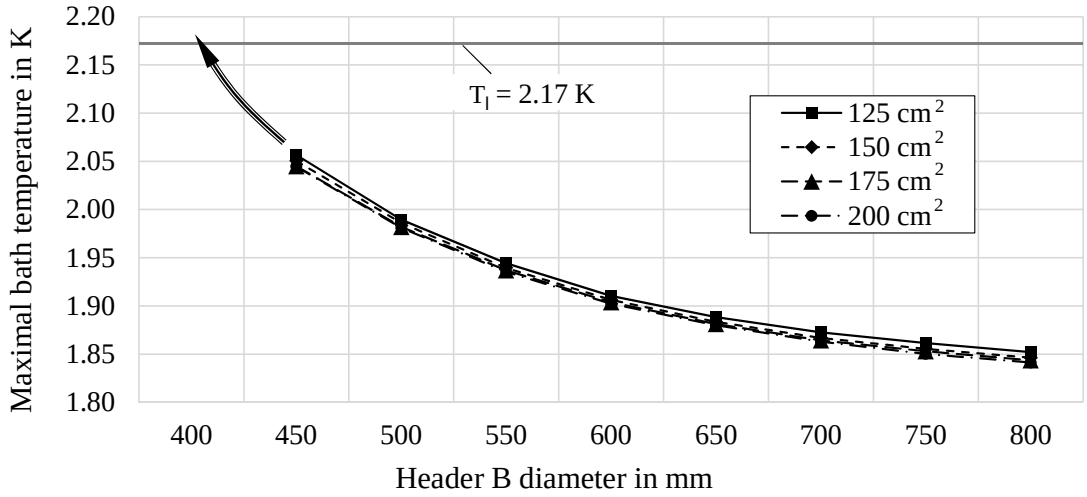

Figure 4.37: Maximal bath temperature (of the last half-cell) of an inclined sector (I-J) vs. the header B diameter operating at the nominal capacity for four different free areas in the iron yoke and a suction pressure of 15 mbar.

The baseline foresees a diameter of 500 mm for the header B. The graphs in the diagram in figure 4.37 yield the possible combinations of free area and helium bath temperature limit. If none of these combinations are acceptable for the magnet design, the header diameter must be increased or additional machinery to transport the helium vapour has to be installed. Figure 4.38 shows the pressure evolution in the headers B (bold lines) and C (thin lines) for the sectors I-J (solid lines) and C-D (dashed lines) for a header B diameter of 500 mm. In case of the sector C-D, the cryoplant has to deliver helium at a pressure of close to 3.05 bar to keep the header C pressure above the limit.

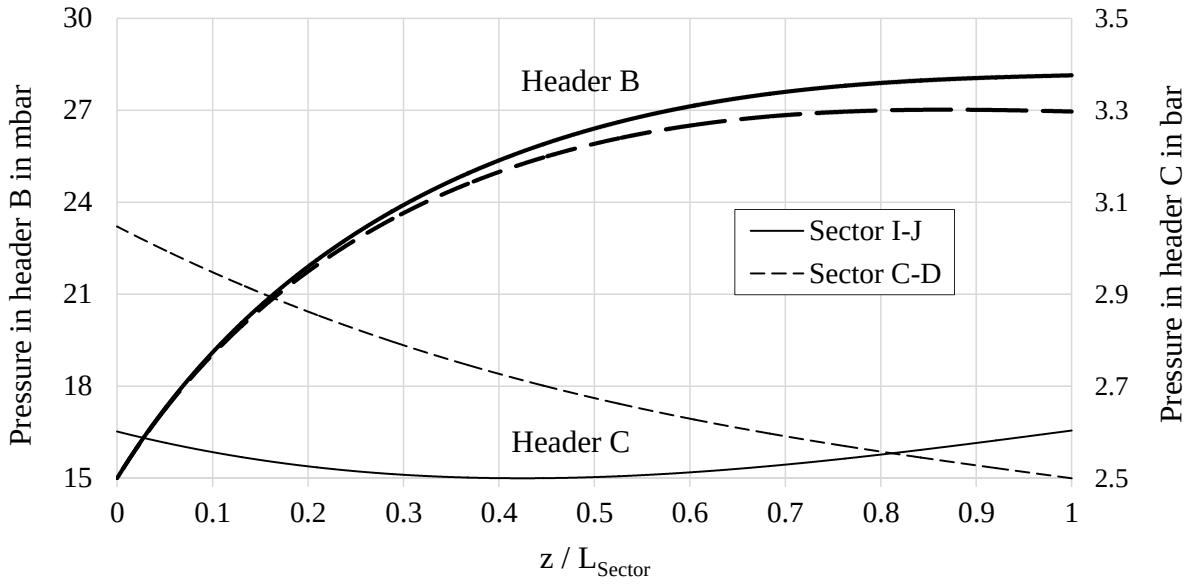

Figure 4.38: Pressure evolution in the headers B (bold lines) and C (thin lines) operating at the nominal capacity and fulfilling the minimal pressure limits vs. the axial coordinate z/L_{Sector} for the sectors I-J (solid line) and C-D (dashed line) and a header B diameter of 500 mm.

4.5.5.4 Exergetic analysis of an FCC cold mass cooling sector

The exergetic efficiency ζ of the sector cooling and distribution is indirectly proportional to the helium bath temperature limit $T_{Bath\,max}$ and the difference of the specific exergies Δe_{CB} of the entering and exiting helium flows.

$$\zeta \propto \left(\frac{T_a}{T_{Bath\,max}} - 1 \right) \frac{1}{\Delta e_{CB}} \tag{4.65}$$

The specific exergy contained in the returning helium vapour is mainly a function of the suction pressure in header B, whose final value is determined by three design parameters:

1. The maximal bath temperature determines the theoretical minimal saturation temperature in the bayonet heat exchangers.
2. The free area in the cold mass determines the difference between the maximal bath temperature and the feeder pipe outlet temperature in the last half-cell.
3. The header B diameter determines the pressure drop in the header B and therefore the saturation pressure of all previous half-cells.

Large header B diameters and free areas approximate the suction pressure and the pressures in the bayonet heat exchangers and therefore increase the exergetic efficiency. Figure 4.39 shows the correlation of the pressure profile in header B and the saturation temperature in the half-cells. The decreasing pressure in header B causes a sub-cooling of all half-cells, except the last one, below the necessary temperature limit.

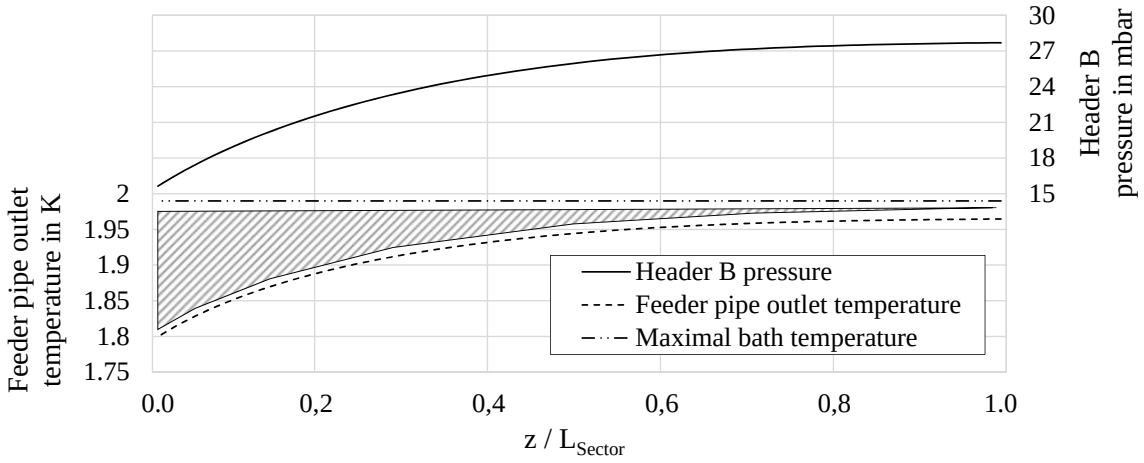

Figure 4.39: Feeder pipe outlet temperature and header B pressure profiles in an inclined sector vs. the axial coordinate z/L_{Sector} for a maximal bath temperature of 1.986 K, a free area of 156 cm^2 and a header B diameter of 500 mm, operating at the nominal capacity. The height of the hatched area represents the difference between the cold mass temperature and its technical and theoretical minimum.

The distribution and discharge system taken into account, one half-cell can be extended by the respective parts of the headers B and C. The diagram in figure 4.40 shows the distribution of the generated exergy losses to the half-cell (grey), the header B (white) and the header C (black) depending on the position of the cooled half-cell in the sector I-J. The dashed line represents the overall exergy consumption per half-cell.

The cryoplant is located at the sector beginning (0.0). At the sector end the major part of the exergy losses is generated in the half-cell. Closer to the cryoplant the losses increase, whereas header B becomes the dominant factor. The losses of header C are negligible. The diagram in figure 4.42 shows the distribution of the relative exergy losses depending on the position of the cooled half-cell in the sector I-J. The sum of the relative exergy losses and the exergetic efficiency yield 100 %, hence the exergetic efficiency can easily be calculated by subtracting the sum of the relative losses from 100 %. The first seven areas represent the losses in the half-cell corresponding and in the same order as in the previous section. Due to the increasing length of the dry section and the decreasing pressure level of the stratified flow, some exergy losses increase close to the cryoplant:

- pressure drop in the stratified flow (dark grey)
- heat transfer from the cold mass to the bayonet heat exchanger (medium grey)
- axial heat transfer in the cold mass (light grey)
- undercutting the bath temperature limit (white)

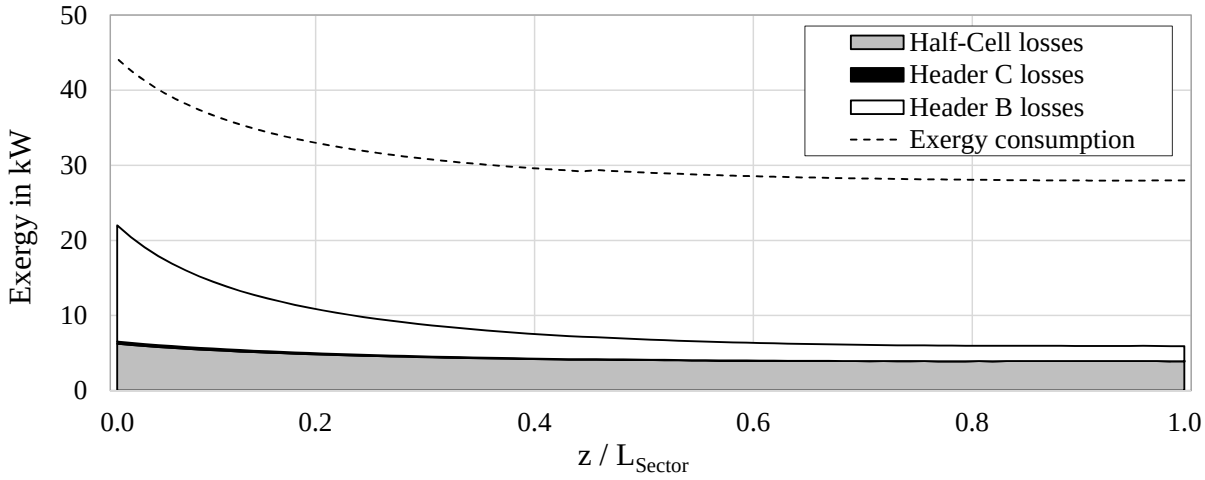

Figure 4.40: Exergy losses in the half-cell (grey), the header B (white) and the header C (black) and the overall exergy consumption per half-cell including the respective distribution and discharge system (corresponding to System I of the "Black Box" design in figure 3.10) vs. the axial coordinate z/L_{Sector} for a maximal bath temperature of 1.986 K, a free area of 156 cm^2 and a header B diameter of 500 mm, operating at the nominal capacity for the sector I-J.

The residual losses consist of the diminishingly small loss in the header C and the loss generated in the header B, which can be distributed to the pressure drop exergy losses (1), the heat leak ($\dot{q}_B$) exergy losses (2) and the mixing exergy losses (3).

1. **Pressure drop losses (small dots)**: Due to the small mass flow rate, the pressure drop losses are very small at the end of the sector. With increasing mass flow rate, they increase very fast to become the major contributor close to the cryoplant.

2. **Heat leak losses (bold dots)**: The heat leak exergy losses show an inverse evolution. At low mass flow rates the same heat intake has a larger impact on the anergy production. With increasing mass flow rate, the influence of the heat leak exergy losses decrease.

3. **Mixing losses (vertically striped):** Mixing losses occur, when the helium vapour exiting the half-cells is combined with the header B mass flow. The mixing losses are reach their maximum, when the two mixed mass flow rates are of the same magnitude. Figure 4.41 shows qualitatively the correlation between the exergy losses due to mixing and the mass flow rates of the two mixed flows with various differences of the specific exergies. With increasing difference of the specific exergy of the mass flows, the peak of the mixing losses is shifted to higher mass flow rates of the fluid with the higher specific exergy.

   Similarly to the heat leak losses, the mixing losses decrease closer to the cryoplant, but they are small in general.

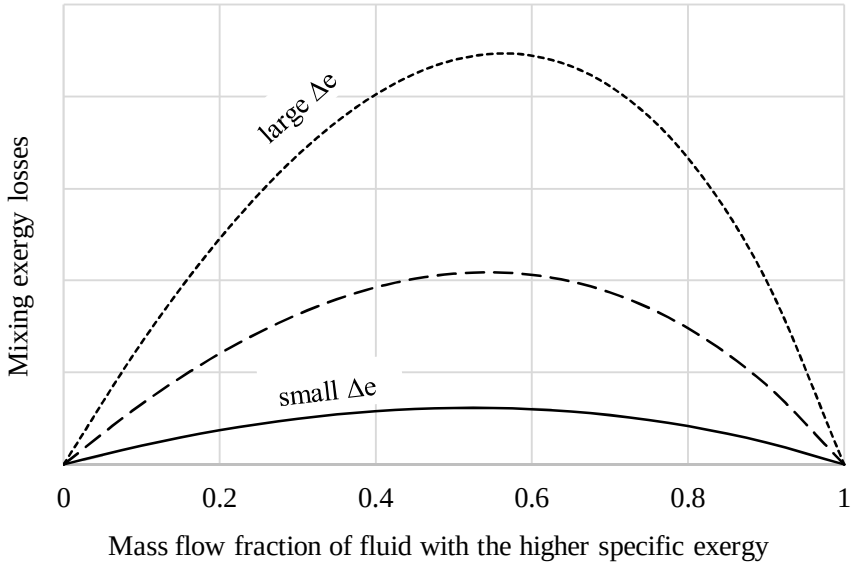

Figure 4.41: Exergy losses due to mixing vs. the mass flow rate fraction of two mixed fluids with different specific exergies (Δe). For larger differences in the specific exergy, the peak of the mixing losses is shifted to a larger fraction of the fluid with the higher specific exergy.

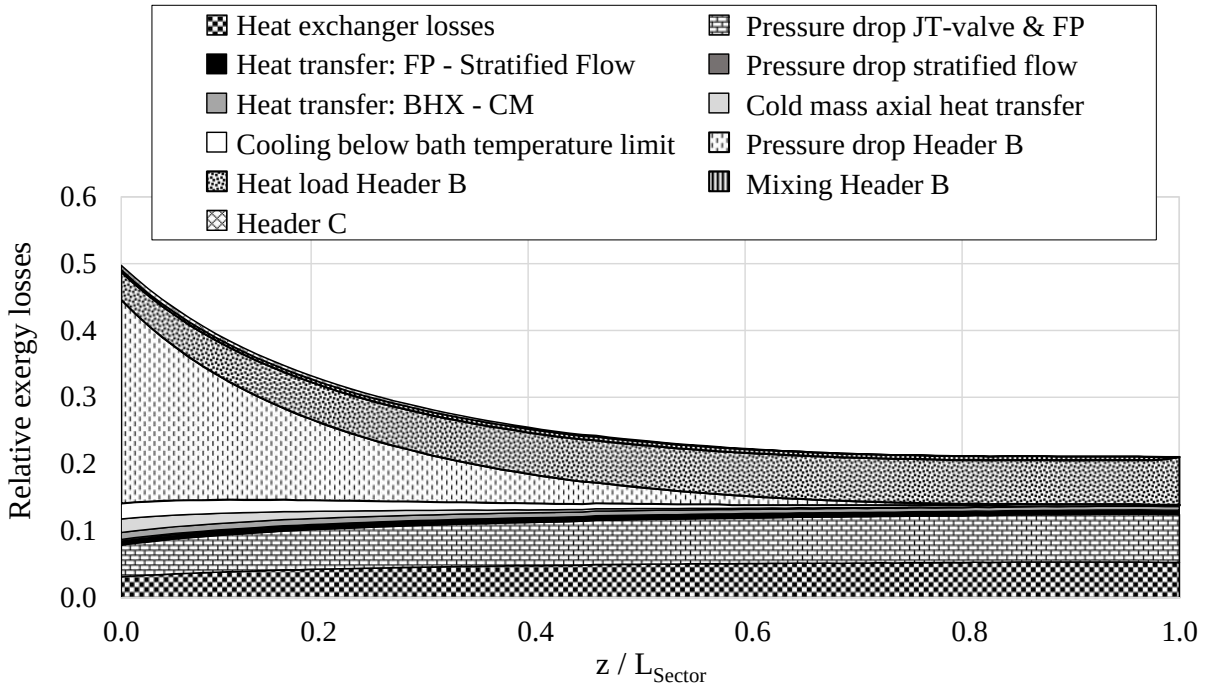

Figure 4.42: Relative exergy losses of the half-cells including the helium distribution and discharge system (corresponding to System I of the "Black Box" design in figure 3.10) vs. the axial coordinate z/L_{Sector} for a maximal bath temperature of 1.986 K, a free area of 156 cm^2 and a header B diameter of 500 mm, operating at the nominal capacity for the sector I-J.

The two big additional sources of anergy are the heat load on the header B and the pressure drop in the header B. The first could be decreased by improving the thermal insulation of the cryogenic distribution line inside and outside. This must be realized without an enlargement of distribution line's size. The pressure drop losses could be reduced by an increase of the header diameter or a decrease of the distributed length or sector length. The second option requires an increase of the number of cryoplants or their positioning in the middle of a sector. The number of cryoplants though should be kept low, mainly to benefit from economy of scale, and also to increase the overall availability of the FCC. By separating the cryoplants from each other, the redundancy is gone. Additionally the construction sides will be doubled, increasing the capital costs and complicating the supply and the organisation.

4.5.5.5 Additional machinery for the helium vapour discharge system

If the maximal helium bath temperature must be kept clearly below 2 K, the helium vapour discharge system must be re-designed. Due to the valuable space in the tunnel, an increase of the header B diameter to more than 500 mm is not an option. To avoid undercutting the minimal suction pressure, the installation of additional machinery could be a solution. Three options are briefly presented and schematically illustrated in figure 4.43:

1) The installation of one or more high speed compressors or blowers along the cryogenic distribution line.
2) Splitting of the helium vapour flow and compression of one partial flow in an additional cold compressor station installed
   (a) at the sector end or
   (b) in the middle of the sector.
3) Splitting of the helium vapour flow and compression of one partial flow in an additional warm compressor station installed at the sector end.

The separated helium flow of the options (2) and (3) has to be conveyed back in an additional header (G) at cryogenic temperature level and should not increase the size of the cryogenic distribution line. The assembly of additional machinery generates additional capital (machines, pipes, civil engineering) and operational costs and decreases the exergetic efficiency.

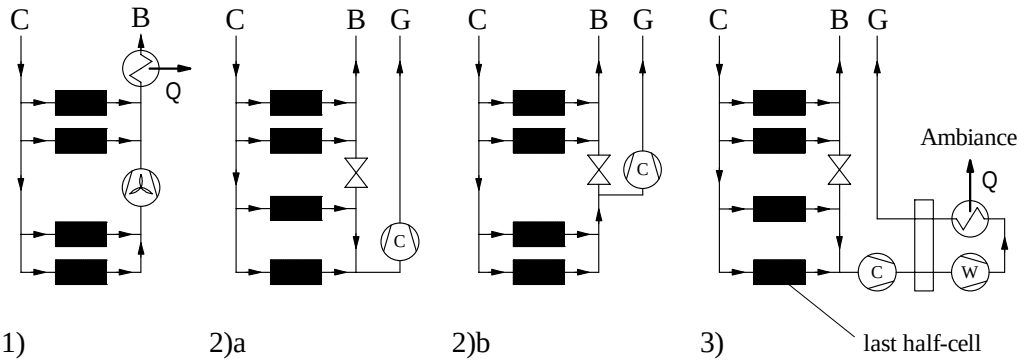

Figure 4.43: Three possibilities of additional machinery to return the helium vapour to the cryoplants to avoid an enlargement of the cryogenic distribution line.

4.6 Cold mass cooling with normalfluid helium

The cold mass refrigeration with superfluid helium at a temperature of 1.9 K is a well-established method, experienced during the long-standing operation of the LHC. The large know-how, the high thermal conductivity of superfluid helium II and the possible savings of superconducting material at lower temperatures are compelling arguments to hold on to this cooling concept. Nevertheless the operation of the FCC-hh cold mass cooling system with normalfluid helium at a temperature of 4 K also yields benefits. Among others

- the capital costs of the cryogenic facilities are reduced (smaller and less sophisticated machines and distribution facilities),
- the operational costs to run the cryogenic system are reduced (higher Carnot factor) and
- the possible downtime due to component failure decreases.

The completely different thermodynamic and fluid-mechanical properties of normalfluid helium, compared to He II at 1.9 K, requires a cryogenic system based on a different concept for cooling the superconducting coils. A simplified illustration of the basic concept is shown in figure 4.44. Single-phase helium at about 4.6 K and 3 bar is supplied by header C and conveyed to several parallel cooled CMUs. The entering cryogen is cooled down by the exiting two-phase helium in a heat exchanger and a separator with integrated heat exchanger and then passes the magnets close to the superconducting material to extract the heat load. At the cooling loop's end the helium flow is expanded in a Joule-Thomson valve, entering the two-phase region. The normalfluid two-phase flow is conveyed back to the cooling loop inlet, re-cooling the counterflowing single-phase helium in regular intervals by being vaporized. The residual liquid helium is collected in a separator and vaporized by the incoming single-phase helium flow. The vapour mass flow cools down the entering helium in a counterflow heat exchanger and then is discharged into header B.

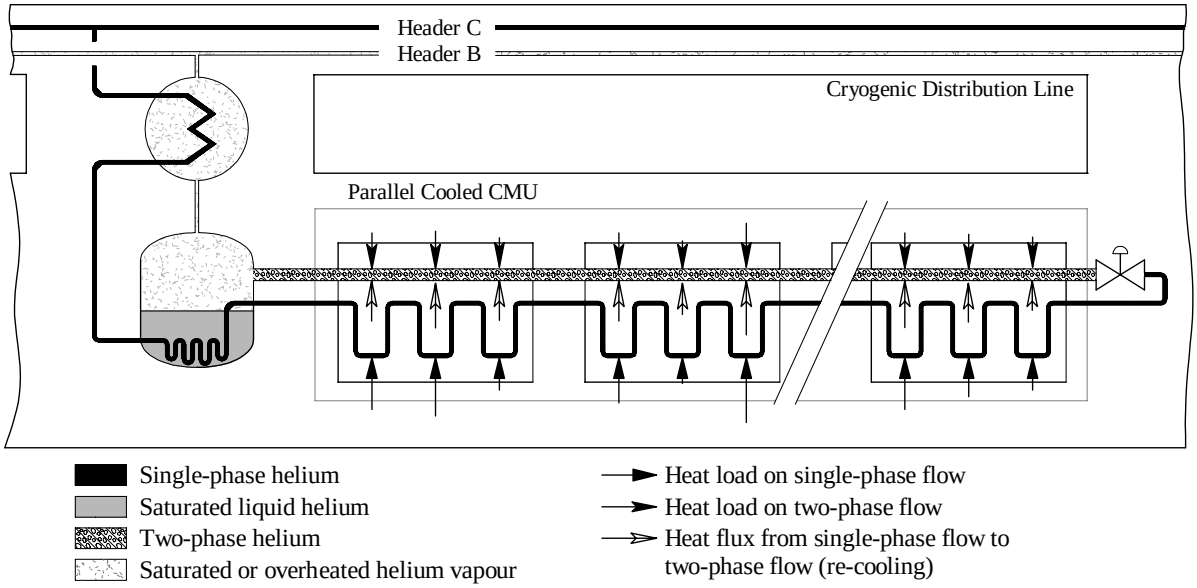

Figure 4.44: Simplified illustration of the basic cold mass cooling concept with helium I.

The results and considerations presented in this section are much more general than the conclusions of the cold mass cooling with superfluid helium. Since it was decided in favour of the cold mass cooling with He II, in the following section only basic correlations are shown. Magnet design,

heat loads and thermodynamic limits had to be assumed and do not represent any developments or findings during the FCC project at any time. The scope of the investigations presented was to create a basic idea of the possible working principles of a cold mass cooling system with normalfluid helium.

4.6.1 General constraints

Primary goal of the cold mass cooling is to keep the temperature of the superconducting coils below a limit $T_{Coil\,max}$ (≈ 4 K). The necessary driving temperature difference $\Delta T_{1\Phi-Coil}$ between the coils and the single-phase helium to transfer the heat depends on the magnet design. These two values define the temperature limit of the single-phase helium $T_{1\Phi\,max}$ passing the magnets.

$$T_{1\Phi\,max} = T_{Coil\,max} - \Delta T_{1\Phi-Coil} \tag{4.66}$$

The temperature of the single-phase helium increases when extracting the heat load, hence the inlet temperature $T_{1\Phi\,in}$ must be lower by at least the value of the sensible temperature rise $\Delta T_{1\Phi}$.

$$T_{1\Phi\,in} = T_{1\Phi\,max} - \Delta T_{1\Phi} \tag{4.67}$$

To reach the necessary (lower) temperature limit, the re-cooling two-phase helium temperature $T_{2\Phi\,max}$ must be even lower. The driving temperature difference for a sufficient heat transfer from the single-phase helium to the two-phase flow $\Delta T_{1\Phi-2\Phi}$ defines the upper pressure limit of the two-phase flow.

$$T_{2\Phi\,max} = T_{1\Phi\,in} - \Delta T_{1\Phi-2\Phi} \tag{4.68}$$

The single-phase helium is exposed to a high magnetic field due to its proximity to the superconducting coils. To avoid the generation of electric arcs, and furthermore, flow instabilities, no vapour phase must be created by operating below the critical pressure ($p_{crit} = 2.27$ bar).

$$p_{1\Phi\,min} > p_{crit} \tag{4.69}$$

The state of the two-phase helium flow moves along the saturation line. With decreasing temperature it approaches to the λ-point, which marks the transition of (normalfluid) helium I to (superfluid) helium II. Cooling below the λ-temperature would make the normalfluid helium cooling concept obsolete, since it would be possible to use superfluid helium cooling with all its advantages. Therefore the λ-point ($T_\lambda \approx 2.17$ K, $p_\lambda \approx 50$ mbar) was determined as the lower limit for the two-phase flow.

$$T_{2\Phi\,min} = T_\lambda \tag{4.70}$$

The phase diagram illustrated in figure 4.45 shows graphically the limits and constraints for the helium flows.

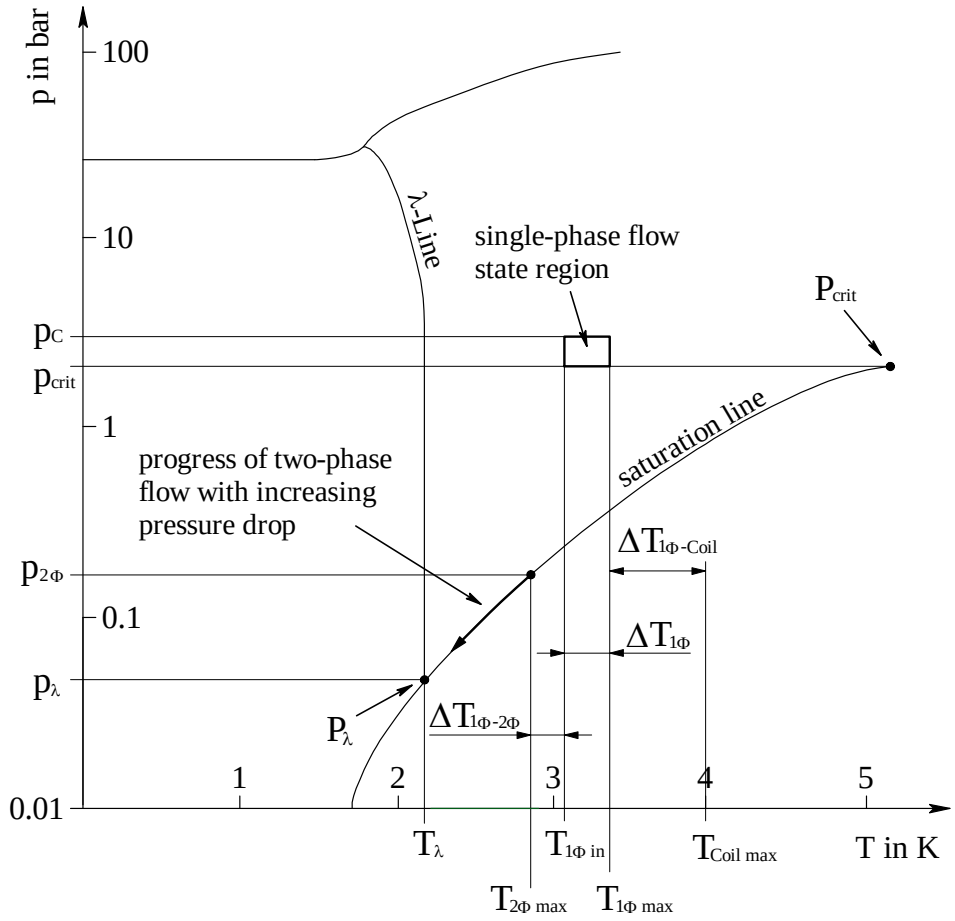

Figure 4.45: Phase diagram of helium with the thermodynamical constraints for the cold mass cooling with normalfluid helium.

4.6.2 Heat transfer in the coils and the collar

The necessary driving temperature difference to extract the heat load from the coils was calculated with a numerical simulation based on the finite volume method with the open source program "OpenFOAM". The same simplified, but enlarged coil geometry was used as presented in the sections 4.4.1 and 4.5.3.1, whereas the thickness of the insulating layers was kept equal and the size of the cables and the titanium pole piece was increased proportionally. Due to the low thermal conductivity of normalfluid helium, the heat also has to be conducted in the stainless steel collar to be transferred to the helium flow channels between the collar and the iron yoke (see explanations and figure 4.48 in section 4.6.4).

One quarter of the stainless steel collar with one half of one coil was modelled and the temperature field was calculated utilizing the symmetry of the geometry. The temperature of the helium was varied until the maximal coil temperature did reach a value of close to 4 K (±0.01 K). The calculated temperature difference between the warmest point of the coil and the helium flow was in the range of 0.55 K for the cold mass cross section, which receives the highest heat load due to beam gas scattering.

4.6.3 Re-cooling

The single-phase flow is re-cooled by the two-phase flow continuously or, if not feasible, regularly. With increasing distance L_{RC} between two points of re-cooling, the single-phase helium inlet temperature has to be decreased or the mass flow rate passing the parallel cooled CMU $\dot{m}_{CMU}$ has to be increased.

$$\dot{m}_{CMU}\,\Delta T_{1\Phi}\,c_p = \dot{q}\,L_{RC} \tag{4.71}$$

The supplied helium mass flow rate though is firmly connected to the cooling loop length by the total vaporization condition. By combining (4.71) and (4.1), a mass-free form of the total vaporization condition can be obtained.

$$\frac{L_{CMU}}{L_{RC}} = \frac{h'' - h_{JT}}{\Delta T_{1\Phi}\,c_p} \tag{4.72}$$

The correlation in (4.72) shows that short re-cooling distances are necessary to keep the sensible temperature rise of the single-phase helium low. But the choice of the re-cooling length has to be adapted to the lengths of the magnets and/or half-cells.

1. **Continuous re-cooling ($\mathbf{L_{RC} \to 0}$):** If the single-phase helium temperature can be thermally connected to the two-phase flow temperature, the re-cooling length is zero. The cold mass cooling systems of HERA and Tevatron (see figures 2.7 and 2.2) are operated with continuous re-cooling. This option though only is advantegeous, if the temperature difference between the two helium flows can be kept small. The higher heat loads of the FCC inherently require increased driving temperature differences.

2. **Re-cooling between adjacent magnets ($\mathbf{L_{RC} = L_{Mag}}$):** The re-cooling after each magnet keeps the re-cooling length of acceptable magnitude. Albeit the installation of hardware for this purpose in the interconnection between two magnets is not possible, due to the scarce available space. The re-cooling must be arranged magnet-internally.

3. **Re-cooling between adjacent half-cells ($\mathbf{L_{RC} = L_{HC}}$):** The re-cooling after each half-cell allows to install the necessary hardware in the jumper connections. The long distance between two re-cooling points though, requires low single-phase helium inlet temperatures and large mass flow rates.

Figure 4.46 illustrates schematically the three possible choices of re-cooling lengths. The continuous re-cooling (top) and the re-cooling between two magnets (middle) require a magnet-internal heat exchange and subsequently a major change of the magnet design for its adaption to cryogenic applications. The lowest scheme shows the re-cooling between two half-cells with the possibility of a magnet-external heat exchange.

If the necessary mass flow rate to keep the single-phase helium temperature below $T_{1\Phi\,max}$ is higher than the vaporized helium in one half-cell, the total vaporization condition sets a lower limit for the parallel cooled CMU length. This requirement can be expressed mathematically by re-arranging (4.72).

$$L_{RC} < \frac{\Delta T_{1\Phi}\,c_p\,L_{HC}}{h'' - h_{JT}} \tag{4.73}$$

If (4.73) is satisfied, only a maximal parallel cooled CMU length is determined. In the opposite case, the necessary mass flow rate of single-phase helium cannot be entirely vaporized within the length of one half-cell. A minimal parallel cooled CMU length exists.

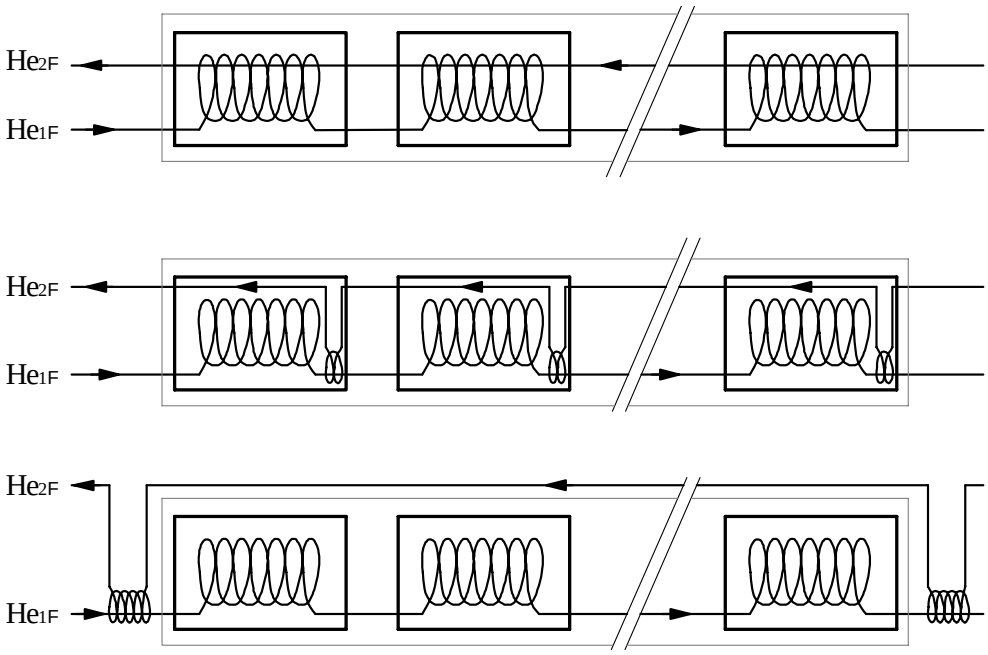

Figure 4.46: Different possibilities for re-cooling lengths: continuous re-cooling (top), re-cooling length corresponds to magnet length (middle) and re-cooling length corresponds to half-cell length (bottom).

In cooling schemes with magnet-internal re-cooling, a fraction of the heat load is directly absorbed by the two-phase helium without taking the detour via the single-phase helium and therefore does not contribute to the temperature rise of the single-phase flow. This effect is taken into account by the introduction of a heat distribution coefficient φ_q, which shall be defined as the ratio of the heat taken by the single-phase helium, when passing the cooling channels between the iron yoke and the stainless steel collar, and the total heat load.

$$\varphi_q = \frac{\dot{q}_{1\Phi}}{\dot{q}_{tot}} \tag{4.74}$$

$$L_{RC} < \frac{\Delta T_{1\Phi}\, c_p\, L_{HC}}{\varphi_q\, (h'' - h_{JT})} \tag{4.75}$$

4.6.4 Cold mass cooling with continuous re-cooling

The possibility of continuous re-cooling entails simple hydraulic schemes with little hardware and auxiliary equipment, decreasing the error-proneness and the downtime due to component failure. The single-phase helium temperature is connected to the two-phase helium temperature, the two only differ by the necessary driving temperature difference to transfer the heat. Figure 4.47 schematically shows the flow scheme of one parallel cooled CMU with continuous re-cooling.

The cold mass cooling with normalfluid helium is based on a forced flow passing the magnets. The single-phase helium must be conveyed as close as possible to the superconducting coils. The stainless steel collar is positioned in the center of the iron yoke by a force-locking system of wedges. Like that, slits are formed, which can be used as channels (as indicated in figure 4.48 on the left).

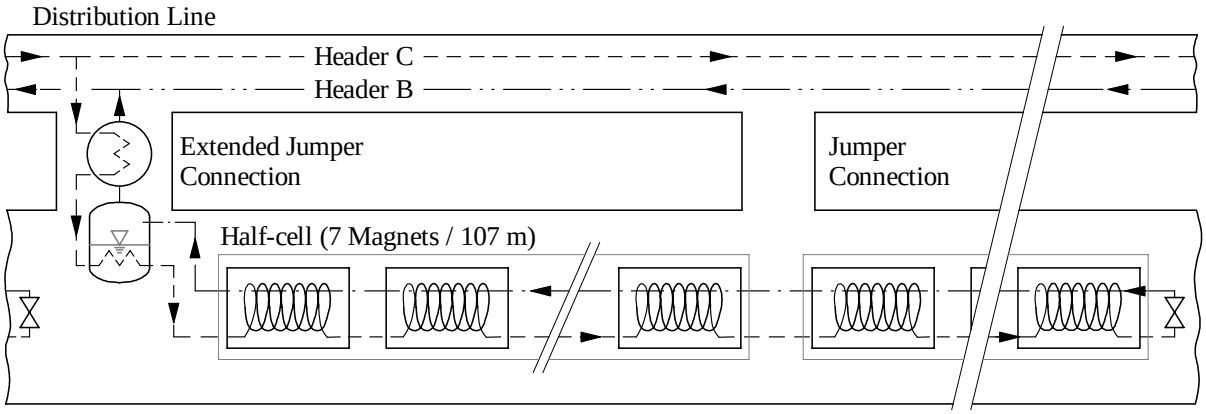

Figure 4.47: Parallel cooled CMU with continuous re-cooling.

- Eight slits at the top and at the bottom of the collar with a breadth of 45 mm and a height of 3 mm.
- Four slits at the left side and the right side of the collar with a breadth of 68 mm and a height of 3 mm.

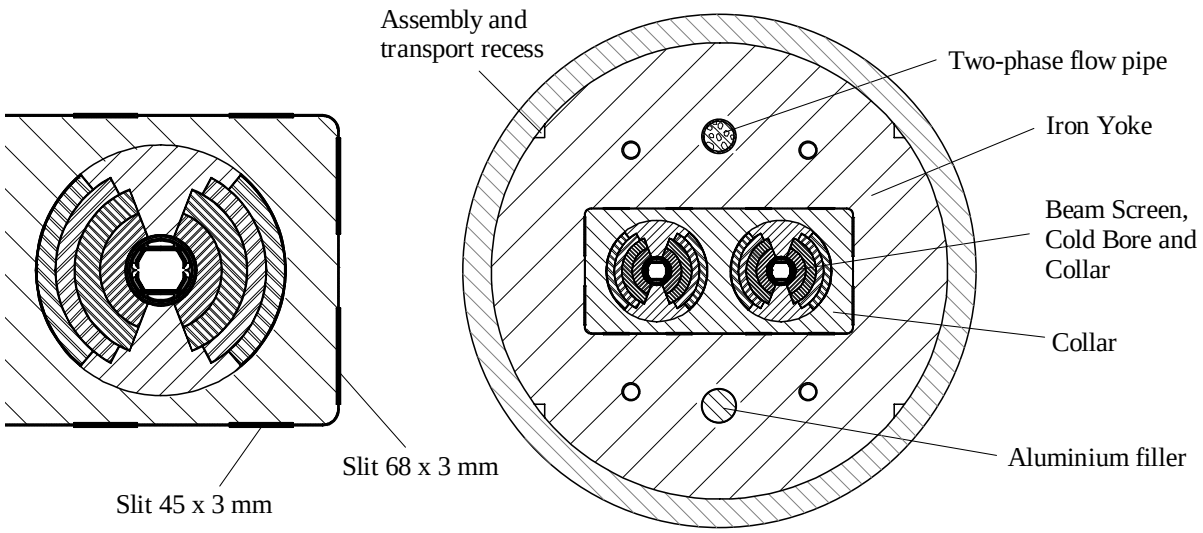

Figure 4.48: Twelve slits between iron yoke and stainless steel collar used as channels for the single-phase fluid (left-hand side) and schematic of the cold mass design for a continuous re-cooling scheme (right-hand side).

On the right side of figure 4.48, the cold mass cross section is schematically illustrated. The lower bore must be closed with a non-magnetic filler (e.g. aluminium) to avoid a bypass flow. Also the assembly and transport recesses have to be blocked at the magnet's ends after assembly. Due to the lack of the superfluid helium's thermal properties, the two-phase flow pipe must be wetted over its whole length. To achieve a sufficient heat transfer, the velocities of the vapour phase and liquid phase have to be assimilated by assuring the two-phase flow to proceed in a probate flow regime, which can be arranged by the variation of the diameter of the leading duct.

The pressure losses in the heat exchangers and separators were neglected, the heat load was assumed to be distributed uniformly along the entire parallel cooled CMU. The Darcy friction factor to calculate the pressure drop in the single-phase helium and vapour flows was obtained with the explicit formula of Swamee-Jain [83]. Several models to calculate the pressure drop in the boiling two-phase flow have been applied.

- The classification according to an adapted flow pattern map for non-adiabatic two-phase flows [79] [77],
- the heterogeneous flow model according to Lockhart and Martinelli [73] and
- the homogeneous flow model.

Experimentally attained data showed a good accordance with the results obtained with the homogeneous flow model, which could be traced to the similarity of the liquid and the gaseoes phase of helium [41] [78]. Even for the stratified flow regime, the homogeneous model yielded similar values for the pressure drop with no significant difference in the final results. Therefore the presented results are calculated with the homogeneous flow model. The viscosity of the gas-liquid mixture was calculated with the formula of McAdams [82]. The helium properties were taken from the library 'HePak' (Cryodata Inc.). Presumed values and numbers and boundary conditions are listed in Table 4.4.

Table 4.4: Normalfluid helium cold mass cooling: Basic data

Input Value	**Symbol**	**Value**	**Unit**
Ambient temperature	T_a	300	K
Ambient pressure	p_a	1.013	bar
Temperature header C	T_C	4.6	K
Terminal temperature difference Separators	$TT\Delta_{Sep}$	0	K
Terminal temperature difference heat exchangers	$TT\Delta_{HX}$	0.5	K
Maximal allowed coil temperature	$T_{Coil\,max}$	4.0	K
Temperature difference for heat extraction from coils	$\Delta T_{Coil-1\Phi}$	0.55	K
Two-phase helium pipe diameter	$d_{2\Phi}$	50	mm
Absolute roughness of the slit channels	ϵ_{Slits}	0.1	mm
Absolute roughness of any pipe	ϵ	15	μm
Slope of the parallel cooled CMUs	α	0	%
Average heat load (nominal capacity)	$\dot{q}$	1.38	W/m

The diagram in figure 4.49 shows the exergetic efficiency vs. the parallel cooled CMU length (expressed as cooled half-cells in series). Two different pressures of the supplied helium from header C were assumed as well as different values for the driving temperature difference to transfer the heat from the single-phase flow to the two-phase flow.

The heat distribution coefficient φ_q is implicitly contained in the temperature difference $\Delta T_{1\Phi-2\Phi}$ - if more heat is directly extracted by the two-phase flow, the driving temperature difference between the two helium flows decreases. With increasing temperature difference (or increasing heat distribution coefficient), the pressure drop in the Joule-Thomson valve must be increased to reach a sufficiently low temperature level in the returning two-phase flow. The last magnet of the parallel cooled CMU dictates the maximal two-phase flow pressure, all the previous magnets are cooled down to an unnecessarily low temperature level (due to the pressure drop).

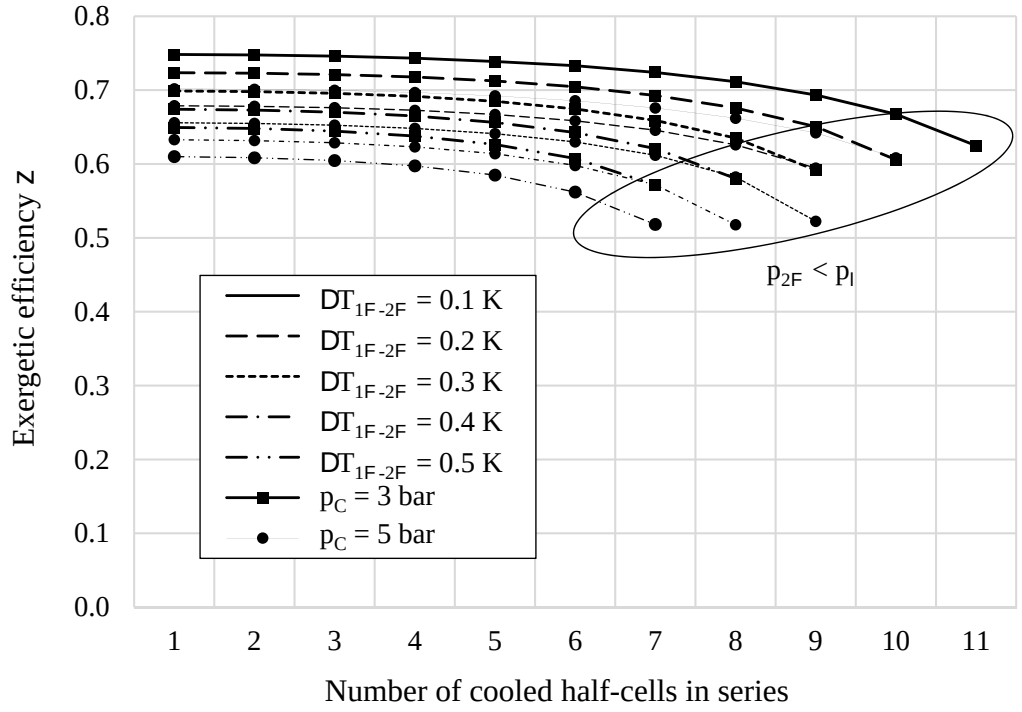

Figure 4.49: Exergetic efficiency vs. number of cooled half-cells in series for the continuous re-cooling scheme, a supply pressure p_C of 3 bar (bold lines with squares) and 5 bar (thin lines with circles) and different driving temperature differences $\Delta T_{1\Phi-2\Phi}$ for the heat transfer from the single-phase flow to the two-phase flow (line shape).

The pressure drop in the two-phase helium flow limits the maximal length of a parallel cooled CMU, due to undercutting the λ-pressure. Since the limiting value is the pressure in the two-phase flow, an increased supply pressure does not yield any benefits. In contrary, the exergetic efficiency decreases, because in the Joule-Thomson valve a higher pressure drop has to be generated to reach the required temperature level.

4.6.4.1 Vapour return line

By the installation of an additional vapour return line and separators, the parallel cooled CMU length can be increased without a large drop of the exergetic efficiency. Figure 4.50 illustrates the extended flow scheme. In each jumper connection vapour phase and liquid phase of the two-phase flow are separated. The high-volumetric helium vapour is conveyed back in an additional return line.

The diagram in figure 4.51 shows the exergetic efficiency vs. the parallel cooled CMU length (expressed as cooled half-cells in series). Two different pressures of the supplied helium from header C were assumed as well as different values for the driving temperature difference to transfer the heat from the single-phase flow to the two-phase flow.

Due to the vapour return line, the pressure drop in the two-phase flow can be kept low. The maximal cooled length is limited by the pressure drop in the single-phase flow. With an increased supply pressure, the parallel cooled CMU length can be increased too.

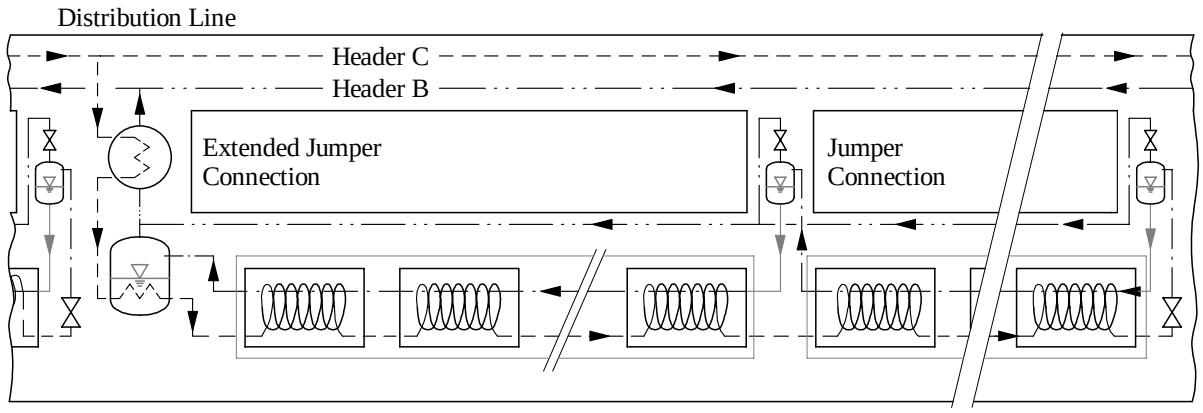

Figure 4.50: Parallel cooled CMU with continuous re-cooling and vapour return line.

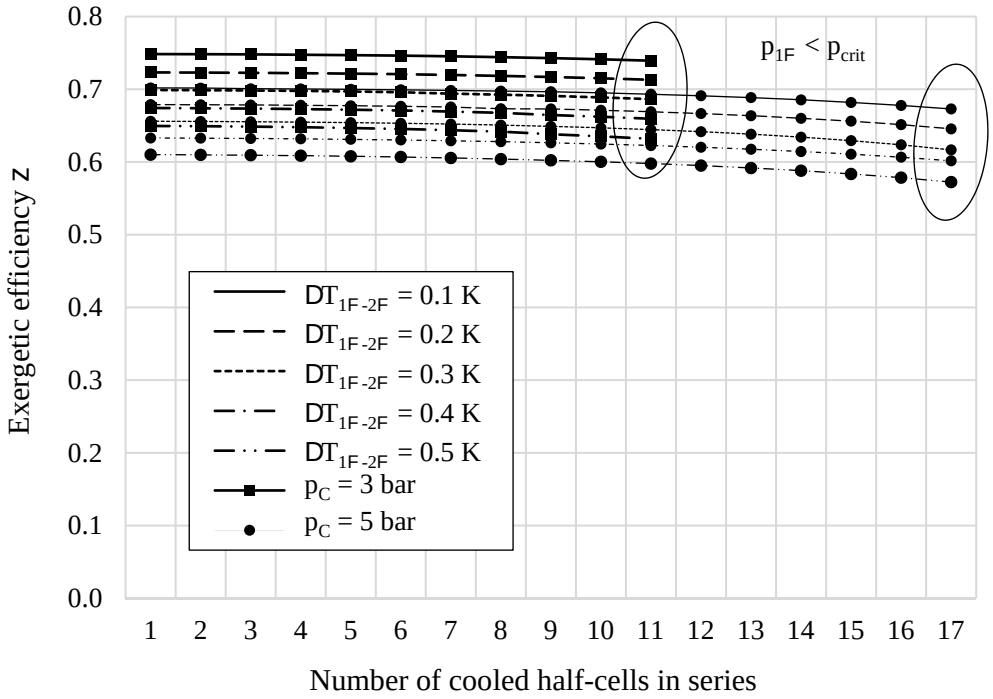

Figure 4.51: Exergetic efficiency vs. number of cooled half-cells in series for the continuous re-cooling scheme with vapour return line, a supply pressure p_C of 3 bar (bold lines with squares) and 5 bar (thin lines with circles) and different driving temperature differences $\Delta T_{1\Phi-2\Phi}$ for the heat transfer from the single-phase flow to the two-phase flow (line shape).

The diameter of the vapour return pipe must be chosen sufficiently large to generate a smaller pressure drop in the vapour return line, than in the two-phase flow to enable the helium vapour discharge. Especially close to the extended jumper connections, the pressure losses in the vapour return line are relatively high. The diagram in figure 4.52 shows the minimal necessary vapour return line diameter to be able to discharge the separated vapour flow.

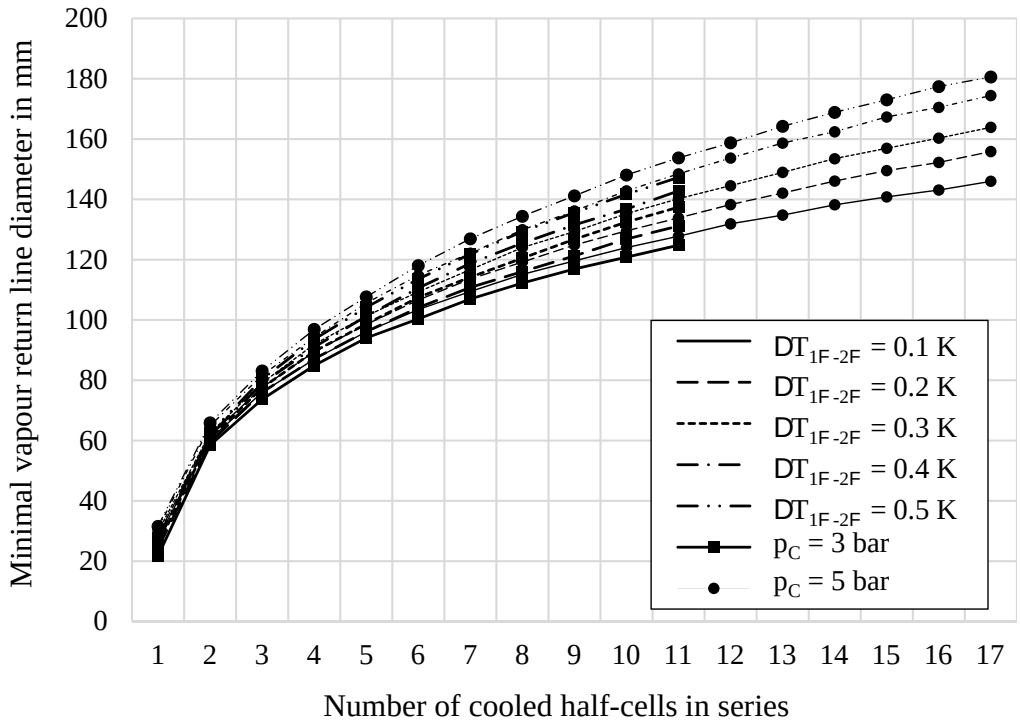

Figure 4.52: Minimal vapour return line diameter vs. number of cooled half-cells in series for the continuous re-cooling scheme with vapour return line, a supply pressure p_C of 3 bar (bold lines with squares) and 5 bar (thin lines with circles) and different driving temperature differences $\Delta T_{1\Phi-2\Phi}$ for the heat transfer from the single-phase flow to the two-phase flow (line shape).

4.6.4.2 Controlling and transient modes

The segmentation of an arc into a small number of cooling loops saves hardware and controlling effort. The cold mass cooling system of long parallel cooled CMUs on the other hand react very inertly to sudden changes of the operational mode - especially to the expected heat loads on the FCC. To run these schemes successfully, the heat load must be anticipated by increasing the mass flow rate in advance. Any abundant helium during transient operation, which exceeds the capacity of the separator in the extended jumper connection, has to be vaporized by electrical heaters creating major losses. Moreover, non-expected load variations can hardly be handled and increase the probability of quenches.

4.6.5 Discontinuous re-cooling schemes without circulator

If the driving temperature difference $\Delta T_{1\Phi-2\Phi}$ to transfer the heat from the single-phase helium to the two-phase flow is (too) high, the re-cooling has to be arranged at regular points. If the re-cooling length is chosen to correspond to a magnet's length, (4.73) can be satisfied and the the parallel cooled CMU length is freely selectable. Due to the little space between two adjacent magnets, the heat exchange has to be designed magnet-internally. Two basic options are presented now.

Parallel single-phase helium flows The single-phase helium passes the magnets in parallel cooling channels. Due to the parallel arrangement, the pressure drop can be kept small, but the hydraulic impedances of these channels have to be designed to convey the requested fractions of the single-phase helium in the respective channel. Figure 4.53 illustrates schematically a magnet design with parallel cooling channels.

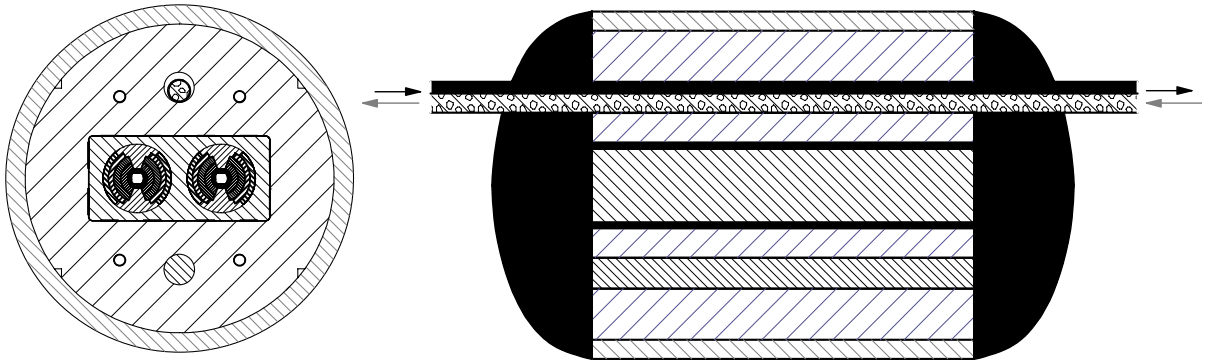

Figure 4.53: Schematic of a possible magnet design with parallel single-phase helium cooling channels.

The two requirements for an efficient helium flow distribution passing the parallel channels are contradictory:

1. Extract the heat load from the coils with a small temperature rise of the single-phase helium: The major flow has to be conveyed in the twelve channels between the collar and the iron yoke. Therefore only a small fraction is re-cooled when passing the channel with the integrated pipe heat exchanger and the re-cooling effect is small.

2. Achieve a low single-phase helium temperature at the magnets' inlet: The major flow has to pass the pipe heat exchanger (i.e. the bore containing the two-phase helium pipe). The temperature of the small helium mass flow rates in the slit channels though rises strongly and causes a low necessary two-phase flow pressure.

Single-phase helium flows in series The single-phase helium passes the channels in series. The sensible temperature rise can be minimized and therefore the two-phase flow pressure maximized. The pressure drop generated in the single-phase flow though increases. However, the order of the single-phase helium passing the channels has an impact on the refrigeration performance. Basically there are two options: The single-phase helium flow is cooled down in the pipe heat exchanger first an then passes the slit channels ("precooling") or the single-phase helium flow is conveyed through the slit channels before it passes the pipe heat exchanger ("aftercooling"). Also the location of the two-phase flow pipe, whether in the top bore or in the bottom bore, can be varied, yielding four design options.

1. Two-phase flow pipe located in the bottom bore and precooling of the single-phase helium (PB)
2. Two-phase flow pipe located in the bottom bore and aftercooling of the single-phase helium (AB)
3. Two-phase flow pipe located in the top bore and precooling of the single-phase helium (PT)

4. Two-phase flow pipe located in the top bore and aftercooling of the single-phase helium (AT)

- With the two-phase flow pipe integrated in the bottom bore, a larger fraction of the heat leaks from the ambiance can be directly absorbed by the two-phase flow by intercepting the heat leaks entering the support post (decreased φ_q).
- By cooling the incoming single-phase helium down before it enters the cooling channels between the iron yoke and the collar, the available temperature range can be increased and whether the necessary mass flow fraction reduced or the two-phase helium pressure increased.

Considering these two aspects the PB-scheme seems to be the preferable option. Figure 4.54 schematically illustrates the flow scheme of the PB-design.

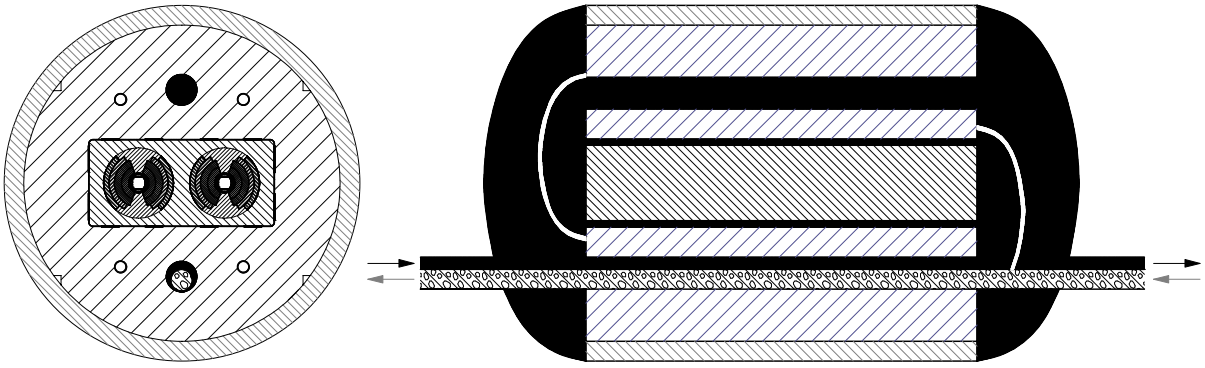

Figure 4.54: Schematic of a possible magnet design with the single-phase helium passing the cooling channels in series. The entering single-phase helium is cooled down first, then extracts the heat load on the coil and then passes the top channel to decrease the heat distribution coefficient φ_q (PB-design).

Table 4.5 contains the input data assumed to perform the numerical simulation. The diagram in figure 4.55 shows the exergetic efficiency vs. the parallel cooled CMU length (expressed as cooled half-cells in series). Two supply pressures and different values for the heat distribution coefficient were assumed. For the cases with a heat distribution factor $\varphi_q < 1$, the heat not extracted by the single-phase helium flow in the slits was distributed equally to the two helium flows in the top bore and in the bottom bore. The results for a precooling and an aftercooling design are presented.

Table 4.5: Normalfluid helium cold mass cooling: Re-cooling length corresponding to a magnet length

Input Value	**Symbol**	**Value**	**Unit**
Terminal temperature difference of the pipe heat exchanger	$TT\Delta_{PipeHX}$	0	K
Two-phase helium pipe outer diameter	$D_{2\Phi}$	60	mm
Diameter of the two bores in the iron yoke	d_{Bore}	93	K
Absolute roughness of the helium channels	ϵ_{Ch}	0.1	mm

Since the total vaporization condition has to be satisfied, short parallel cooled CMUs cause small mass flow rates. Small helium mass flow rates require a low two-phase helium temperature (i.e. a low saturation pressure) and therefore yield low exergetic efficiencies.

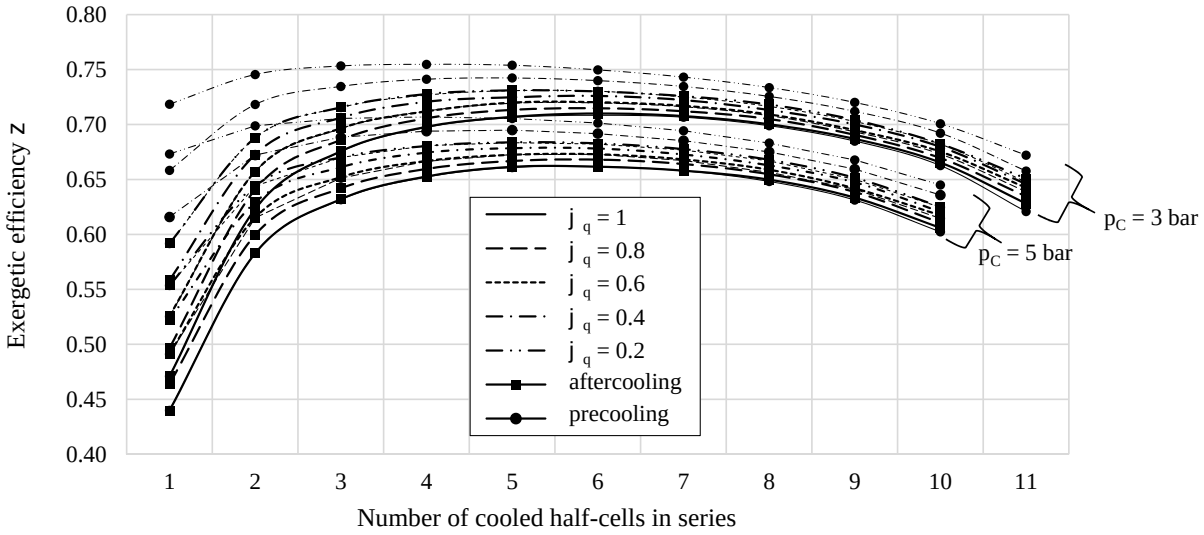

Figure 4.55: Exergetic efficiency vs. number of cooled half-cells in series for a cooling scheme with a re-cooling length corresponding to the magnet length without vapour return line. Results are presented for two supply pressures p_C of 3 bar and 5 bar and different heat distribution coefficients φ_q (line shape) for a precooling (thin lines with circles) and an aftercooling (bold lines with squares) design.

With increasing number of half-cells cooled in series, the mass flow rate increases and the pressure level of the two-phase helium can be kept high, resulting in higher exergetic efficiencies. If the parallel cooled CMU length increases even more, the pressure drop in the two-phase flow reduces the exergetic efficiency. Therefore a maximum can be found at intermediate parallel cooled CMU lengths.

Interestingly, by supplying helium at a pressure of 5 bar, the maximal parallel cooled CMU length decreases compared to a supply pressure of 3 bar. First of all the specific heat capacity of the single-phase helium decreases with increasing pressure in the relevant thermodynamic regime, which causes larger necessary mass flows. Secondly, the isenthalpic expansion in the Joule-Thomson valve generates a larger vapour mass fraction. These two effects cause a higher volumetric flow in the two-phase pipe and the lower pressure limit (p_λ) is reached at shorter cooling loop lengths.

Similarly to the results of the continuous re-cooling scheme without vapour return line, an increased supply pressure decreases the efficiency. The parallel cooled CMU length cannot be increased, since the limiting factor is the pressure drop in the two-phase helium flow. Cases with low heat distribution coefficients and the precooling-design perform at higher efficiencies.

The installation of a vapour return line can increase the exergetic efficiency for longer parallel cooled CMUs. The results are illustrated in the diagram in figure 4.56. The controlling and the handling of transient modes of these schemes face the same difficulties and disadvantages as discussed for the continuous re-cooling schemes.

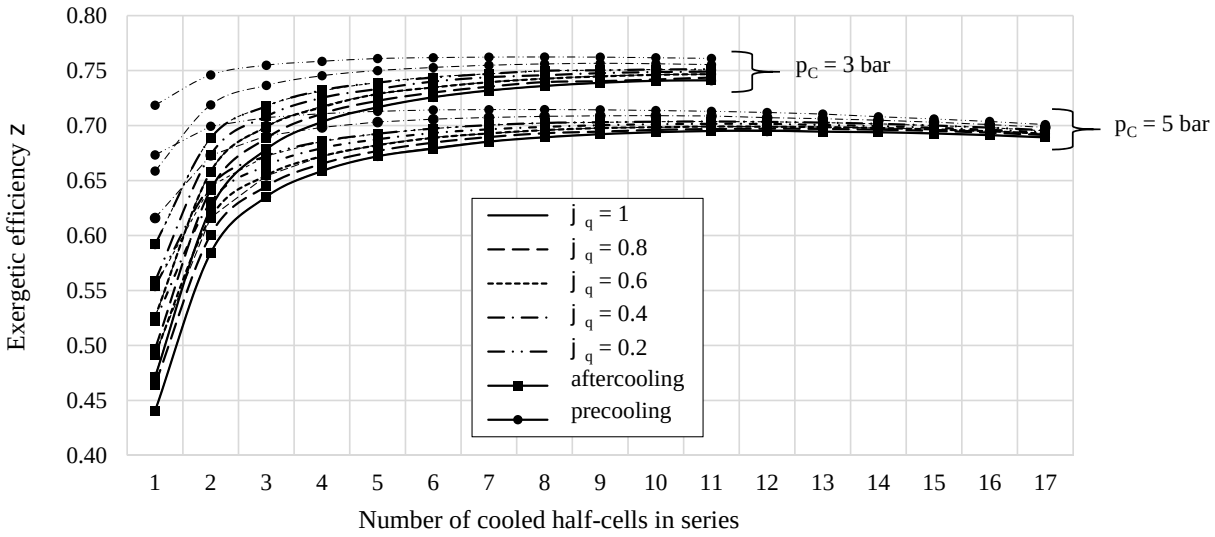

Figure 4.56: Exergetic efficiency vs. number of cooled half-cells in series for a cooling scheme with an re-cooling length corresponding to the magnet length with vapour return line. Results are presented for two supply pressures p_C of 3 bar and 5 bar and different heat distribution coefficients φ_q (line shape) for a precooling (thin lines with circles) and an aftercooling (bold lines with squares) design.

4.6.6 Discontinuous re-cooling schemes with circulator

By increasing the re-cooling length to a half-cell length, (4.73) cannot be satisfied anymore and a lower limit for the parallel cooled CMU length appears. The diagram in figure 4.57 illustrates the constraint regarding the minimal parallel cooled CMU length (expressed in number of half-cells per parallel cooled CMU) and the minimal supply pressure set by the total vaporization condition depending on the temperature rise of the single-phase helium. The primary ordinate is presented in a logarithmic scale for easier presentation.

The minimal parallel cooled CMU length almost only depends on the choice of the supply pressure p_C (for a supply pressure of 3 bar, at least 12 half-cells have to be cooled in series). The occurring temperature rise in one half-cell depends on the heat distribution. The results were calculated for the pressure drop according to the magnet design of the continuous re-cooling scheme.

However, to keep the temperature rise of the single-phase helium low (and therefore the two-phase helium pressure high), the parallel cooled CMU length and the supply pressure of the helium delivered by header C must be increased. Apart from the low exergetic efficiencies, the controlling of a cooling loop of this length entails many difficulties, if at all possible.

By installing circulators in the parallel cooled CMUs, the total vaporization condition can be circumvented. Also transient operation could be handled easier and more efficiently. The drawback is additional hardware, increased capital costs and the accompanying probability increase of downtime due to component failure. Table 4.6 contains the input data assumed to perform the numerical simulation for cooling schemes with additional circulator(s).

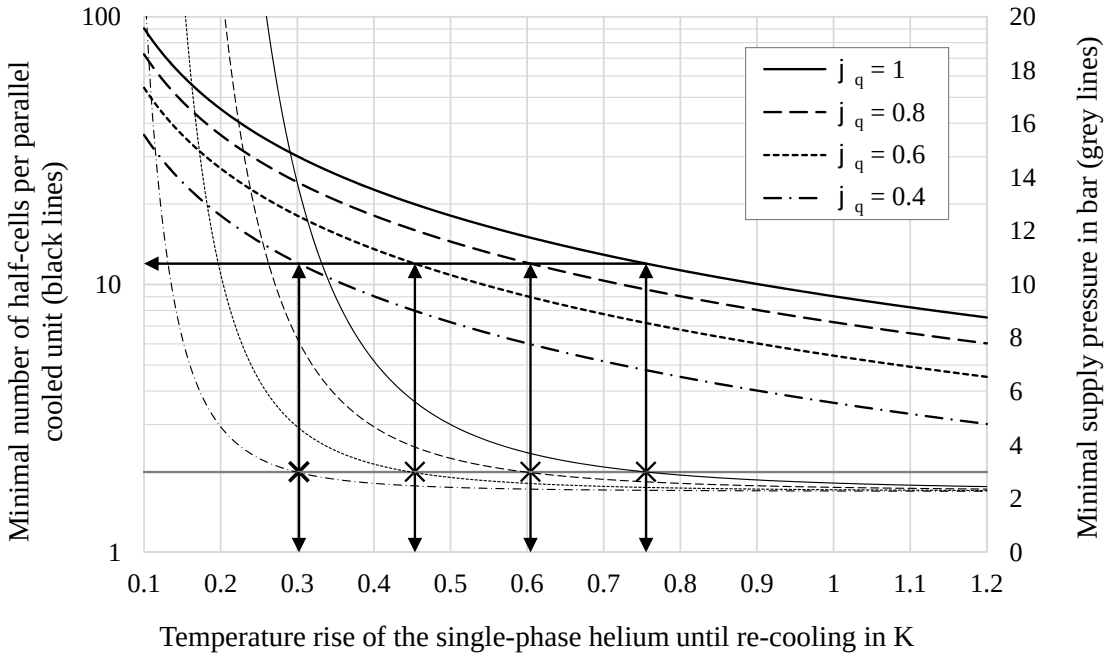

Figure 4.57: Minimal number of half-cells per parallel cooled CMU (primary ordinate, bold lines) and minimal supply pressure p_C (secondary ordinate, thin lines) vs. the sensible temperature rise of the single-phase helium until re-cooling ($L_{RC} = L_{HC}$) for different heat distribution coefficients (line shape). The bold grey line marks a supply pressure of 3 bar, the arrows illustrate the minimal parallel cooled CMU length and the corresponding temperature rise for different heat distribution coefficients.

Table 4.6: Normalfluid helium cold mass cooling: Re-cooling length corresponding to a half-cell length with additional circulator(s)

Input Value	**Symbol**	**Value**	**Unit**
High pressure helium return pipe diameter	$d_{1\Phi R}$	150	mm
Entropic efficiency of the circulators	η_{sCirc}	0.7	-

4.6.6.1 Hydraulically connected cycles

The cold mass cooling scheme presented in this section is based on the concept of SSC [84]. Figure 4.58 shows the hydraulic scheme with circulator in the single-phase helium cycle to re-pressurize non-vaporized helium. After extracting the heat load of all the half-cells in a parallel cooled CMU, the single-phase helium is conveyed back in a return line. For feeding the separators in the jumper connections, the returning single-phase helium flow is partly branched and expanded into the two-phase region by Joule-Thomson valves. All the abundant single-phase helium is re-pressurized and mixed with "fresh" single-phase helium supplied by header C. This design allows to decouple the mass flow rate from the parallel cooled CMU length, which enables a simple variation of the mass flow rate during transient modes or in part load operation.

Contrarily to the previous discussed cooling schemes, the single-phase helium is not expanded entirely in a Joule-Thomson valve at the parallel cooled CMU's end. The influence of the pressure drop of the single-phase helium on the exergetic efficiency increases and has to be kept small. The

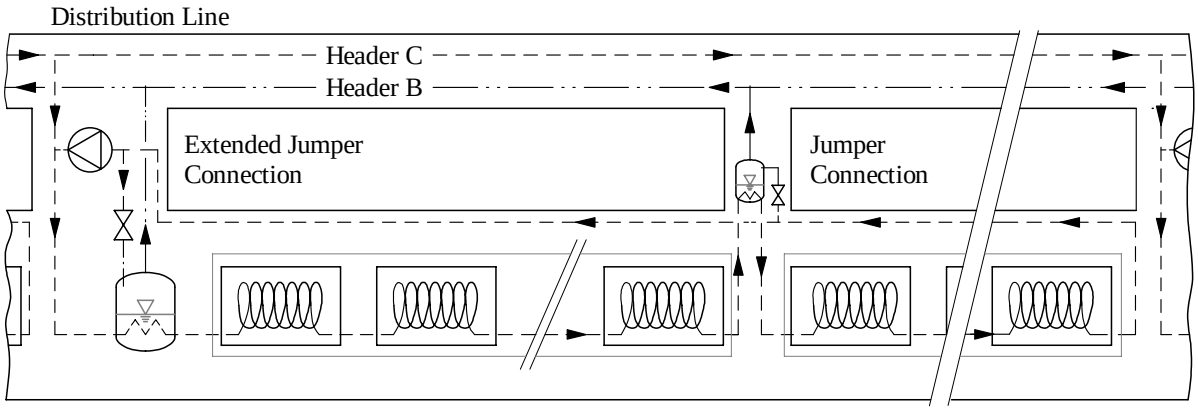

Figure 4.58: Hydraulic scheme with non-separated helium cycles and a circulator to re-pressurize non-vaporized helium based on the SSC design.

magnet-external heat exchangers enable the possibility of parallel channels in the cold mass (see figure 4.59). The size and the number of the parallel channels determine the mass flow rates passing through the different channels.

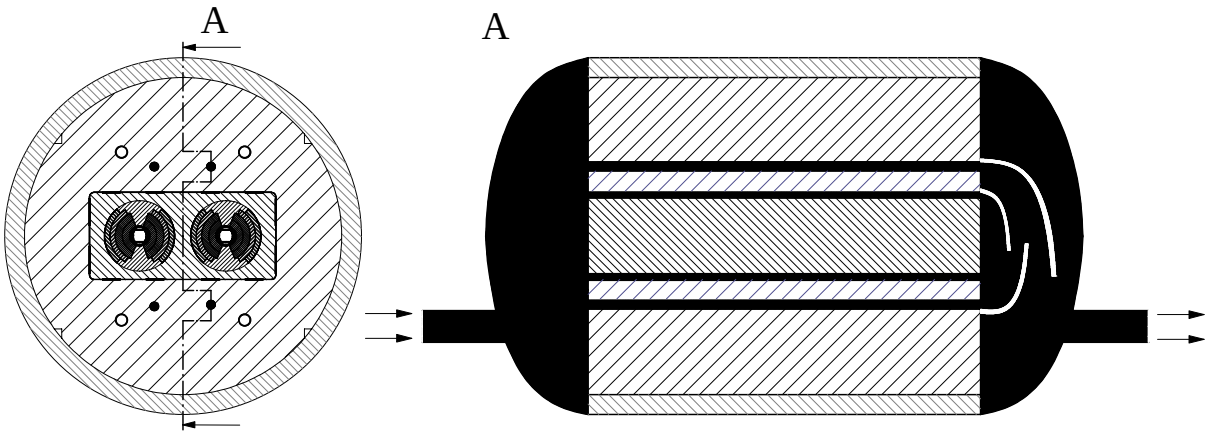

Figure 4.59: Schematic of a the cold mass design with parallel bypass channels for cooling schemes with long re-cooling lengths ($L_{RC} = L_{HC}$).

An elaborate parallel channel design allows to intercept part of the heat load and decreases the heat distribution coefficient. With increasing mass flow rate, the average temperature rise between two points of re-cooling is kept low, but the necessary circulation power and the effort to extract it at cryogenic temperature level increase.

For the results presented in this section, the number of parallel channels was chosen to be four and the supply pressure was assumed to be 3 bar. The diagram in figure 4.60 shows the exergetic efficiency (bold lines) and the maximal parallel cooled CMU length (thin lines) vs. the total mass flow rate for a heat distribution coefficient $\varphi_q = 1$. Tendentially the exergetic efficiencies and the parallel cooled CMU lengths can be assumed to be slightly higher.

Below a mass flow rate of about 75 g/s, the necessary saturation pressure in the separators must be lower than the λ-pressure to satisfy the temperature condition. With slightly higher mass flow rates, the maximal parallel cooled CMU length is determined by the total vaporization condition. By increasing the mass flow rate even more, the number of half-cells cooled in series can be increased

at first, but high mass flow rates generate high pressure drops and after exceeding a certain mass flow rate, the maximal cooling loop length is limited by the lower pressure limit of the single-phase helium (p_{crit}).

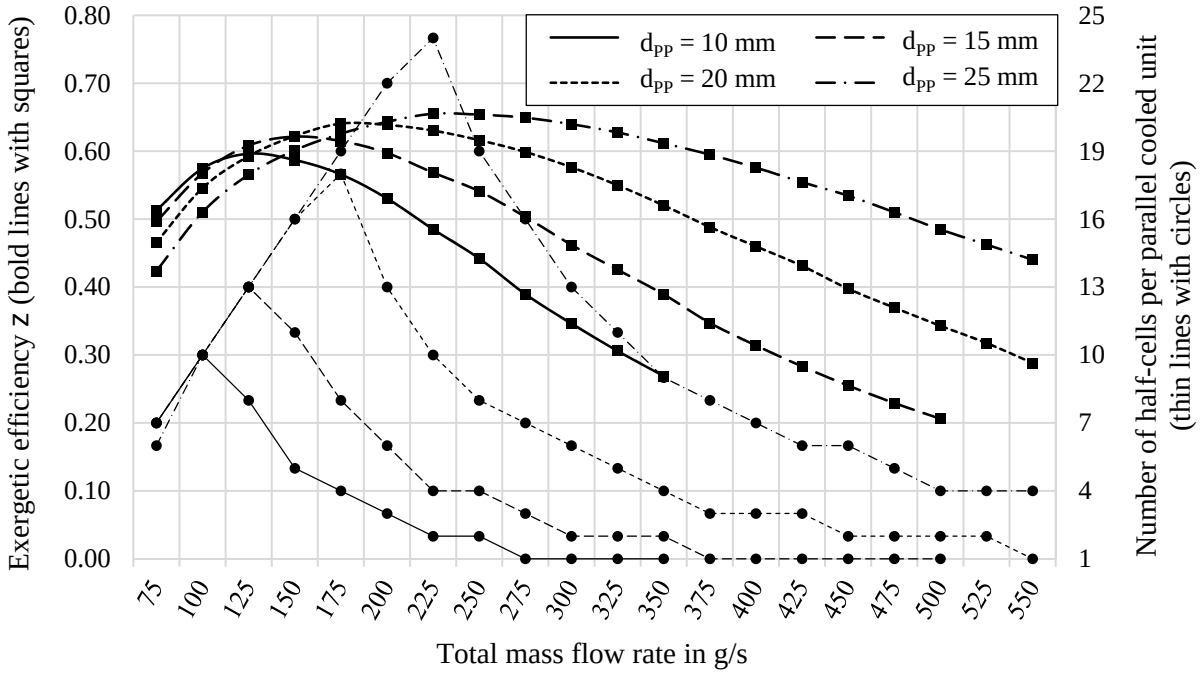

Figure 4.60: Exergetic efficiency (primary ordinate, bold lines with squares) and maximal number of half-cells cooled in series (secondary ordinate, thin lines with circles) vs. the the total mass flow rate of single-phase helium for different diameters of the four parallel channels (line shape) and a supply pressure p_C of 3 bar.

Interestingly, the maximal parallel cooled CMU length at a mass flow rate of 75 g/s is smaller for a large parallel channel diameter. First of all, the large parallel channel diameter, the mass flow rate passing the slits decreases and the saturation pressure in the separators has to be lower. Secondly, the lower pressure drop in the magnets results in a higher absolute pressure of the single-phase helium in the return line. These two effects result in large necessary pressure drop in the Joule-Thomson valves and cause an increased vapour production (as qualitatively shown in figure 4.61).

Due to the increased vapour production, less liquid helium is available for re-cooling and the total vaporization of the helium decreases the parallel cooled CMU length. The longest cooling loops can be achieved, if the two limits (total vaporization of the helium flow and reaching the critical pressure) are close together.

For each mass flow rate, the operation of the cold mass cooling system with the maximal parallel cooled CMU length, also yields the highest exergetic efficiencies. By cooling less half-cells in series, the returning (non-vaporized) single-phase helium generates additional exergy losses due to

- increased mixing losses of the re-pressurized and the supplied flows,
- increased necessary circulation power and
- the extraction of the increased circulation power at cryogenic temperature level.

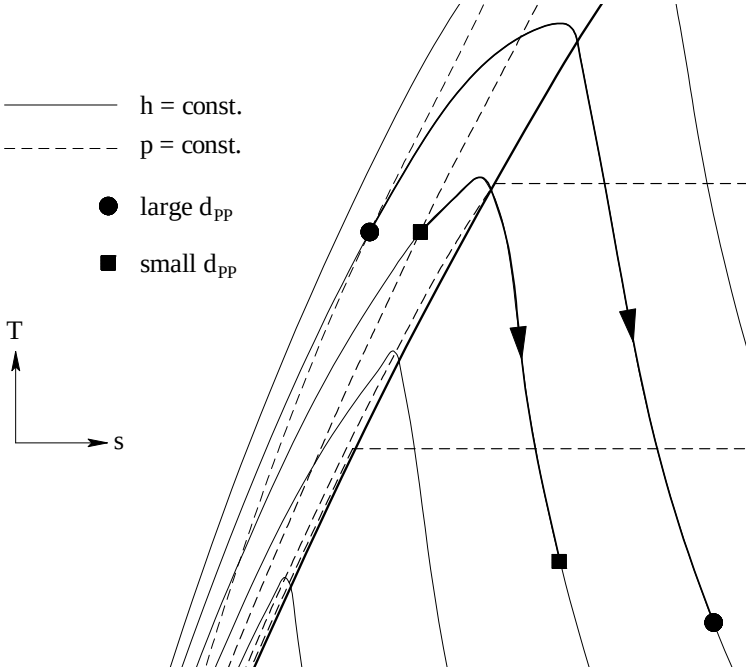

Figure 4.61: Increased vapour production during an isenthalpic expansion in a Joule-Thomson valve for different initial and final pressure levels displayed in a small section of the T s-diagram. The isenthalpic expansion marked with dots corresponds to a large parallel channel diameter, the isenthalpic expansion marked with squares corresponds to a small parallel channel diameter.

The evolution of exergetic efficiency show maxima slightly shifted to higher mass flow rates with respect to the maximal parallel cooled CMU length. Lower mass flow rates than the "most efficient" one, call for lower saturation pressures in the separators, decreasing the efficiencies. Higher mass flow rates than the "most efficient" one, increase the pressure losses in the cooling channels and therefore the circulation power and the mixing losses increase.

Compared to the previous hydraulic schemes, the exergetic efficiency is significantly lower. It could be increased by transferring heat from the single-phase helium delivered by header C to the returning low-pressure helium vapour. The installation of a heat exchangers only is reasonable close to the cold compressor station, where the mass flow rates in the two headers are identical.

4.6.6.2 Hydraulically separated cycles

By separating the cold mass cooling hydraulically into two cycles (primary cycle (cold mass cooling) and secondary cycle (supply/return)), the pressure of the primary cycle can be chosen independently of the supply pressure in header C. This enables the opportunity to combine the entire arc to one cooling loop, using only one circulator as illustrated in figure 4.62. The total vaporization condition can be circumvented entirely and does not restrict the cooling loop length in one way or the other.

The diagram in figure 4.63 shows the exergetic efficiency (bold lines) and the optimal helium mass flow rate (thin lines) (10 g/s-resolution) to achieve it vs. the circulator outlet pressure. The results are presented for a heat distribution coefficient of $\varphi_q = 1$. With decreasing heat distribution coefficient, the exergetic efficiencies slightly increase, the variation of the optimal mass flow rate is negligible.

Low supply pressures and small diameters of the parallel pipes result in small mass flow rates to keep the helium pressure above the critical pressure. Additionally, low mass flow rates cause a low saturation pressure in the separators and therefore the efficiencies are low. Hig supply pressures and large parallel channel diameters, on the other hand, enable high mass flow rates and therefore a low temperature rise of the helium between to re-cooling points.

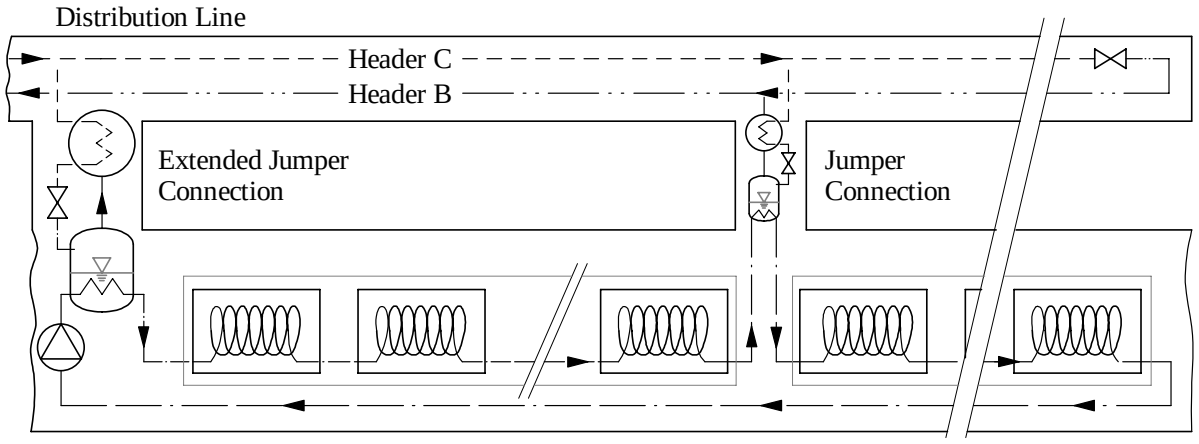

Figure 4.62: Hydraulic scheme with separated helium cycles and a circulator to re-pressurize the helium flow of the primary cycle.

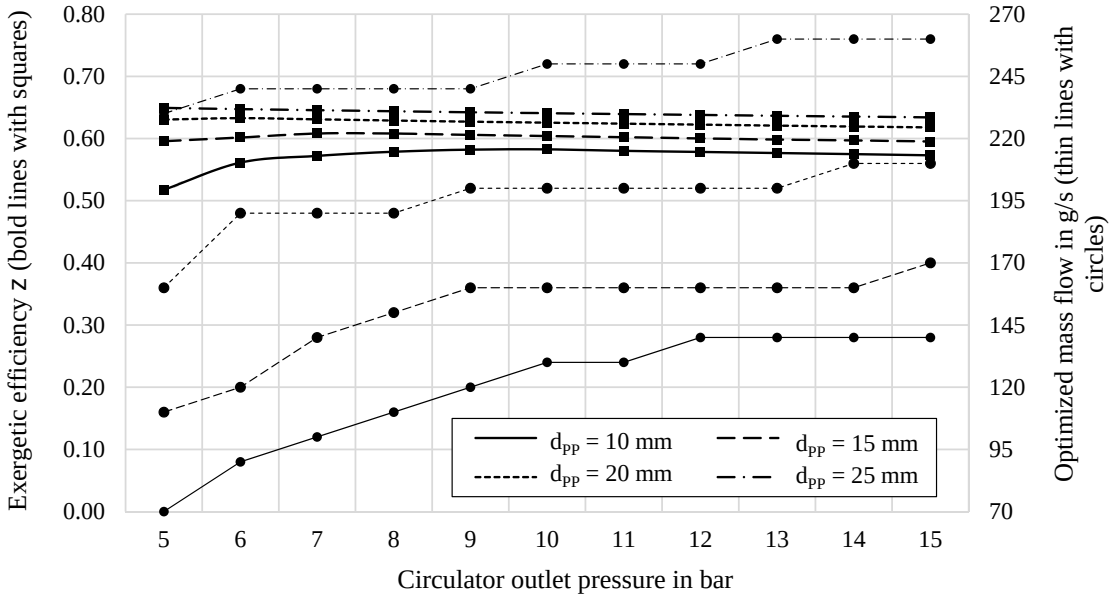

Figure 4.63: Exergetic efficiency (primary ordinate, bold lines) and optimized mass flow rate (10 g/s-resolution) to achieve it (secondary ordinate, thin lines) vs. the primary cycle circulator outlet pressure for different diameters of the four parallel channels (line shape).

The exergetic efficiency of the calculations with small parallel channels increase at first. With parallel channels large enough, the saturation temperature in the separators can be kept high also with low pressure levels in the primary cycle. The decrease of the efficiency with increasing pressure level is caused by the decreasing specific heat capacity of helium resulting in lower re-cooling temperatures (i.e. a lower saturation pressure in the separators).

4.6.6.3 Controlling and transient operations

The possibility of re-pressurizing non-vaporized helium simplifies the controlling and handling of transient operations. The mass flows can be adjusted in advance (e.g. before beam injection) and excess liquid helium needs not be stored or artificially vaporized, but can be circulated during transient operation. The subsequent lower exergetic efficiency of the steady-state operation can be traded with the dependable operation of the machine.

5 Beam Screen Cooling and thermal shield cooling

The concept of a so-called beam screen was chosen following its successful use in the LHC, the first accelerator to feature this type of component. The beam screen, among other functions, works as a thermal shield, protecting the cold mass from the beam-induced heat loads, most of which is due to synchrotron radiation. It is separately cooled at a higher temperature level (40 – 60 K) than the cold mass (≈ 2 K). The extraction of the synchrotron radiation heat load by the cold mass cooling system would call for a disproportionally large cooling capacity, given the low operating temperature. Apart from the technical efforts needed, if at all possible, the electrical power consumption would be enormous.

5.1 Requirements

The choice of the beam screen temperature level depends on several aspects. First of all the temperature can be optimized regarding the exergetic consumption of the cooling scheme. The main part of the heat load $\dot{Q}_{BS}$ is extracted by the cooling channels of the beam screen. A smaller part $\dot{Q}_{CM}$ though will be transferred to the cold mass by radiation $\dot{Q}_{\sigma}$ and heat conduction $\dot{Q}_{k}$ passing the supports, which keep the beam screen centered in the cold bore (as schematically illustrated in figure 5.1).

The electrical power $\dot{P}_{el}$ to extract the heat load depends on the temperature levels of the beam screen and the cold mass. Based on experiences during the operation of the LHC and assuming similar heat distribution and Carnot efficiencies of the refrigerators for the different temperature levels (ξ_{CM} and ξ_{BS}), the exergetic effort based on the temperature levels of the beam screen T_{BS} and the cold mass T_{CM} can be estimated by upscaling [85]. For comparison, four results for the four initially discussed possibilities are shown in the diagram in figure 5.2:

- A cold mass temperature T_{CM} of 1.9 K and a synchrotron radiation power P_{SR} of 44.3 W/m (in an FCC of 80 km of circumference)
- A cold mass temperature T_{CM} of 1.9 K and a synchrotron radiation power P_{SR} of 28.4 W/m (in an FCC of 100 km of circumference) → actual design case
- A cold mass temperature T_{CM} of 4.5 K and a synchrotron radiation power P_{SR} of 44.3 W/m (in an FCC of 80 km of circumference)
- A cold mass temperature T_{CM} of 4.5 K and a synchrotron radiation power P_{SR} of 28.4 W/m (in an FCC of 100 km of circumference)

$$\dot{P}_{el} = \frac{\dot{Q}_{BS}}{\xi_{BS}} \left(\frac{T_a}{T_{BS}} - 1 \right) + \frac{\dot{Q}_{CM}}{\xi_{CM}} \left(\frac{T_a}{T_{CM}} - 1 \right) \tag{5.1}$$

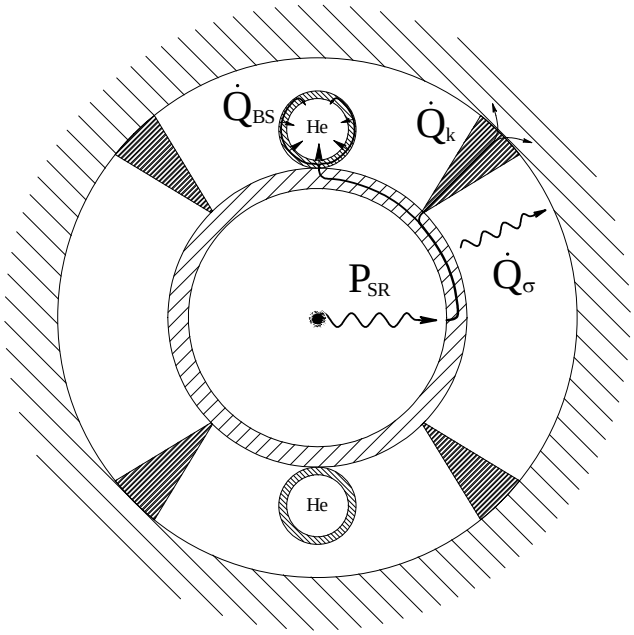

Figure 5.1: Schematic of the heat fluxes in the beam screen, transferred to the cooling channels and to the cold mass.

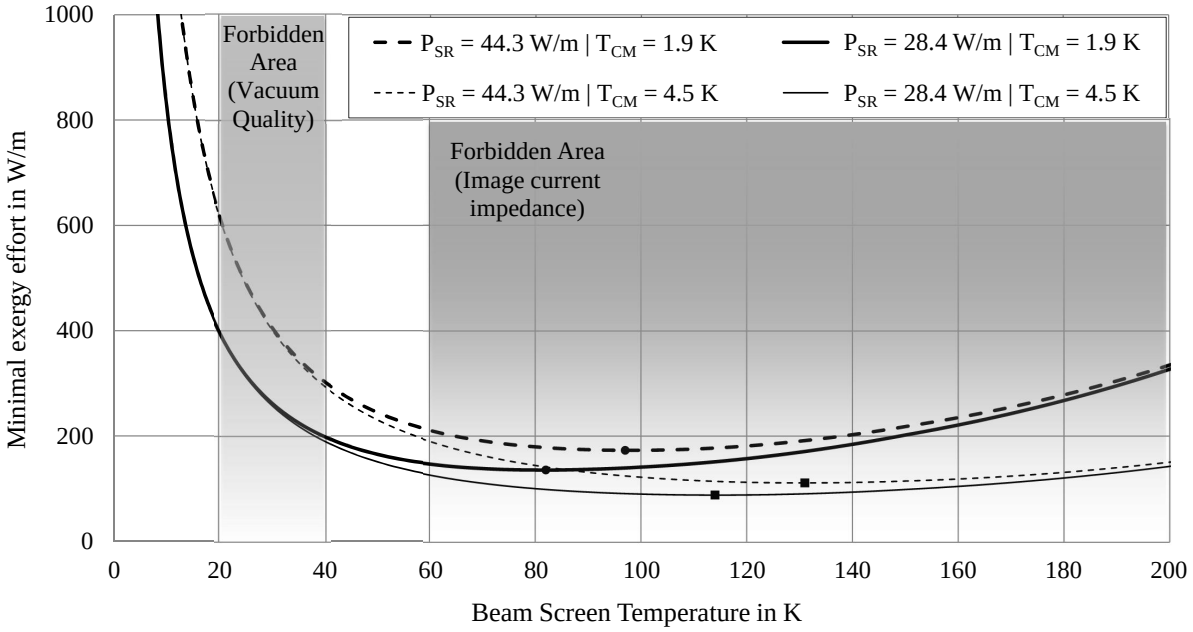

Figure 5.2: Exergetic effort to extract the heat load from the beam screen and the cold bore as a function of the beam screen temperature (obtained by upscaling of LHC data).

The exergetic effort has a global minimum, which would be reasonable and economical to work at, but there are technical restrictions [86][87].

1. **Vacuum quality:** To preserve a good vacuum quality, the beam screen materials have to be prevented from outgassing. Especially the degassing of hydrogen molecules from the steel disables the temperature range between 20 K and 40 K. Also at temperatures above 60 K the degassing of different molecules degrade the vacuum.

2. **Resistive-wall impedance:** The circulating proton bunches induce a so-called image current in the beam screen. The electric resistivity of the materials surrounding the beam has to be kept low [88]. A beam screen temperature above 60 K has negative effects on the wall impedance.

Considering these physical constraints, two temperature windows were taken into account for operating the beam screen. One from absolute zero to 20 K and a second one between 40 K and 60 K. Since the exergetic costs increase tremendously at very low temperatures, the temperature range from 40 K to 60 K was chosen to operate the beam screen cooling system.

5.2 Beam Screen

Several constraints influenced the design of the beam screen. Highest priority, and therefore main constraint, was the maximal diameter of the cold bore to keep the costs of the superconducting materials at a reasonable level. Moreover, the beam screen has to be designed to discharge degassed molecules from the inside to the cold bore effectively by cryo-pumping to preserve the required vacuum quality. The cooling of at least the length of one dipole/quadrupole continuously has to be possible. The latest design conceptualized by the VSC group (**V**acuum, **S**urfaces and **C**oatings) of the TE-Department at CERN combines all the requirements and also gives scope for different concepts of the beam screen cooling system [93]. The general structure of the design is illustrated in figure 5.3 on the left side.

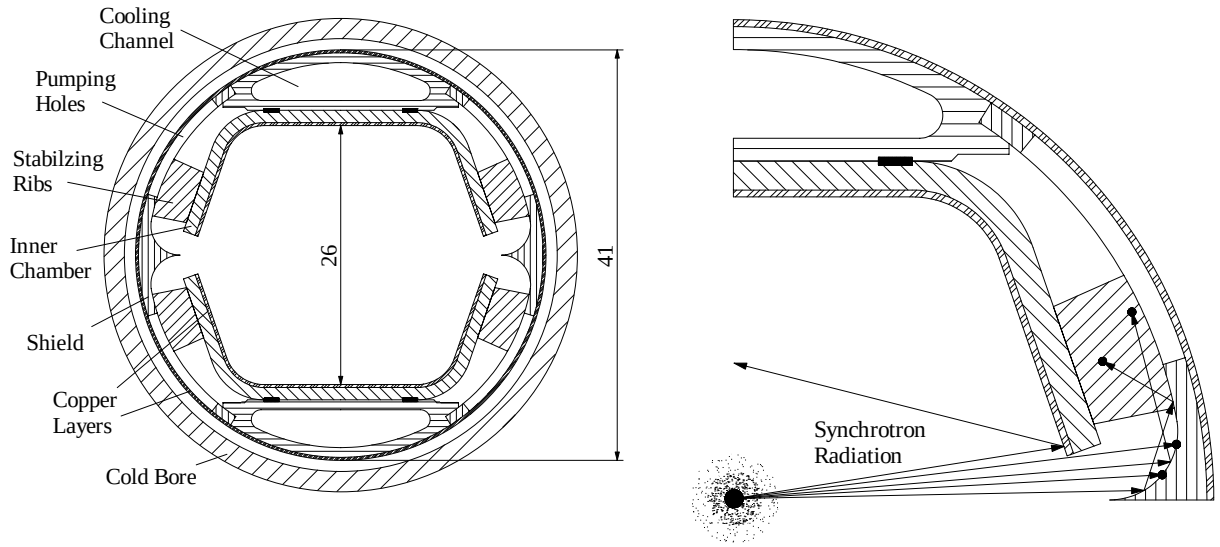

Figure 5.3: Cross section of the beam screen (left-hand side) and working principle of the antechamber (right-hand side).

Centrepiece of the design is the inner chamber. It is split into two half-shells containing the proton beam and leading the image current. The main part of the tube is made out of 1.3 mm of

stainless steel to withstand the forces during a quench, whereas the inside surface is coated with an 0.3 mm copper layer to reduce the electrical impedance. An additional advantage of the copper layer is its good thermal conductivity to transfer the resistive heat, generated by the image current, to the cooling channels.

Around the inner chamber a shield is mounted, forming antechambers with the inner chamber. Its main body is made out of 1.0 mm of stainless steel and a 0.3 mm copper layer laminated on the outside surface. Unlike the copper layer of the inner chamber, its only task is to improve the heat transfer from the shield to the cooling channels. To withstand mechanical forces during a quench, stabilizing ribs are mounted every 7 cm supported by the inner chamber.

The slits between the inner chamber shells are designed and positioned to let pass the major part of the synchrotron radiation (dispersion angle $< 10^{o}$) to avoid a heat impact on the shells. The synchrotron radiation is emitted only to the outside with respect to circular collider's center - the second slit on the opposite side (closer to the FCC center) is designed to preserve a symmetric design. The synchrotron radiation has a large velocity component tangentially to the tube axis, which causes the impact of the photons several metres after its generation and small angles of incidence with the surface of the shield. About half of the photons will partly be reflected and hits the stabilizing ribs almost frontally, which therefore will absorb half of the heat load (see figure 5.3 on the right side).

At the top and at the bottom of the inner chamber, oval shaped cooling channels will be mounted, made of stainless steel with a wall thickness of 1.0 mm. The channel cross section area A_{CC} is 53.8 mm^2, the hydraulic diameter d_h 5.61 mm.

The three parts (inner chamber, shield and cooling channels) will be assembled by spot-welding. Four welds will be performed as butt joints, each between the ends of the shield and the cooling channels, and four welds will be performed as lap welds to connect the cooling channels to the inner chamber shells. These welds are the constructional heat bridges to transfer the energy from the shield and the inner chamber to the cooling channels. The stabilizing ribs are rigidly connected by welding only to the shield to decrease the heat transfer from the ribs to the inner chamber.

The beam screen will be centered in the cold bore by sliding rings, mounted every 70 to 100 cm. These supports must be designed to compensate for the temperature dependent changes of the length of the cold bore and the beam screen as well as for their diameters.

5.2.1 Heat transfer in the beam screen

The driving temperature difference between the warmest part of the inner chamber and the cryogen in the cooling channels ΔT_{CC-iCh} determines the maximal allowed helium temperature $T_{CC\,max}$.

$$T_{CC\,max} = T_{iCh\,max} - \Delta T_{CC-iCh} \tag{5.2}$$

A 2D-simulation based on the method of finite differences was performed to estimate the temperature difference needed for the heat transfer in the beam screen. For the calculation a cross section containing a stabilizing rib was chosen. The heat load received by the ribs is conducted mainly by the shield to the cooling channels. The small breadth of the ribs is the bottleneck for the heat transfer. By varying the heat load on the stabilizing ribs, the ratio of rib thickness and the length of the shield contributing to the heat transfer can be qualitatively changed in the simulation. The following assumptions and simplifications were made (including the values shown in table 5.1):

- The heat transfer from the ribs to the inner chamber was neglected, but an additional heat load was applied for compensation in consultation with the VSC group

- The heat transfer from the inner chamber to the cooling channels between the welds was neglected, but the welds were assumed to be continuous in axial direction
- No contact resistance was assumed between the steel and the copper
- The heat load on the ribs and on the peak is uniformly distributed
- The material properties of copper and steel are constant, independent of the temperature

Table 5.1: Beam screen geometry and material properties

Input Value	**Symbol**	**Value**	**Unit**
Copper thermal conductivity	k_{Co}	375 (700)	W/(m·K)
Steel thermal conductivity	k_{St}	6.5 (5.0)	W/(m·K)
Copper specific heat capacity	c_{Co}	140	J/(kg·K)
Steel specific heat capacity	c_{St}	170	J/(kg·K)
Copper density	ρ_{Co}	9860	kg/m^3
Steel density	ρ_{St}	7700	kg/m^3
Length of lap welds (connecting the inner chamber with the cooling channels)	L_{Weld}	2	mm
Helium temperature	T_{CC}	40	K
Helium pressure	p_{CC}	50	bar
Cooling channels absolute roughness	ϵ_{CC}	1.5	μm
Helium mass flow rate per cooling channel (for cooling a half-cell continuously)	$\dot{m}_{CC}$	15.35	g/s

Two different combinations of copper/steel were assumed, the thermal properties can be found in table 5.1 (different values proposed by the VSC group in brackets). The helium properties needed to obtain the heat transfer in the cooling channels were calculated based on a helium temperature of 40 K and a helium pressure of 50 bar. To obtain the heat transfer coefficient of the flow, a Nusselt function (4.21) was used [73]. The temperature field was computed with two different approaches:

1. **Gauss-Seidel method with relaxation:** The steady-state temperature field can be described with the Poisson equation [89]. Appendix E contains the discretized equations for polar coordinates and Cartesian coordinates for a cell not neighboured to any boundaries [90]. The procedure to calculate the temperatures to fulfil the boundary conditions is identical as illustrated in Appendix D. Underrelaxation ($\omega \leq 0.5$) was necessary to achieve convergence of the numerical calculation [91].

2. **Crank-Nicolson method with ADI:** The transient heat conduction can be described with the heat (conduction) equation [89]. The discretization of the equation in polar coordinates and the approach to solve the semi-implicit set of equations can be found in Appendix D. The discretization of the heat equation in Cartesian coordinates is carried out analogously, the basic discretized equations for a cell not neighboured to any boundaries can be found at the end of Appendix D.

The proof of the energy consistency of the discretization of the heat equation for polar coordinates is illustrated in Appendix F. Due to the symmetry of the geometry and the heat load with respect to the horizontal plane, only one half of the beam screen was modelled. Figure 5.4 shows the

used mesh for a heated quarter of the beam screen and the assumed boundary conditions. The solid lines mark adiabatic boundaries and the dashed lines mark boundaries modelled with a constant heat flux entering (von Neumann boundary condition). In the cooling channel (dash-dotted line) a constant constant heat transfer coefficient was assumed (Cauchy/Robin boundary condition), calculated with the values given in table 5.1 [92]. The synchrotron radiation hitting the stabilizing rib was taken into account as a heat source.

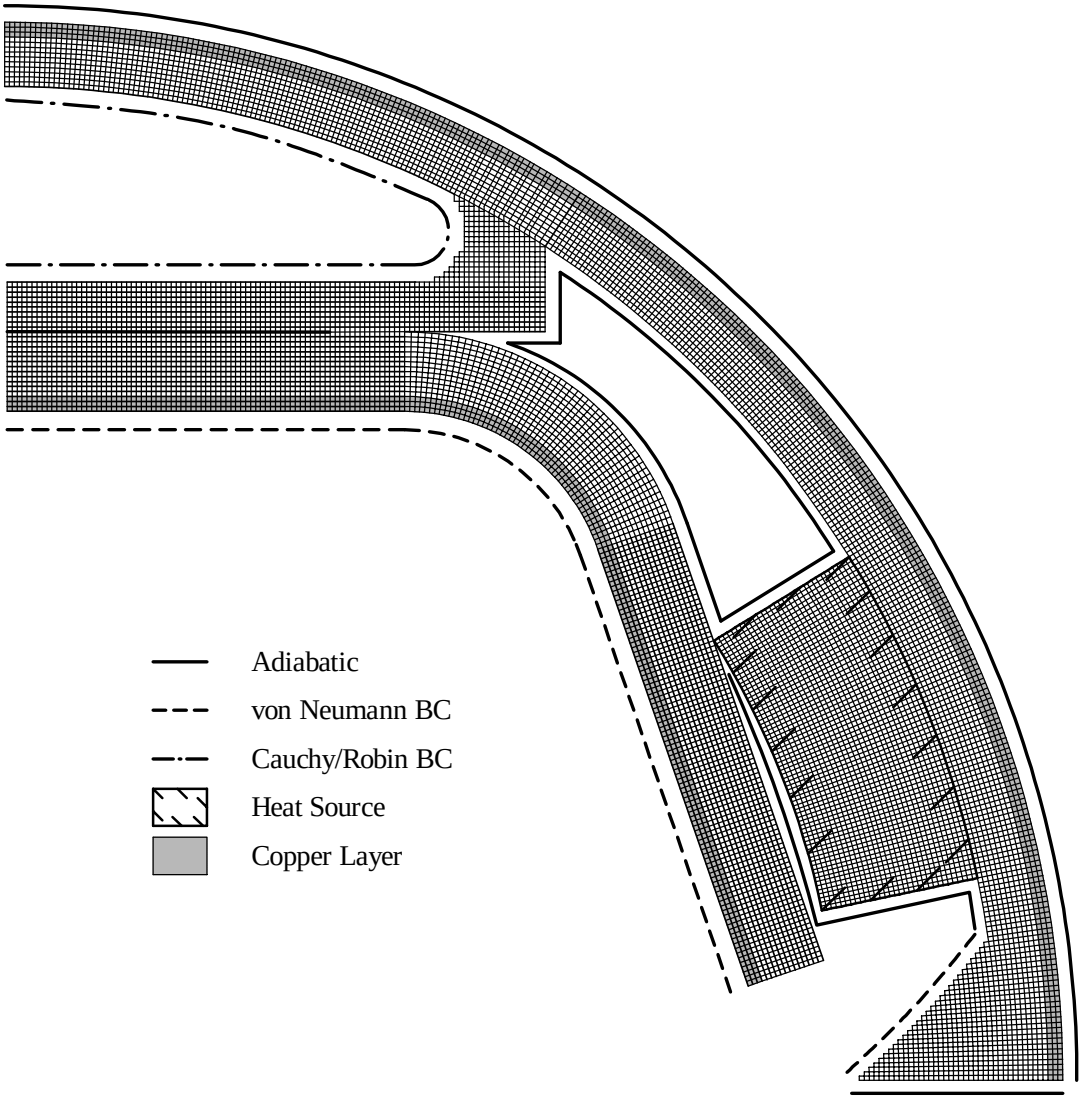

Figure 5.4: Mesh of the beam screen model (only one quarter affected by the synchrotron radiation). The bold lines represent the used boundary conditions (solid: adiabatic boundary, dashed: defined heat flux, dashed-dotted: heat transfer by convection). A heat source term simulates the heat load on the rib due to the synchrotron radiation, the cells modelling the copper layers are coloured in grey.

A mesh independency analysis has been performed. The grid was refined until the resulting temperature fields varied by less than 20 mK for the solutions with the most heterogeneous temperature distribution, whereas the refinement of the grid was accompanied by a decrease of the

calculated temperatures. Figure 5.4 illustrates the used grid, which seemed to be a good compromise between accuracy and necessary calculation time. With the faster, but more inaccurate Gauss-Seidel solver a rough solution was calculated. The results then were used as the initial temperature distribution for the Crank-Nicolson method. The following truncation conditions were chosen for the simulations:

- **Gauss-Seidel:** The temperature change of each cell was smaller than 10^{-8} K in one iteration step.
- **Crank-Nicolson:** The temperature change of each cell was smaller than 10^{-5} K in 10 simulated seconds.

The diagram in figure 5.5 shows the maximal temperature of the inner chamber for the temperature field solved with the Crank-Nicolson method (transient / parabolic PDE) and the Gauss-Seidel method (steady-state / elliptic PDE). In the most pessimistic case, the heat is conducted only in a slice of the shield corresponding to the rib thickness t_{Rib} of 1 mm. By increasing t_{Rib}, the source term is decreased, which corresponds to a larger slice of the shield contributing to the thermal conduction from the ribs to the cooling channels.

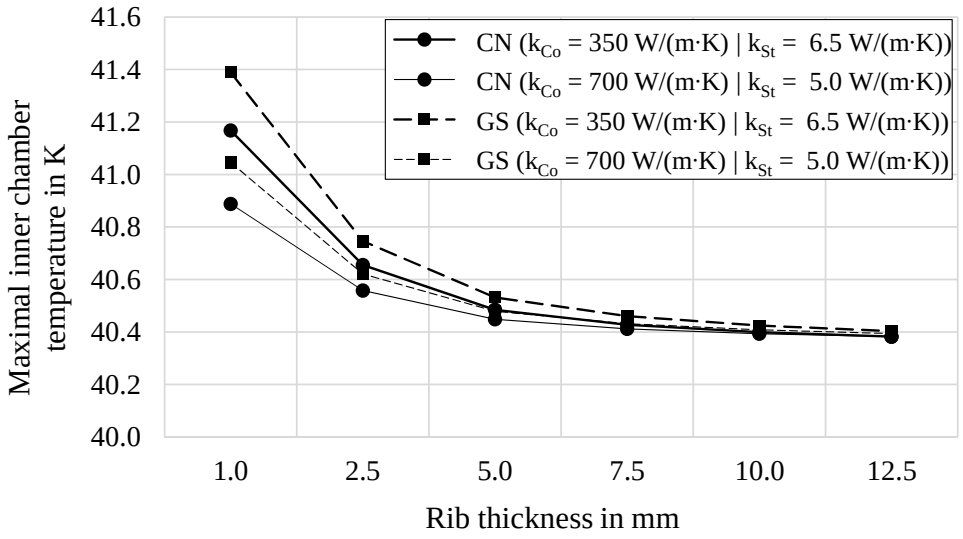

Figure 5.5: Maximal temperature of the inner chamber vs. different heat source terms in the stabilizing ribs (expressed as the rib thickness). The solid lines correspond to the results obtained with the Crank-Nicolson method, the dashed lines correspond to the results obtained with the Gauss-Seidel method. The color indicates the assumed thermal conductivities of copper (bold lines: 350 W/(m·K) / thin lines: 700 W/(m·K)) and steel (bold lines: 6.5 W/(m·K) / thin lines: 5 W/(m·K)).

The results show a maximal temperature of the inner chamber of about 1.2 K in the pessimistic case for the Crank-Nicolson solver, which yields lower values, than the Gauss-Seidel method. With increasing rib thickness, the temperature seems to approach asymptotically smaller values. With an increased thermal conductivity of the copper layers (thin lines), the temperature of the inner chamber can be decreased. The results could be compared to a parallel heat transfer calculation performed by the VSC group, where the beam screen was designed and a thermal simulation was performed with a 3D model. The resulting temperature of 40.4 K corresponds to a rib thickness of

about 10 mm as can be seen in figure 5.5. Due to the good accordance with the results obtained by the parallel simulation of the VSC group (i.e. a driving temperature difference of close to 0.4 K), a maximal allowed helium temperature in the cooling channels $T_{CC\,max}$ of 59.6 K was assumed for the following calculations.

5.3 Parallel cooled beam screen unit (BSU)

The helium flow in the beam screen cooling channels is modelled as a quasi-one-dimensional flow. Since the mass flow rate is constant and no phase change occurs, only momentum (5.3) and energy (5.4) balance equations were solved, where only the steady-state operation was considered.

Momentum The pressure of the helium flow is assumed to be constant over the entire flow cross section. Due to the slope of the FCC tunnel, the helium can flow in descending or ascending direction depending of the location of the BSU. The quasi one-dimensional momentum balance reads

$$\underbrace{\dot{m}_{CC}\frac{dw_{CC}}{dz}}_{Change\ of\ momentum} = \underbrace{-A_{CC}\frac{dp}{dz}}_{Pressure\ forces} \underbrace{-\tau_P L_P}_{Friction\ forces} \pm \underbrace{g\,\rho_{CC}\,A_{CC}\,sin\,\alpha}_{Weight} \tag{5.3}$$

$\dot{m}_{CC}$ denotes the mass flow rate in the cooling channel, A_{CC} denotes the cross sectional area of the cooling channel, L_P denotes the inner perimeter of the cooling channel and τ_P the corresponding shear stresses. The shear stresses between the pipe wall and the fluids were calculated with the Darcy friction factor derived by the formula of Swamee-Jane (5.21), which is discussed in the next sections.

Thermal Energy In the energy balance, the longitudinal heat conduction was neglected. Transversal heat transfer due to synchrotron radiation and resistive heating was accounted for. dh denotes the change of specific enthalpy of the helium and $\dot{q}_{BS}$ denotes the heat flux transferred to the cooling channel in W/m^2.

$$\dot{m}_{CC}\,dh = \dot{q}_{BS}\,dz \tag{5.4}$$

5.3.1 General constraints

The 8.4 km long beam screen of one long arc cannot be cooled in series, but has to be arranged in parallel supplied cooling loops. The continuously cooled length of a parallel loop must correspond to an integer number of magnets in series and shall be called a parallel cooled beam screen unit (BSU). The actual available temperature range ΔT_{CC} for cooling a parallel cooled BSU can be calculated by subtracting the necessary driving temperature difference in the beam screen from the temperature limit of the inner chamber.

$$\Delta T_{CC} = T_{CC\,max} - T_{CC\,in} \tag{5.5}$$

where $T_{CC\,in}$ denotes the cooling channel inlet temperature and $T_{CC\,max}$ corresponds to the cooling channel outlet temperature. With increasing mass flow rate $\dot{m}_{CC}$ passing through the cooling channels, the continuously cooled length can be increased, but there are two additional constraints.

1. **Pressure drop:** By combining energy conservation and the equation of Darcy and Weisbach, the dependency of the frictional pressure drop on the parallel cooled BSU length L_{BSU} (or the mass flow rate respectively) to the third power can be shown.

$$\dot{m}_{CC} = \frac{\dot{q}_{BS}\, L_{BSU}}{c_p\, \Delta T_{CC}} \tag{5.6}$$

$$\Delta p_f = \frac{f\, L_{BSU}}{2\, d_h\, A_{CC}^2} \frac{\dot{m}_{CC}^2}{\rho_{CC}} \tag{5.7}$$

$$\Delta p_f = \frac{f\, \dot{q}_{BS}^2}{2\, d_h\, A_{CC}^2\, c_p^2\, \Delta T_{CC}^2\, \rho_{CC}}\, L_{BSU}^3 \tag{5.8}$$

where f denotes the Darcy friction factor, ρ_{CC} the density of the helium and c_p the specific heat capacity of the helium.

The maximal allowed pressure drop in a parallel cooled BSU was determined to be 80 % of the supply pressure p_0. This limit was chosen as the technical constraint to operate the control valves mounted at the parallel cooled BSUs' ends. By means of exergetic efficiency, this pressure drop exceeds the tolerable losses by far.

The pressure evolution in the beam screen cooling channels is driven by the frictional pressure Δp_f drop for reasonably long parallel cooled BSUs. With a scaling analysis this statement is substantiated. The frictional pressure drop shown in (5.7) can be rearranged.

$$\Delta p_f = \frac{\dot{m}_{CC}^2}{A_{CC}^2} \frac{f\, L_{BSU}}{2\, d_h\, \rho_{CC}} \tag{5.9}$$

The pressure drop Δp_m generated by the acceleration of the warmed up helium can be calculated with (5.10).

$$\Delta p_m = \frac{\dot{m}_{CC}}{A_{CC}}\, \Delta v_{CC} = \frac{\dot{m}_{CC}^2}{A_{CC}^2}\, \Delta \frac{1}{\rho_{CC}} \tag{5.10}$$

The factor $(\dot{m}_{CC}/A_{CC})^2$ in the two equations is identical, only the terms $(f\, L_{BSU})\,/\,(2\, d_h\, \rho_{CC})$ in (5.9) and $\Delta \rho_{CC}^{-1}$ in (5.10) have to be compared:

- The Darcy friction factor f is in the order of 10^{-2}.
- The hydraulic diameter d_h is in the order of 10^{-3} m.
- The length of one magnet is 15 m, therefore the parallel cooled BSU length is at least in the order of 10^1 m
- The density of the helium in the corresponding temperature and pressure ranges is in the order of $10^1 - 10^2$ kg/m^3 as well as the density difference $\Delta \rho_{CC}^{-1}$ at the parallel cooled BSU inlet and outlet.

$$\frac{f\, L_{BSU}}{2\, d_h\, \rho_{CC}} \rightarrow \frac{10^{-2}\, 10^{1.5}}{10^{-3}\, 10^{1.5}} = 10^1 \tag{5.11}$$

$$\Delta \frac{1}{\rho_{CC}} \rightarrow \frac{10^0}{10^{1.5}} = 10^{-1.5}\ in\ \frac{m^3}{kg} \tag{5.12}$$

The pressure drop due to the acceleration of the helium is two orders of magnitude smaller than the frictional pressure drop. To estimate the pressure losses of the flow in an inclined pipe Δp_g, the maximal expected slope α of the FCC tunnel of 0.3 % is assumed.

$$\Delta p_g = \rho_{CC}\, g\, \Delta h \; in \; \frac{m^3}{kg} \tag{5.13}$$

The order of magnitude of the gravitational acceleration g is 10^1, for a parallel cooled BSU length L_{BSU} of 10^1 m of order of magnitude, the difference in height Δh results in a order of magnitude of 10^{-1}.

$$\rho_{CC}\, g\, \Delta h \rightarrow 10^{1.5}\, 10^1\, 10^{-1} = 10^{1.5} \; in \; Pa \tag{5.14}$$

For a mass flow rate in the cooling channels of at least an order of magnitude of 10^{-3} kg/s and the cooling channel cross section area with an order of magnitude of 10^{-5} m^2, the overall order of magnitude of the frictional pressure drop results in (5.15).

$$\frac{\dot{m}_{CC}^2}{A_{CC}^2} \frac{f\, L_{BSU}}{2\, d_h\, \rho_{CC}} \rightarrow \frac{10^{-6}}{10^{-10}} \frac{10^{-2}\, 10^{1.5}}{10^{-3}\, 10^{1.5}} = 10^5 \; in \; Pa \tag{5.15}$$

The influence of the hydrostatic head and the acceleration of the helium due to the decrease of the density are negligible compared to the frictional pressure drop.

2. **Flow velocity:** As experience gained during the operation of the LHC has shown, high helium velocities cause vibrations, which lead to fatigue of materials and further to component failure due to alternating stresses. Based on the experimental data of the LHC, the limit for the maximal flow velocity was determined to be 10 % of the sound velocity.

5.3.2 Maximal parallel cooled BSU length

With increasing parallel cooled BSU length the mass flow rate must be increased to keep the cryogen's temperature below the necessary limit. The mass flow rate can be raised, until the pressure drop limit or the flow velocity limit is reached. After reaching this point, an increase of the mass flow rate decreases the parallel cooled BSU length, since one of the limits is reached even earlier. There exists a maximal possible parallel cooled BSU length connected to a certain mass flow rate.

To maximize the parallel cooled BSU length, the supply temperature T_0 should be chosen as low as possible (40 K). The supply pressure p_0 is limited by the strength of the cooling channels. In the investigated regime the density of helium is directly proportional to the pressure for equal temperatures. Two helium flows (1 and 2) of different inlet pressure have the same initial velocity v_0, if the ratio of the mass flow rates $\dot{m}$ corresponds to the ratio of the densities ρ_0.

$$\frac{p_{01}}{p_{02}} \approx \frac{\rho_{01}}{\rho_{02}} = \frac{\dot{m}_1}{\dot{m}_2} \quad \rightarrow \quad v_{01} = v_{02} \tag{5.16}$$

In both cases the length L_{BS} can be cooled, if the ratio of the specific heat loads correspond to the ratio of the mass flow rates (assuming a constant heat capacity, which is viable due to their small dependency on the pressure).

$$L_{BS} = \frac{\dot{m}_1 \, c_p \, \Delta T}{\dot{q}_1} = \frac{\dot{m}_2 \, c_p \, \Delta T}{\dot{q}_2} \rightarrow \frac{\dot{m}_1}{\dot{q}_1} = \frac{\dot{m}_2}{\dot{q}_2} \tag{5.17}$$

The correlation in (5.17) applies for the entire cooled length L_{BS}, hence the temperature profiles along the coordinate z parallel to the beam screen in both cases are equal. To calculate the frictional pressure drop, the Darcy-Weisbach equation (5.7) can be used.

$$T_1 \, (z) = T_2 \, (z) \tag{5.18}$$

$$\Delta p = \frac{f}{2 \, d_h} \, L_{BS} \, v^2 \, \rho \tag{5.19}$$

The influence of the variation of the Darcy friction factor depending on the change of the pressure can be estimated with the explicit formula of Swamee-Jain (5.21), which appeared a well-matching formula in the investigated regime of Reynolds numbers (by comparison with the Moody diagram). Only the Reynolds number Re is a variable parameter influencing the resulting Darcy friction factor. To obtain the magnitude of influence of the different terms of (5.21), a scaling analysis can be performed.

$$Re = \frac{d_h v}{\nu} \tag{5.20}$$

$$f = 0.25 \left[log_{10} \left(\frac{\epsilon}{3.7 d_h} + \frac{5.74}{Re^{0.9}} \right) \right]^{-2} \tag{5.21}$$

- The absolute roughness ϵ for a well-treated steel surface is of the order of 10^{-5} m.
- The hydraulic diameter d_h is of the order of 10^{-3} m.
- The maximal flow velocity was determined to be 10 % of the sound velocity. The sound velocity is predominant by a function of the temperature ($a \, (T_{CC} = 50 \; K) \approx 10^2$ – 10^3 m/s), hence the order of the flow velocity is in the order of 10^1 m/s.
- The kinematic viscosity ν of helium is typically in the order of 10^{-7} m^2/s in the investigated temperature and pressure regimes.

$$\frac{\epsilon}{3.7 \, d_h} \rightarrow \frac{10^{-5}}{10^{-3} \, 10^0} = 10^{-2} \; (dimensionless) \tag{5.22}$$

$$\frac{5.74}{Re^{0.9}} \rightarrow \frac{10^{0.5}}{(10^{-3} \, 10^1 \, 10^7)^{0.9}} = 10^{-4} \; (dimensionless) \tag{5.23}$$

The Reynolds number-dependent term is about two orders of magnitude smaller than the constant term. The Darcy friction factor can be assumed to be constant.

$$\Delta p = \underbrace{\frac{f}{2 \, d_h}}_{C} \, L_{BS} \, v^2 \rho \tag{5.24}$$

$$\frac{\Delta p_{01}}{\Delta p_{02}} = \underbrace{\frac{C}{C}\frac{L_{BS}}{L_{BS}}\frac{v_{01}^2}{v_{02}^2}}_{=1}\frac{\rho_{01}}{\rho_{02}} = \frac{p_{01}}{p_{02}} \rightarrow \frac{\Delta p_{01}}{p_{01}} = \frac{\Delta p_{02}}{p_{02}} \tag{5.25}$$

The absolute pressure drop is proportional to the supply pressure, ergo the pressure drop relative to the supply pressure is equal for the two helium flows. Moreover, the velocities of the two flows are equal along the entire length L_{BS} and therefore the pressure drop limit and the velocity limit are reached at the same point.

The velocity is inversely proportional to the density (and to the pressure). By inserting the determined limits for pressure drop and velocity, a initial velocity limit $v_{0\,lim}$ can be estimated.

$$\frac{v}{v_0} = \frac{\rho_0}{\rho} = \frac{p_0}{p} = \frac{p_0}{p_0 - \Delta p} = \frac{1}{1 - \Delta p/p_0} \tag{5.26}$$

$$v_{max} = 0.1\, v_{Sound} = \frac{v_0}{1 - \Delta p_{max}/p_0} = \frac{v_0}{1 - 0.8} \tag{5.27}$$

$$v_{0\,lim} = 0.02\, v_{Sound} \tag{5.28}$$

To extract larger heat loads, higher mass flow rates are necessary accompanied by higher initial velocities. If the initial velocity exceeds about 2 % of the speed of sound, the crucial constraint limiting the parallel cooled BSU length is the flow velocity. If little heat has to be extracted, the pressure drop limit is decisive.

A numerical simulation, solving the discretized momentum and energy consistency equations (5.3)–(5.4), was performed using variable helium properties and the cooling channel geometry of the FCC beam screen. In table 5.2 the simulation input data is listed. The helium properties were taken from the library 'HePak' (Cryodata Inc.).

Table 5.2: Beam screen cooling: Maximal parallel cooled BSU length

Input Value	**Symbol**	**Value**	**Unit**
Maximal beam screen outlet temperature	$T_{CC\,max}$	59.6	K
Cooling channels hydraulic diameter	d_h	5.61	mm
Cooling channels cross section area	A_{CC}	53.8	mm^2
Total heat load per beam screen	$\dot{q}_{BS}$	31.1	W/m

The diagram in figure 5.6 shows the correlation between pressure drop and maximal parallel cooled BSU length for several (inlet) conditions. With increasing inlet temperature the available temperature range is decreased and the higher mass flow rates shorten the maximal parallel cooled BSU length. The diagram illustrated in figure 5.7 shows the same results, but for the relative pressure drop $\Delta p/p_0$.

The diagram in figure 5.8 shows the results for the particular heat load expected on the FCC beam screen and the parallel cooled BSU length expressed as the number of magnets cooled in series for different pressure levels. In each case the velocity limit is the limiting constraint. However, even with small supply pressures, it is feasible to cool parallel cooled BSUs with a length corresponding to a lattice half-cell.

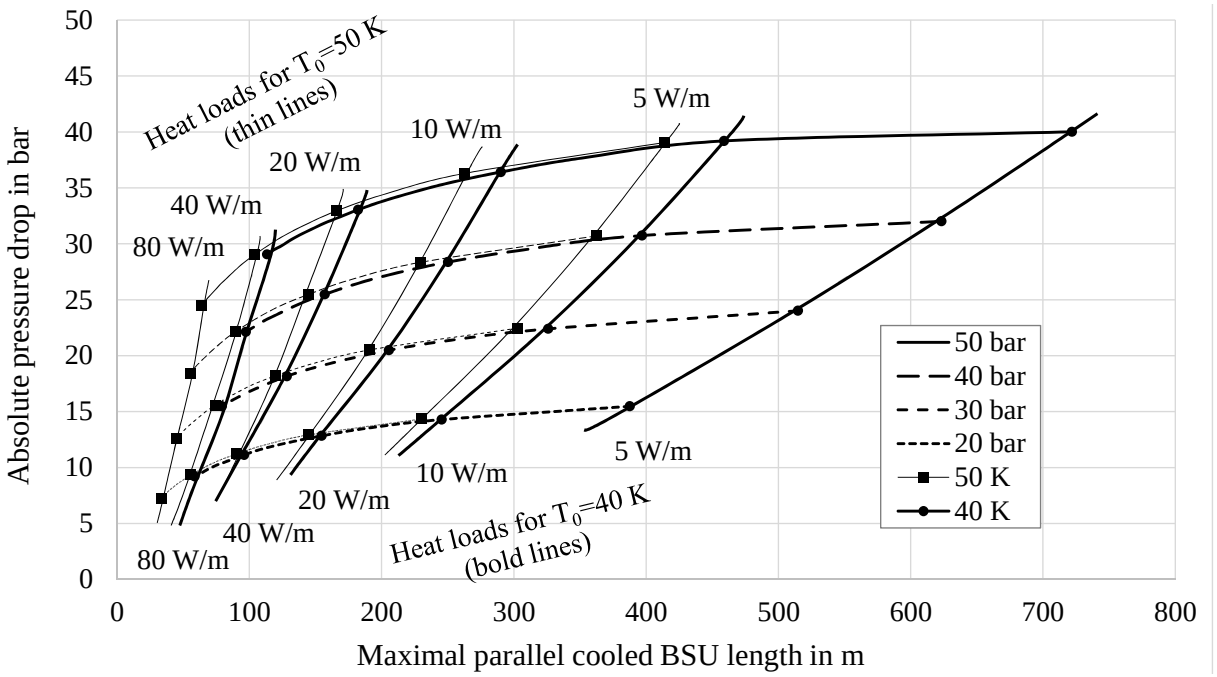

Figure 5.6: Correlation between the maximal parallel cooled BSU length and the absolute pressure drop for different heat loads per beam screen, different inlet temperatures T_0 (line thickness) and different inlet pressures p_0 (line shape).

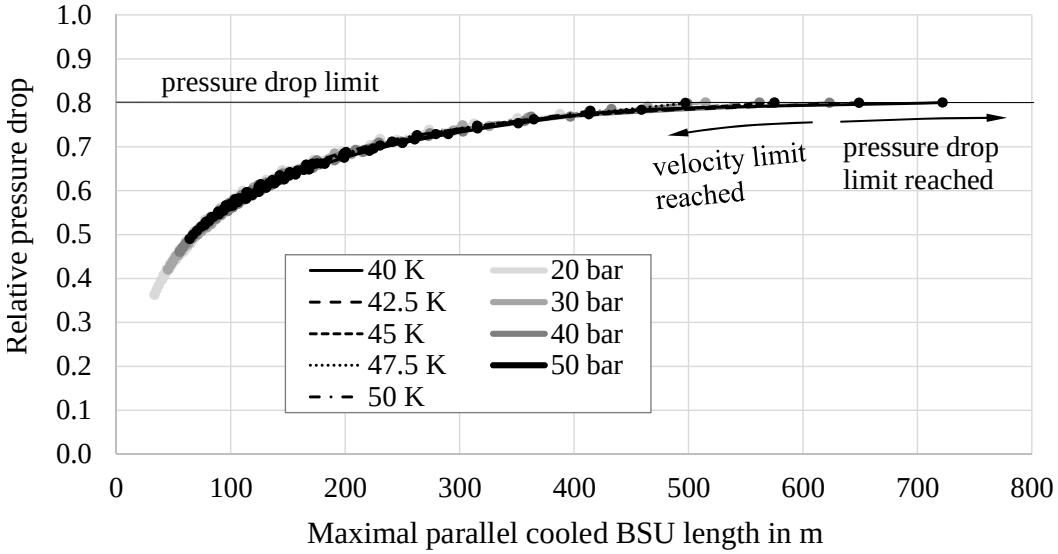

Figure 5.7: Correlation between the maximal parallel cooled BSU length and the relative pressure drop $\Delta p/p_0$ for different heat loads per beam screen, different inlet temperatures T_0 (line shape) and different inlet pressures p_0 (line color).

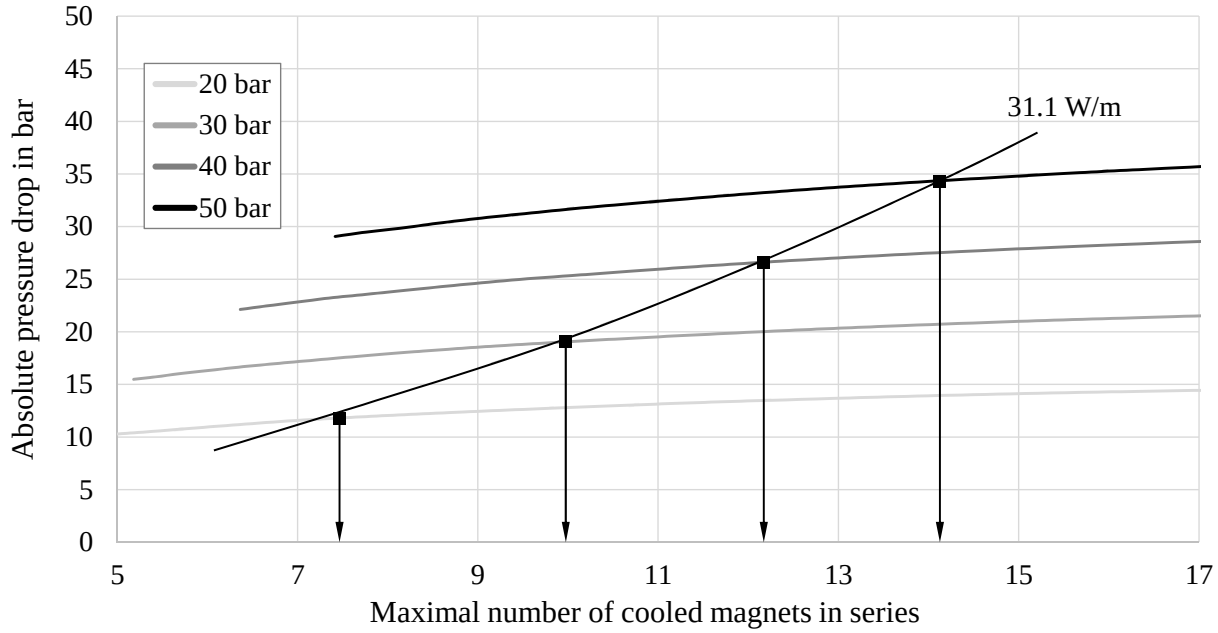

Figure 5.8: Correlation between the maximal number of magnets per parallel cooled BSU and the absolute pressure drop for the expected heat load per FCC beam screen (synchrotron radiation and image current) and different inlet pressures p_0 (line shape).

5.3.3 Choice of the parallel cooled BSU length

The choice of the parallel cooled BSU length is influenced by two opposing arguments one tends to short, the other tends to long parallel cooled BSUs.

1. The pressure drop generated in the cooling channels is proportional to number of magnets in a parallel cooled BSU n_{Mag} to the third power. Short parallel cooled BSUs can be cooled more efficiently, which leads to lower operational costs.

$$\Delta p \propto n_{Mag}^3 \tag{5.29}$$

2. The more magnets are combined to a parallel cooled BSU, the less gauges, pipes, valves and any auxiliary equipment for measurements and controlling are needed. To increase the availability of the cryogenic system and decrease capital costs, long parallel cooled BSUs are advantageous.

The goal of the investigation of the beam screen cooling system is to find a good compromise between capital costs, controlling effort and risk of downtime due to component failure (short parallel cooled BSUs) and the operational costs (long parallel cooled BSUs).

5.3.4 Choice of the supply pressure

High supply pressures not only increase the possible parallel cooled BSU length, but also come with higher efficiencies. First of all, the higher density decreases the volumetric flow and hence reduces the pressure drop. Secondly, the compression ratios are lower, if the pressure level is

higher. Smaller compressors are necessary and they operate with higher efficiency and reliability. The supply pressure therefore was chosen to be as high as reasonable (50 bar), the upper limit was the strength of the cooling channels [94].

5.4 Sector distribution and discharge system

The actual segmentation of the FCC cryogenic system foresees ten sectors with lengths up to 10.4 km (with 8.4 km of arc), which have to be cooled continuously and the supplying cryoplant located at one end. In this arrangement, part of the cryogen has to be circulated over close to 17 km. When bent, each beam emits synchrotron radiation of a specific heat load of 28.4 W/m and generates resistive heating (due to the image current) of 2.7 W/m. The beam screen cooling system has to extract an overall beam induced heating power of 62.2 W/m.

The operating temperature of the beam screen cooling also is suitable for the thermal shielding application. Therefore the two cooling tasks are combined. Heat leaks from the ambiance of about 9.3 W/m are expected, whereas 5.3 W/m enter the system by passing the vacuum jacket, which contains the cold mass. 4 W/m will enter the cryogenic distribution line (QRL). The overall specific heat load on the beam bending sections (arcs) will reach up to 71.5 W/m in nominal operation. A schematic of the sector design is illustrated in figure 5.9.

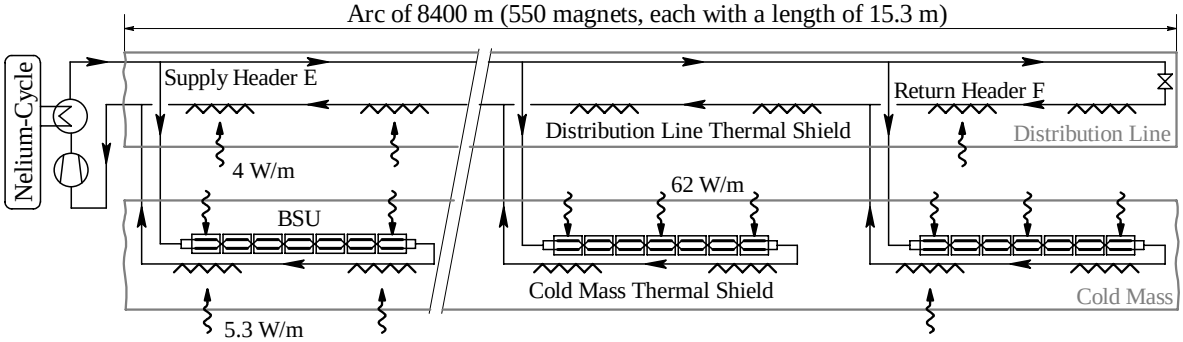

Figure 5.9: Heat loads on an FCC long sector's beam screen cooling system.

The beam screen cooling loop is designed with an integrated circulator (see the "Integrated Circulator" design in figure 3.10 on the right side). The heat is extracted by a refrigerator operated with a helium-neon blend (Nelium).

Table 5.3: Beam screen cooling: Sector distribution and discharge system

Input Value	**Symbol**	**Value**	**Unit**
Circulator outlet pressure	p_0	50	bar
Heat exchanger outlet temperature	T_{out}	40	K
Headers (and manifold) absolute roughness	ϵ_H	15	μm
Thermal shielding pipe diameter (Cold Mass)	d_{TS}	50	mm
Thermal shielding pipe absolute roughness (Cold Mass)	ϵ_{TS}	7.5	μm
Heat load on cold mass thermal shield	$\dot{q}_{TS\,CM}$	5.3	W/m
Heat load on distribution line thermal shield	$\dot{q}_{TS\,QRL}$	4	W/m

5.4.1 Uncontrolled parallel cooled BSU mass flow rates

Figure 5.9 shows the basic flow scheme. The cryogen flows in the supply header and in the return header point in opposed directions in the further descriptions it shall be called counter flow (scheme). On the other hand, the discharged helium flows could be collected in a return header with the same flow direction as the supply header. This flow scheme could be advantageous, if no control valves can or should be used. The flow scheme illustrated in figure 5.10 shall be referred to as parallel flow (scheme).

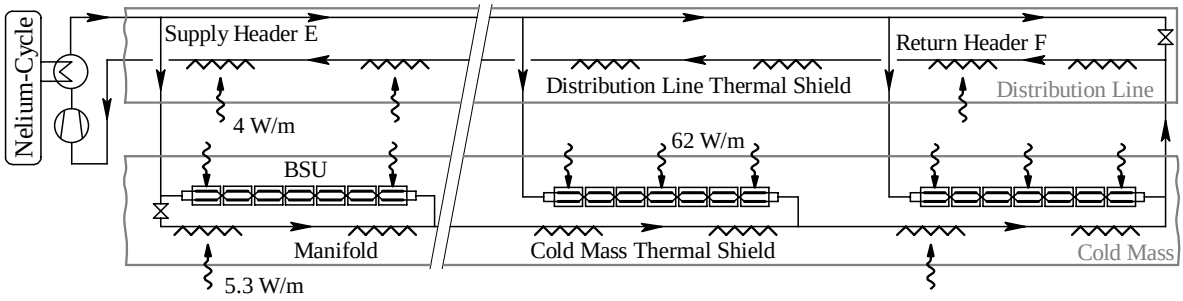

Figure 5.10: Schematic of a sector design with parallel flow direction in supply and return header.

Due to the positions of the cryoplants with respect to the FCC, the warmed-up cryogen collected at the arc's end would have to be conveyed back to the cryoplant in an additional header at cryogenic temperature level. To avoid an intolerable increase of the cryogenic distribution line's diameter, the manifold collecting the helium after leaving the beam screen could be integrated into the cold mass vacuum jacket and used to thermally shield the cold mass. The return header F extracts the heat load on the cryogenic distribution line.

By sparing the control valves, not only the capital costs can be decreased, but also the probability of shut-downs due to component failure. The mass flow rates passing the parallel cooled parallel cooled BSUs set in accordance to the pressure drops. In the following, some simplifications are assumed to derive the basic correlations (5.34) and (5.37) as presented in Appendix G:

- All the headers and the manifold are of the same diameter
- Highly turbulent flow in all ducts (constant Darcy friction factors)
- Small pressure drops compared to the absolute pressure in the return header and manifold

The last assumption is a necessary condition to keep the circulation power P_{Circ} low.

$$P_{Circ} \propto \dot{m}_{tot}\, \Delta p_{Circ} \tag{5.30}$$

where $\dot{m}_{tot}$ denotes the total mass flow rate and Δp_{Circ} denotes the pressure increase in the circulator.

5.4.1.1 Counter flow scheme

The mass flow rates in the supply header and the return header are equal between two parallel cooled BSUs. According to figure 5.11, the pressure drop in parallel cooled BSU i equals the sum of the pressure drops of the supply header, the parallel cooled BSU $i+1$ and the return header. To fulfil (5.31), the mass flow rate in the parallel cooled BSU i must be larger than in the parallel cooled BSU $i+1$. An additional mass flow rate has to pass through parallel cooled BSU i to compensate for the pressure drops in the headers.

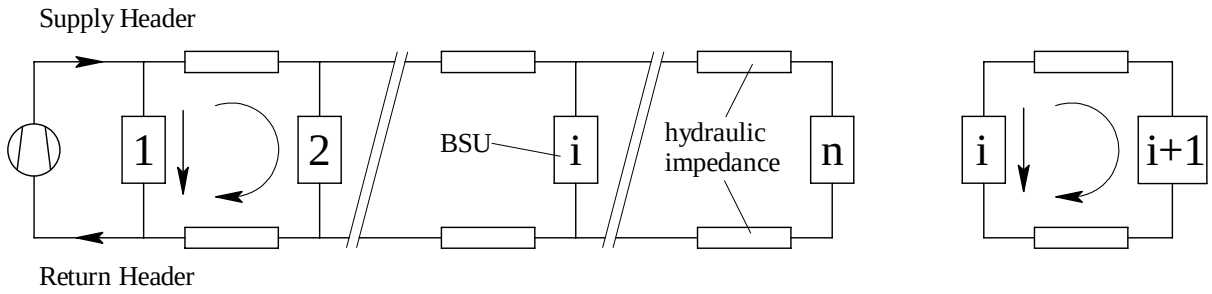

Figure 5.11: Hydraulic circuit diagram of the counter flow scheme for the sector and one cell.

$$\Delta p_i \left(\dot{m}_i^2\right) = \Delta p_{SH\,i} \left[\left(\dot{m}_{tot} - \sum_{j=1}^{i} \dot{m}_j\right)^2\right] + \Delta p_{i+1} \left(\dot{m}_{i+1}^2\right) + \Delta p_{RH\,i} \left[\left(\dot{m}_{tot} - \sum_{j=1}^{i} \dot{m}_j\right)^2\right] \tag{5.31}$$

$$\dot{m}_i > \dot{m}_{i+1} \tag{5.32}$$

By rearranging, simplifying and substituting as illustrated in Appendix G, (5.31) can be transformed into (5.34), where $\hat{Z}$ represent the hydraulic impedances per meter of length and kg/s of mass flow rate of the supply header (subscript SH), the return header (subscript RH) and the four parallel cooling channels (subscript BSU).

$$\frac{f_{SH}}{d_{SH}\, A_{SH}^2} \approx \frac{f_{RH}}{d_{RH}\, A_{RH}^2} = \hat{Z}_H \tag{5.33}$$

$$\frac{\hat{Z}_H}{\hat{Z}_{BSU}} \frac{\dot{m}_{H\,i}^2}{\dot{m}_{BSU\,i+1}} \approx \Delta\dot{m}_{BSU\,i} \tag{5.34}$$

where $\dot{m}_{H\,i}$ denotes the mass flow rate in the headers at the position i and $\dot{m}_{BSU\,i+1}$ denotes the mass flow rate in the parallel cooled BSU at the position $i+1$. Large additional mass flow rates $\Delta\dot{m}_{BSU\,i}$ for pressure compensation increase the total mass flow rate, which is a self-amplifying effect, since it is in the numerator of (5.34). Large header mass flow rates also cause a high pressure drop, therefore the compensation mass flow rates should be kept small. There are three options to achieve that goal:

- A low hydraulic impedance of the headers ($\hat{Z}_H$), which is limited by the available space in the cryogenic distribution line.
- A high hydraulic impedance of the cooling channels ($\hat{Z}_{BSU}$), which would result in an undesirable reduction of the cooling channels' size with respect to the cryogenics application.
- Long parallel cooled BSUs and subsequently not only low compensation mass flow rates, but also fewer of them, since there are less parallel parallel cooled BSUs to cool.

The pressure increase done in the circulator can be distributed to the pressure drops in the supply and in the return header and a "basic" pressure drop Δp_0 in the last parallel cooled BSU. In the counter flow scheme it corresponds to the smallest pressure difference Δp_{min} between the headers.

$$\Delta p_{Circ} = \Delta p_{SH} + \Delta p_0 + \Delta p_{RH} \tag{5.35}$$

- Short parallel cooled BSUs cause high compensation mass flows and, subsequently, high pressure losses in the headers.
- Long parallel cooled BSUs cause a high basic pressure drop in the last parallel cooled BSU, but the total mass flow reduces close to its technical minimum.
- The choice of a medium parallel cooled BSU length results in a minimal circulation power.

A numerical simulation with variable helium properties was performed to investigate the counter flow scheme without control valves. The figure 5.12 shows the pressure evolution in the supply header (bold lines) and the return header (thin lines) for three different lengths of parallel cooled BSUs and a header diameter of 0.25 m for the counter flow scheme without control valves. The high compensation mass flow rates increase the compression ratio for short parallel cooled BSUs due to the pressure drop in the headers (solid lines). With increasing hydraulic impedance (longer parallel cooled BSUs), the total pressure drop can be decreased (dashed lines). For even longer parallel cooled BSUs, the basic pressure drop in the last parallel cooled BSU Δp_0 causes higher compression ratios (dash-dotted lines).

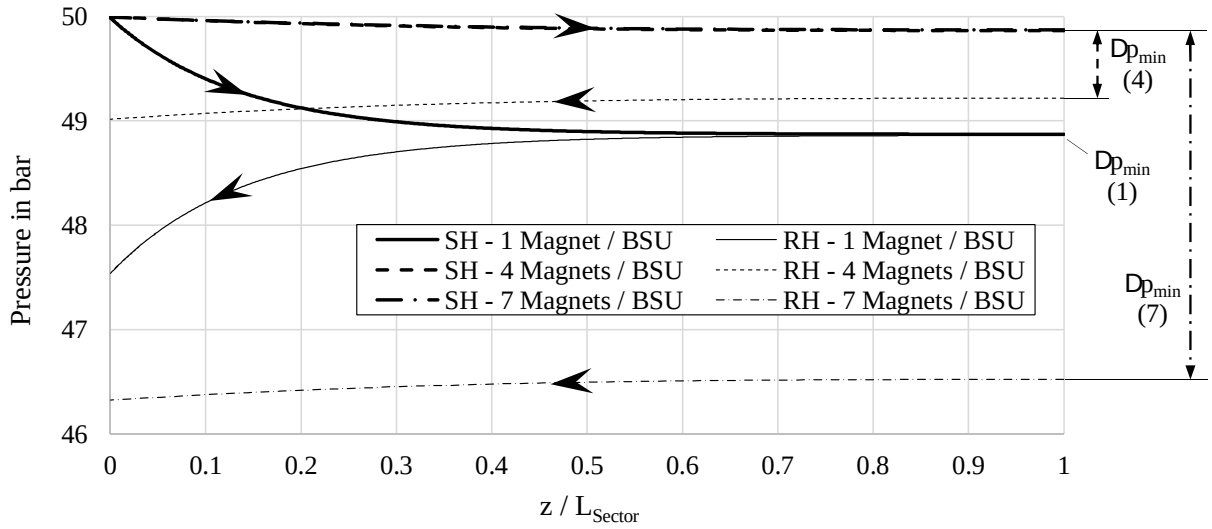

Figure 5.12: Pressure evolution in the supply header (bold lines) and the return header (thin lines) vs. the axial coordinate z/L_{Sector} for parallel cooled BSUs containing one (solid lines), four (dashed lines) and seven (dash-dotted lines) magnets in series and a header diameter of 0.25 m.

The figure 5.13 shows the mass flow rate evolution in the headers for three different lengths of parallel cooled BSUs and a header diameter of 0.25 m for the counter flow scheme without control valves. The mass flow rates in the supply and the return header are identical in the counterflow scheme. The mass flow rate increases exponentially towards the circulator for short parallel cooled BSUs (solid line), due to the compensation mass flow rates needed. For longer parallel cooled BSUs (dashed and dash-dotted lines), the mass flow rate increases almost linearly and the total mass flow rate is close to the theoretical minimum.

In figure 5.13 also the calculated circulation powers are displayed. A medium parallel cooled BSU length minimizes the circulation power.

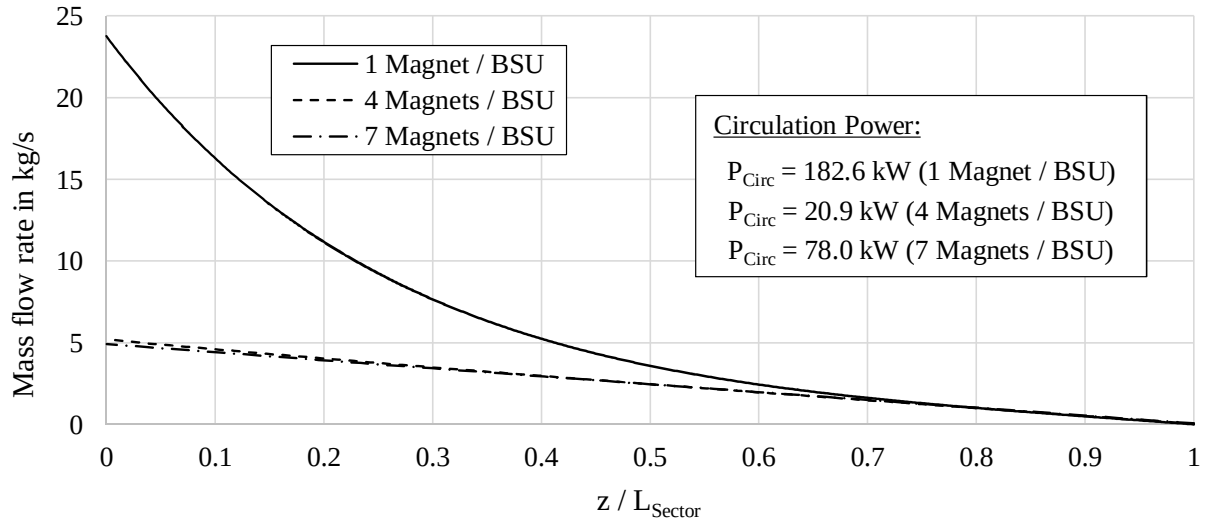

Figure 5.13: Mass flow rate evolution in the headers vs. the axial coordinate z/L_{Sector} for parallel cooled BSUs containing one (solid lines), four (dashed lines) and seven (dash-dotted lines) magnets in series and a header diameter of 0.25 m.

5.4.1.2 Parallel flow scheme

All the mass flows cooling the beam screen leave the supply header and enter the manifold at the same parallel cooled BSU. According to figure 5.14 the pressure drop in parallel cooled BSU i plus the pressure drop in the manifold must be equal to the sum of the pressure drops of the supply header and the parallel cooled BSU $i+1$. Contrarily to the counter flow scheme, (5.36) theoretically allows the pressure drop compensation without additional mass flow rates (if for example the diameter of the headers vary accordingly).

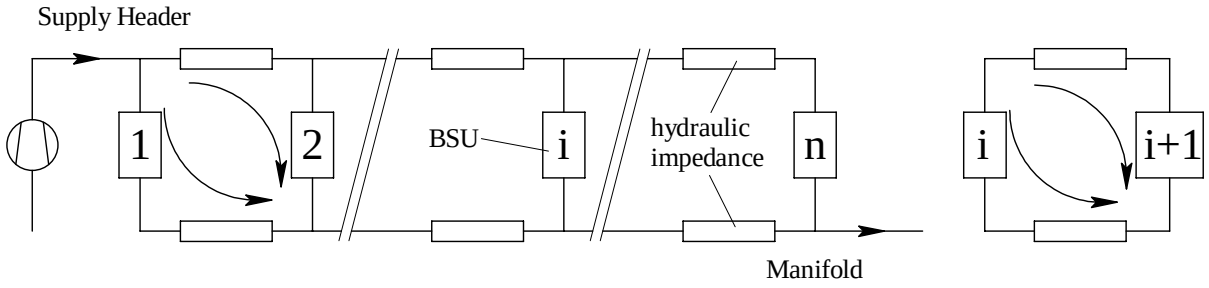

Figure 5.14: Hydraulic circuit diagram of the parallel flow scheme for the sector and one cell.

$$\Delta p_i\left(\dot{m}_i^2\right) + \Delta p_{SH\,i}\left[\left(\sum_{j=1}^{i}\dot{m}_j\right)^2\right] = \Delta p_{i+1}\left(\dot{m}_{i+1}^2\right) + \Delta p_{MF\,i}\left[\left(\dot{m}_{tot} - \sum_{j=1}^{i}\dot{m}_j\right)^2\right] \tag{5.36}$$

By rearranging, simplifying and substituting as illustrated in Appendix G, (5.36) can be transformed into (5.37), where $\Delta\dot{m}_{BSU\,i+1}$ denotes the additional mass flow rate in the adjacent parallel cooled BSU to compensate the pressure drops in the headers.

$$\frac{\hat{Z}_H}{\hat{Z}_{BSU}} \frac{\dot{m}_{tot}\,(\dot{m}_{MF\,i} - \dot{m}_{SH\,i})}{2\,\dot{m}_{BSU\,i}} \approx \Delta\dot{m}_{BSU\,i+1} \tag{5.37}$$

Similarly to the counter flow scheme, the total mass flow rate can be kept low by increasing the ratio of the hydraulic impedances. Since the total mass flow rate is in the numerator of (5.37), the self-amplification is stronger, causing very high compensation mass flow rates.

A numerical simulation with variable helium properties was performed to investigate the parallel flow scheme without control valves. The diagram in figure 5.15 shows the pressure evolution in the supply header (black), the manifold (dark grey) and the return header (light grey) for two different lengths of parallel cooled BSUs and a header diameter of 0.25 m for the parallel flow scheme without control valves. Ignoring the pressure drop generated in the return header F, the compression ratio of the parallel flow scheme is lower compared to the counter flow scheme for parallel cooled BSUs containing four (dashed lines) and seven magnets (dash-dotted lines).

The minimal pressure difference Δp_{min} between the headers occurs in the middle of the arc. The maximal pressure loss in the supply header and the manifold is generated at different ends of the arc. Therefore, in case the compensation mass flow rates are kept small, the parallel flow scheme performs slightly better than the counter flow scheme. However, the additional pressure drop in the return header F annihilates the advantages of the parallel flow scheme.

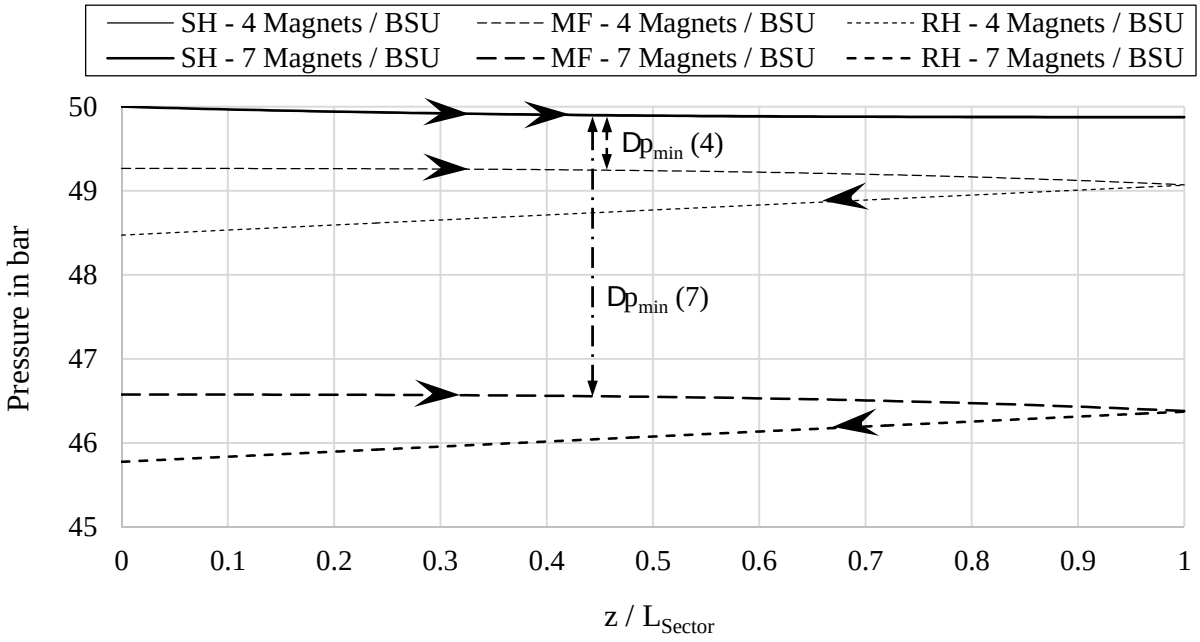

Figure 5.15: Pressure evolution in the supply header (solid lines), the manifold (long dashed lines) and the return header (short dashed lines) vs. the axial coordinate z/L_{Sector} for parallel cooled BSUs containing four (thin lines) and seven (bold lines) magnets in series and a header diameter of 0.25 m.

The diagram in figure 5.16 shows the pressure evolution in the supply header (solid line) and the manifold (dashed line) a parallel cooled BSU length corresponding to a magnet length and a header diameter of 0.25 m for the parallel flow scheme without control valves. The low hydraulic impedance causes large mass flow rates and accordingly high pressure losses. The calculation for this scenario was truncated, when the pressure in the manifold undercut the ambient pressure.

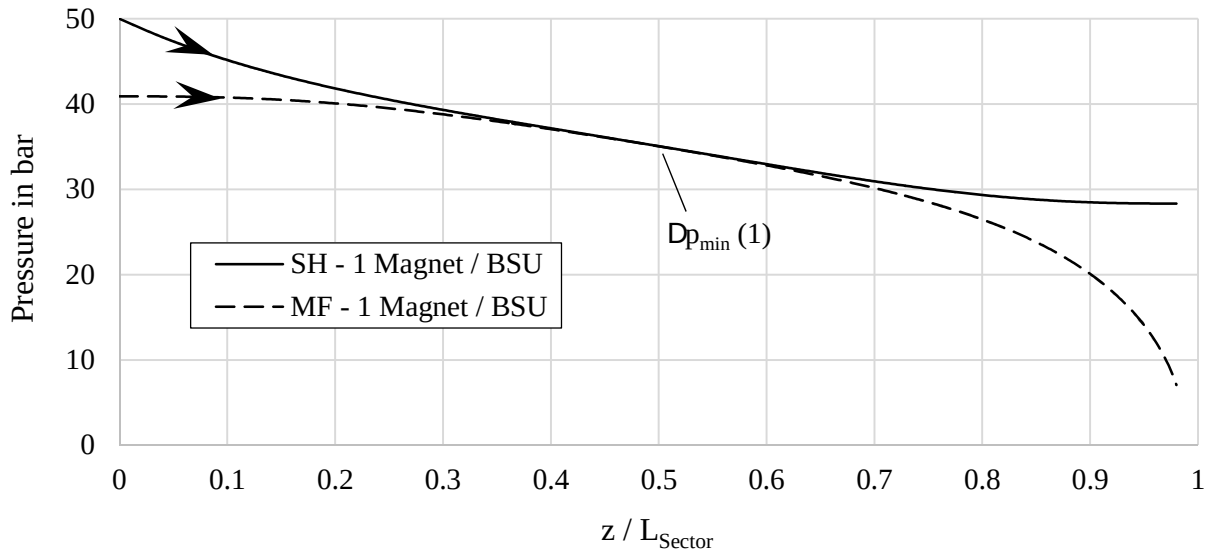

Figure 5.16: Pressure evolution in the supply header (solid line) and the manifold (dashed lines) vs. the axial coordinate z/L_{Sector} for parallel cooled BSUs containing one (solid lines) magnet and a header diameter of 0.25 m. Due to the large compensation mass flow rates the pressure in the manifold falls below atmospheric and the calculation was stopped.

The diagram in figure 5.17 shows the mass flow rate evolution in the supply header (solid lines) an the manifold (dashed lines) for two different lengths of parallel cooled BSUs and a header diameter of 0.25 m for the parallel flow scheme without control valves. The mass flow rates are mirror-inverted, since the helium exiting the the supply header is collected in the manifold. The almost linear evolution of the curves insinuates, that the total mass flow rate is close to its theoretical minimum.

The diagram in figure 5.18 shows the mass flow rate evolution in the supply header (solid line) an the manifold (dashed line) for a parallel cooled BSU length corresponding to a magnet length and a header diameter of 0.25 m for the parallel flow scheme without control valves. Due to the large necessary compensation mass flow rates, the total mass flow rate increases strongly towards the arc's ends.

In figure 5.17 also the calculated circulation powers are displayed. Due to the pressure drop in the additional return header, the exergetic performance of the parallel flow scheme is lower than the one of the counter flow scheme, even for long parallel cooled BSUs.

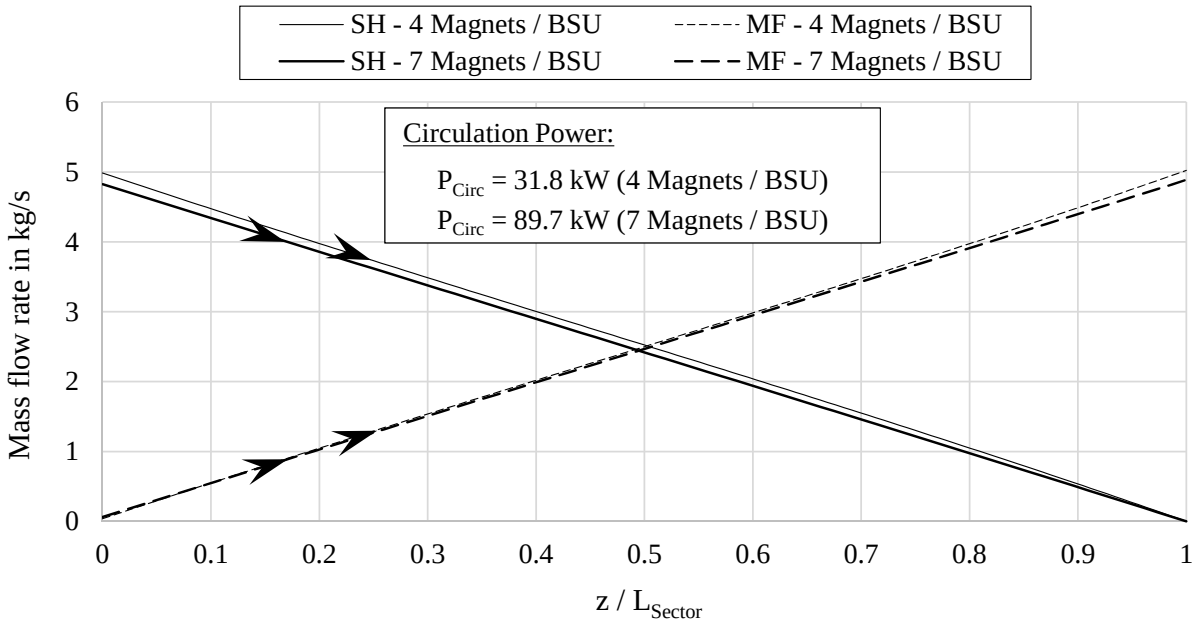

Figure 5.17: Mass flow rate evolution in the supply header (solid lines) and the manifold (dashed lines) vs. the axial coordinate z/L_{Sector} for parallel cooled BSUs containing four (thin lines) and seven (bold lines) magnets in series and a header diameter of 0.25 m.

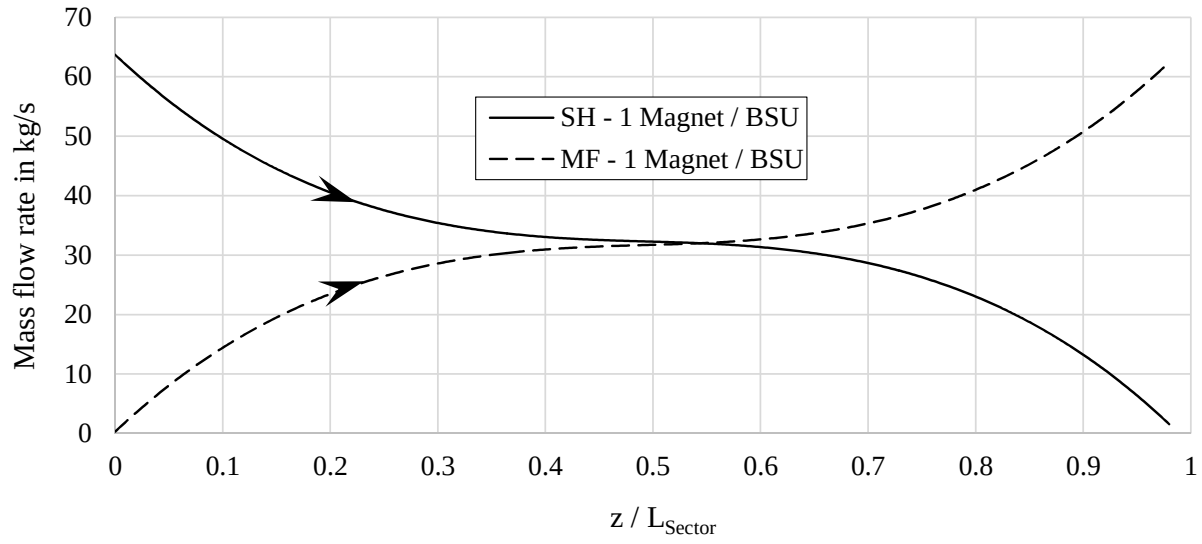

Figure 5.18: Mass flow rate evolution in the supply header (solid lines) and the manifold (dashed lines) vs. the axial coordinate z/L_{Sector} for parallel cooled BSUs containing one magnets in series and a header diameter of 0.25 m. Due to the large compensation mass flow rates the pressure in the manifold falls below atmospheric and the calculation was truncated.

5.4.2 Actively controlled parallel cooled BSU mass flow rates

Several advantages call for the installation of valves to control the mass flow rates, passing through the single parallel cooled BSUs. Among others:

- The total mass flow rate (and the circulation power) can be minimized, since no increase is necessary to compensate for the pressure drop in the headers. Subsequently, the number of magnets in a parallel cooled BSU is not restricted by a lower limit.
- The mass flow rates cooling the single parallel cooled BSUs can be regulated individually. This option enables the operation of the machine, even when there is an increase of the hydraulic impedance or heat load in one parallel cooled BSU. Without valves all the other parallel cooled BSUs are affected by a variation of the mass flow rate or the pressure drop in one single parallel cooled BSU.

The advantages of control valves outweigh the disadvantages, therefore it was decided to use them, but to reduce the number. Using valves, the parallel flow does not entail any advantages and therefore, the beam screen cooling system is operated in counter flow.

5.4.2.1 Control strategy

The decision to install valves prompts questions regarding the control strategy. High-frequent immediate reactions of the beam screen cooling system on fast variations of control variables are difficult to handle, due to the mere size of a sector. Assuming an approximate sound velocity of 400 m/s, the pressure information of a changed circulator status takes almost 30 seconds to reach the last parallel cooled BSU. A robust control strategy has to be chosen, allowing the circulators to operate in (almost) the same working point regardless of the FCC operational mode. The baseline now foresees to keep the supplied mass flow rate constant, independent of the operational mode [97]. The single parallel helium flows passing the parallel cooled BSUs are measured (e.g. by Coriolis mass flow meters) and regulated by the control valves. Measurements of temperature and pressure are of observing character and influence the machine status only, if determined limits are exceeded.

By installing valves, the pressure losses in a parallel cooled BSU consists of two parts: One part generated by the hydraulic impedance of the cooling channels and the second part generated by the control valve. For the pressure drop generated in the valves to control the mass flow rates, it was assumed to need 20 % of the pressure drop created in the parallel cooled BSU, but at least one bar [95].

5.4.2.2 Positioning of the valves

The Joule-Thomson coefficient in the considered state of helium is negative, with a valve close to zero.

$$\left(\frac{\partial T}{\partial p}\right)_{h=const.} < 0 \tag{5.38}$$

Since the isenthalpic expansion cannot be used to decrease the helium temperature, the positioning of the control valves at the parallel cooled BSU outlets decreases the pressure losses for two reasons. First of all, the density of the helium flow is higher and secondly, in the considered temperature range, the heat capacity of helium increases with increasing pressure. Both effects decrease the flow velocity, reducing the pressure losses and the risk to reach the sound velocity limit.

One reason to install the valves at the parallel cooled BSU inlets, compared to their installation at the BSU outlets, is the possible use of smaller valves and the lower flow velocities in the valves themselves, reducing capital costs and the error-proneness of the auxiliary equipment. However, it was decided to install the control valves at the parallel cooled BSU outlets.

5.4.3 Thermal shielding

The intermediate temperatures of the beam screen cooling system can also be used to cool the cryostat thermal shield. It is only necessary in machine sections at cryogenic temperature level, i.e. in the beam bending sections (arcs). The pressure losses due to branching and unifying the helium flows in the supply and the return header were neglected. The Darcy friction factor f was obtained by the explicit formula of Swamee-Jain [83]. Table 5.4 contains input data to calculate the exergetic efficiency in the headers. The heat loads on the beam screen and on the thermal shields can be found in tables 5.2 and 5.3.

Table 5.4: Beam screen cooling: Ambient state

Input Value	**Symbol**	**Value**	**Unit**
Ambient temperature	T_a	300	K
Ambient pressure	p_a	1.013	bar

5.4.3.1 Supply Header/Return Header Shielding

To keep the cryogenic distribution line small, the supply header and the return header of the beam screen cooling loop are used for the thermal shielding, as illustrated in figure 5.19.

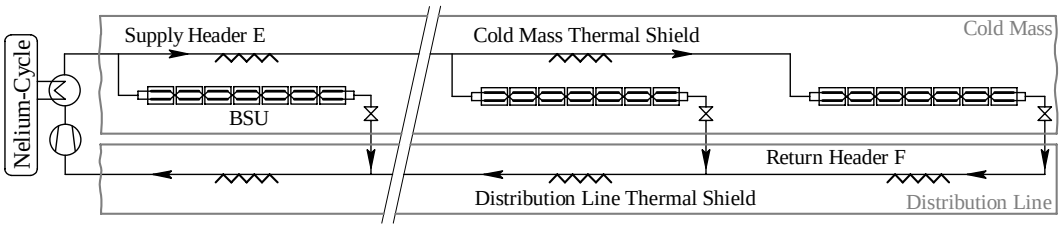

Figure 5.19: Schematic of the beam screen cooling system with Supply Header/Return Header Shielding.

The supply header is led on the inside of the magnet vacuum jacket and shields the cold mass. The return header thermally shields the cryogenic distribution line. In this arrangement, the helium temperature in the supply header increases on its way to the last parallel cooled BSU. Especially close to the arc's end, when the mass flow rate in the header is small, the temperature rises even more. The increased temperature at the parallel cooled BSU inlets calls for higher parallel cooled BSU mass flow rates to extract the heat within the available temperature range. Higher pressure drops in the parallel cooled BSUs occur and the highest one in the last parallel cooled BSU. Due to the pressure evolution in the headers, the pressure difference at the arc's end dictates the minimal pressure difference between the headers (see figure 5.12). The valves of all the previous parallel cooled BSUs therefore must generate an additional pressure drop to compensate for the (increasing) pressure difference in the headers towards the circulator.

The diagram in figure 5.20 shows the overall pressure drop ($\widehat{=}\Delta p_{Circ}$) and the exergetic efficiency of the beam screen cooling cycle with SH/RH-Shielding-concept without taking into account the cryoplant losses.

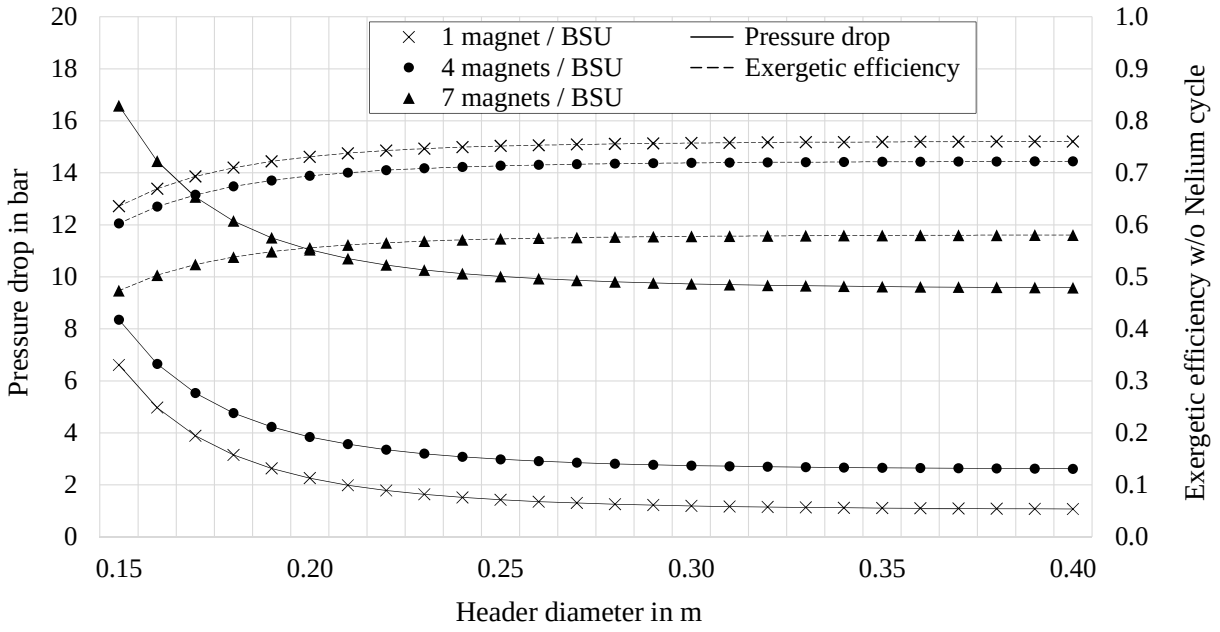

Figure 5.20: Pressure drop (solid lines) and exergetic efficiency (dashed lines) of the beam screen cooling cycle without the cryoplant efficiency (corresponding to System I of the "Integrated Circulator" design in figure 3.10) with SH/RH Shielding vs. the header diameter for 3 different parallel cooled BSU lengths.

5.4.3.1.1 Supply Header/Return Header Shielding with bypass

To lower the additionally generated pressure drop in the single control valves, the helium inlet temperature at the last parallel cooled BSU has to be decreased. By installing a bypass to connect supply and return header at the end of the distribution line (as indicated in figure 5.21), additional helium is circulated to reduce the parallel cooled BSU inlet temperature. The larger available temperature range decreases the necessary mass flow rate in the last parallel cooled BSUs and therefore the pressure drop. The reduction of the pressure loss in the parallel cooled BSUs of course is accompanied by an increase of the total mass flow rate and higher pressure losses in the headers.

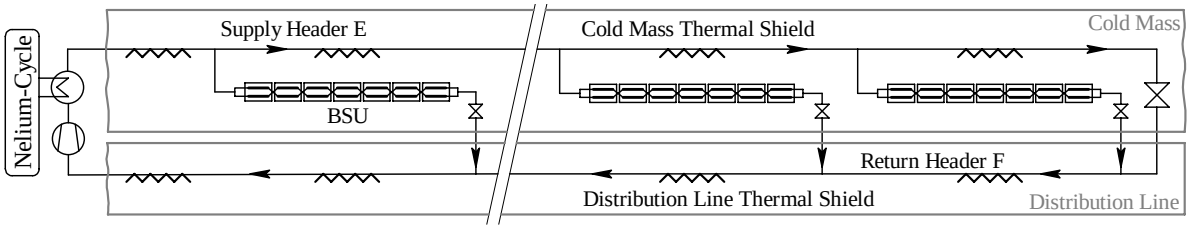

Figure 5.21: Schematic of the beam screen cooling system with Supply Header/Return Header-Shielding with bypass.

A bypass connecting the supply header and the return header at the arc's end will be installed anyway for the cool-down and warm-up of the FCC. The bypassed mass flow rate needed to maximize the efficiency depends on the header diameter and parallel cooled BSU length. The diagram in figure 5.22 shows the necessary bypass mass flow rate at nominal operation to achieve maximal

exergetic efficiencies for different header diameters and parallel cooled BSU lengths. By comparing the exergetic efficiencies depicted in the diagrams in the figures 5.20 and 5.22, the increasing advantage of the use of the bypass for longer parallel cooled BSUs and smaller header diameters can be seen.

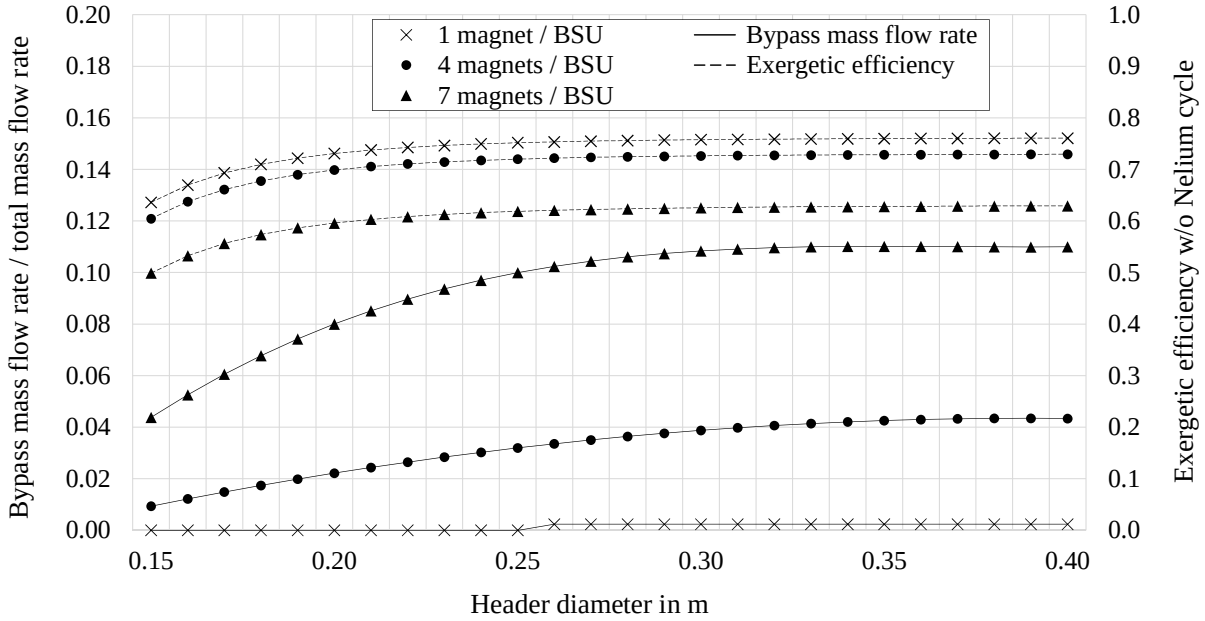

Figure 5.22: Optimized bypass mass flow fraction (solid line) and exergetic efficiency (dashed line) of the beam screen cooling cycle without the cryoplant efficiency (corresponding to System I of the "Integrated Circulator" design in figure 3.10) vs. header diameter for 3 different parallel cooled BSU lengths.

5.4.3.2 Separate Shielding

To minimize the mass flow rates in the parallel cooled BSUs, the inlet temperature must be as low as possible. If the supply header is led well-insulated in the cryogenic distribution line, the temperature of the helium could be kept almost constant at 40 K over the entire arc's length. In this case, all the parallel cooled BSUs can be cooled with the same (minimal) mass flow rates, hence the total mass flow rate is minimized and consequently the pressure drop. In this concept, additional pipes have to be installed to thermally shield the cold mass. After cooling the beam screen, the helium is conveyed in a thermal shielding pipe for the distance corresponding to the length of a parallel cooled BSU. The helium then is collected in the return header, which shields the distribution line like in the previous schemes. The Separate Shielding-scheme is schematically illustrated in figure 5.23.

The diagram in figure 5.24 shows the overall pressure drop ($\widehat{=}\Delta p_{Circ}$) and the exergetic efficiency of the beam screen cooling cycle for the Separate Shielding-concept without taking into account the cryoplant losses.

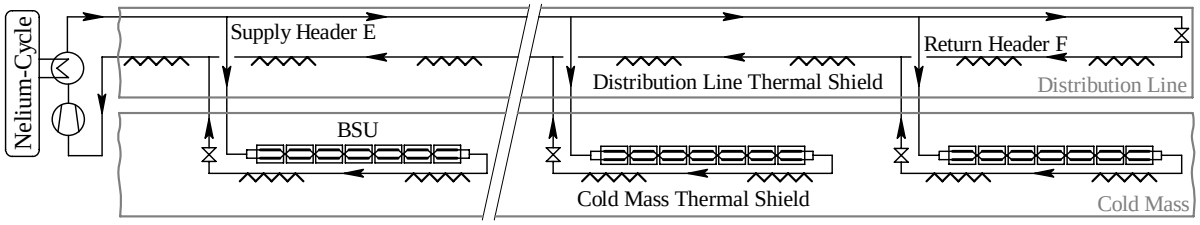

Figure 5.23: Schematic of the beam screen cooling system with partly separated thermal shield.

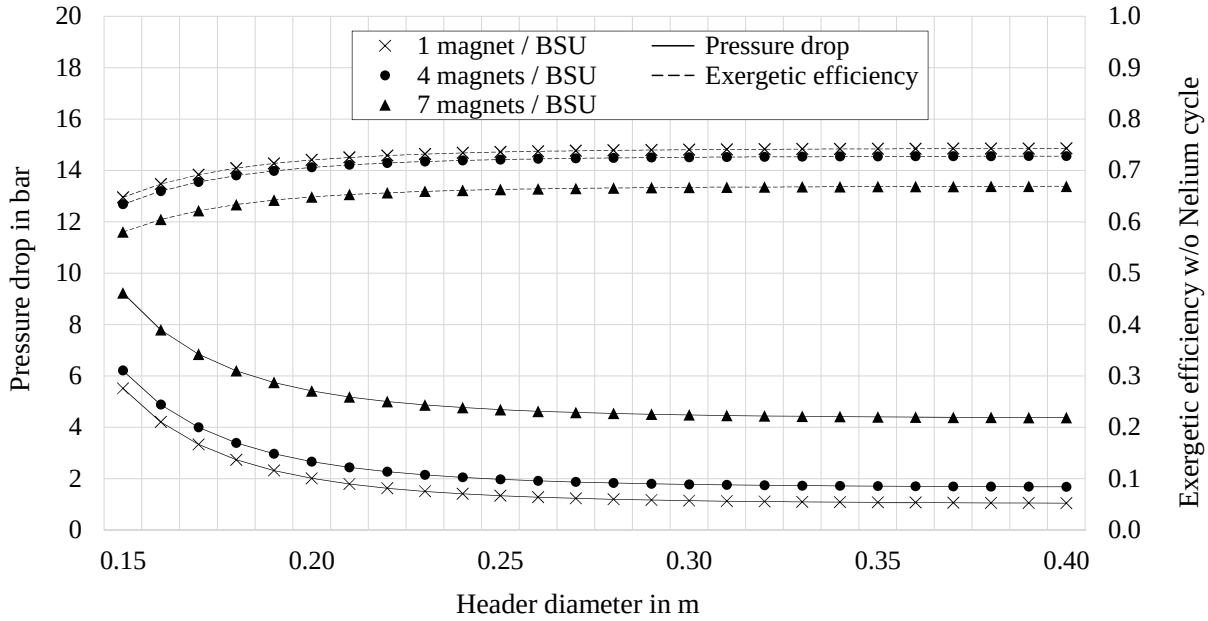

Figure 5.24: Pressure drop (solid lines) and exergetic efficiency (dashed lines) of the beam screen cooling cycle without the cryoplant efficiency (corresponding to System I of the "Integrated Circulator" design in figure 3.10) with Separate Shielding vs. header diameter for 3 different parallel cooled BSU lengths

5.4.4 Choice of beam screen cooling cycle concept

The pressure loss generated in the beam screen cooling cycle is the decisive influence quantity for the power consumption. Since the sector dimensions, the beam screen design and the heat loads are determined, the main parameters to reduce the pressure drop are header diameter, the number of magnets per parallel cooled BSU and the thermal shielding concept.

With increasing header diameter, the pressure drop approaches asymptotically the "basic" pressure drop Δp_0 in the last parallel cooled BSU. A diameter of about 0.25 m seems to be a good choice to keep the capital costs and space requirements at a reasonable magnitude as well as to achieve a good exergetic performance. Additionally the headers will be used also for cool-down and warm-up purposes, which also requires diameters of this size to keep the necessary cool-down and warm-up times reasonable [45].

The highest exergetic efficiencies can be achieved by cooling each magnet in parallel. But parallel cooled BSUs containing several magnets in series are necessary to reduce the number of control valves. Other applications and cryogenic infrastructure already are supposed to follow the pattern

of lattice half-cells of a length corresponding to seven magnets in series ($\widehat{=}$ 107 m). Adjusting the beam screen cooling cycle units to this pattern simplifies the assembly, the maintenance and the organisation, paying for these conveniences with increased operational costs. With increasing parallel cooled BSU length, the Separate Shielding concept is the most economical and the installation of additional thermal shielding pipes is easily compensated by the improved exergetic performance.

The diagrams shown in figure 5.25 compare the evolution of the pressure difference between the supply and the return header for a header diameter of 0.25 m and 7 magnets per parallel cooled BSU for the SH/RH Shielding concept without bypass, for the SH/RH Shielding concept with bypass (bypass mass flow rate 0.57 kg/s corresponds to 10 % of the total mass flow rate) and for the Separate Shielding-concept. The black area represents the pressure drop in the cooling channels of the beam screen, the grey area represents the pressure drop generated to control the mass flow rates and the white area represents the additionally generated pressure drop in the valves to compensate for the pressure difference between the headers.

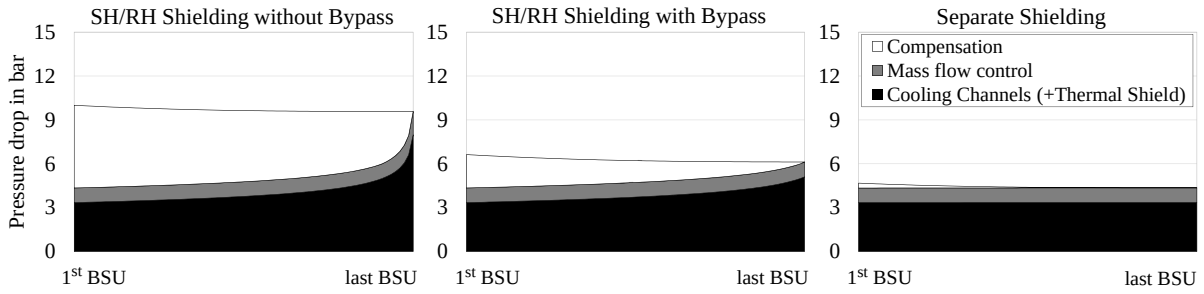

Figure 5.25: Comparison of the pressure difference in supply and return header divided into the pressure losses in the cooling channels (black), the pressure drop to control the single mass flow rates (grey) and the additional pressure drop for the compensation of the pressure difference between the headers (white) vs. the sector length for different thermal shielding concepts.

For the specific case of a parallel cooled BSU length corresponding to a half-cell length, the pressure drop can be halved, if supply header E conveys the helium isothermally. For the Separate Shielding scheme, a parallel cooled BSU length corresponding to a half-cell length and a header diameter of 0.25 m were chosen to be the baseline design.

5.4.4.1 Variable number of magnets per string

To avoid the installation of additional thermal shielding pipes, the assembly of different parallel cooled BSU lengths was discussed. With shorter parallel cooled BSUs at the arc's end and an increasing number of magnets per magnets string towards the circulator, the pressure difference in the headers can be kept low, even if the supply header thermally shields the cold mass. A certain consolidation of the magnets to several parallel cooled BSUs though, only can be optimized for one operational mode of the FCC. Another drawback is the complicated assembly and the different layouts of machine sections. Therefore this option was dropped.

5.4.5 Connection to the Nelium cycle

The heat absorbed in the beam screen cooling cycle will be transferred to a refrigeration cycle using a helium-neon mixture (Nelium) as cryogen, which is under development by Dresden University of Technology [44]. The heat exchanged consists of the heat loads from the synchrotron radiation

$\dot{Q}_{SR}$, the image current $\dot{Q}_{IC}$ and the thermal shield of the cold mass (summarized in the heat load extracted from the beam screen $\dot{Q}_{BS}$), the heat load on the cryogenic distribution line (QRL) thermal shields $\dot{Q}_{TS}$ and the circulation power P_{Circ}.

5.4.5.1 Cold circulation cycle

A simplified flow scheme of the "cold circulation cycle" is illustrated in figure 5.26.

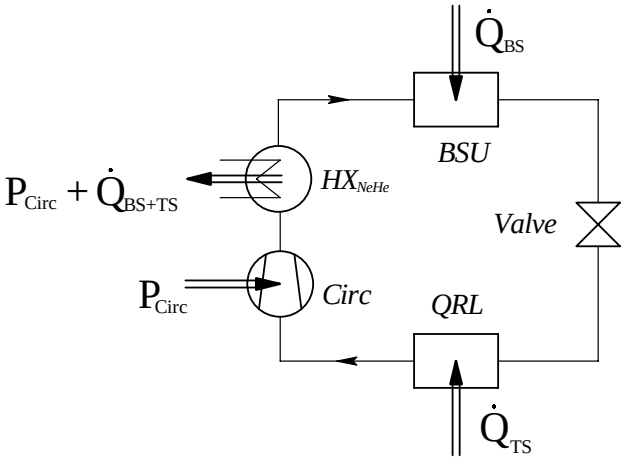

Figure 5.26: Cold circulation cycle of the beam screen cooling system. The extracted heat load $\dot{Q}_{BS+TS}$ and the circulation power P_{Circ} is transferred to the Nelium cycle via the heat exchanger HX_{NeHe}.

The exergy provided by the Nelium cryoplant $\dot{X}_{NeHe}$ to extract the heat can be estimated with (5.39), using the mean helium temperature $\overline{T_{HX}}$ of the heat transfer in the heat exchanger.

$$\dot{X}_{NeHe} = \left(\dot{Q}_{TS} + \dot{Q}_{BS} + P_{Circ}\right)\left(\frac{T_a}{\overline{T_{HX}}} - 1\right) \tag{5.39}$$

5.4.5.1.1 Extensions of the heat sink for the cold circulation cycle

The heat sink positioned downstream of the circulator maximizes the possible temperature range for extracting the heat load, decreases the necessary mass flow rate and releases the heat at higher temperature. A disadvantage of this kind of arrangement could be the varying circulator inlet temperature, e.g. during transient modes. Circulators operating at cryogenic temperature level have small compression fields and need stable inlet conditions to guarantee dependable operation and high efficiencies. The compression field is generated by the compression ratio and the reduced mass flow $\dot{m}_{red}$ [96].

$$\dot{m}_{red} = \dot{m}_{tot}\sqrt{\frac{T}{T_0}}\frac{p_0}{p} \tag{5.40}$$

The subscript 0 in (5.40) refers to the reference conditions at the circulator inlet. Based on the chosen control strategy ($\dot{m}_{tot}$ = const.), the variations of inlet temperature and pressure affect the reduced mass flow.

The second parameter is the pressure ratio upstream and downstream of the circulator. The inlet pressure variations over the bandwidth of operational modes depends on the chosen length of the parallel cooled BSUs. Two possible extensions of the basic refrigeration scheme by supplemental components to stabilize the reduced mass flow have been investigated. A more elaborate design of course is accompanied by increasing capital costs and controlling effort.

- The installation of two heat exchangers downstream and upstream of the circulator allows the use of the maximal sensible temperature range for extracting the heat load and enables the regulation of the circulator inlet temperature (see figure 5.27 on the left side).
- The installation of a bypass requires less expensive components, but decreases the average temperature at which the heat is extracted, which causes an increase of the exergetic effort (see figure 5.27 on the right side).

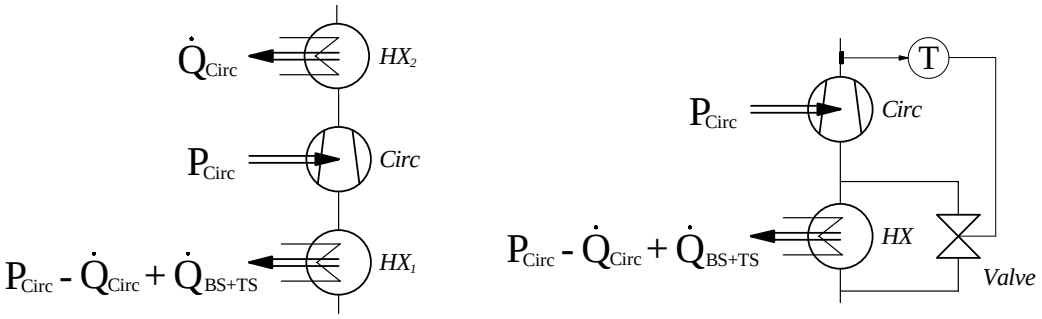

Figure 5.27: Two possible extensions of the heat sink for the cold circulation scheme: Two heat exchangers (left-hand side) and a Bypass (right-hand side).

Calculations of the transient modes of the beam screen cooling system showed that the changes of temperature and pressure compensate each other [97]. Therefore no extensions of the connection with Nelium cycle are considered in the baseline design.

5.4.5.2 Warm circulation cycle

The heat load necessarily is received at cryogenic temperature level. The circulation power though can be introduced (and also extracted) at a higher temperature level, at ambient temperature in best case. The scheme to run the circulator at ambient temperature level shall be called "warm circulation cycle".

After cooling the beam screens and the thermal shields, the helium is warmed up to ambient temperature in an internal heat exchanger (HX_i) and pressurized by the circulator operating at ambient temperature level. The major part of the circulation power P_{Circ} is extracted cheaply in a common water-cooled heat exchanger (HX_a) at ambient temperature. The helium is cooled down, passing through the high-pressure side of the internal heat exchanger and then is conveyed to the heat exchanger connected to the Nelium cycle (HX_{NeHe}) (see figure 5.28).

The internal heat exchanger generates a thermal bypass, dividing the cooling cycle into a cold and a warm section. Due to the driving temperature difference in the internal heat exchanger, a small fraction of the circulation power is transferred to the cold section and has to be extracted at cryogenic temperature level. With a smaller terminal temperature difference of the internal heat exchanger, less heat $\dot{Q}_{TT\Delta}$ slips from the warm into the cold section.

A positive Joule-Thomson coefficient c_{JT} decreases the mean temperature level of the internal heat exchanger. A small fraction $f_{cold \rightarrow warm}$ of the heat load received at cryogenic temperature level can be elevated to the warm section and could be extracted at ambient temperature. Since the Joule-Thomson coefficient in the respective state of helium is negative, the helium temperature increases, when expanded. The energy due to the increased pressure is transformed into heat $\dot{Q}_{JT}$ and also has to be extracted at cryogenic temperature level ($f_{cold \rightarrow warm} < 0$).

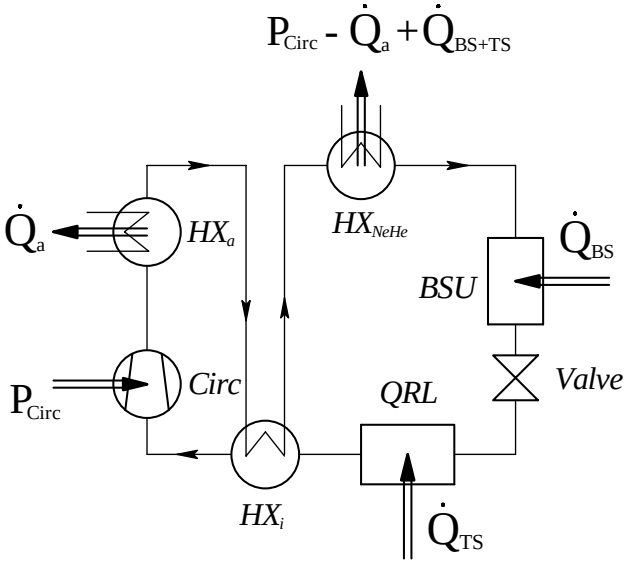

Figure 5.28: Warm circulation cycle of the beam screen cooling system. The circulation power P_{Circ} is introduced and mainly extracted at ambient temperature. An internal heat exchanger HX_i divides the scheme into a warm and a cold section.

$c_{JT} > 0 \rightarrow f_{cold \rightarrow warm} > 0,\ \dot{Q}_{JT}$ *extracted at ambient temperature level*
$c_{JT} = 0 \rightarrow f_{cold \rightarrow warm} = 0,\ \dot{Q}_{JT} = 0$
$c_{JT} < 0 \rightarrow f_{cold \rightarrow warm} < 0,\ \dot{Q}_{JT}$ *extracted at cryogenic temperature level*

$$P_{Circ} - \dot{Q}_a = \dot{Q}_{TT\Delta} + \dot{Q}_{JT} \tag{5.41}$$

$$\dot{X}_{NeHe} + \dot{X}_a = \underbrace{\left(\dot{Q}_{TS} + \dot{Q}_{BS} + \dot{Q}_{TT\Delta} + \dot{Q}_{JT}\right)}_{\dot{Q}_{NeHe}} \left(\frac{T_a}{\overline{T_{HX}}} - 1\right) + \dot{Q}_a \left(1 - \frac{T_a}{\overline{T_{HX_a}}}\right) \tag{5.42}$$

The diagram in figure 5.29 shows the distribution of the heat $\dot{Q}_{NeHe}$ extracted by the Nelium cycle, depending on the terminal temperature of the warm heat exchanger's end. It is divided into the heat load received at cryogenic temperature level $\dot{Q}_{BSU+TS}$, the heat generation $\dot{Q}_{JT}$ in the cold section due to the negative Joule Thomson-coefficient and the heat $\dot{Q}_{TT\Delta}$ slipping into the cold section due to the terminal temperature difference of the internal heat exchanger. The diagram also contains a graph, which represents the ratio of the terminal temperature differences at the cold side $TT\Delta_{cold}$ and at the warm side $TT\Delta_{warm}$.

By neglecting the small exergetic effort of the heat discharge at ambient temperature $\dot{X}_a$ in (5.42) and assuming equal mean temperatures of the heat transfer to the Nelium cycle, the total exergetic effort of the cold circulation cycle $\dot{X}_{cC}$ and the warm circulation cycle $\dot{X}_{wC}$ can easily be compared. ξ_{NeHe} denotes the Carnot efficiency of the Nelium-plant.

$$\dot{X}_{cC} = \dot{X}_{NeHe} + P_{Circ} = \frac{\dot{Q}_{TS} + \dot{Q}_{BS} + P_{Circ\,cC}}{\xi_{NeHe}} \left(\frac{T_a}{\overline{T_{HX}}} - 1\right) + P_{Circ\,cC} \tag{5.43}$$

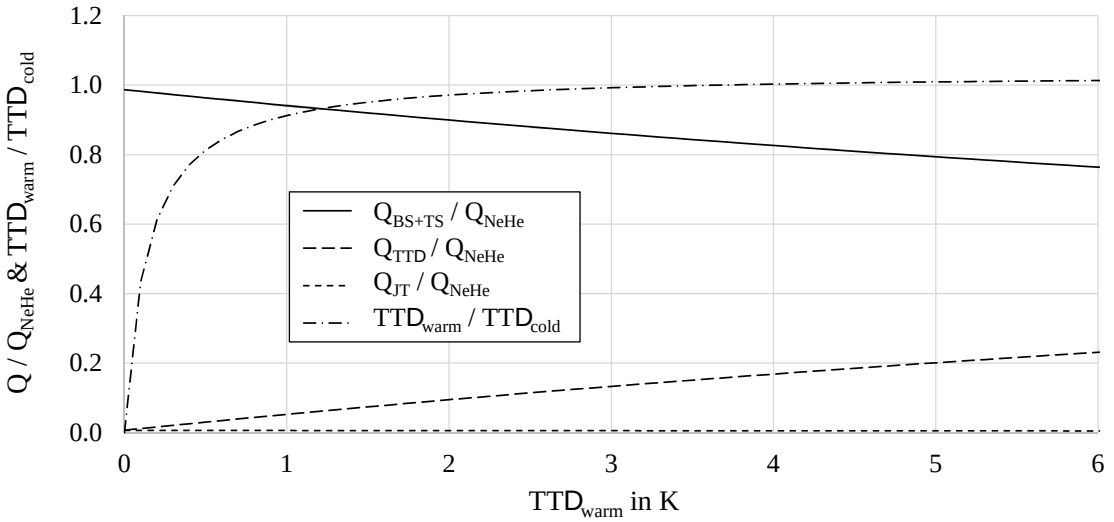

Figure 5.29: $\dot{Q}_{BS+TS}/\dot{Q}_{NeHe}$ (solid line), $\dot{Q}_{TT\Delta}/\dot{Q}_{NeHe}$ (long-dashed line), $\dot{Q}_{JT}/\dot{Q}_{NeHe}$ (short-dashed line) and $TT\Delta_{cold}/TT\Delta_{warm}$ (dashed-dotted line) vs. the terminal temperature difference of the warm side $TT\Delta_{warm}$ of the internal heat exchanger for an FCC long arc with separate shielding, a header diameter of 0.25 m and a parallel cooled BSU length corresponding to a half-cell length.

$$\dot{X}_{wC} = \dot{X}_{NeHe} + P_{Circ} = \frac{\dot{Q}_{TS} + \dot{Q}_{BS} + P_{Circ\,wC} - \dot{Q}_a}{\xi_{NeHe}} \left(\frac{T_a}{\overline{T_{HX}}} - 1 \right) + P_{Circ\,wC} \tag{5.44}$$

$$P_{Circ\,cC} \left[1 + \frac{1}{\xi_{NeHe}} \left(\frac{T_a}{\overline{T_{HX}}} - 1 \right) \right] \geqslant \left(\dot{Q}_{JT} + \dot{Q}_{TT\Delta} \right) \frac{1}{\xi_{NeHe}} \left(\frac{T_a}{\overline{T_{HX}}} - 1 \right) + P_{Circ\,wC} \tag{5.45}$$

The correlation in (5.45) can be used to find the more economical cooling scheme. As the diagram in figure 5.29 shows, the heat $\dot{Q}_{JT}$ can be neglected. The circulation power can be calculated as product of the pressure difference and the volumetric flow rate. The pressure increase Δp_{Circ} in the circulator and the mass flow rate are equal for the two circulation concepts. The density ratio of the helium, by a first estimation, is inversely proportional to the temperature ratio. The non-isentropic compression is taken into account by introducing an isentropic efficiency η_s.

$$P_{Circ} = \frac{\int \dot{V}\,(p)\,dp}{\eta_s} \approx \frac{\overline{\dot{V}}\,\Delta p_{Circ}}{\eta_s} = \frac{\dot{m}\,\Delta p_{Circ}}{\overline{\rho}\,\eta_s} \tag{5.46}$$

$$\frac{\overline{T_{cC}}}{\overline{T_{wC}}} \approx \frac{\overline{\rho_{wC}}}{\overline{\rho_{cC}}} = \frac{P_{Circ\,cC}}{P_{Circ\,wC}} \frac{\eta_{s\,cC}}{\eta_{s\,wC}} \tag{5.47}$$

$$P_{Circ\,cC} \left[1 + \frac{1}{\xi_{NeHe}} \left(\frac{T_a}{\overline{T_{HX}}} - 1 \right) \right] \geqslant \dot{Q}_{TT\Delta} \frac{1}{\xi_{NeHe}} \left(\frac{T_a}{\overline{T_{HX}}} - 1 \right) + P_{Circ\,cC} \frac{\eta_{s\,cC}}{\eta_{s\,wC}} \frac{\overline{T_{wC}}}{\overline{T_{cC}}} \tag{5.48}$$

The additional heat $\dot{Q}_{TT\Delta}$ to extract at cryogenic temperature level can be substituted with (5.49). Combining and rearranging yield (5.50), where the variables can be substituted by the values presented in table 5.5.

$$\dot{Q}_{TT\Delta} = \dot{m}\,\overline{c_p}\,TT\Delta_i \tag{5.49}$$

$$\frac{P_{Circ\,cC}}{\dot{m}TT\Delta_i} \gtrless \frac{\overline{c_p}}{\xi_{NeHe}}\left(\frac{T_a}{\overline{T_{HX}}} - 1\right) \Big/ \left[1 + \frac{1}{\xi_{NeHe}}\left(\frac{T_a}{\overline{T_{HX}}} - 1\right) - \frac{\eta_{s\,cC}}{\eta_{s\,wC}}\frac{\overline{T_{wC}}}{\overline{T_{cC}}}\right] \tag{5.50}$$

Table 5.5: Beam screen cooling: Circulation scheme comparison

Input Value	**Symbol**	**Value**	**Unit**
Specific heat capacity of helium in cold section	$\overline{c_p}$	5000	J/(kg K)
Carnot efficiency Nelium plant [44]	ξ_{NeHe}	0.42	-
Mean temperature heat transfer to the Nelium cycle	$\overline{T_{HX}}$	50	K
Cold ciruclator isentropic efficiency [44]	$\eta_{s\,cC}$	0.7	-
Warm ciruclator isentropic efficiency [44]	$\eta_{s\,wC}$	0.83	-
Mean temperature during compression cold circulation	$\overline{T_{cC}}$	60	K
Mean temperature during compression warm circulation	$\overline{T_{wC}}$	300	K

$$\frac{P_{Circ\,cC}}{\dot{m}TT\Delta_i} \gtrless 6850\ \frac{W}{kg/s \cdot K} \tag{5.51}$$

By comparison with the results of the numerical simulation of the beam screen cooling and thermal shielding system as presented in the following sections, the estimated value is about 20 % too high. For each Kelvin of terminal temperature difference of the internal heat exchanger, the cold circulation can introduce roughly 5.6 kW per kg/s of circulated helium on the beam screen cooling cycle to be equally economic.

The necessary mass flow rate is only dependent on the thermal shielding concept and doesn't change significantly. Therefore the pressure losses in the beam screen cooling system are crucial for the choice of the circulation scheme. The main parameters are the parallel cooled BSU length and the header diameter.

5.5 Exergetic analysis of the beam screen and thermal shield cooling system

The pressure losses in the heat exchangers were neglected, the Darcy friction factor f was obtained by the explicit formula of Swamee-Jain [83]. Presumed values and numbers not presented yet are listed in Table 5.6.

Table 5.6: Beam screen cooling: Warm circulation cycle

Input Value	**Symbol**	**Value**	**Unit**
Internal heat exchanger HX_i NTU [44]	NTU	40	-
Ambient heat exchanger HX_a outlet temperature	T_{HXa}	301	K

To assess the more economic option for the beam screen cooling sector design, the exergetic effort including the Carnot efficiency ξ_{NeHe} of the Nelium cryoplant is of interest. Based on the assumptions made, the overall pressure drop is independent of the type of circulator used. The diagram in figure 5.30 shows the electric power consumption for a cold circulation (solid line) and a warm circulation (dashed line) depending on the pressure drop generated in the beam screen cooling cycle for different parallel cooled BSU lengths and a header diameter of 0.25 m. The intersection point of the two power curves is at a higher pressure drop ($\approx$ 11.5 bar) than generated with a parallel cooled BSU length corresponding to a half-cell length, hence exergetically the cold circulation cycle is preferable. There are advantages of choosing a warm circulation too, for example easier handling, less error proneness and the possibility of multi-purpose use (e.g. during cool-down and warm-up).

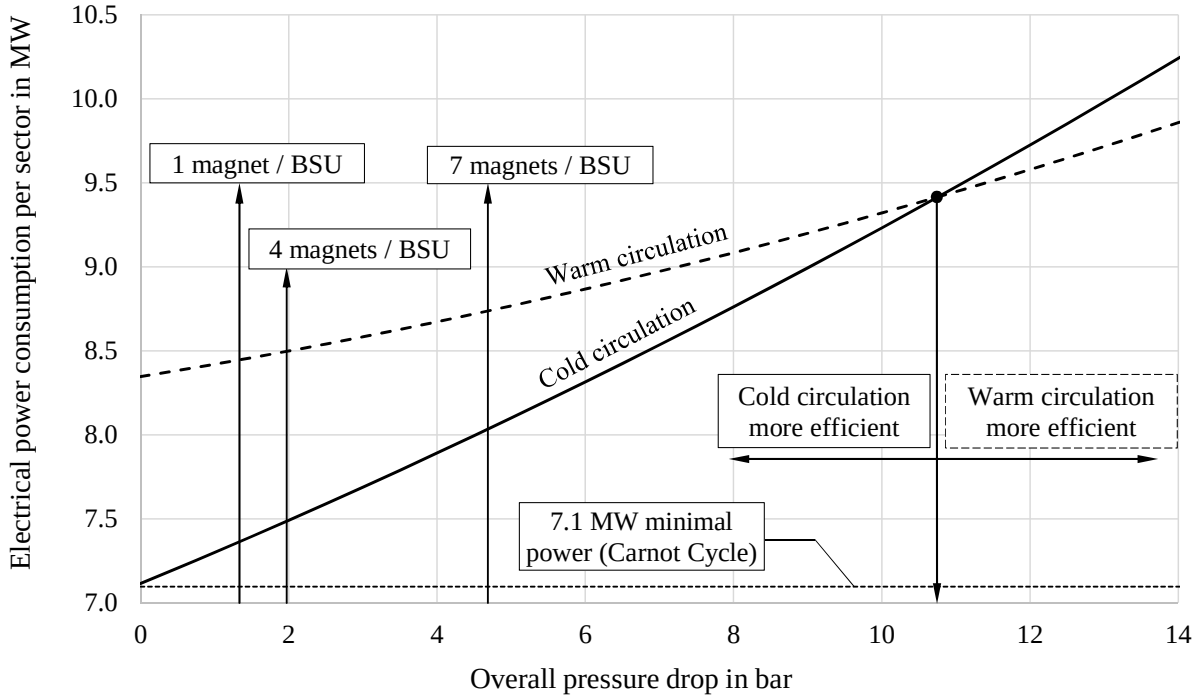

Figure 5.30: Electric power consumption per sector of the beam screen cooling system including the cryoplant efficiency (corresponding to System II of the "Integrated Circulator" design in figure 3.10) vs. the overall pressure drop for the cold circulation concept (solid line) and the warm circulation concept (dashed line) for three different lengths of parallel cooled BSUs.

The diagram in figure 5.31 shows the distribution of exergy losses of the beam screen cooling cycle for the cold circulation concept and the warm circulation concept, different lengths of parallel cooled BSUs and a header diameter of 0.25 m. Every bar in the diagram represents the sum of the relative exergy losses. The sum of the relative exergy losses and the exergetic efficiency yield 100 %, hence the exergetic efficiency can easily be calculated by subtracting the sum of the relative losses from 100 %.

Heat transfer in the beam screen The lowest bar (chequered pattern) represents the exergy losses due to the temperature difference between the warmest part of the inner chamber and the helium in the cooling channels ($\approx$ 0.4 K). The absolute value of these losses is almost constant for every scenario, but its relative contribution to the total losses decreases with increasing parallel cooled BSU length.

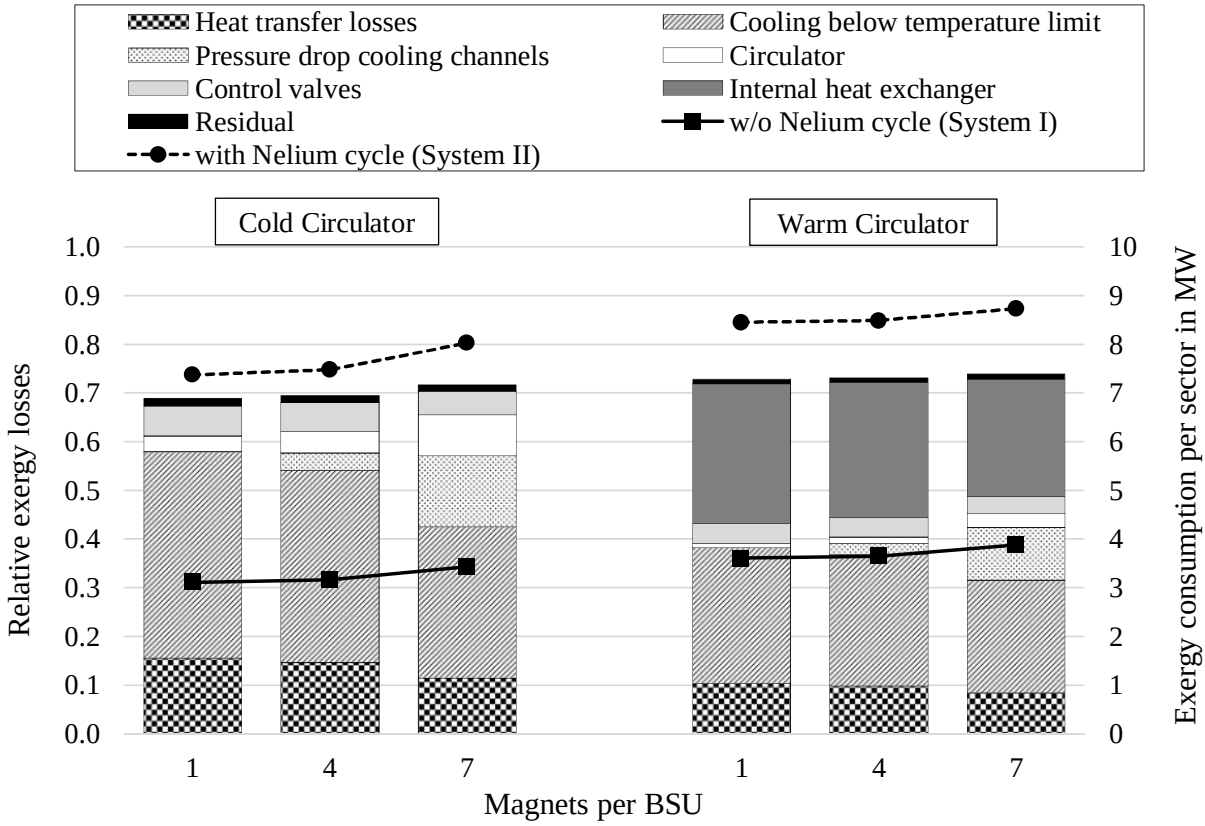

Figure 5.31: Relative exergy losses (bars) and overall exergy consumption (lines) in MW for the beam screen cooling distribution system (corresponding to System I of the "Integrated Circulator" design in figure 3.10) and for the entire beam screen cooling system (corresponding to System II of the "Integrated Circulator" design in figure 3.10) for different parallel cooled BSU lengths and schemes with cold circulation and warm circulation.

Cooling below the temperature limit The second bar (diagonally striped) represents the exergy losses due to the refrigeration below the temperature limit of 60 K. Compared to the cold mass cooling, the helium in the beam screen cooling channels in the single-phase regime and therefore its temperature rises during heat absorption. The contribution of this effect therefore is very large.

Pressure drop in the beam screen cooling channels The third bar (dotted) represents the exergy losses due to the pressure drop in the beam screen cooling channels. These losses increase strongly with increasing length of parallel cooled BSUs and become a non-negligible part of the total losses for a parallel cooled BSU length corresponding to a half-cell length.

Circulator The fourth, white bar represents the losses due to the circulator. Although the power of the warm circulation is much higher, the losses are significantly larger in the cold circulation scheme, due to the extraction at cryogenic temperature level.

Control valves The fifth, light grey bar represents the losses due to the pressure drop in the control valves. In the Separate-Shielding scheme, they can be kept relatively small.

Internal heat exchanger The sixth, dark grey bar represents the losses due to the terminal temperature difference of the internal heat exchanger ($TT\Delta_{HXi} \approx 5.75$ K). The heat $\dot{Q}_{TT\Delta}$ passes the heat exchanger and has to be extracted at cryogenic temperature level, calling for an additional exergetic effort. These losses of course only occur in the warm circulation scheme and they are crucial for the worse performance compared to cold circulation scheme.

Ambient heat exchanger and pressure loss in the thermal shielding pipes and the headers The topmost, black bar represents the residual losses, consisting of the exergy losses of the heat exchanger at ambient temperature level (only warm circulation scheme) and due to the pressure losses in the headers and the thermal shielding pipes. Their contribution is relatively small and there is no margin for improvements.

Heat load on the thermal shields The technical purpose of the thermal shielding is to absorb the heat leaks from the ambiance. Although all the used exergy is transferred to ambient temperature level (and therefore becomes anergy by classic definition), the technical purpose only can be achieved by this transformation, hence the exergy difference due to the heat absorption is counted as a benefit. Therefore no exergy losses of the thermal shielding except the pressure losses occur.

Exergy consumption (secondary ordinate) The lines depicted in the diagram in figure 5.31 represent the exergetic effort (i.e. electric power consumption) necessary to operate the beam screen cooling system. The solid lines correspond to the exergy consumed by the beam screen cycle without the Nelium plant (System I of the "Integrated Circulator" design in figure 3.10). The dashed lines correspond to the exergy consumed by the entire beam screen cooling system including the Nelium plant (System II of the "Integrated Circulator" design in figure 3.10).

Following the chosen flow scheme, there are only a few possibilities to improve the exergetic performance.

- **Heat transfer in the beam screen:** To decrease the driving temperature difference, the beam screen design must be changed. Albeit it has to be designed to fit into the cold bore, to withstand the forces during a quench and preserve a good vacuum quality. The optimization of the heat transition in the beam screen is of secondary order.
- **Quasi-isothermal heat extraction:** A small temperature increase of the cryogen enables the choice of temperatures close to the limit. This could be arranged with large mass flow rates or a cryogen in the two-phase state. Since the size of the cooling channels cannot be increased, both options would cause much higher pressure losses, annihilating the benefit. Furthermore, parallel flows of fluids with two phases are difficult to control, and the dependable cooling could not be guaranteed.
- **Internal heat exchanger:** By decreasing the terminal temperature difference in the internal heat exchanger, the exergetic performance of the warm circulation scheme could be significantly improved.

6 Conclusions

The LHC, the largest particle collider existing, is about to reach its technical limits. In 2019 the European particle physics society has to decide, which path will be be taken to gather new knowledge and explore the mysteries of matter. One option is the Future Circular Collider (FCC), a machine of unprecedented size to perform physics experiments. The FCC technology is based on the quantum mechanical phenomenon of superconduction at cryogenic temperatures in proper materials. The mere size of the machine requires an effective and reliable cryogenic distribution and discharge system to make the scientific research possible and affordable.

6.1 Scope and approach

The scope of this thesis is the investigation and assessment of different methods to provide helium at high pressure and low temperature to the superconducting magnets and to propose a preliminary design of the cryogenic distribution and discharge system for the FCC beam-bending sections (arcs). The main tasks are the arrangement of the cryogenic consumers into separately cooled parallel units, the intelligent integration of the thermal shielding into the beam screen cooling loop and the dimensioning of the necessary pipes and headers to provide and discharge the cryogen at the appropriate thermodynamic states.

Cryogenics in particle colliders is an ancillary system which has to be subordinated to the main purpose of the machine: to perform particle physics experiments. The design of the cryogenic distribution and discharge system has to be adapted to the stringent requirements given by the optics, the beam dynamics and the needs of the superconducting material. The reliable refrigeration has to be enabled within the allowed temperature ranges under consideration of economical, spatial and functional aspects. Taking into account all these requirements, the possible parameters have been varied within the available limits to calculate the according exergetic efficiencies as a measure for the operational costs of the cooling system. By combining the operational costs with the respective capital costs (number of auxiliary equipment, pipe diameters, needed space in the underground tunnel, ...) a good compromise was supposed to be found. Finally, the risk of downtime due to component/system failure and the compatibility with the optical lattice were considered to be able to propose a probate design.

6.2 Methods

Due to the early project stage of the FCC, no specimen have been produced and tested and no experiments have been performed. The main work presented consists of pressure drop and heat transfer calculations for which different analytical and numerical methods have been applied. Only the steady-state operation of the cryogenic system was considered, the transient processes during a beam lifetime cycle are not part of this thesis.

Pressure drop calculations The pipe flows over long distances (up to several kilometres) prompt to be treated as one-dimensional flows. In the numerical simulations the influence of the discretized length on the results were analysed and adapted to find a good compromise between calculation time and accuracy. Scaling analyses have been made to estimate the influence of friction, acceleration and weight on the pressure drop.

Heat transfer calculations The resulting temperature field due to heat conduction in solid bodies was calculated with numerical simulations based on the finite differences and the finite volume method. Mesh independency analyses have been performed to disable a major influence of the meshing on the result. The heat transfer in pipe heat exchangers were calculated for quasi one-dimensional flows using empirical correlations for Nusselt functions to obtain the needed heat transfer coefficients.

6.3 Summary of the most important results

Based on the expected heat loads, a preliminary FCC design and upscaling of LHC data a conceptual design of the FCC-hh cryogenic distribution and discharge system for the beam-bending sections (arcs) has been developed and exergetically analysed for the steady-state operation. Table 6.1 summarizes the results.

Cold Mass Cooling (CMC) The cold mass cooling is operated below the λ-temperature of helium to take advantage of the remarkable heat transfer properties of superfluid helium. The parallel cooled CMUs are reduced to their technically minimal length corresponding to one half-cell to minimize the necessary space for cryogenics in the cold mass. The exergetic efficiency of the refrigeration of single half-cells is close to the technical maximum, small losses in steady-state operation have to be accepted for dependable controlling and handling of (unexpected) transient processes.

The low return pressures require sufficiently large return headers considering the 8.4 km of length to transport the helium to the cold compressor stations. Due to the restricted space in the FCC tunnel, the return line for the cold mass cooling is limited to a diameter of 500 mm. Without additional machinery to re-pressurize the returning helium flow, the operating temperature of the superconducting coils would be higher than 2 K. Also, the return header size limit reduces the exergetic efficiency significantly due to the occurring pressure losses. The exergetic performance of long arcs and short arcs therefore differ for the cold mass cooling.

To estimate the electric power consumption, an overall Carnot efficiency of 0.18 was assumed for the cryoplants and cold compressor stations [100] [52].

Beam Screen Cooling and Thermal Shielding (BSC) The beam screen cooling cycle and the thermal shielding cycle were combined, since they operate at the same temperature range between 40 and 60 K. The separately cooled units were designed to match to the pattern specified by the lattice half-cells to simplify the assembly, the maintenance and hydraulic scheme. This advantage has to be paid by an increased pressure drop, which is the crucial influence quantity for the electric power consumption. The installation of additional thermal shielding pipes are accepted to minimize the pressure losses of the beam screen cooling. An adequate header diameter was chosen, close to the noticeable influence on the exergetic efficiency, which also fits to their use during the cool-down and the warm-up operations of the FCC.

The circulation with a cold machine clearly is the more efficient option for the expected pressure losses. The capacity of the Nelium-cycle driving the beam screen cooling is sufficiently high to perform the cool-down and the warm-up operations, which require a warm circulation. The baseline foresees to install a cold and a warm circulation, whereas the warm circulation in steady-state operation only is used for redundancy [55].

Current Lead Cooling (CLC) For the current lead cooling only a rough estimation based on upscaled LHC data was made, since no specific data concerning the design of the current leads or the electric supply is developed. The considerations made to be able to estimate the magnitude of the exergy consumption can be found in Appendix H.

Due to the high necessary currents to generate the magnetic field and the long sector lengths, three parallel circuits could be used increasing the necessary amounts of current leads and cooling capacity by the factor three. To estimate the electric power consumption, a Carnot efficiency of 0.29 was assumed for the re-cooling and re-pressurizing of the helium flows supplied at 4.6 K and a Carnot efficiency of 0.42 was assumed for the re-cooling and re-pressurizing of the helium flows supplied at 40 K to cool the current leads.

Table 6.1: Overview about the exergy consumption and efficiencies of the FCC cryogenic distribution system

Value	**Symbol**	**Unit**	**CMC**	**BSC**	**CLC**	**Σ**
Exergy consumption per long arc w/o cryoplant	$\dot{X}_I$	MW	2.44	3.43	0.21	6.08
Exergetic efficiency w/o cryoplant	ζ_I	-	0.714	0.7	0.842	0.71
Electric power consumption long arc	$\dot{X}_{II}$	MW	13.55	8.03	0.56	22.14
Total exergetic efficiency per long arc	ζ_{II}	-	0.129	0.299	0.311	0.195
Electric power consumption FCC	P_{el}	MW	131.5	80.3	6.8	218.5
Fraction of the total power consumption	-	-	0.602	0.367	0.031	1
Total exergetic efficiency FCC	ζ_{FCC}	-	0.133	0.299	0.311	0.199

The total exergetic efficiency of the FCC cryogenic distribution and discharge system for the beam-bending sections is close 20 %. The major part of the electric power is used to operate the cold mass cooling system ($\approx$ 60 %), the second largest consumer is the beam screen cooling and thermal shielding cycle with a fraction of close to 40 %. The relative power consumption of the current lead cooling is in the single-digit percentage range and almost negligible compared to the others. The total electric power results in about 220 MW for the cryogenic refrigeration of the FCC beam-bending sections in nominal operation.

6.4 Outlook

Considering the early stage of the Future Circular Collider Study, the presented results are just a preliminary estimation of the order of magnitude of electric power, the cryogenic distribution system of the beam-bending sections has to deal with. The calculated exergetic efficiencies of the distribution system itself seem to come close to the technically possible, bearing in mind the physical and spatial constraints to enable the unimpaired function of the FCC as a physics experiment and to keep the complexity of the cryogenic applications and the necessary space to embed them on a reasonable level. The particle physicists' society has to decide, what's the most promising way

to poke for nature's secrets. The construction and operation of the Future Circular Collider could be an ambitious possibility, which pushes the edge of the envelope and the success is anything but certain. The investigations presented in this thesis though provide cautious optimism that cryogenics will not be the obstacle.

APPENDIX

A Diameter constraint of the bayonet heat exchanger due to a pressure drop condition

The density of the helium vapour is about 300 times lower than the density of the liquid helium phase. Therefore, for the sake of simplification, it is assumed that only the vapour phase passes the outer pipe of the bayonet heat exchanger - the volumetric flow of the liquid phase is neglected. The subscript "0" refers to the helium flow state at the bayonet heat exchanger's end.

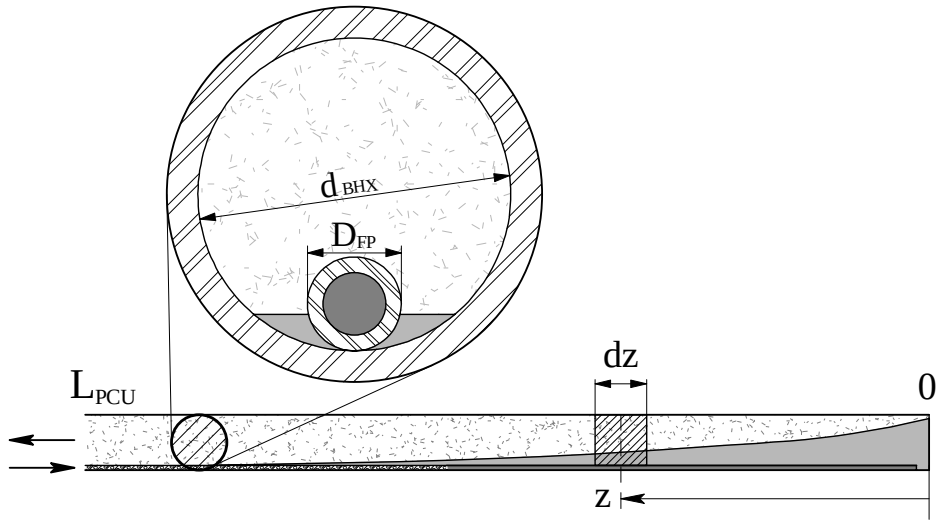

Figure A.1: Schematic of the Bayonet heat exchanger

The available flow cross section for the helium flow in the outer pipe of the bayonet heat exchanger A_{BHX} can be calculated by subtracting the outer cross section area of the feeder pipe from the inner cross section area of the bayonet heat exchanger.

$$A_{BHX} = \frac{d_{BHX}^2 \pi}{4} - \frac{D_{FP}^2 \pi}{4} \tag{A.1}$$

The differential pressure drop then can be calculated with the formula of Darcy and Weissbach. As mentioned in the beginning, only the vapour mass flow rate $\dot{m}_{Vap}$ is taken into account.

$$dp = \underbrace{\frac{f}{2\,A_{BHX}^2\,(d_{BHX} - D_{FP})\,\rho_{Vap}}}_{C} \dot{m}_{Vap}^2\,(z)\,dz \tag{A.2}$$

Depending on the quality of the heat transfer between the helium flow in the outer pipe of the bayonet heat exchanger and the feeder pipe flow, the vapour mass fraction of the helium exiting

the feeder pipe ξ_0 varies. The initial vapour mass flow rate can be expressed with (A.3), where $\dot{m}_{CMU}$ denotes the total helium mass flow rate.

$$\dot{m}_{Vap\,0} = \xi_0 \, \dot{m}_{CMU} \tag{A.3}$$

Due to the dependency of vapour mass fraction ξ on the axial coordinate z, the vapour mass flow rate at any position z can be expressed with (A.4) and furthermore, the vapour mass fraction can be substituted as shown in (A.5).

$$\dot{m}_{Vap}\,(z) = \xi\,(z)\;\dot{m}_{CMU} \tag{A.4}$$

$$\xi\,(z) = \xi_0 + \Delta\xi\,(z) \tag{A.5}$$

The mass flow rate must be constant. By assuming a constant heat load over the entire length of the bayonet heat exchanger as well as constant vaporization enthalpy r, the variation of the vapour mass fraction as a function of the axial coordinate is constant. Therefore the vapour mass fraction varies linearly with z.

$$\frac{d\xi}{dz} = \frac{\dot{q}}{r\,\dot{m}} = const. \quad \text{with} \quad r = h'' - h' \tag{A.6}$$

$$\Delta\xi\,(z) = \frac{\dot{q}\,\Delta z}{r\,\dot{m}} \tag{A.7}$$

By assuming a total vaporization of the helium flow, the vaporized helium in the outer pipe of the bayonet heat exchanger $\Delta\dot{m}_{Evap}$ equals the specific heat load multiplied with the length of the parallel cooled CMU and divided by the vaporization enthalpy.

$$\Delta\dot{m}_{Evap} = \dot{m}_{CMU}\;(1 - \xi_0) \tag{A.8}$$

$$\dot{q}\,L_{CMU} \stackrel{!}{=} \Delta\dot{m}_{Evap}\,r \rightarrow \dot{m}_{CMU} = \frac{\dot{q}\,L_{CMU}}{r\;(1 - \xi_0)} \tag{A.9}$$

By combining (A.7) and (A.9) and rearranging, (A.10) can be obtained, which, in a next step, is used to rewrite (A.2) to (A.11).

$$\xi\,(z) = \xi_0 + \frac{z}{L_{CMU}}\;(1 - \xi_0) \tag{A.10}$$

$$dp = C\,\dot{m}^2_{CMU}\left[\xi_0 + \frac{z}{L_{CMU}}\;(1 - \xi_0)\right]^2 dz \tag{A.11}$$

By integrating (A.11) from $z = 0$ to z, the pressure drop $\Delta p\,(z)$ generated up to the position z can be calculated.

$$\Delta p\,(z) = C\,\dot{m}^2_{CMU} \int_{z=0}^{z} \left[\xi_0 + \frac{z}{L_{CMU}}\;(1 - \xi_0)\right]^2 dz \tag{A.12}$$

$$\Delta p\,(z) = C\,\dot{m}^2_{CMU}\left[\xi_0^2\,z + \xi_0\,\frac{z^2}{L_{CMU}}\;(1 - \xi_0) + \frac{z^3}{L^2_{CMU}}\,\frac{(1 - \xi_0)^2}{3}\right] \tag{A.13}$$

If the mass flow rate in (A.13) is substituted according to (A.9), the total pessure drop for the entire length of the bayonet heat exchanger ($z = L_{CMU}$) is obtained with (A.15).

$$\Delta p\left(z = L_{CMU}\right) = C\left[\frac{\dot{q}\, L_{CMU}}{r\left(1-\xi_0\right)}\right]^2 \left[\xi_0^2 L_{CMU} + \xi_0 \frac{L_{CMU}^2}{L_{CMU}}\left(1-\xi_0\right) + \frac{L_{CMU}^3}{L_{CMU}^2}\frac{\left(1-\xi_0\right)^2}{3}\right] \tag{A.14}$$

$$\Delta p\left(z = L_{CMU}\right) = C\frac{\dot{q}^2}{r^2}\frac{L_{CMU}^3}{3}\frac{1-\xi_0^3}{\left(1-\xi_0\right)^3} \tag{A.15}$$

B Quasi one-dimensional balance equations for the stratified flow

The derivation of the the quasi one-dimensional mass, momentum and energy balances for a helium flow in the stratified regime with phase changes are presented by a circular pipe without integrated feeder pipe.

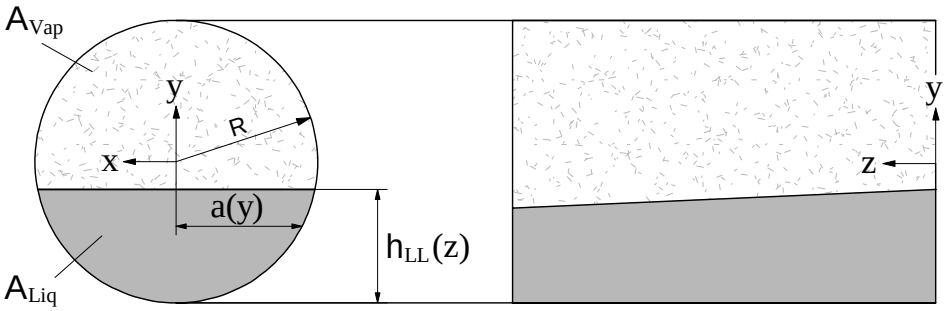

Figure B.1: Schematic of the Bayonet heat exchanger without feeder pipe

Kinematic Boundary Condition The liquid level h_{LL} in one cross section is assumed to be constant and therefore is no function of the x-coordinate. Hence the surface of the interface F is a function of z and y only and can be described with (B.1), where y corresponds to the liquid level.

$$F\left(x,y,z\right) = 0 = y - \left(R + \left(z\right)\right) \tag{B.1}$$

By introducing the velocity vector $\vec{v}$, the material derivative of the surface of the interface yields the kinematic boundary condition.

$$\vec{v} = \begin{pmatrix} u \\ v \\ w \end{pmatrix} \tag{B.2}$$

$$\frac{dF}{dt} = \frac{\partial F}{\partial t} + \vec{v} \cdot \vec{\nabla} F = v - w \frac{dh_{LL}}{dz}\bigg|_{IF} = \frac{\dot{m}''}{\rho}\bigg|_{IF} \tag{B.3}$$

where $\dot{m}''$ is obtained in kg/(m^{2}s)$^{-1}$.

Dynamic Boundary Condition The static pressure at the interface is equal for the liquid phase and the vapour phase. Since the interface is assumed not to be curved, no capillary pressure acts on it.

$$p_{Liq}\,(y{=}h_{LL}) = p_{Vap}\,(y{=}h_{LL}) = p_{IF} \tag{B.4}$$

where p_{IF} denotes the static pressure of the interface.

B.1 Mass balance

The differential mass balance has to be integrated over the corresponding cross section (for the liquid phase and for the vapour phase).

$$\int\limits_{A_\Phi} \left(\frac{\partial \rho_\Phi u_\Phi}{\partial x} + \frac{\partial \rho_\Phi v_\Phi}{\partial y} + \frac{\partial \rho_\Phi w_\Phi}{\partial z} \right) dA_\Phi = 0 \tag{B.5}$$

In the following, the subscripts *Liq* and *Vap* are written in the final forms of the equations only.

B.1.1 Liquid Phase

In (B.6) the phase cross sectional area is substituted by the corresponding Cartesian coordinates and the limits of the integral are introduced. The first term at the LHS corresponds to mass transport in x-direction and vanishes due to the no-slip condition.

$$\underbrace{\int\limits_{-R}^{-R+h_{LL}(z)} \int\limits_{-a(y)}^{a(y)} \frac{\partial \rho u}{\partial x}\, dx\, dy}_{0,\ due\ to\ no{-}slip\ condition} + \int\limits_{-R}^{-R+h_{LL}(z)} \int\limits_{-a(y)}^{a(y)} \frac{\partial \rho v}{\partial y}\, dx\, dy + \int\limits_{-R}^{-R+h_{LL}(z)} \int\limits_{-a(y)}^{a(y)} \frac{\partial \rho w}{\partial z}\, dx\, dy = 0 \tag{B.6}$$

By applying the Leibniz Rule twice, (B.6) can be rewritten as (B.8).

$$\int\limits_{-R}^{-R+h_{LL}(z)} \frac{\partial}{\partial y} \int\limits_{-a(y)}^{a(y)} \rho v\, dx\, dy + \int\limits_{-R}^{-R+h_{LL}(z)} \frac{\partial}{\partial z} \int\limits_{-a(y)}^{a(y)} \rho w\, dx\, dy = 0 \tag{B.7}$$

$$\begin{aligned} \frac{\partial}{\partial y} \int\limits_{-R}^{-R+h_{LL}(z)} \int\limits_{-a(y)}^{a(y)} \rho v\, dx\, dy + \frac{\partial}{\partial z} \int\limits_{-R}^{-R+h_{LL}(z)} \int\limits_{-a(y)}^{a(y)} \rho w\, dx\, dy - \\ - \int\limits_{-a(y)}^{a(y)} \rho w\big|_{y=-R+h_{LL}(z)} \frac{\partial h_{LL}}{\partial z}\, dx = 0 \end{aligned} \tag{B.8}$$

In the first term of the LHS of (B.8), the two integrals can be combined, since the direction of the differential operator corresponds to the one of the outer integral. The integral in the third

term of the LHS of (B.8) has to be solved only at the interface. The integrands of the two terms can be combined in one integral yielding (B.10).

$$\int_{-a(-R+h_{LL}(z))}^{a(-R+h_{LL}(z))} \rho v \, dx + \frac{\partial}{\partial z} \int_{-R}^{-R+h_{LL}(z)} \int_{-a(y)}^{a(y)} \rho w \, dx \, dy - \int_{-a(-R+h_{LL}(z))}^{a(-R+h_{LL}(z))} \frac{dh_{LL}}{dz} \rho w\big|_{IF} \, dx = 0 \tag{B.9}$$

$$\underbrace{\frac{\partial}{\partial z} \int_{-R}^{-R+h_{LL}(z)} \int_{-a(y)}^{a(y)} \rho w \, dx \, dy}_{d\dot{m}/dz} + \int_{-a(-R+h_{LL}(z))}^{a(-R+h_{LL}(z))} \underbrace{\left[\rho v - \frac{dh_{LL}}{dz} \rho w\big|_{IF}\right]}_{\dot{m}''} dx = 0 \tag{B.10}$$

The first term of the LHS of (B.10) corresponds to the change of the liquid helium mass, the integrand in the second term can be substituted with the kinematic boundary condition. By rearranging, one obtains the final form of the equation (B.11).

$$\frac{d\dot{m}_{Liq}}{dz} = -\dot{m}'\big|_{IF} = -\dot{m}_{CMU} \frac{d\xi}{dz} = \frac{d}{dz} \left(A_{Liq} \rho_{Liq} w_{Liq}\right) \tag{B.11}$$

B.1.2 Vapour Phase

In (B.12) the phase cross sectional area is substituted by the corresponding Cartesian coordinates and the limits of the integral are introduced. The first term at the LHS corresponds to mass transport in x-direction and vanishes due to the no-slip condition.

$$\underbrace{\int_{-R+h_{LL}(z)}^{R} \int_{-a(y)}^{a(y)} \frac{\partial \rho u}{\partial x} \, dx \, dy}_{0, \textit{ due to no-slip condition}} + \int_{-R+h_{LL}(z)}^{R} \int_{-a(y)}^{a(y)} \frac{\partial \rho v}{\partial y} \, dx \, dy + \int_{-R+h_{LL}(z)}^{R} \int_{-a(y)}^{a(y)} \frac{\partial \rho w}{\partial z} \, dx \, dy = 0 \tag{B.12}$$

By applying the Leibniz Rule twice, (B.12) can be rewritten as (B.14).

$$\int_{-R+h_{LL}(z)}^{R} \frac{\partial}{\partial y} \int_{-a(y)}^{a(y)} \rho v \, dx \, dy + \int_{-R+h_{LL}(z)}^{R} \frac{\partial}{\partial z} \int_{-a(y)}^{a(y)} \rho w \, dx \, dy = 0 \tag{B.13}$$

$$\begin{aligned} \frac{\partial}{\partial y} \int_{-R+h_{LL}(z)}^{R} \int_{-a(y)}^{a(y)} \rho v \, dx \, dy + \frac{\partial}{\partial z} \int_{-R+h_{LL}(z)}^{R} \int_{-a(y)}^{a(y)} \rho w \, dx \, dy + \\ + \int_{-a(y)}^{a(y)} \rho w\big|_{-R+h_{LL}(z)} \frac{\partial h_{LL}}{\partial z} \, dx = 0 \end{aligned} \tag{B.14}$$

In the first term of the LHS of (B.14), the two integrals can be combined, since the direction of the differential operator corresponds to the one of the outer integral. The integral in the third term of the LHS of (B.14) has to be solved only at the interface. The integrands of the two terms can be combined in one integral yielding (B.16).

$$-\int_{-a(-R+h_{LL}(z))}^{a(-R+h_{LL}(z))} \rho v\,dx + \frac{\partial}{\partial z}\int_{-R+h_{LL}(z)}^{R}\int_{-a(y)}^{a(y)} \rho w\,dx\,dy + \int_{-a(-R+h_{LL}(z))}^{a(-R+h_{LL}(z))} \frac{dh_{LL}}{dz}\rho w\big|_{IF}\,dx = 0 \tag{B.15}$$

$$\underbrace{\frac{\partial}{\partial z}\int_{-R+h_{LL}(z)}^{R}\int_{-a(y)}^{a(y)} \rho w\,dx\,dy}_{d\dot{m}/dz} + \int_{-a(-R+h_{LL}(z))}^{a(-R+h_{LL}(z))} \underbrace{\left[-\rho v + \frac{dh_{LL}}{dz}\rho w\big|_{IF}\right]}_{-\dot{m}''} dx = 0 \tag{B.16}$$

The first term of the LHS of (B.16) corresponds to the change of the liquid helium mass, the integrand in the second term can be substituted with the kinematic boundary condition. By rearranging, one obtains the final form of the equation (B.17).

$$\frac{d\dot{m}_{Vap}}{dz} = \dot{m}'\big|_{IF} = \dot{m}_{CMU}\frac{d\xi}{dz} = \frac{d}{dz}\left(A_{Vap}\rho_{Vap}w_{Vap}\right) \tag{B.17}$$

B.2 Momentum balance

The differential momentum balance has to be integrated over the corresponding cross section (for the liquid phase and for the vapour phase).

$$\begin{aligned}\int_{A_\Phi}\left(\frac{\partial \rho_\Phi u_\Phi w_\Phi}{\partial x} + \frac{\partial \rho_\Phi v_\Phi w_\Phi}{\partial y} + \frac{\partial \rho_\Phi w_\Phi w_\Phi}{\partial z}\right) dA_\Phi = \\ = \int_{A_\Phi}\left(-\frac{\partial p_\Phi}{\partial z} + \frac{\partial \tau_{zx\,\Phi}}{\partial x} + \frac{\partial \tau_{zy\,\Phi}}{\partial y} + \frac{\partial \tau_{zz\,\Phi}}{\partial z} + \rho_\Phi\, g\, sin\,\alpha\right) dA_\Phi\end{aligned} \tag{B.18}$$

In the following, the subscripts *Liq* and *Vap* are written in the final forms of the equations only.

B.2.1 Liquid Phase

For the sake of presentability, the LHS and the RHS of (B.18) are dealt with one after the other. We start with the LHS.

In (B.19) the phase cross sectional area is substituted by the corresponding Cartesian coordinates and the limits of the integral are introduced. The first term corresponds to mass transport in x-direction and vanishes due to the no-slip condition.

$$\underbrace{\int_{-R}^{-R+h_{LL}(z)} \int_{-a(y)}^{a(y)} \frac{\partial \rho u w}{\partial x}\, dx\, dy}_{0,\ due\ to\ no-slip\ condition} + \int_{-R}^{-R+h_{LL}(z)} \int_{-a(y)}^{a(y)} \frac{\partial \rho v w}{\partial y}\, dx\, dy + \\ + \int_{-R}^{-R+h_{LL}(z)} \int_{-a(y)}^{a(y)} \frac{\partial \rho w w}{\partial z}\, dx\, dy = LHS \tag{B.19}$$

By applying the Leibniz Rule twice, (B.19) can be rewritten as (B.21).

$$\int_{-R}^{-R+h_{LL}(z)} \frac{\partial}{\partial y} \int_{-a(y)}^{a(y)} \rho v w\, dx\, dy + \int_{-R}^{-R+h_{LL}(z)} \frac{\partial}{\partial z} \int_{-a(y)}^{a(y)} \rho w w\, dx\, dy = LHS \tag{B.20}$$

$$\int_{-a(-R+h_{LL}(z))}^{a(-R+h_{LL}(z))} \rho v w\, dx + \frac{\partial}{\partial z} \int_{-R}^{-R+h_{LL}(z)} \int_{-a(y)}^{a(y)} \rho w w\, dx\, dy - \\ - \int_{-a(y)}^{a(y)} \rho w w\big|_{-R+h_{LL}(z)} \frac{\partial h_{LL}}{\partial z}\, dx = LHS \tag{B.21}$$

In the first term of (B.21), the two integrals can be combined, since the direction of the differential operator corresponds to the one of the outer integral. The integral in the third term of (B.21) has to be solved only at the interface. The integrands of the two terms can be combined in one integral yielding (B.23).

$$\int_{-a(-R+h_{LL}(z))}^{a(-R+h_{LL}(z))} \rho v w\, dx + \frac{\partial}{\partial z} \int_{-R}^{-R+h_{LL}(z)} \int_{-a(y)}^{a(y)} \rho w w\, dx\, dy - \\ - \int_{-a(-R+h_{LL}(z))}^{a(-R+h_{LL}(z))} \frac{dh_{LL}}{dz} \rho w w\big|_{IF}\, dx = LHS \tag{B.22}$$

$$\frac{\partial \left(\overline{\rho w w} A\right)}{\partial z} + \underbrace{\int_{-a(-R+h_{LL}(z))}^{a(-R+h_{LL}(z))} \rho w \left[v - \frac{dh_{LL}}{dz} w\big|_{IF}\right] dx}_{w \dot{m}'\big|_{IF}} = LHS \tag{B.23}$$

The first term of (B.23) expresses the quasi one-dimensional momentum of the helium phase in z-direction. The second term corresponds to the momentum transfer passing the interface and

the change of momentum due to the variation of the liquid level. It can be substituted using the kinematic boundary condition.

Now we discuss the RHS. In (B.24) the phase cross sectional area is substituted by the corresponding Cartesian coordinates and the limits of the integral are introduced. The first term corresponds to the change of momentum due to pressure forces. The subsequent three terms describe the change of momentum due to normal and shear stresses. The last term describes the change of momentum by the change of the hydrostatic head.

$$\begin{aligned} -\int_{-R}^{-R+h_{LL}(z)}\int_{-a(y)}^{a(y)}\frac{\partial p}{\partial z}\,dx\,dy+\int_{-R}^{-R+h_{LL}(z)}\int_{-a(y)}^{a(y)}\frac{\partial \tau_{xz}}{\partial x}\,dx\,dy+\int_{-R}^{-R+h_{LL}(z)}\int_{-a(y)}^{a(y)}\frac{\partial \tau_{yz}}{\partial y}\,dx\,dy+ \\ \int_{-R}^{-R+h_{LL}(z)}\int_{-a(y)}^{a(y)}\frac{\partial \tau_{zz}}{\partial z}\,dx\,dy+\rho g A\sin\alpha = RHS \end{aligned} \tag{B.24}$$

By applying the Leibniz Rule twice, (B.24) can be rewritten as (B.26).

$$\begin{aligned} -\int_{-R}^{-R+h_{LL}(z)}\frac{\partial}{\partial z}\int_{-a(y)}^{a(y)}p\,dx\,dy+\int_{-R}^{-R+h_{LL}(z)}\frac{\partial}{\partial x}\int_{-a(y)}^{a(y)}\tau_{xz}\,dx\,dy+ \\ +\int_{-R}^{-R+h_{LL}(z)}\left[\frac{\partial}{\partial y}\int_{-a(y)}^{a(y)}\tau_{yz}\,dx-\tau_{yz}\big|_{P+}\frac{\partial\left(a\left(y\right)\right)}{\partial y}+\tau_{yz}\big|_{P-}\frac{\partial\left(-a\left(y\right)\right)}{\partial y}\right]dy+ \\ +\int_{-R}^{-R+h_{LL}(z)}\frac{\partial}{\partial z}\int_{-a(y)}^{a(y)}\tau_{zz}\,dx\,dy+\rho g A\sin\alpha = RHS \end{aligned} \tag{B.25}$$

$$\begin{aligned} -\frac{\partial}{\partial z}\int_{-R}^{-R+h_{LL}(z)}\int_{-a(y)}^{a(y)}p\,dx\,dy+\int_{-a(y)}^{a(y)}p\big|_{-R+h_{LL}(z)}\frac{\partial h_{LL}}{\partial z}\,dx+ \\ +\int_{-R}^{-R+h_{LL}(z)}\left[\tau_{xz}\big|_{P+}-\tau_{xz}\big|_{P-}\right]dy+ \\ +\int_{-a(-R+h_{LL}(z))}^{a(-R+h_{LL}(z))}\tau_{yz}\big|_{IF}\,dx+\int_{-R}^{-R+h_{LL}(z)}\left[-\tau_{yz}\big|_{P+}\frac{\partial\left(a\left(y\right)\right)}{\partial y}+\tau_{yz}\big|_{P-}\frac{\partial\left(-a\left(y\right)\right)}{\partial y}\right]dy+ \\ +\frac{\partial}{\partial z}\int_{-R}^{-R+h_{LL}(z)}\int_{-a(y)}^{a(y)}\tau_{zz}\,dx\,dy-\int_{-a(y)}^{a(y)}\tau_{zz}\big|_{-R+h_{LL}(z)}\frac{\partial h_{LL}}{\partial z}\,dx+\rho g A\sin\alpha = RHS \end{aligned} \tag{B.26}$$

where the subscripts $P+$ and $P-$ correspond the pipe wall in positive coordinate direction and in negative coordinate direction respectively. By rearranging (B.26), (B.28) can be obtained.

$$
\begin{aligned}
&-\frac{\partial}{\partial z}\int_{-R}^{-R+h_{LL}(z)}\int_{-a(y)}^{a(y)} p\,dx\,dy+\frac{dh_{LL}}{dz}\int_{-a(-R+h_{LL}(z))}^{a(-R+h_{LL}(z))} p\big|_{IF}\,dx+\\
&\qquad+\int_{-R}^{-R+h_{LL}(z)}\left[\tau_{xz}\big|_{P+}-\tau_{xz}\big|_{P-}\right]dy+\\
&+\int_{-a(-R+h_{LL}(z))}^{a(-R+h_{LL}(z))}\tau_{yz}\big|_{IF}\,dx+\int_{-R}^{-R+h_{LL}(z)}\left[-\tau_{yz}\big|_{P+}\frac{\partial\left(a\left(y\right)\right)}{\partial y}+\tau_{yz}\big|_{P-}\frac{\partial\left(-a\left(y\right)\right)}{\partial y}\right]dy+\\
&+\frac{\partial}{\partial z}\int_{-R}^{-R+h_{LL}(z)}\int_{-a(y)}^{a(y)}\tau_{zz}\,dx\,dy-\frac{dh_{LL}}{dz}\int_{-a(-R+h_{LL}(z))}^{a(-R+h_{LL}(z))}\tau_{zz}\big|_{IF}\,dx+\rho gA\,sin\,\alpha=RHS
\end{aligned}
\tag{B.27}
$$

$$
\begin{aligned}
&-\frac{\partial\left(\overline{p}A\right)}{\partial z}+\int_{-a(-R+h_{LL}(z))}^{a(-R+h_{LL}(z))}\left[\frac{dh_{LL}}{dz}p\big|_{IF}+\tau_{yz}\big|_{IF}-\frac{dh_{LL}}{dz}\tau_{zz}\big|_{IF}\right]dx+\\
&\underbrace{\int_{-R}^{-R+h_{LL}(z)}\left[\tau_{xz}\big|_{P+}-\tau_{xz}\big|_{P-}-\tau_{yz}\big|_{P+}\frac{\partial\left(a\left(y\right)\right)}{\partial y}+\tau_{yz}\big|_{P-}\frac{\partial\left(-a\left(y\right)\right)}{\partial y}\right]dy}_{-\overline{\tau_P}\,L_P(z)}+\\
&\qquad+\frac{\partial\left(\overline{\tau_{zz}}A\right)}{\partial z}+\rho gA\,sin\,\alpha=RHS
\end{aligned}
\tag{B.28}
$$

The first term of (B.28) expresses the quasi one-dimensional change of momentum due to the static pressure. The second term describes momentum changing processes in the interface and the third term corresponds to momentum change due to the wall shear stresses. The fourth term is describes the momentum change due to viscous normal stresses and the last term corresponds to the momentum change due to the change of the hydrostatic head. Now we combine the LHS and the RHS and substitute several terms as shown in (B.29).

$$
\begin{aligned}
&\overbrace{\frac{\partial\left(\overline{\rho w w}A\right)}{\partial z}}^{d(\dot{m}\overline{w})/dz}+\overbrace{w\dot{m}'\big|_{IF}}^{-w\big|_{IF}\dot{m}_{CMU}\,d\xi/dz}=-\frac{\partial\left(\overline{p}A\right)}{\partial z}+\overbrace{\int_{-a(-R+h_{LL}(z))}^{a(-R+h_{LL}(z))}\frac{dh_{LL}}{dz}p\big|_{IF}\,dx}^{p_{IF}\,dA/dz}+\\
&+\underbrace{\int_{-a(-R+h_{LL}(z))}^{a(-R+h_{LL}(z))}\tau_{yz}\big|_{IF}\,dx}_{L_{VL}\tau_{VL}}-\underbrace{\int_{-a(-R+h_{LL}(z))}^{a(-R+h_{LL}(z))}\frac{dh_{LL}}{dz}\tau_{zz}\big|_{IF}\,dx}_{\tau_{zz}\big|_{IF}\,dA/dz}-\overline{\tau_P}\,L_P\left(z\right)+\frac{\partial\left(\overline{\tau_{zz}}A\right)}{\partial z}+\rho gA\,sin\,\alpha
\end{aligned}
\tag{B.29}
$$

Now we discuss the terms containing the pressure and the viscous normal stresses. Due to the low hydrostatic head compared to the absolute pressure, the pressure over the entire flow cross section can be assumed to be constant ($p = p_{IF} \neq f(x,y)$). With this assumption, the first and the second term of (B.29) can be combined and simplified.

$$-\frac{d\left(\overline{p}A\right)}{dz} + p_{IF}\frac{dA}{dz} = -p_{IF}\frac{dA}{dz} - A\frac{dp_{IF}}{dz} + p_{IF}\frac{dA}{dz} = -A\frac{dp_{IF}}{dz} \tag{B.30}$$

Another assumption shall be made regarding the velocity of the interface, which we assume to be equal to the quasi one-dimensional velocity the liquid phase ($\mu_{Liq} > \mu_{Vap}$) [70].

$$w\big|_{IF} = \overline{w} \tag{B.31}$$

Based on this assumption, the terms containing the viscous normal stresses τ_{zz} can be rewritten [101] as

$$\overline{\tau_{zz}} = 2\mu\frac{d\overline{w}}{dz} \rightarrow \frac{\partial\left(\overline{\tau_{zz}}A\right)}{\partial z} = \frac{d\left(2\mu A\right)}{dz}\frac{d\overline{w}}{dz} + 2\mu A\frac{d^2\overline{w}}{dz^2} \tag{B.32}$$

$$\tau_{zz}\big|_{IF} = 2\mu\left.\frac{dw}{dz}\right|_{IF} \rightarrow \tau_{zz}\big|_{IF}\frac{dA}{dz} = 2\mu\frac{dA}{dz}\frac{dw|_{IF}}{dz} = 2\mu\frac{dA}{dz}\frac{d\overline{w}}{dz} \tag{B.33}$$

$$\frac{\partial\left(\overline{\tau_{zz}}A\right)}{\partial z} - \tau_{zz}\big|_{IF}\frac{dA}{dz} = 2\mu A\frac{d^2\overline{w}}{dz^2} = \underbrace{2\nu\frac{d\dot{m}}{dz}\frac{d\overline{w}}{dz}}_{small} \tag{B.34}$$

The terms containing the viscous normal stresses τ_{zz} are relatively small and can be neglected. Equation (B.36) shows the final form of the quasi one-dimensional momentum balance for the liquid phase.

$$\dot{m}\frac{d\overline{w}}{dz} + \overline{w}\frac{d\dot{m}}{dz} = -A\frac{dp}{dz} - \overline{\tau_P}L_P + \overline{\tau_{VL}}L_{VL} + \rho g A\,sin\,\alpha + \underbrace{\dot{m}_{CMU}\frac{d\xi}{dz}}_{d\dot{m}/dz}\overline{w} \tag{B.35}$$

$$\dot{m}_{Liq}\frac{d\overline{w_{Liq}}}{dz} = -A_{Liq}\frac{dp}{dz} - \overline{\tau_{P\,Liq}}L_{P\,Liq} + \overline{\tau_{VL}}L_{VL} + \rho g A_{Liq}\,sin\,\alpha \tag{B.36}$$

B.2.2 Vapour Phase

For the sake of presentability, the LHS and the RHS of (B.18) are dealt with one after the other. We start with the LHS.

In (B.37) the phase cross sectional area is substituted by the corresponding Cartesian coordinates and the limits of the integral are introduced. The first term corresponds to mass transport in x-direction and vanishes due to the no-slip condition.

$$\underbrace{\int_{-R+h_{LL}(z)}^{R}\int_{-a(y)}^{a(y)}\frac{\partial \rho uw}{\partial x}\,dx\,dy}_{0,\ due\ to\ no-slip\ condition}+\int_{-R+h_{LL}(z)}^{R}\int_{-a(y)}^{a(y)}\frac{\partial \rho vw}{\partial y}\,dx\,dy+ \\ +\int_{-R+h_{LL}(z)}^{R}\int_{-a(y)}^{a(y)}\frac{\partial \rho ww}{\partial z}\,dx\,dy = LHS \tag{B.37}$$

By applying the Leibniz Rule twice, (B.37) can be rewritten as (B.39).

$$\int_{-R+h_{LL}(z)}^{R}\frac{\partial}{\partial y}\int_{-a(y)}^{a(y)}\rho vw\,dx\,dy+\int_{-R+h_{LL}(z)}^{R}\frac{\partial}{\partial z}\int_{-a(y)}^{a(y)}\rho ww\,dx\,dy = LHS \tag{B.38}$$

$$-\int_{-a(-R+h_{LL}(z))}^{a(-R+h_{LL}(z))}\rho vw\,dx+\frac{\partial}{\partial z}\int_{-R+h_{LL}(z)}^{R}\int_{-a(y)}^{a(y)}\rho ww\,dx\,dy+ \\ +\int_{-a(y)}^{a(y)}\rho ww\big|_{-R+h_{LL}(z)}\frac{\partial h_{LL}}{\partial z}\,dx = LHS \tag{B.39}$$

In the first term of (B.39), the two integrals can be combined, since the direction of the differential operator corresponds to the one of the outer integral. The integral in the third term of (B.39) has to be solved only at the interface. The integrands of the two terms can be combined in one integral yielding (B.41).

$$-\int_{-a(-R+h_{LL}(z))}^{a(-R+h_{LL}(z))}\rho vw\,dx+\frac{\partial}{\partial z}\int_{-R+h_{LL}(z)}^{R}\int_{-a(y)}^{a(y)}\rho ww\,dx\,dy+ \\ +\frac{dh_{LL}}{dz}\int_{-a(-R+h_{LL}(z))}^{a(-R+h_{LL}(z))}\rho ww\big|_{IF}\,dx = LHS \tag{B.40}$$

$$\frac{\partial\left(\overline{\rho ww}A\right)}{\partial z}-\underbrace{\int_{-a(-R+h_{LL}(z))}^{a(-R+h_{LL}(z))}\rho w\left[v-\frac{dh_{LL}}{dz}w\big|_{IF}\right]dx}_{\dot{w m}\big|_{IF}} = LHS \tag{B.41}$$

The first term of (B.41) expresses the quasi one-dimensional momentum of the helium phase in z-direction. The second term corresponds to the momentum transfer passing the interface and

the change of momentum due to the variation of the liquid level. It can be substituted using the kinematic boundary condition.

Now we discuss the RHS. In (B.42) the phase cross sectional area is substituted by the corresponding Cartesian coordinates and the limits of the integral are introduced. The first term corresponds to the change of momentum due to pressure forces. The subsequent three terms describe the change of momentum due to normal and shear stresses. The last term describes the change of momentum by the change of the hydrostatic head.

$$\begin{aligned} -\int_{-R+h_{LL}(z)}^{R}\int_{-a(y)}^{a(y)}\frac{\partial p}{\partial z}\,dx\,dy+\int_{-R+h_{LL}(z)}^{R}\int_{-a(y)}^{a(y)}\frac{\partial \tau_{xz}}{\partial x}\,dx\,dy+\int_{-R+h_{LL}(z)}^{R}\int_{-a(y)}^{a(y)}\frac{\partial \tau_{yz}}{\partial y}\,dx\,dy+ \\ \int_{-R+h_{LL}(z)}^{R}\int_{-a(y)}^{a(y)}\frac{\partial \tau_{zz}}{\partial z}\,dx\,dy+\rho g A\,sin\,\alpha = RHS \end{aligned} \tag{B.42}$$

By applying the Leibniz Rule twice, (B.42) can be rewritten as (B.44).

$$\begin{aligned} -\int_{-R+h_{LL}(z)}^{R}\frac{\partial}{\partial z}\int_{-a(y)}^{a(y)}p\,dx\,dy+\int_{-R+h_{LL}(z)}^{R}\frac{\partial}{\partial x}\int_{-a(y)}^{a(y)}\tau_{xz}\,dx\,dy+ \\ +\int_{-R+h_{LL}(z)}^{R}\left[\frac{\partial}{\partial y}\int_{-a(y)}^{a(y)}\tau_{yz}\,dx-\tau_{yz}\big|_{P+}\frac{\partial\left(a\left(y\right)\right)}{\partial y}+\tau_{yz}\big|_{P-}\frac{\partial\left(-a\left(y\right)\right)}{\partial y}\right]dy+ \\ +\int_{-R+h_{LL}(z)}^{R}\frac{\partial}{\partial z}\int_{-a(y)}^{a(y)}\tau_{zz}\,dx\,dy+\rho g A\,sin\,\alpha = RHS \end{aligned} \tag{B.43}$$

$$\begin{aligned} -\frac{\partial}{\partial z}\int_{-R+h_{LL}(z)}^{R}\int_{-a(y)}^{a(y)}p\,dx\,dy-\int_{-a(y)}^{a(y)}p\big|_{-R+h_{LL}(z)}\frac{\partial h_{LL}}{\partial z}\,dx+ \\ +\int_{-R+h_{LL}(z)}^{R}\left[\tau_{xz}\big|_{P+}-\tau_{xz}\big|_{P-}\right]dy- \\ -\int_{-a(-R+h_{LL}(z))}^{a(-R+h_{LL}(z))}\tau_{yz}\big|_{IF}\,dx+\int_{-R+h_{LL}(z)}^{R}\left[-\tau_{yz}\big|_{P+}\frac{\partial\left(a\left(y\right)\right)}{\partial y}+\tau_{yz}\big|_{P-}\frac{\partial\left(-a\left(y\right)\right)}{\partial y}\right]dy+ \\ +\frac{\partial}{\partial z}\int_{-R+h_{LL}(z)}^{R}\int_{-a(y)}^{a(y)}\tau_{zz}\,dx\,dy+\int_{-a(y)}^{a(y)}\tau_{zz}\big|_{-R+h_{LL}(z)}\frac{\partial h_{LL}}{\partial z}\,dx+\rho g A\,sin\,\alpha = RHS \end{aligned} \tag{B.44}$$

where the subscripts $P+$ and $P-$ correspond the pipe wall in positive coordinate direction and in negative coordinate direction respectively. By rearranging (B.44), (B.46) can be obtained.

$$
\begin{aligned}
&-\frac{\partial}{\partial z}\int_{-R+h_{LL}(z)}^{R}\int_{-a(y)}^{a(y)} p\,dx\,dy-\frac{dh_{LL}}{dz}\int_{-a(-R+h_{LL}(z))}^{a(-R+h_{LL}(z))} p\big|_{IF}\,dx+\\
&\qquad+\int_{-R+h_{LL}(z)}^{R}\left[\tau_{xz}\big|_{P+}-\tau_{xz}\big|_{P-}\right]dy-\\
&-\int_{-a(-R+h_{LL}(z))}^{a(-R+h_{LL}(z))}\tau_{yz}\big|_{IF}\,dx+\int_{-R+h_{LL}(z)}^{R}\left[-\tau_{yz}\big|_{P+}\frac{\partial\left(a\left(y\right)\right)}{\partial y}+\tau_{yz}\big|_{P-}\frac{\partial\left(-a\left(y\right)\right)}{\partial y}\right]dy+\\
&+\frac{\partial}{\partial z}\int_{-R+h_{LL}(z)}^{R}\int_{-a(y)}^{a(y)}\tau_{zz}\,dx\,dy+\frac{dh_{LL}}{dz}\int_{-a(-R+h_{LL}(z))}^{a(-R+h_{LL}(z))}\tau_{zz}\big|_{IF}\,dx+\rho gA\,sin\,\alpha=RHS
\end{aligned}
\tag{B.45}
$$

$$
\begin{aligned}
&-\frac{\partial\left(\overline{p}A\right)}{\partial z}+\int_{-a(-R+h_{LL}(z))}^{a(-R+h_{LL}(z))}\left[-\frac{dh_{LL}}{dz}p\big|_{IF}-\tau_{yz}\big|_{IF}+\frac{dh_{LL}}{dz}\tau_{zz}\big|_{IF}\right]dx+\\
&\underbrace{\int_{-R+h_{LL}(z)}^{R}\left[\tau_{xz}\big|_{P+}-\tau_{xz}\big|_{P-}-\tau_{yz}\big|_{P+}\frac{\partial\left(a\left(y\right)\right)}{\partial y}+\tau_{yz}\big|_{P-}\frac{\partial\left(-a\left(y\right)\right)}{\partial y}\right]dy}_{-\overline{\tau_P}\,L_P(z)}+\\
&\qquad+\frac{\partial\left(\overline{\tau_{zz}}A\right)}{\partial z}+\rho gA\,sin\,\alpha=RHS
\end{aligned}
\tag{B.46}
$$

The first term of (B.46) expresses the quasi one-dimensional change of momentum due to the static pressure. The second term describes momentum changing processes in the interface and the third term corresponds to momentum change due to the wall shear stresses. The fourth term describes the momentum change due to viscous normal stresses and the last term corresponds to the momentum change due to the change of the hydrostatic head. Now we combine the LHS and the RHS and substitute several terms as shown in (B.47).

$$
\begin{aligned}
&\overbrace{\frac{\partial\left(\overline{\rho w w}A\right)}{\partial z}}^{d(\dot{m}\,\overline{w})/dz}-\overbrace{w\big|_{IF}\,\dot{m}_{CMU}\,d\xi/dz}^{w\dot{m}'|_{IF}}=-\frac{\partial\left(\overline{p}A\right)}{\partial z}-\overbrace{\int_{-a(-R+h_{LL}(z))}^{a(-R+h_{LL}(z))}\frac{dh_{LL}}{dz}p\big|_{IF}\,dx}^{-p_{IF}\,dA/dz}-\\
&\underbrace{-\int_{-a(-R+h_{LL}(z))}^{a(-R+h_{LL}(z))}\tau_{yz}\big|_{IF}\,dx}_{\tau_{VL}\,L_{VL}}+\underbrace{\int_{-a(-R+h_{LL}(z))}^{a(-R+h_{LL}(z))}\frac{dh_{LL}}{dz}\tau_{zz}\big|_{IF}\,dx}_{-\tau_{zz}|_{IF}\,dA/dz}-\overline{\tau_P}\,L_P\left(z\right)+\frac{\partial\left(\overline{\tau_{zz}}A\right)}{\partial z}+\rho gA\,sin\,\alpha
\end{aligned}
\tag{B.47}
$$

Now we discuss the terms containing the pressure and the viscous normal stresses. Due to the low hydrostatic head compared to the absolute pressure, the pressure over the entire flow cross section can be assumed to be constant ($p = p_{IF} \neq f(x,y)$). With this assumption, the first and the second term of (B.47) can be combined and simplified.

$$-\frac{d\left(\overline{p}A\right)}{dz} + p_{IF}\frac{dA}{dz} = -p_{IF}\frac{dA}{dz} - A\frac{dp_{IF}}{dz} + p_{IF}\frac{dA}{dz} = -A\frac{dp_{IF}}{dz} \tag{B.48}$$

Another assumption shall be made regarding the velocity of the interface, which we assume to be equal to the quasi one-dimensional velocity the liquid phase ($\mu_{Liq} > \mu_{Vap}$) [70].

$$w\big|_{IF} = \overline{w_{Liq}} \tag{B.49}$$

Based on this assumption, the terms containing the viscous normal stresses τ_{zz} can be rewritten [101] as

$$\overline{\tau_{zz}} = 2\mu\frac{d\overline{w}}{dz} \rightarrow \frac{\partial\left(\overline{\tau_{zz}}A_{Liq}\right)}{\partial z} = \frac{d\left(2\mu A\right)}{dz}\frac{d\overline{w}}{dz} + 2\mu A\frac{d^2\overline{w}}{dz^2} \tag{B.50}$$

$$\tau_{zz}\big|_{IF} = 2\mu\frac{dw}{dz}\bigg|_{IF} \rightarrow \tau_{zz}\big|_{IF}\frac{dA}{dz} = 2\mu\frac{dA}{dz}\frac{dw|_{IF}}{dz} = 2\mu\frac{dA}{dz}\frac{d\overline{w_{Liq}}}{dz} \tag{B.51}$$

$$\frac{\partial\left(\overline{\tau_{zz}}A_{Liq}\right)}{\partial z} + \tau_{zz}\big|_{IF}\frac{dA}{dz} = 2\mu A\frac{d^2\overline{w}}{dz^2} = \underbrace{2\nu\frac{d\dot{m}}{dz}\frac{d\overline{w}}{dz}}_{small} \tag{B.52}$$

The terms containing the viscous normal stresses τ_{zz} are relatively small and can be neglected. Equation (B.54) shows the final form of the quasi one-dimensional momentum balance for the liquid phase.

$$\dot{m}\frac{d\overline{w}}{dz} + \overline{w}\underbrace{\frac{d\dot{m}}{dz}}_{\dot{m}_{CMU}\,d\xi/dz} = -A\frac{dp}{dz} + \overline{\tau_P}L_P - \overline{\tau_{VL}}L_{VL} + \rho g A\,sin\,\alpha + \dot{m}_{CMU}\frac{d\xi}{dz}\overline{w_{Liq}} \tag{B.53}$$

$$\dot{m}_{Vap}\frac{d\overline{w_{Vap}}}{dz} = -A_{Vap}\frac{dp}{dz} - \overline{\tau_{PVap}}L_{PVap} - \overline{\tau_{VL}}L_{VL} + \rho g A_{Vap}\,sin\,\alpha - \dot{m}_{CMU}\frac{d\xi}{dz}\left(\overline{w_{Vap}} - \overline{w_{Liq}}\right) \tag{B.54}$$

B.3 Thermal energy balance

The differential thermal energy balance has to be integrated over the corresponding cross section (for the liquid phase and for the vapour phase). Since an open system in steady-state shall be modelled, in the thermal energy balance the enthalpy h is used instead of the inner energy [101].

$$\int_{A_\Phi}\left(\frac{\partial\rho_\Phi h_\Phi u_\Phi}{\partial x} + \frac{\partial\rho_\Phi h_\Phi v_\Phi}{\partial y} + \frac{\partial\rho_\Phi h_\Phi w_\Phi}{\partial z}\right)dA_\Phi = -\int_{A_\Phi}\left(\frac{\partial q_{x\,\Phi}}{\partial z} + \frac{\partial q_{y\,\Phi}}{\partial x} + \frac{\partial q_{z\,\Phi}}{\partial y}\right)dA_\Phi \tag{B.55}$$

In the following, the subscripts *Liq* and *Vap* are written in the final forms of the equations only.

B.3.1 Liquid Phase

In (B.56) the phase cross sectional area is substituted by the corresponding Cartesian coordinates and the limits of the integral are introduced. The first term corresponds to the energy transport by mass in x-direction and vanishes due to the no-slip condition.

$$\underbrace{\int_{-R}^{-R+h_{LL}(z)}\int_{-a(y)}^{a(y)}\frac{\partial \rho h u}{\partial x}\,dx\,dy}_{0,\ due\ to\ no-slip\ condition}+\int_{-R}^{-R+h_{LL}(z)}\int_{-a(y)}^{a(y)}\frac{\partial \rho h v}{\partial y}\,dx\,dy+\int_{-R}^{-R+h_{LL}(z)}\int_{-a(y)}^{a(y)}\frac{\partial \rho h w}{\partial z}\,dx\,dy= \tag{B.56}$$
$$-\int_{-R}^{-R+h_{LL}(z)}\int_{-a(y)}^{a(y)}\frac{\partial q_x}{\partial x}\,dx\,dy-\int_{-R}^{-R+h_{LL}(z)}\int_{-a(y)}^{a(y)}\frac{\partial q_y}{\partial y}\,dx\,dy-\int_{-R}^{-R+h_{LL}(z)}\int_{-a(y)}^{a(y)}\frac{\partial q_z}{\partial z}\,dx\,dy$$

By applying the Leibniz Rule twice, (B.56) can be rewritten as (B.58).

$$\begin{aligned}\int_{-R}^{-R+h_{LL}(z)}\frac{\partial}{\partial y}\int_{-a(y)}^{a(y)}\rho h v\,dx\,dy+\int_{-R}^{-R+h_{LL}(z)}\frac{\partial}{\partial z}\int_{-a(y)}^{a(y)}\rho h w\,dx\,dy=\\ =-\int_{-R}^{-R+h_{LL}(z)}\frac{\partial}{\partial x}\int_{-a(y)}^{a(y)}q_x\,dx\,dy-\\ -\int_{-R}^{-R+h_{LL}(z)}\left[\frac{\partial}{\partial y}\int_{-a(y)}^{a(y)}q_y\,dx-q_y\big|_{P+}\frac{\partial\left(a\left(y\right)\right)}{\partial y}+q_y\big|_{P-}\frac{\partial\left(-a\left(y\right)\right)}{\partial y}\right]dy-\\ -\int_{-R}^{-R+h_{LL}(z)}\frac{\partial}{\partial z}\int_{-a(y)}^{a(y)}q_z\,dx\,dy\end{aligned} \tag{B.57}$$

$$\begin{aligned}\int_{-a(-R+h_{LL}(z))}^{a(-R+h_{LL}(z))}\rho h v\big|_{IF}\,dx+\frac{\partial}{\partial z}\int_{-R}^{-R+h_{LL}(z)}\int_{-a(y)}^{a(y)}\rho h w\,dx\,dy-\int_{-a(y)}^{a(y)}\rho h w\big|_{-R+h_{LL}(z)}\frac{\partial h_{LL}}{\partial z}\,dx=\\ =-\int_{-R}^{-R+h_{LL}(z)}\left[q_x\big|_{P+}-q_x\big|_{P-}\right]dy-\int_{-a(-R+h_{LL}(z))}^{a(-R+h_{LL}(z))}q_y\big|_{IF}\,dx+\\ +\int_{-R}^{-R+h_{LL}(z)}\left[q_y\big|_{P+}\frac{\partial\left(a\left(y\right)\right)}{\partial y}-q_y\big|_{P-}\frac{\partial\left(-a\left(y\right)\right)}{\partial y}\right]dy-\\ -\frac{\partial}{\partial z}\int_{-R}^{-R+h_{LL}(z)}\int_{-a(y)}^{a(y)}q_z\,dx\,dy+\int_{-a(y)}^{a(y)}q_z\big|_{-R+h_{LL}(z)}\frac{\partial h_{LL}}{\partial z}\,dx\end{aligned} \tag{B.58}$$

where the subscripts $P+$ and $P-$ correspond the pipe wall in positive coordinate direction and in negative coordinate direction respectively. Equation (B.58) can be rearranged by combining several terms to obtain (B.59).

$$\begin{aligned}\frac{\partial\left(\overline{\rho h w}\,A\right)}{\partial z}+\overbrace{\int_{-a(-R+h_{LL}(z))}^{a(-R+h_{LL}(z))}\left[h\dot{m}''\big|_{IF}-\frac{dh_{LL}}{dz}\,q_z\big|_{IF}+q_y\big|_{IF}\right]dx}^{heat\ transfer\ at\ Interface}=\\ =\underbrace{-\int_{-R}^{-R+h_{LL}(z)}\left[-q_x\big|_{P+}+q_x\big|_{P-}+q_y\big|_{P+}\frac{\partial\left(a\left(y\right)\right)}{\partial y}-q_y\big|_{P-}\frac{\partial\left(-a\left(y\right)\right)}{\partial y}\right]dy}_{\overline{q_{CM}}\,P_{CM}}-\underbrace{\frac{\partial\left(\overline{q_z}\,A\right)}{\partial z}}_{\substack{axial\ heat\\ conduction}}\end{aligned} \tag{B.59}$$

The first term on the LHS in (B.59) corresponds to the convective heat transfer, the second term to the heat transfer over the interface. On the RHS the first term describes the heat conduction via the pipe walls and the second term the axial heat conduction in the helium phase. If the axial heat conduction and energy passing the interface due to conduction are neglected, (B.59) reads as (B.61).

$$\frac{d\left(\overline{\rho h w}\,A\right)}{dz}+h\dot{m}'\big|_{IF}=\overline{q_{CM}}\,P_{CM} \tag{B.60}$$

$$\frac{d\left(\overline{h_{Liq}}\,\dot{m}_{Liq}\right)}{dz}=\overline{q_{CM}}\,P_{CM}-h''\dot{m}_{CMU}\frac{d\xi}{dz} \tag{B.61}$$

B.3.2 Vapour Phase

In (B.62) the phase cross sectional area is substituted by the corresponding Cartesian coordinates and the limits of the integral are introduced. The first term corresponds to the energy transport by mass in x-direction and vanishes due to the no-slip condition.

$$\begin{aligned}\underbrace{\int_{-R+h_{LL}(z)}^{R}\int_{-a(y)}^{a(y)}\frac{\partial\rho h u}{\partial x}\,dx\,dy}_{0,\ due\ to\ no-slip\ condition}+\int_{-R+h_{LL}(z)}^{R}\int_{-a(y)}^{a(y)}\frac{\partial\rho h v}{\partial y}\,dx\,dy+\int_{-R+h_{LL}(z)}^{R}\int_{-a(y)}^{a(y)}\frac{\partial\rho h w}{\partial z}\,dx\,dy=\\ -\int_{-R+h_{LL}(z)}^{R}\int_{-a(y)}^{a(y)}\frac{\partial q_x}{\partial x}\,dx\,dy-\int_{-R+h_{LL}(z)}^{R}\int_{-a(y)}^{a(y)}\frac{\partial q_y}{\partial y}\,dx\,dy-\int_{-R+h_{LL}(z)}^{R}\int_{-a(y)}^{a(y)}\frac{\partial q_z}{\partial z}\,dx\,dy\end{aligned} \tag{B.62}$$

By applying the Leibniz Rule twice, (B.62) can be rewritten as (B.64).

$$\int_{-R+h_{LL}(z)}^{R} \frac{\partial}{\partial y} \int_{-a(y)}^{a(y)} \rho h v \, dx \, dy + \int_{-R+h_{LL}(z)}^{R} \frac{\partial}{\partial z} \int_{-a(y)}^{a(y)} \rho h w \, dx \, dy =$$
$$= - \int_{-R+h_{LL}(z)}^{R} \frac{\partial}{\partial x} \int_{-a(y)}^{a(y)} q_x \, dx \, dy -$$
$$- \int_{-R+h_{LL}(z)}^{R} \left[\frac{\partial}{\partial y} \int_{-a(y)}^{a(y)} q_y \, dx - q_y\big|_{P+} \frac{\partial \left(a\left(y\right)\right)}{\partial y} + q_y\big|_{P-} \frac{\partial \left(-a\left(y\right)\right)}{\partial y} \right] dy -$$
$$- \int_{-R+h_{LL}(z)}^{R} \frac{\partial}{\partial z} \int_{-a(y)}^{a(y)} q_z \, dx \, dy \tag{B.63}$$

$$- \int_{-a(-R+h_{LL}(z))}^{a(-R+h_{LL}(z))} \rho h v\big|_{IF} \, dx + \frac{\partial}{\partial z} \int_{-R+h_{LL}(z)}^{R} \int_{-a(y)}^{a(y)} \rho h w \, dx \, dy - \int_{-a(y)}^{a(y)} \left[-\rho h w\big|_{-R+h_{LL}(z)} \frac{\partial h_{LL}}{\partial z} \right] dx =$$
$$= - \int_{-R+h_{LL}(z)}^{R} \left[q_x\big|_{P+} - q_x\big|_{P-} \right] dy + \int_{-a(-R+h_{LL}(z))}^{a(-R+h_{LL}(z))} q_y\big|_{IF} \, dx +$$
$$+ \int_{-R+h_{LL}(z)}^{R} \left[q_y\big|_{P+} \frac{\partial \left(a\left(y\right)\right)}{\partial y} - q_y\big|_{P-} \frac{\partial \left(-a\left(y\right)\right)}{\partial y} \right] dy -$$
$$- \frac{\partial}{\partial z} \int_{-R+h_{LL}(z)}^{R} \int_{-a(y)}^{a(y)} q_z \, dx \, dy - \int_{-a(y)}^{a(y)} \left[q_z\big|_{-R+h_{LL}(z)} \frac{\partial h_{LL}}{\partial z} \right] dx \tag{B.64}$$

where the subscripts $P+$ and $P-$ correspond the pipe wall in positive coordinate direction and in negative coordinate direction respectively. Equation (B.64) can be rearranged by combining several terms to obtain (B.65).

$$\frac{\partial \left(\overline{\rho h w} \, A \right)}{\partial z} - \overbrace{\int_{-a(-R+h_{LL}(z))}^{a(-R+h_{LL}(z))} \left[h \dot{m}''\big|_{IF} - \frac{dh_{LL}}{dz} q_z\big|_{IF} + q_y\big|_{IF} \right] dx}^{heat\ transfer\ at\ Interface} =$$
$$= \underbrace{- \int_{-R+h_{LL}(z)}^{R} \left[-q_x\big|_{P+} + q_x\big|_{P-} + q_y\big|_{P+} \frac{\partial \left(a\left(y\right)\right)}{\partial y} - q_y\big|_{P-} \frac{\partial \left(-a\left(y\right)\right)}{\partial y} \right] dy}_{\overline{q_{CM}} P_{CM}} - \underbrace{\frac{\partial \left(\overline{q_z} \, A \right)}{\partial z}}_{\substack{axial\ heat \\ conduction}} \tag{B.65}$$

The first term on the LHS in (B.65) corresponds to the convective heat transfer, the second term to the heat transfer over the interface. On the RHS the first term describes the heat conduction via the pipe walls and the second term the axial heat conduction in the helium phase. If the axial heat conduction and energy passing the interface due to conduction are neglected, (B.65) reads as (B.67).

$$\frac{d\left(\overline{\rho h w}\, A\right)}{dz} - h\dot{m}'\big|_{IF} = \overline{q_{CM}}\, P_{CM} \tag{B.66}$$

$$\frac{d\left(\overline{h_{Vap}}\,\dot{m}_{Vap}\right)}{dz} = \overline{q_{CMVap}}\, P_{CMVap} + h''\dot{m}\frac{d\xi}{dz} \tag{B.67}$$

The enthalpy contained in the vaporized helium in (B.61) and (B.67) are identical, therefore the two equations can be combined. After rearranging the (B.70) is obtained. By adding the heat received from the feeder pipe flow (4.20) is obtained.

$$\frac{d\left(\overline{h_{Vap}}\,\dot{m}_{Vap}\right)}{dz} = \overline{q_{CM}}\, P_{CM} - \frac{d\left(\overline{h_{Liq}}\,\dot{m}_{Liq}\right)}{dz} \tag{B.68}$$

$$\dot{m}_{CMU}\,\frac{d\left(h''\,\xi\right)}{dz} = \overline{q_{CM}}\, P_{CM} + \dot{m}_{CMU}\,\frac{d\left(h'\,\xi\right)}{dz} \tag{B.69}$$

$$\dot{m}_{CMU}\,\left(h'' - h'\right)\,d\xi = \overline{q_{CM}}\, P_{CM}\, dz \tag{B.70}$$

C Heat transport in the bayonet heat exchanger copper pipe

The iron yoke temperature (i.e. the temperature of the static superfluid helium bath) can be treated to be uniform in the entire cross section. Also the two helium phases of the stratified flow are assumed to be in thermial equilibrium. The rate of heat transfer between liquid helium and the copper pipe exceeds the one between the vapour phase and the copper pipe by far. Therefore, part of the heat received by the dry part of the copper pipe is tangentially conducted to the wetted perimeter and released to the liquid helium as indicated in figure C.1.

Figure C.1: Heat flux in one half of the bayonet heat exchanger. Due the much higher thermal resistance of the dry perimeter, part of the heat is tangentially conducted to the wetted inner surface along the copper pipe.

R_{BHX} ... radius of the bayonet heat exchanger

φ_{LL} ... angle defined by the liquid level in the bayonet heat exchanger

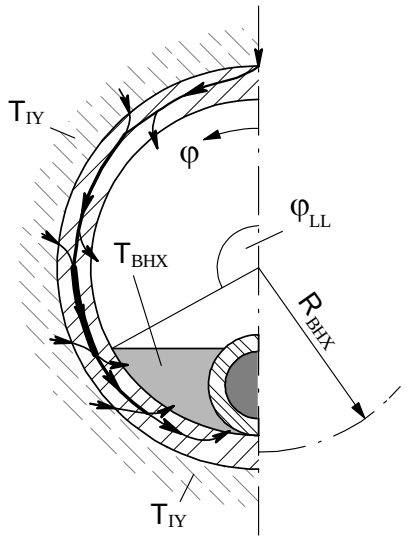

C.1 Tangential heat transfer in the bayonet heat exchanger copper pipe

With the Laplace equation (C.1) the temperature profile in the copper pipe can be described.

$$-\frac{d^2T}{d\varphi^2}\frac{t_{BHX}\,k_{Co}}{R_{BHX}^2} = h_{out}\,(T_{IY} - T) - h_{in}\,(T - T_{BHX}) \tag{C.1}$$

where t_{BHX} denotes the thickness of the outer copper pipe, k_{Co} denotes the thermal conductivity of copper, T_{IY} denotes the temperature of the iron yoke, T_{BHX} denotes the temperature of the helium in the pipe and h_{out} and h_{in} denote the heat transfer coefficients at the outer surface and

the inner surface of the copper pipe. By rearranging (C.1), it can be transformed into the classical notation of a linear partial differential equation of the second order.

$$-\frac{d^2T}{d\varphi^2}\,\frac{t_{BHX}\,k_{Co}}{R_{BHX}^2} = -T\,(h_{out}+h_{in}) + h_{in}\,T_{BHX} + h_{out}\,T_{IY} \tag{C.2}$$

$$\underbrace{\frac{d^2T}{d\varphi^2}}_{T''} - \underbrace{(h_{out}+h_{in})\,\overbrace{\frac{R_{BHX}^2}{t_{BHX}\,k_{Co}}}^{C_0}}_{C_2}\,T + \underbrace{(h_{in}\,T_{BHX} - h_{out}\,T_{IY})\,\overbrace{\frac{R_{BHX}^2}{t_{BHX}\,k_{Co}}}^{C_0}}_{C_1} = 0 \tag{C.3}$$

$$T'' - C_2\,T + C_1 = 0 \tag{C.4}$$

To solve (C.4), an approach according to (C.5) can be used [102]. Two equations, one for the dry perimeter and one for the wetted perimeter, yield four unknown constants A_i.

$$T = T_h + T_p \tag{C.5}$$

$$T_h = A_1\,e^{f_1\,\varphi} + A_2\,e^{f_2\,\varphi} \tag{C.6}$$

$$T_p = \frac{-C_1}{-C_2} = \frac{h_{out}\,T_{IY} + h_{in}\,T_{BHX}}{h_{out}+h_{in}} \tag{C.7}$$

$$f_{1,2} = \pm\sqrt{C_2} \tag{C.8}$$

The angle φ_{LL}, defined by the liquid level, divides the inner pipe wall in a dry perimeter and in a wetted perimeter. The heat transfer coefficient at the inner pipe wall changes suddenly and therefore different constants C_i have to be used.

$$\begin{aligned} h_{in} &= h_{Dry} && C_1 \to C_{D1} \quad \& \quad C_2 \to C_{D2} \\ h_{in} &= h_{Wet} && C_1 \to C_{W1} \quad \& \quad C_2 \to C_{W2} \end{aligned}$$

Four boundary and/or transition conditions are necessary to solve for the four unknown constants A_{D1}, A_{D2}, A_{W1} and A_{W1}:

BC1 The tangential temperature gradient at $\varphi = 0$ vanishes:

$$\left.\frac{dT_{Dry}}{d\varphi}\right|_{\varphi=0} = 0$$

BC2 The tangential temperature gradient at $\varphi = \pi$ vanishes:

$$\left.\frac{dT_{Wet}}{d\varphi}\right|_{\varphi=\pi} = 0$$

TC1 The tangential temperature gradient of the dry perimeter equals the tangential temperature gradient of the wetted perimeter at $\varphi = \varphi_{LL}$:

$$\left.\frac{dT_{Dry}}{d\varphi}\right|_{\varphi=\varphi_{LL}} = \left.\frac{dT_{Wet}}{d\varphi}\right|_{\varphi=\varphi_{LL}}$$

TC2 The temperature of the dry perimeter equals the temperature of the wetted perimeter at $\varphi = \varphi_{LL}$:

$$T_{Dry}\big|_{\varphi=\varphi_{LL}} = T_{Wet}\big|_{\varphi=\varphi_{LL}}$$

From the first boundary condition **BC1** the correlation (C.9) can be obtained, which relates the constants A_{D1} and A_{D2}.

$$\left.\frac{dT}{d\varphi}\right|_{\varphi=0} = \left.\frac{d\left(T_h + T_p\right)}{d\varphi}\right|_{\varphi=0} = 0 \tag{C.9}$$

$$\left[f_{D1}\, A_{D1}\, e^{f_{D1}\,\varphi} + f_{D2}\, A_{D2}\, e^{f_{D2}\,\varphi}\right]_{\varphi=0} = \sqrt{C_{D2}}\, A_{D1} - \sqrt{C_{D2}}\, A_{D2} = 0 \tag{C.10}$$

$$\rightarrow A_{D1} = A_{D2} \tag{C.11}$$

From the second boundary condition **BC2** the correlation (C.14) can be obtained, which connects the constants A_{W1} and A_{W2}.

$$\left.\frac{dT}{d\varphi}\right|_{\varphi=\pi} = \left.\frac{d\left(T_h + T_p\right)}{d\varphi}\right|_{\varphi=\pi} = 0 \tag{C.12}$$

$$\begin{aligned}\left[f_{W1}\, A_{W1}\, e^{f_{W1}\,\varphi} + f_{W2}\, A_{W2}\, e^{f_{W2}\,\varphi}\right]_{\varphi=\pi} = \\ = \sqrt{C_{W2}}\, A_{W1}\, e^{\sqrt{C_{W2}}\,\pi} - \sqrt{C_{W2}}\, A_{W2}\, e^{-\sqrt{C_{W2}}\,\pi} = 0\end{aligned} \tag{C.13}$$

$$\rightarrow \frac{A_{W2}}{A_{W1}} = e^{\sqrt{C_{W2}}\,2\,\pi} \tag{C.14}$$

From the first transition condition **TC1** the correlation (C.20) can be obtained, which relates the constants A_{D1} and A_{W1}.

$$\left.\frac{d\left(T_{h\,D}+T_{p\,D}\right)}{d\varphi}\right|_{\varphi=\varphi_{LL}} = \left.\frac{d\left(T_{h\,W}+T_{p\,W}\right)}{d\varphi}\right|_{\varphi=\varphi_{LL}} \tag{C.15}$$

$$\left(f_{D1}\,A_{D1}\,e^{f_{D1}\,\varphi}+f_{D2}\,A_{D2}\,e^{f_{D2}\,\varphi}\right)_{\varphi=\varphi_{LL}} = \left(f_{W1}\,A_{W1}\,e^{f_{W1}\,\varphi}+f_{W2}\,A_{W2}\,e^{f_{W2}\,\varphi}\right)_{\varphi=\varphi_{LL}} \tag{C.16}$$

$$f_{D1}\,A_{D1}\,e^{f_{D1}\,\varphi_{LL}}+f_{D2}\,A_{D2}\,e^{f_{D2}\,\varphi_{LL}} = f_{W1}\,A_{W1}\,e^{f_{W1}\,\varphi_{LL}}+f_{W2}\,A_{W2}\,e^{f_{W2}\,\varphi_{LL}} \tag{C.17}$$

In (C.17) the constants A_{D2} and A_{W2} are substituted by the correlations found in (C.11) and (C.14) respectively.

$$\begin{aligned}\sqrt{C_{D2}}\,A_{D1}\,e^{\sqrt{C_{D2}}\,\varphi_{LL}}-\sqrt{C_{D2}}\,A_{D1}\,e^{-\sqrt{C_{D2}}\,\varphi_{LL}} = \\ = \sqrt{C_{W2}}\,A_{W1}\,e^{\sqrt{C_{W2}}\,\varphi_{LL}}-\sqrt{C_{W2}}\,A_{W1}\,e^{\sqrt{C_{W2}}\,2\,\pi}\,e^{-\sqrt{C_{W2}}\,\varphi_{LL}}\end{aligned} \tag{C.18}$$

$$\begin{aligned}A_{D1}\,\sqrt{C_{D2}}\,2\,sinh\left(\sqrt{C_{D2}}\,\varphi_{LL}\right) = \\ = A_{W1}\,\sqrt{C_{W2}}\left(e^{\sqrt{C_{W2}}\,\varphi_{LL}}-e^{\sqrt{C_{W2}}\,2\,\pi}\,e^{-\sqrt{C_{W2}}\,\varphi_{LL}}\right)\end{aligned} \tag{C.19}$$

$$\begin{aligned}A_{D1} = \frac{A_{W1}\,\sqrt{C_{W2}}\left(e^{\sqrt{C_{W2}}\,\varphi_{LL}}-e^{\sqrt{C_{W2}}\,(2\,\pi-\varphi_{LL})}\right)}{\sqrt{C_{D2}}\,2\,sinh\left(\sqrt{C_{D2}}\,\varphi_{LL}\right)} = \\ = A_{W1}\,\sqrt{\frac{C_{W2}}{C_{D2}}}\,\frac{e^{\sqrt{C_{W2}}\,\pi}\,sinh\left[\sqrt{C_{W2}}\,(\varphi_{LL}-\pi)\right]}{sinh\left(\sqrt{C_{D2}}\,\varphi_{LL}\right)}\end{aligned} \tag{C.20}$$

From the second transition condition **TC2** the correlation (C.24) can be obtained, which provides a second relation between the constants A_{D1} and A_{W1}.

$$\left(T_{h\,D}+T_{p\,D}\right)_{\varphi=\varphi_{LL}} = \left(T_{h\,W}+T_{p\,W}\right)_{\varphi=\varphi_{LL}} \tag{C.21}$$

$$A_{D1}\,e^{f_{D1}\,\varphi_{LL}}+A_{D2}\,e^{f_{D2}\,\varphi_{LL}}+\frac{C_{D1}}{C_{D2}} = A_{W1}\,e^{f_{W1}\,\varphi_{LL}}+A_{W2}\,e^{f_{W2}\,\varphi_{LL}}+\frac{C_{W1}}{C_{W2}} \tag{C.22}$$

In (C.23) the constants A_{D1} and A_{W1} are substituted by the correlations found in (C.11) and (C.14) respectively.

$$A_{D1}\,e^{f_{D1}\,\varphi_{LL}}+A_{D1}\,e^{f_{D2}\,\varphi_{LL}}+\frac{C_{D1}}{C_{D2}} = A_{W1}\,e^{f_{W1}\,\varphi_{LL}}+A_{W1}\,e^{\sqrt{C_{W2}}\,2\,\pi}\,e^{f_{W2}\,\varphi_{LL}}+\frac{C_{W1}}{C_{W2}} \tag{C.23}$$

$$A_{D1} = \frac{A_{W1}\left(e^{\sqrt{C_{W2}}\,\varphi_{LL}} + e^{\sqrt{C_{W2}}\,(2\pi-\varphi_{LL})}\right) + \frac{C_{W1}}{C_{W2}} - \frac{C_{D1}}{C_{D2}}}{2\,cosh\left(\sqrt{C_{D2}}\,\varphi_{LL}\right)} = \tag{C.24}$$

$$= \frac{A_{W1}\,e^{\sqrt{C_{W2}}\pi}\,2\,cosh\left[\sqrt{C_{W2}}\,(\varphi_{LL}-\pi)\right] + \frac{C_{W1}}{C_{W2}} - \frac{C_{D1}}{C_{D2}}}{2\,cosh\left(\sqrt{C_{D2}}\,\varphi_{LL}\right)}$$

Combining the equations (C.20) and (C.24) by substituting A_{D1} by the respective expression on the RHS yields A_{W1} in (C.26).

$$\frac{A_{W1}\,e^{\sqrt{C_{W2}}\pi}\,2\,cosh\left[\sqrt{C_{W2}}\,(\varphi_{LL}-\pi)\right] + \frac{C_{W1}}{C_{W2}} - \frac{C_{D1}}{C_{D2}}}{2\,cosh\left(\sqrt{C_{D2}}\,\varphi_{LL}\right)} = \tag{C.25}$$

$$= A_{W1}\sqrt{\frac{C_{W2}}{C_{D2}}}\,\frac{e^{\sqrt{C_{W2}}\pi}\,sinh\left[\sqrt{C_{W2}}\,(\varphi_{LL}-\pi)\right]}{sinh\left(\sqrt{C_{D2}}\,\varphi_{LL}\right)}$$

$$A_{W1} = \frac{\frac{C_{D1}}{C_{D2}} - \frac{C_{W1}}{C_{W2}}}{2\,e^{\sqrt{C_{W2}}\pi}\left\{cosh\left[\sqrt{C_{W2}}\,(\varphi_{LL}-\pi)\right] - \sqrt{\frac{C_{W2}}{C_{D2}}}\,\frac{sinh\left[\sqrt{C_{W2}}(\varphi_{LL}-\pi)\right]}{tanh\left(\sqrt{C_{D2}}\,\varphi_{LL}\right)}\right\}} \tag{C.26}$$

Based on the known constant A_{W1}, all the other constants A_i can be calculated by solving the equations (C.24), (C.14), and (C.11) in this order. After determining all unknown constants, the differential equations for the dry and for the wetted perimeter can be solved. Below a short summary of the formulas and the values of the used variables and constants is shown.

Dry Perimeter:

$$T_{Dry}(\varphi) = A_{D1}\,e^{f_{D1}\,\varphi} + A_{D2}\,e^{f_{D2}\,\varphi} + \frac{C_{D1}}{C_{D2}} \tag{C.27}$$

$$Q_{Dry}(\varphi) = -\left(f_{D1}\,A_{D1}\,e^{f_{D1}\,\varphi} - f_{D2}\,A_{D2}\,e^{f_{D2}\,\varphi}\right)\cdot \frac{R_{BHX}}{C_0} \tag{C.28}$$

Wetted Perimeter:

$$T_{Wet}(\varphi) = A_{W1}\,e^{f_{W1}\,\varphi} + A_{W2}\,e^{f_{W2}\,\varphi} + \frac{C_{W1}}{C_{W2}} \tag{C.29}$$

$$Q_{Wet}(\varphi) = -\left(f_{W1}\,A_{W1}\,e^{f_{W1}\,\varphi} - f_{W2}\,A_{W2}\,e^{f_{W2}\,\varphi}\right)\cdot \frac{R_{BHX}}{C_0} \tag{C.30}$$

$$C_0 = \frac{R_{BHX}^2}{t_{BHX}\, k_{Co}}$$

$$A_{D1} = A_{W1}\sqrt{\frac{C_{W2}}{C_{D2}}}\frac{e^{\sqrt{C_{W2}}\pi}\, sinh\left[\sqrt{C_{W2}}\,(\varphi_{LL}-\pi)\right]}{sinh\left(\sqrt{C_{D2}}\,\varphi_{LL}\right)}$$

$$A_{D2} = \frac{A_{W1}\, e^{\sqrt{C_{W2}}\pi}\, 2\, cosh\left[\sqrt{C_{W2}}\,(\varphi_{LL}-\pi)\right] + \frac{C_{W1}}{C_{W2}} - \frac{C_{D1}}{C_{D2}}}{2\, cosh\left(\sqrt{C_{D2}}\,\varphi_{LL}\right)}$$

$$f_{D1} = -f_{D2} = \sqrt{C_{D2}}$$

$$C_{D1} = C_0\,(h_{out}\, T_{IY} + h_{Dry}\, T_{BHX})$$

$$C_{D2} = C_0\,(h_{out} + h_{Dry})$$

$$A_{W1} = \frac{\frac{C_{D1}}{C_{D2}} - \frac{C_{W1}}{C_{W2}}}{2\, e^{\sqrt{C_{W2}}\pi}\left\{cosh\left[\sqrt{C_{W2}}\,(\varphi_{LL}-\pi)\right] - \sqrt{\frac{C_{W2}}{C_{D2}}}\frac{sinh\left[\sqrt{C_{W2}}(\varphi_{LL}-\pi)\right]}{tanh\left(\sqrt{C_{D2}}\,\varphi_{LL}\right)}\right\}}$$

$$A_{W2} = A_{W1}\, e^{\sqrt{C_{W2}}\, 2\pi}$$

$$f_{W1} = -f_{W2} = \sqrt{C_{W2}}$$

$$C_{W1} = C_0\,(h_{out}\, T_{IY} + h_{Wet}\, T_{BHX})$$

$$C_{W2} = C_0\,(h_{out} + h_{Wet})$$

C.2 Radial temperature profile in the bayonet heat exchanger copper pipe

The two-dimensional Laplace equation in polar coordinates describes the temperature field in a pipe.

$$\frac{1}{r}\frac{\partial}{\partial r}\left(r\frac{\partial T}{\partial r}\right) + \frac{1}{r^2}\frac{\partial^2 T}{\partial \varphi^2} = 0 \tag{C.31}$$

Dimensionless variables are marked with an asterisk. By substituting the dimensionless variables in (C.31) and rearranging, (C.34) is obtained.

$$T^* = \frac{T}{T_{BHX}}$$

$$r^* = \frac{r}{R_{BHX}}$$

$$r^*\varphi^* = \frac{r\varphi}{R_{BHX}\varphi_{LL}}$$

$$\frac{1}{R_{BHX}^2}\frac{1}{r^*}\frac{\partial}{\partial r^*}\left(r^*\frac{\partial T^*}{\partial r^*}\right) + \frac{1}{r^{*2}}\frac{\partial^2 T^*}{\partial \varphi^{*2}}\frac{1}{R_{BHX}^2\varphi_{LL}^2} = 0 \tag{C.32}$$

$$\frac{1}{r^*}\frac{\partial}{\partial r^*}\left(r * \frac{\partial T^*}{\partial r^*}\right) + \frac{1}{r^{*2}}\frac{\partial^2 T^*}{\partial \varphi^{*2}}\frac{1}{\varphi_{LL}^2} = 0 \tag{C.33}$$

$$r^* \frac{\partial}{\partial r^*} \left(r^* \frac{\partial T^*}{\partial r^*} \right) + \underbrace{\frac{\partial^2 T^*}{\partial \varphi^{*2}} \frac{1}{\varphi_{LL}^2}}_{small} = 0 \tag{C.34}$$

The last term on the LHS of (C.34) can be considered to be small in comparison to the first term, as illustrated in the diagram in figure 4.23, which depicts the results calculated with the correlations found in the beginning of Appendix C. We therefore assume the tangential heat transfer to be negligible compared to the radial one. The solution of the differential equation (C.34) reads

$$r^* \frac{\partial T^*}{\partial r^*} = const. = C_1^* \tag{C.35}$$

$$T^* = C_1^* ln\left(r^*\right) + C_2^* \tag{C.36}$$

The boundary conditions for the inner and the outer surface read

$$h \Delta T^* = -k \frac{\partial T^*}{\partial r^*} \tag{C.37}$$

By combining the boundary condition for the outer surface and the differential equation (considering the outer surface at higher temperature than the inner surface), the unknown constant C_2^* can be explicitly written as function of C_1^*.

$$h_{out} \left[T_{IY}^* - C_1^* ln\left(R_{out}^*\right) - C_2^* \right] = k \frac{C_1^*}{R_{out}^*} \tag{C.38}$$

$$C_2^* = T_{IY}^* - C_1^* \left[\frac{k}{h_{out} R_{out}^*} + ln\left(R_{out}^*\right) \right] \tag{C.39}$$

By combining the boundary condition for the inner surface and the differential equation (considering the outer surface at higher temperature than the inner surface), the unknown constants C_1^* and C_2^* read

$$h_{in} \left[C_1^* ln\left(R_{in}^*\right) + C_2^* - T_{BHX}^* \right] = k \frac{C_1^*}{R_{in}^*} \tag{C.40}$$

$$h_{in} \left[C_1 ln\left(R_{in}^*\right) - T_{BHX}^* + \left(T_{IY}^* - C_1 \left[\frac{k}{h_{out} R_{out}^*} + ln\left(R_{out}^*\right) \right] \right) \right] = k \frac{C_1}{R_{in}^*} \tag{C.41}$$

$$C_1 = \frac{T_{IY}^* - T_{BHX}^*}{ln\left(\frac{R_{out}^*}{R_{in}^*}\right) + \frac{k}{h_{in} R_{in}^*} + \frac{k}{h_{out} R_{out}^*}} \tag{C.42}$$

$$C_2 = T^*_{IY} - \frac{T^*_{IY} - T^*_{BHX}}{ln\left(\frac{R^*_{out}}{R^*_{in}}\right) + \frac{k}{h_{in}R^*_{in}} + \frac{k}{h_{out}R^*_{out}}} \left[\frac{k}{h_{out}R^*_{out}} + ln\left(R^*_{out}\right)\right] \tag{C.43}$$

For the dry section of the inner surface ($0 \leq \varphi \leq \varphi_{LL}$), the constants C^*_{D1} and C^*_{D2} can be written as:

$$C^*_{D1} = \frac{T^*_{IY} - T^*_{BHX}}{ln\left(\frac{R^*_{out}}{R^*_{in}}\right) + \frac{k}{h_{Dry}R^*_{in}} + \frac{k}{h_{out}R^*_{out}}} \tag{C.44}$$

$$C^*_{D2} = T^*_{IY} - C^*_{D1}\left[\frac{k}{h_{out}R^*_{out}} + ln\left(R^*_{out}\right)\right] \tag{C.45}$$

For the wet section of the inner surface ($\varphi_{LL} \leq \varphi \leq \pi$), the constants C^*_{W1} and C^*_{W2} can be written as:

$$C^*_{W1} = \frac{T^*_{IY} - T^*_{BHX}}{ln\left(\frac{R^*_{out}}{R^*_{in}}\right) + \frac{k}{h_{Wet}R^*_{in}} + \frac{k}{h_{out}R^*_{out}}} \tag{C.46}$$

$$C^*_{W2} = T^*_{IY} - C^*_{W1}\left[\frac{k}{h_{out}R^*_{out}} + ln\left(R^*_{out}\right)\right] \tag{C.47}$$

The radial heat transition as a function of φ_{LL} can be calculated for the dry inner surface and the wetted inner surface. Their sum yields the total transferred heat $\dot{Q}_{tot}$ per meter of bayonet heat exchanger.

$$\dot{Q}_{Dry} = 2\varphi_{LL}\left[\frac{1}{h_{out}R_{out}} + \frac{ln\left(R_{out}/R_{in}\right)}{k} + \frac{1}{h_{Dry}R_{in}}\right]^{-1}\left(T_{IY} - T_{BHX}\right) \tag{C.48}$$

$$\dot{Q}_{Wet} = 2\left(\pi - \varphi_{LL}\right)\left[\frac{1}{h_{out}R_{out}} + \frac{ln\left(R_{out}/R_{in}\right)}{k} + \frac{1}{h_{Wet}R_{in}}\right]^{-1}\left(T_{IY} - T_{BHX}\right) \tag{C.49}$$

$$\dot{Q}_{tot} = \dot{Q}_{Wet} + \dot{Q}_{Dry} \tag{C.50}$$

The radial temperature profile in the dry and the wetted perimeter can be calculated with the equations (C.51) and (C.52).

$$T^*_{Dry}\left(r^*\right) = C^*_{D1} ln\left(r^*\right) + C^*_{D2} \tag{C.51}$$

$$T^*_{Wet}\left(r^*\right) = C^*_{W1} ln\left(r^*\right) + C^*_{W2} \tag{C.52}$$

D Discretization of the two-dimensional heat conduction equation in polar coordinates

The two-dimensional heat conduction equation in polar coordinates reads

$$\underbrace{\frac{\partial T}{\partial t}}_{\textit{time derivative}} = \frac{k}{\rho\, c_p}\left(\underbrace{\frac{\partial^2 T}{\partial r^2} + \frac{1}{r}\frac{\partial T}{\partial r}}_{\textit{radial derivative}} + \underbrace{\frac{1}{r^2}\frac{\partial^2 T}{\partial \varphi^2}}_{\textit{tangential derivative}}\right) + \underbrace{\frac{\dot{q}}{\rho\, c_p}}_{\textit{heat source}} \tag{D.1}$$

D.1 Basic discretization with the method of finite differences

The discretization of the time derivative is shown in (D.2). For the discretization of the spatial derivative the central difference can be used as shown in (D.3). Figure D.1 illustrates the notation of the cells in a polar grid.

$$\left(\frac{\partial T}{\partial t}\right)_{i,j}^{n+1} = \frac{T_{i,j}^{n+1} - T_{i,j}^{n}}{\Delta t} \tag{D.2}$$

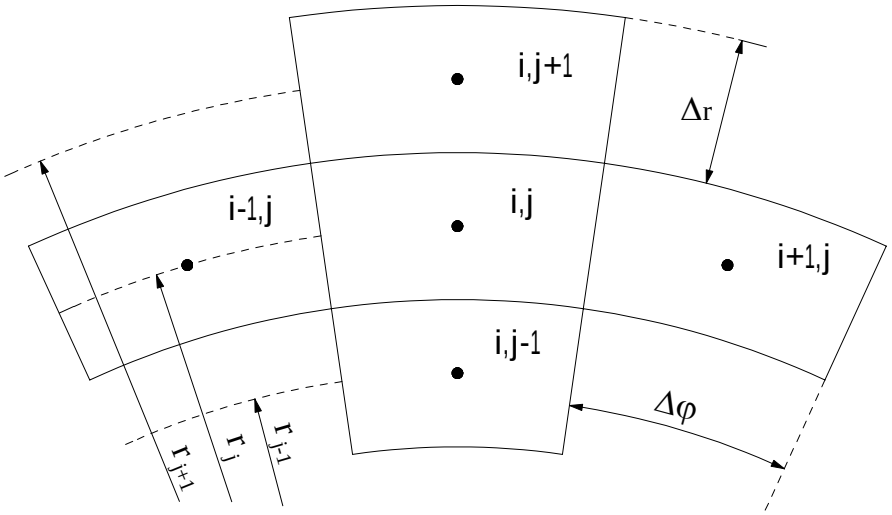

Figure D.1: Indexing of the grid in polar coordinates.

$$\begin{aligned}
\left(\frac{\partial^2 T}{\partial r^2}+\frac{1}{r}\frac{\partial T}{\partial r}+\frac{1}{r^2}\frac{\partial^2 T}{\partial \varphi^2}\right)_i^{n+1} &= \\
= \Theta\left(\frac{T_{i,j+1}^{n+1}-2T_{i,j}^{n+1}+T_{i,j-1}^{n+1}}{\Delta r^2}+\frac{1}{r_j}\frac{T_{i,j+1}^{n+1}-T_{i,j-1}^{n+1}}{2\,\Delta r}\right)+ & \\
+(1-\Theta)\left(\frac{T_{i,j+1}^{n}-2T_{i,j}^{n}+T_{i,j-1}^{n}}{\Delta r^2}+\frac{1}{r_j}\frac{T_{i,j+1}^{n}-T_{i,j-1}^{n}}{2\,\Delta r}\right)+ & \\
+\Theta\left(\frac{1}{r_j^2}\frac{T_{i+1,j}^{n+1}-2T_{i,j}^{n+1}+T_{i-1,j}^{n+1}}{\Delta\varphi^2}\right)+ & \\
+(1-\Theta)\left(\frac{1}{r_j^2}\frac{T_{i+1,j}^{n}-2T_{i,j}^{n}+T_{i-1,j}^{n}}{\Delta\varphi^2}\right) &
\end{aligned} \tag{D.3}$$

The factor Θ can take values between 0 (explicit calculation) and 1 (implicit calculation). In the special case of $\Theta = 0.5$, the method is named after J. Crank and P. Nicolson, which is unconditionally stable (like the implicit method), but with a smaller approximation error than the implicit method.

$$\begin{aligned}
\Theta = 0 &\rightarrow explicit \\
\Theta = \frac{1}{2} &\rightarrow Crank-Nicolson \\
\Theta = 1 &\rightarrow implicit
\end{aligned}$$

By equalizing the discretized time and spatial derivatives, the two-dimensional transient heat transfer equation in its discretized form is obtained.

$$\begin{aligned}
\frac{T_{i,j}^{n+1}-T_{i,j}^{n}}{\Delta t} &= \Theta\frac{k}{\rho\,c_p}\left(\frac{T_{i,j+1}^{n+1}-2T_{i,j}^{n+1}+T_{i,j-1}^{n+1}}{\Delta r^2}+\frac{1}{r_j}\frac{T_{i,j+1}^{n+1}-T_{i,j-1}^{n+1}}{2\,\Delta r}\right)+ \\
&+(1-\Theta)\frac{k}{\rho\,c_p}\left(\frac{T_{i,j+1}^{n}-2T_{i,j}^{n}+T_{i,j-1}^{n}}{\Delta r^2}+\frac{1}{r_j}\frac{T_{i,j+1}^{n}-T_{i,j-1}^{n}}{2\,\Delta r}\right)+ \\
&+\Theta\frac{k}{\rho\,c_p}\left(\frac{1}{r_j^2}\frac{T_{i+1,j}^{n+1}-2T_{i,j}^{n+1}+T_{i-1,j}^{n+1}}{\Delta\varphi^2}\right)+ \\
&+(1-\Theta)\frac{k}{\rho\,c_p}\left(\frac{1}{r_j^2}\frac{T_{i+1,j}^{n}-2T_{i,j}^{n}+T_{i-1,j}^{n}}{\Delta\varphi^2}\right)+\frac{\dot{q}_{i,j}}{\rho\,c_p}
\end{aligned} \tag{D.4}$$

To apply the Crank-Nicolson method on (D.4), the ADI (Alternating Direction Implicit) method is used. At first the discrete time step Δt is halved (D.4) is split up in two equations (D.5) and (D.6).

$$\begin{aligned}
\frac{T_{i,j}^{n+1/2}-T_{i,j}^{n}}{\Delta t} &= \Theta\frac{k}{\rho\,c_p}\left(\frac{1}{r_j^2}\frac{T_{i+1,j}^{n+1/2}-2T_{i,j}^{n+1/2}+T_{i-1,j}^{n+1/2}}{\Delta\varphi^2}\right)+ \\
&+(1-\Theta)\frac{k}{\rho\,c_p}\left(\frac{T_{i,j+1}^{n}-2T_{i,j}^{n}+T_{i,j-1}^{n}}{\Delta r^2}+\frac{1}{r_j}\frac{T_{i,j+1}^{n}-T_{i,j-1}^{n}}{2\,\Delta r}\right)+\frac{\dot{q}_{i,j}}{2\,\rho\,c_p}
\end{aligned} \tag{D.5}$$

$$\frac{T_{i,j}^{n+1} - T_{i,j}^{n+1/2}}{\Delta t} = \Theta \frac{k}{\rho c_p} \left(\frac{T_{i,j+1}^{n+1} - 2T_{i,j}^{n+1} + T_{i,j-1}^{n+1}}{\Delta r^2} + \frac{1}{r_j} \frac{T_{i,j+1}^{n+1} - T_{i,j-1}^{n+1}}{2\Delta r} \right) + \\ + (1-\Theta) \frac{k}{\rho c_p} \left(\frac{1}{r_j^2} \frac{T_{i+1,j}^{n+1/2} - 2T_{i,j}^{n+1/2} + T_{i-1,j}^{n+1/2}}{\Delta \varphi^2} \right) + \frac{\dot{q}_{i,j}}{2\rho c_p} \tag{D.6}$$

After rearranging (D.5) and (D.6), the final forms (D.9) and (D.10) are obtained, which are called i-sweep and j-sweep according to their calculation direction as indicated in figure D.2 [103].

$$T_{i,j}^{n+1/2} - T_{i,j}^{n} = \underbrace{\frac{\Theta \Delta t k}{\rho c_p r_j^2 \Delta \varphi^2}}_{M_\varphi^+} \left(T_{i+1,j}^{n+1/2} - 2T_{i,j}^{n+1/2} + T_{i-1,j}^{n+1/2} \right) + \\ + \underbrace{\frac{(1-\Theta)\,\Delta t k}{\rho c_p \Delta r^2}}_{M_r^0} \left(T_{i,j+1}^{n} - 2T_{i,j}^{n} + T_{i,j-1}^{n} + \underbrace{\frac{\Delta r}{2r_j}}_{\mu} \left(T_{i,j+1}^{n} - T_{i,j-1}^{n} \right) \right) + \underbrace{\dot{q}_{i,j} \frac{\Delta t}{2\rho c_p}}_{S_{i,j}} \tag{D.7}$$

$$T_{i,j}^{n+1} - T_{i,j}^{n+1/2} = \underbrace{\frac{\Theta \Delta t k}{\rho c_p \Delta r^2}}_{M_r^+} \left(T_{i,j+1}^{n+1} - 2T_{i,j}^{n+1} + T_{i,j-1}^{n+1} + \underbrace{\frac{\Delta r}{2r_j}}_{\mu} \left(T_{i,j+1}^{n+1} - T_{i,j-1}^{n+1} \right) \right) + \\ + \underbrace{\frac{(1-\Theta)\,\Delta t k}{\rho c_p r_j^2 \Delta \varphi^2}}_{M_\varphi^0} \left(T_{i+1,j}^{n+1/2} - 2T_{i,j}^{n+1/2} + T_{i-1,j}^{n+1/2} \right) + \underbrace{\dot{q}_{i,j} \frac{\Delta t}{2\rho c_p}}_{S_{i,j}} \tag{D.8}$$

i-sweep:

$$\underbrace{-M_\varphi^+}_{a_{I\,i,j}} T_{i-1,j}^{n+1/2} + \underbrace{\left(1 + 2M_\varphi^+\right)}_{b_{I\,i,j}} T_{i,j}^{n+1/2} \underbrace{-M_\varphi^+}_{c_{I\,i,j}} T_{i+1,j}^{n+1/2} = \\ = \underbrace{\overbrace{M_r^0\,(1-\mu)}^{\alpha_{I\,i,j}} T_{i,j-1}^{n} + \overbrace{\left(1 - 2M_r^0\right)}^{\beta_{I\,i,j}} T_{i,j}^{n} + \overbrace{M_r^0\,(1+\mu)}^{\gamma_{I\,i,j}} T_{i,j+1}^{n}}_{d_{I\,i,j}} + \overbrace{S_{i,j}\,(+\dots)}^{\delta_{I\,i,j}} \tag{D.9}$$

j-sweep:

$$\underbrace{-M_r^+\,(1-\mu)}_{a_{J\,i,j}} T_{i,j-1}^{n+1} + \underbrace{\left(1 + 2M_r^+\right)}_{b_{J\,i,j}} T_{i,j}^{n+1} \underbrace{-M_r^+\,(1+\mu)}_{c_{J\,i,j}} T_{i,j+1}^{n+1} = \\ = \underbrace{\overbrace{M_\varphi^0}^{\alpha_{J\,i,j}} T_{i-1,j}^{n+1/2} + \overbrace{\left(1 - 2M_\varphi^0\right)}^{\beta_{J\,i,j}} T_{i,j}^{n+1/2} + \overbrace{M_\varphi^0}^{\gamma_{J\,i,j}} T_{i+1,j}^{n+1/2}}_{d_{J\,i,j}} + \overbrace{S_{i,j}\,(+\dots)}^{\delta_{J\,i,j}} \tag{D.10}$$

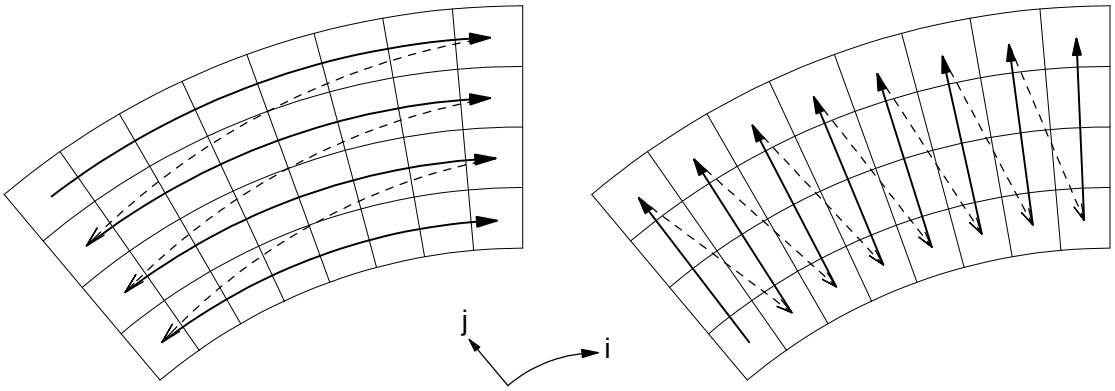

Figure D.2: Calculation pattern of the i-Sweep (left-hand side) and the j-Sweep (right-hand side).

For each cell of the grid two equations like (D.9) and (D.10) can be determined. Each set of equations for the i-sweep and the j-sweep yields a linear system of equations in the form of (D.11).

$$\overline{\overline{A}}\,\overline{x}^T = \overline{B} \tag{D.11}$$

i-sweep:

$$\underbrace{\begin{bmatrix} b_{I0,j} & c_{I0,j} & 0 & 0 & \dots & \dots & \dots & 0 \\ a_{I1,j} & b_{I1,j} & c_{I1,j} & 0 & \dots & \dots & \dots & 0 \\ 0 & a_{I2,j} & b_{I2,j} & c_{I2,j} & \dots & \dots & \dots & 0 \\ \vdots & \vdots & \vdots & \vdots & \ddots & \ddots & \ddots & \vdots \\ 0 & 0 & 0 & 0 & \dots & a_{Ik-1,j} & b_{Ik-1,j} & c_{Ik-1,j} \\ 0 & 0 & 0 & 0 & \dots & 0 & a_{Ik,j} & b_{Ik,j} \end{bmatrix}}_{\overline{\overline{A}}} \underbrace{\begin{bmatrix} T_{0,j}^{n+1/2} \\ T_{1,j}^{n+1/2} \\ T_{2,j}^{n+1/2} \\ \vdots \\ T_{k-1,j}^{n+1/2} \\ T_{k,j}^{n+1/2} \end{bmatrix}}_{\overline{x}^T} = \underbrace{\begin{bmatrix} d_{0,j} + \delta_{0,j} \\ d_{1,j} + \delta_{1,j} \\ d_{2,j} + \delta_{2,j} \\ \vdots \\ d_{k-1,j} + \delta_{k-1,j} \\ d_{k,j} + \delta_{k,j} \end{bmatrix}}_{\overline{B}} \tag{D.12}$$

j-sweep:

$$\underbrace{\begin{bmatrix} b_{Ji,0} & c_{Ji,0} & 0 & 0 & \dots & \dots & \dots & 0 \\ a_{Ji,1} & b_{Ji,1} & c_{Ji,1} & 0 & \dots & \dots & \dots & 0 \\ 0 & a_{Ji,2} & b_{Ji,2} & c_{Ji,2} & \dots & \dots & \dots & 0 \\ \vdots & \vdots & \vdots & \vdots & \ddots & \ddots & \ddots & \vdots \\ 0 & 0 & 0 & 0 & \dots & a_{Ji,l-i} & b_{Ji,l-1} & c_{Jk-1,j} \\ 0 & 0 & 0 & 0 & \dots & 0 & a_{Ji,l} & b_{Ji,l} \end{bmatrix}}_{\overline{\overline{A}}} \underbrace{\begin{bmatrix} T_{i,0}^{n+1} \\ T_{i,1}^{n+1} \\ T_{i,2}^{n+1} \\ \vdots \\ T_{i,l-1}^{n+1} \\ T_{i,l}^{n+1} \end{bmatrix}}_{\overline{x}^T} = \underbrace{\begin{bmatrix} d_{i,0} + \delta_{i,0} \\ d_{i,1} + \delta_{i,1} \\ d_{i,2} + \delta_{i,2} \\ \vdots \\ d_{i,l-1} + \delta_{i,l-1} \\ d_{i,l} + \delta_{i,l} \end{bmatrix}}_{\overline{B}} \tag{D.13}$$

These linear equation systems contain the temperatures of the time steps $n + 1/2$ and $n + 1$ implicitly and can be solved with the Thomas-Algorithm [104]. For the sake of presentability the coefficients of the different temperatures are summarized in tables. The δ-terms in $\overline{B}$ due to heat **S**ources, **B**oundary Conditions and **T**ransitional Conditions are shown in the column titled with **"SBT"**.

Table D.1: Basic coefficients i-sweep

i-sweep	$\boldsymbol{a_{I\,i,j}}$ / $\boldsymbol{\alpha_{I\,i,j}}$	$\boldsymbol{b_{I\,i,j}}$ / $\boldsymbol{\beta_{I\,i,j}}$	$\boldsymbol{c_{I\,i,j}}$ / $\boldsymbol{\gamma_{I\,i,j}}$
$\boldsymbol{n+1/2}$	$-M_\varphi^+$	$1+2\,M_\varphi^+$	$-M_\varphi^+$
$\boldsymbol{n}$	$M_r^0\,(1-\mu)$	$1-2\,M_r^0$	$M_r^0\,(1+\mu)$
SBT	$S_{i,j}$		

Table D.2: Basic coefficients j-sweep

j-sweep	$\boldsymbol{a_{J\,i,j}}$ / $\boldsymbol{\alpha_{J\,i,j}}$	$\boldsymbol{b_{J\,i,j}}$ / $\boldsymbol{\beta_{J\,i,j}}$	$\boldsymbol{c_{J\,i,j}}$ / $\boldsymbol{\gamma_{J\,i,j}}$
$\boldsymbol{n+1/2}$	$-M_r^+\,(1-\mu)$	$1+2\,M_r^+$	$-M_r^+\,(1+\mu)$
$\boldsymbol{n}$	M_φ^0	$1-2\,M_\varphi^0$	M_φ^0
SBT	$S_{i,j}$		

The coefficients shown in the tables D.1 and D.2 can only applied to cells in the middle of the modelled domain. For cells located at a boundary or at a transition zone, the coefficients must be adapted.

D.2 Boundary Conditions

At the boundaries of the modelled body the standard coefficients have to be substituted by terms containing a mathematical correlation for the corresponding condition.

D.2.1 Dirichlet: Constant boundary temperature ($T_B = const.$)

If the boundary of the body has a constant temperature, the condition is named after J. Dirichlet. In the following text the necessary coefficients to fulfil the boundary condition are presented for the i-sweep and the j-sweep and dependning on the location of the boundary with respect to the cell (i-coordinate: left/right — j-coordinate: inside/outside). The derivation of the temperature T_B of the fictional cell simulating the boundary (ghost cell) is illustrated above the respective tables.

- **Tangential left boundary ($\boldsymbol{i-1}$)**

$$T_{i-1/2,j} = T_B \tag{D.14}$$

$$T_{i-1,j} = T_{i,j} - 2\,(T_{i,j} - T_B) = 2T_B - T_{i,j} \tag{D.15}$$

Table D.3: Dirichlet coefficients left i-sweep

i-sweep	$\boldsymbol{a_{I\,i,j}}$ / $\boldsymbol{\alpha_{I\,i,j}}$	$\boldsymbol{b_{I\,i,j}}$ / $\boldsymbol{\beta_{I\,i,j}}$	$\boldsymbol{c_{I\,i,j}}$ / $\boldsymbol{\gamma_{I\,i,j}}$
$\boldsymbol{n+1/2}$	0	$1+3\,M_\varphi^+$	$-M_\varphi^+$
$\boldsymbol{n}$	$M_r^0\,(1-\mu)$	$1-2\,M_r^0$	$M_r^0\,(1+\mu)$
SBT	$S_{i,j} + 2\,M_\varphi^+ T_B$		

Table D.4: Dirichlet coefficients left j-sweep

j-sweep	$\boldsymbol{a_{J\,i,j}}$ / $\boldsymbol{\alpha_{J\,i,j}}$	$\boldsymbol{b_{J\,i,j}}$ / $\boldsymbol{\beta_{J\,i,j}}$	$\boldsymbol{c_{J\,i,j}}$ / $\boldsymbol{\gamma_{J\,i,j}}$
$\boldsymbol{n+1}$	$-M_r^+\,(1-\mu)$	$1+2\,M_r^+$	$-M_r^+\,(1+\mu)$
$\boldsymbol{n+1/2}$	0	$1-3\,M_\varphi^0$	M_φ^0
SBT	$S_{i,j}+2\,M_\varphi^0 T_B$		

- **Tangential right boundary $(i+1)$**

$$T_{i+1/2,j} = T_B \tag{D.16}$$

$$T_{i+1,j} = T_{i,j} - 2\,(T_{i,j} - T_B) = 2T_B - T_{i,j} \tag{D.17}$$

Table D.5: Dirichlet coefficients right i-sweep

i-sweep	$\boldsymbol{a_{I\,i,j}}$ / $\boldsymbol{\alpha_{I\,i,j}}$	$\boldsymbol{b_{I\,i,j}}$ / $\boldsymbol{\beta_{I\,i,j}}$	$\boldsymbol{c_{I\,i,j}}$ / $\boldsymbol{\gamma_{I\,i,j}}$
$\boldsymbol{n+1/2}$	$-M_\varphi^+$	$1+3\,M_\varphi^+$	0
$\boldsymbol{n}$	$M_r^0\,(1-\mu)$	$1-2\,M_r^0$	$M_r^0\,(1+\mu)$
SBT	$S_{i,j}+2\,M_\varphi^+ T_B$		

Table D.6: Dirichlet coefficients right j-sweep

j-sweep	$\boldsymbol{a_{J\,i,j}}$ / $\boldsymbol{\alpha_{J\,i,j}}$	$\boldsymbol{b_{J\,i,j}}$ / $\boldsymbol{\beta_{J\,i,j}}$	$\boldsymbol{c_{J\,i,j}}$ / $\boldsymbol{\gamma_{J\,i,j}}$
$\boldsymbol{n+1}$	$-M_r^+\,(1-\mu)$	$1+2\,M_r^+$	$-M_r^+\,(1+\mu)$
$\boldsymbol{n+1/2}$	M_φ^0	$1-3\,M_\varphi^0$	0
SBT	$S_{i,j}+2\,M_\varphi^0 T_B$		

- **Radial inner boundary $(j-1)$**

$$T_{i,j-1/2} = T_B \tag{D.18}$$

$$T_{i,j-1} = T_{i,j} - 2\,(T_{i,j} - T_B) = 2T_B - T_{i,j} \tag{D.19}$$

Table D.7: Dirichlet coefficients inner i-sweep

i-sweep	$\boldsymbol{a_{I\,i,j}}$ / $\boldsymbol{\alpha_{I\,i,j}}$	$\boldsymbol{b_{I\,i,j}}$ / $\boldsymbol{\beta_{I\,i,j}}$	$\boldsymbol{c_{I\,i,j}}$ / $\boldsymbol{\gamma_{I\,i,j}}$
$\boldsymbol{n+1/2}$	$-M_\varphi^+$	$1+2\,M_\varphi^+$	$-M_\varphi^+$
$\boldsymbol{n}$	0	$1-M_r^0\,(3-\mu)$	$M_r^0\,(1+\mu)$
SBT	$S_{i,j}+2\,M_r^0\,(1-\mu)\,T_B$		

Table D.8: Dirichlet coefficients inner j-sweep

j-sweep	$\boldsymbol{a_{J\,i,j}}$ / $\boldsymbol{\alpha_{J\,i,j}}$	$\boldsymbol{b_{J\,i,j}}$ / $\boldsymbol{\beta_{J\,i,j}}$	$\boldsymbol{c_{J\,i,j}}$ / $\boldsymbol{\gamma_{J\,i,j}}$
$\boldsymbol{n+1}$	0	$1 + M_r^+ \,(3-\mu)$	$-M_r^+ \,(1+\mu)$
$\boldsymbol{n+1/2}$	M_φ^0	$1 - 2\,M_\varphi^0$	M_φ^0
SBT	$S_{i,j} + 2\,M_r^+ \,(1-\mu)\,T_B$		

- **Radial outer boundary $(j+1)$**

$$T_{i,j+1/2} = T_B \tag{D.20}$$

$$T_{i,j+1} = T_{i,j} - 2\,(T_{i,j} - T_B) = 2T_B - T_{i,j} \tag{D.21}$$

Table D.9: Dirichlet coefficients outer i-sweep

i-sweep	$\boldsymbol{a_{I\,i,j}}$ / $\boldsymbol{\alpha_{I\,i,j}}$	$\boldsymbol{b_{I\,i,j}}$ / $\boldsymbol{\beta_{I\,i,j}}$	$\boldsymbol{c_{I\,i,j}}$ / $\boldsymbol{\gamma_{I\,i,j}}$
$\boldsymbol{n+1/2}$	$-M_\varphi^+$	$1 + 2\,M_\varphi^+$	$-M_\varphi^+$
$\boldsymbol{n}$	$M_r^0 \,(1-\mu)$	$1 - M_r^0 \,(3+\mu)$	0
SBT	$S_{i,j} + 2\,M_r^0 \,(1+\mu)\,T_B$		

Table D.10: Dirichlet coefficients outer j-sweep

j-sweep	$\boldsymbol{a_{J\,i,j}}$ / $\boldsymbol{\alpha_{J\,i,j}}$	$\boldsymbol{b_{J\,i,j}}$ / $\boldsymbol{\beta_{J\,i,j}}$	$\boldsymbol{c_{J\,i,j}}$ / $\boldsymbol{\gamma_{J\,i,j}}$
$\boldsymbol{n+1}$	$-M_r^+ \,(1-\mu)$	$1 + M_r^+ \,(3+\mu)$	0
$\boldsymbol{n+1/2}$	M_φ^0	$1 - 2\,M_\varphi^0$	M_φ^0
SBT	$S_{i,j} + 2\,M_r^+ \,(1+\mu)\,T_B$		

D.2.2 Von Neumann: Temperature independent heat supply/removal: ($\dot{q}_B \neq f\,(T)$)

If the boundary of the body has a constant (temperature-independent) heat flux $\dot{q}_B$, the condition is named after J. von Neumann. In the following text the necessary coefficients to fulfil the boundary condition are presented for the i-sweep and the j-sweep and dependning on the location of the boundary with respect to the cell (i-coordinate: left/right — j-coordinate: inside/outside). The derivation of the temperature T_B of the fictional cell simulating the boundary (ghost cell) is illustrated above the respective tables. For an adiabatic boundary $\dot{q}_B = 0$ and k denotes the thermal conductivity.

- **Tangential left boundary $(i-1)$**

$$\dot{q}_B = -k\,\frac{\Delta T}{r_j\,\Delta\varphi} \tag{D.22}$$

$$T_{i-1,j} = \frac{\dot{q}_B}{k} r_j \Delta\varphi + T_{i,j} \tag{D.23}$$

Table D.11: Von Neumann coefficients left i-sweep

i-sweep	$\boldsymbol{a_{I\,i,j}}$ / $\boldsymbol{\alpha_{I\,i,j}}$	$\boldsymbol{b_{I\,i,j}}$ / $\boldsymbol{\beta_{I\,i,j}}$	$\boldsymbol{c_{I\,i,j}}$ / $\boldsymbol{\gamma_{I\,i,j}}$
$\boldsymbol{n+1/2}$	0	$1 + M_\varphi^+$	$-M_\varphi^+$
$\boldsymbol{n}$	$M_r^0\,(1-\mu)$	$1 - 2\,M_r^0$	$M_r^0\,(1+\mu)$
SBT	$S_{i,j} + M_\varphi^+ \frac{\dot{q}_B}{k} r_j \Delta\varphi$		

Table D.12: Von Neumann coefficients left j-sweep

j-sweep	$\boldsymbol{a_{J\,i,j}}$ / $\boldsymbol{\alpha_{J\,i,j}}$	$\boldsymbol{b_{J\,i,j}}$ / $\boldsymbol{\beta_{J\,i,j}}$	$\boldsymbol{c_{J\,i,j}}$ / $\boldsymbol{\gamma_{J\,i,j}}$
$\boldsymbol{n+1}$	$-M_r^+\,(1-\mu)$	$1 + 2\,M_r^+$	$-M_r^+\,(1+\mu)$
$\boldsymbol{n+1/2}$	0	$1 - M_\varphi^0$	M_φ^0
SBT	$S_{i,j} + M_\varphi^0 \frac{\dot{q}_B}{k} r_j \Delta\varphi$		

- **Tangential right boundary $(i+1)$**

$$\dot{q}_B = -k \frac{\Delta T}{r_j \Delta\varphi} \tag{D.24}$$

$$T_{i+1,j} = \frac{\dot{q}_B}{k} r_j \Delta\varphi + T_{i,j} \tag{D.25}$$

Table D.13: Von Neumann coefficients right i-sweep

i-sweep	$\boldsymbol{a_{I\,i,j}}$ / $\boldsymbol{\alpha_{I\,i,j}}$	$\boldsymbol{b_{I\,i,j}}$ / $\boldsymbol{\beta_{I\,i,j}}$	$\boldsymbol{c_{I\,i,j}}$ / $\boldsymbol{\gamma_{I\,i,j}}$
$\boldsymbol{n+1/2}$	$-M_\varphi^+$	$1 + M_\varphi^+$	0
$\boldsymbol{n}$	$M_r^0\,(1-\mu)$	$1 - 2\,M_r^0$	$M_r^0\,(1+\mu)$
SBT	$S_{i,j} + M_\varphi^+ \frac{\dot{q}_B}{k} r_j \Delta\varphi$		

Table D.14: Von Neumann coefficients right j-sweep

j-sweep	$\boldsymbol{a_{J\,i,j}}$ / $\boldsymbol{\alpha_{J\,i,j}}$	$\boldsymbol{b_{J\,i,j}}$ / $\boldsymbol{\beta_{J\,i,j}}$	$\boldsymbol{c_{J\,i,j}}$ / $\boldsymbol{\gamma_{J\,i,j}}$
$\boldsymbol{n+1}$	$-M_r^+\,(1-\mu)$	$1 + 2\,M_r^+$	$-M_r^+\,(1+\mu)$
$\boldsymbol{n+1/2}$	M_φ^0	$1 - M_\varphi^0$	0
SBT	$S_{i,j} + M_\varphi^0 \frac{\dot{q}_B}{k} r_j \Delta\varphi$		

- **Radial inner boundary $(j-1)$**

$$\dot{q}_B = -k\,\frac{\Delta T}{\Delta r} \tag{D.26}$$

$$T_{i,j-1} = \frac{\dot{q}_B}{k}\,\Delta r + T_{i,j} \tag{D.27}$$

Table D.15: Von Neumann coefficients inner i-sweep

i-sweep	$\boldsymbol{a_{I\,i,j}}$ / $\boldsymbol{\alpha_{I\,i,j}}$	$\boldsymbol{b_{I\,i,j}}$ / $\boldsymbol{\beta_{I\,i,j}}$	$\boldsymbol{c_{I\,i,j}}$ / $\boldsymbol{\gamma_{I\,i,j}}$
$\boldsymbol{n+1/2}$	$-M_\varphi^+$	$1+2\,M_\varphi^+$	$-M_\varphi^+$
$\boldsymbol{n}$	0	$1-M_r^0\,(1+\mu)$	$M_r^0\,(1+\mu)$
SBT	$S_{i,j}+M_r^0\,(1-\mu)\,\frac{\dot{q}_B}{k}\,\Delta r$		

Table D.16: Von Neumann coefficients inner j-sweep

j-sweep	$\boldsymbol{a_{J\,i,j}}$ / $\boldsymbol{\alpha_{J\,i,j}}$	$\boldsymbol{b_{J\,i,j}}$ / $\boldsymbol{\beta_{J\,i,j}}$	$\boldsymbol{c_{J\,i,j}}$ / $\boldsymbol{\gamma_{J\,i,j}}$
$\boldsymbol{n+1}$	0	$1+M_r^+\,(1+\mu)$	$-M_r^+\,(1+\mu)$
$\boldsymbol{n+1/2}$	M_φ^0	$1-2\,M_\varphi^0$	M_φ^0
SBT	$S_{i,j}+M_r^+\,(1-\mu)\,\frac{\dot{q}_B}{k}\,\Delta r$		

- **Radial outer boundary $(j+1)$**

$$\dot{q}_B = -k\,\frac{\Delta T}{\Delta r} \tag{D.28}$$

$$T_{i,j+1} = \frac{\dot{q}_B}{k}\,\Delta r + T_{i,j} \tag{D.29}$$

Table D.17: Von Neumann coefficients outer i-sweep

i-sweep	$\boldsymbol{a_{I\,i,j}}$ / $\boldsymbol{\alpha_{I\,i,j}}$	$\boldsymbol{b_{I\,i,j}}$ / $\boldsymbol{\beta_{I\,i,j}}$	$\boldsymbol{c_{I\,i,j}}$ / $\boldsymbol{\gamma_{I\,i,j}}$
$\boldsymbol{n+1/2}$	$-M_\varphi^+$	$1+2\,M_\varphi^+$	$-M_\varphi^+$
$\boldsymbol{n}$	$M_r^0\,(1-\mu)$	$1-M_r^0\,(1-\mu)$	0
SBT	$S_{i,j}+M_r^0\,(1+\mu)\,\frac{\dot{q}_B}{k}\,\Delta r$		

Table D.18: Von Neumann coefficients outer j-sweep

j-sweep	$\boldsymbol{a_{J\,i,j}}$ / $\boldsymbol{\alpha_{J\,i,j}}$	$\boldsymbol{b_{J\,i,j}}$ / $\boldsymbol{\beta_{J\,i,j}}$	$\boldsymbol{c_{J\,i,j}}$ / $\boldsymbol{\gamma_{J\,i,j}}$
$\boldsymbol{n+1}$	$-M_r^+\,(1-\mu)$	$1+M_r^+\,(1-\mu)$	0
$\boldsymbol{n+1/2}$	M_φ^0	$1-2\,M_\varphi^0$	M_φ^0
SBT	$S_{i,j}+M_r^+\,(1+\mu)\,\frac{\dot{q}_B}{k}\,\Delta r$		

D.2.3 Robin/Cauchy: Mixed boundary condition

If the boundary of the body is in touch with a fluid, the condition named after V. Robin and A. Cauchy can be used. In the following text the necessary coefficients to fulfil the boundary condition are presented for the i-sweep and the j-sweep and depending on the location of the boundary with respect to the cell (i-coordinate: left/right — j-coordinate: inside/outside). The derivation of the temperature T_B of the fictional cell simulating the boundary (ghost cell) is illustrated above the respective tables. h denotes the heat transfer coefficient and T_{Ref} denotes the temperature of the fluid.

- **Tangential left boundary ($i-1$)**

$$\dot{q} = h\left(T_{i-1/2,j} - T_{Ref}\right) = -k\frac{\Delta T}{r_j\,\Delta\varphi} \tag{D.30}$$

$$\begin{aligned}\left(\frac{3}{2}T_{i,j} - \frac{T_{i+1,j}}{2} - T_{Ref}\right)h &= k\frac{T_{i,j}-T_{i-1,j}}{r_j\,\Delta\varphi} \rightarrow \\ T_{i-1,j} = T_{i,j} - \underbrace{\frac{h}{k}r_j\,\Delta\varphi}_{Bi}&\left(\frac{3}{2}T_{i,j} - \frac{T_{i+1,j}}{2} - T_{Ref}\right)\end{aligned} \tag{D.31}$$

Table D.19: Robin/Cauchy coefficients left i-sweep

i-sweep	$\boldsymbol{a_{I\,i,j}}$ / $\boldsymbol{\alpha_{I\,i,j}}$	$\boldsymbol{b_{I\,i,j}}$ / $\boldsymbol{\beta_{I\,i,j}}$	$\boldsymbol{c_{I\,i,j}}$ / $\boldsymbol{\gamma_{I\,i,j}}$
$\boldsymbol{n+1/2}$	0	$1 + M_\varphi^+\left(1+\frac{3}{2}Bi\right)$	$-M_\varphi^+\left(1+\frac{Bi}{2}\right)$
$\boldsymbol{n}$	$M_r^0\,(1-\mu)$	$1 - 2\,M_r^0$	$M_r^0\,(1+\mu)$
SBT	$S_{i,j} + M_\varphi^+\,Bi\,T_{Ref}$		

Table D.20: Robin/Cauchy coefficients left j-sweep

j-sweep	$\boldsymbol{a_{J\,i,j}}$ / $\boldsymbol{\alpha_{J\,i,j}}$	$\boldsymbol{b_{J\,i,j}}$ / $\boldsymbol{\beta_{J\,i,j}}$	$\boldsymbol{c_{J\,i,j}}$ / $\boldsymbol{\gamma_{J\,i,j}}$
$\boldsymbol{n+1}$	$-M_r^+\,(1-\mu)$	$1 + 2\,M_r^+$	$-M_r^+\,(1+\mu)$
$\boldsymbol{n+1/2}$	0	$1 - M_\varphi^0\left(1+\frac{3}{2}Bi\right)$	$M_\varphi^0\left(1+\frac{Bi}{2}\right)$
SBT	$S_{i,j} + M_\varphi^0\,Bi\,T_{Ref}$		

- **Tangential right boundary ($i-1$)**

$$\dot{q} = h\left(T_{i+1/2,j} - T_{Ref}\right) = -k\frac{\Delta T}{r_j\,\Delta\varphi} \tag{D.32}$$

$$\begin{aligned}\left(\frac{3}{2}T_{i,j} - \frac{T_{i-1,j}}{2} - T_{Ref}\right)h &= k\frac{T_{i,j}-T_{i+1,j}}{r_j\,\Delta\varphi} \rightarrow \\ T_{i+1,j} = T_{i,j} - \underbrace{\frac{h}{k}r_j\,\Delta\varphi}_{Bi}&\left(\frac{3}{2}T_{i,j} - \frac{T_{i-1,j}}{2} - T_{Ref}\right)\end{aligned} \tag{D.33}$$

Table D.21: Robin/Cauchy coefficients right i-sweep

i-sweep	$\boldsymbol{a_{I\,i,j}}$ / $\boldsymbol{\alpha_{I\,i,j}}$	$\boldsymbol{b_{I\,i,j}}$ / $\boldsymbol{\beta_{I\,i,j}}$	$\boldsymbol{c_{I\,i,j}}$ / $\boldsymbol{\gamma_{I\,i,j}}$
$\boldsymbol{n+1/2}$	$-M_\varphi^+\left(1+\frac{Bi}{2}\right)$	$1+M_\varphi^+\left(1+\frac{3}{2}Bi\right)$	0
$\boldsymbol{n}$	$M_r^0\,(1-\mu)$	$1-2\,M_r^0$	$M_r^0\,(1+\mu)$
SBT	$S_{i,j}+M_\varphi^+\,Bi\,T_{Ref}$		

Table D.22: Robin/Cauchy coefficients right j-sweep

j-sweep	$\boldsymbol{a_{J\,i,j}}$ / $\boldsymbol{\alpha_{J\,i,j}}$	$\boldsymbol{b_{J\,i,j}}$ / $\boldsymbol{\beta_{J\,i,j}}$	$\boldsymbol{c_{J\,i,j}}$ / $\boldsymbol{\gamma_{J\,i,j}}$
$\boldsymbol{n+1}$	$-M_r^+\,(1-\mu)$	$1+2\,M_r^+$	$-M_r^+\,(1+\mu)$
$\boldsymbol{n+1/2}$	$M_\varphi^0\left(1+\frac{Bi}{2}\right)$	$1-M_\varphi^0\left(1+\frac{3}{2}Bi\right)$	0
SBT	$S_{i,j}+M_\varphi^0\,Bi\,T_{Ref}$		

- **Radial inner boundary $(j-1)$**

$$\dot{q}=h\left(T_{i,j-1/2}-T_{Ref}\right)=-k\,\frac{\Delta T}{\Delta r} \tag{D.34}$$

$$\begin{aligned}&\left(\frac{3}{2}T_{i,j}-\frac{T_{i,j+1}}{2}-T_{Ref}\right)h=k\,\frac{T_{i,j}-T_{i,j-1}}{\Delta r}\rightarrow\\&T_{i,j-1}=T_{i,j}-\underbrace{\frac{h}{k}\Delta r}_{Bi}\left(\frac{3}{2}T_{i,j}-\frac{T_{i,j+1}}{2}-T_{Ref}\right)\end{aligned} \tag{D.35}$$

Table D.23: Robin/Cauchy coefficients inner i-sweep

i-sweep	$\boldsymbol{a_{I\,i,j}}$ / $\boldsymbol{\alpha_{I\,i,j}}$	$\boldsymbol{b_{I\,i,j}}$ / $\boldsymbol{\beta_{I\,i,j}}$	$\boldsymbol{c_{I\,i,j}}$ / $\boldsymbol{\gamma_{I\,i,j}}$
$\boldsymbol{n+1/2}$	$-M_\varphi^+$	$1+2\,M_\varphi^+$	$-M_\varphi^+$
$\boldsymbol{n}$	0	$1-M_r^0\left[2-(1-\mu)\left(1-\frac{3}{2}Bi\right)\right]$	$M_r^0\left[\frac{Bi}{2}\,(1-\mu)+(1+\mu)\right]$
SBT	$S_{i,j}+M_r^0\,(1-\mu)\,Bi\,T_{Ref}$		

Table D.24: Robin/Cauchy coefficients inner j-sweep

j-sweep	$\boldsymbol{a_{J\,i,j}}$ / $\boldsymbol{\alpha_{J\,i,j}}$	$\boldsymbol{b_{J\,i,j}}$ / $\boldsymbol{\beta_{J\,i,j}}$	$\boldsymbol{c_{J\,i,j}}$ / $\boldsymbol{\gamma_{J\,i,j}}$
$\boldsymbol{n+1}$	0	$1+M_r^+\left[2-(1-\mu)\left(1-\frac{3}{2}Bi\right)\right]$	$-M_r^+\left[\frac{Bi}{2}\,(1-\mu)+(1+\mu)\right]$
$\boldsymbol{n+1/2}$	M_φ^0	$1-2\,M_\varphi^0$	M_φ^0
SBT	$S_{i,j}+M_r^0\,(1-\mu)\,Bi\,T_{Ref}$		

- **Radial outer boundary $(j+1)$**

$$\dot{q} = h\left(T_{i,j+1/2} - T_{Ref}\right) = -k\frac{\Delta T}{\Delta r} \tag{D.36}$$

$$\begin{aligned}\left(\frac{3}{2}T_{i,j} - \frac{T_{i,j-1}}{2} - T_{Ref}\right) h &= k\frac{T_{i,j} - T_{i,j+1}}{\Delta r} \rightarrow \\ T_{i,j+1} &= T_{i,j} - \underbrace{\frac{h}{k}\Delta r}_{Bi}\left(\frac{3}{2}T_{i,j} - \frac{T_{i,j-1}}{2} - T_{Ref}\right)\end{aligned} \tag{D.37}$$

Table D.25: Robin/Cauchy coefficients outer i-sweep

i-sweep	$\boldsymbol{a_{I\,i,j}}$ / $\boldsymbol{\alpha_{I\,i,j}}$	$\boldsymbol{b_{I\,i,j}}$ / $\boldsymbol{\beta_{I\,i,j}}$	$\boldsymbol{c_{I\,i,j}}$ / $\boldsymbol{\gamma_{I\,i,j}}$
$\boldsymbol{n+1/2}$	$-M_\varphi^+$	$1+2\,M_\varphi^+$	$-M_\varphi^+$
$\boldsymbol{n}$	$M_r^0\left[\frac{Bi}{2}\,(1+\mu)+(1-\mu)\right]$	$1-M_r^0\left[2-(1+\mu)\left(1-\frac{3}{2}\,Bi\right)\right]$	0
SBT	$S_{i,j}+M_r^0\,(1+\mu)\,BiT_{Ref}$		

Table D.26: Robin/Cauchy coefficients outer j-sweep

j-sweep	$\boldsymbol{a_{J\,i,j}}$ / $\boldsymbol{\alpha_{J\,i,j}}$	$\boldsymbol{b_{J\,i,j}}$ / $\boldsymbol{\beta_{J\,i,j}}$	$\boldsymbol{c_{J\,i,j}}$ / $\boldsymbol{\gamma_{J\,i,j}}$
$\boldsymbol{n+1}$	$-M_r^+\left[\frac{Bi}{2}\,(1+\mu)+(1-\mu)\right]$	$1+M_r^+\left[2-(1+\mu)\left(1-\frac{3}{2}\,Bi\right)\right]$	0
$\boldsymbol{n+1/2}$	M_φ^0	$1-2\,M_\varphi^0$	M_φ^0
SBT	$S_{i,j}+M_r^+\,(1+\mu)\,BiT_{Ref}$		

D.3 Transitional Conditions

At inhomogeneities in the modelled domain (e.g. two mesh regions of different material and/or variable cell sizes) transitional conditions must be applied. In the following text the necessary coefficients to fulfil the transitional condition are presented for the i-sweep and the j-sweep and depending on the location of the boundary with respect to the cell (i-coordinate: left/right — j-coordinate: inside/outside). The derivation of the temperature T_IF of the fictional cell simulating the interface (ghost cell) is illustrated above the respective tables.

- **Tangential left boundary $(i-1)$**

$$k_{i,j}\frac{T_{i,j} - T_{IF}}{r_j\,\Delta\varphi_{i,j}/2} = k_{i-1,j}\frac{T_{IF} - T_{i-1,j}}{r_j\,\Delta\varphi_{i-1,j}/2} \tag{D.38}$$

$$T_{IF} = \left(T_{i,j} + T_{i-1,j}\,\frac{k_{i-1,j}}{k_{i,j}}\,\frac{r_j\,\Delta\varphi_{i,j}}{r_j\,\Delta\varphi_{i-1,j}}\right) \Big/ \left(1 + \frac{k_{i-1,j}}{k_{i,j}}\,\frac{r_j\,\Delta\varphi_{i,j}}{r_j\,\Delta\varphi_{i-1,j}}\right) \tag{D.39}$$

$$k_{i,j}\,\frac{T_{i,j}-T_{IF}}{r_j\,\Delta\varphi_{i,j}/2}=k_{i,j}\,\frac{T_{i,j}-T_{i-1,j}}{r_j\,\Delta\varphi_{i,j}} \tag{D.40}$$

$$T_{i-1,j}=2\,T_{IF}-T_{i,j} \tag{D.41}$$

Table D.27: Interface coefficients left i-sweep

i-sweep	$\boldsymbol{a_{I\,i,j}}$ / $\boldsymbol{\alpha_{I\,i,j}}$	$\boldsymbol{b_{I\,i,j}}$ / $\boldsymbol{\beta_{I\,i,j}}$	$\boldsymbol{c_{I\,i,j}}$ / $\boldsymbol{\gamma_{I\,i,j}}$
$\boldsymbol{n+1/2}$	0	$1+3\,M_\varphi^+$	$-M_\varphi^+$
$\boldsymbol{n}$	$M_r^0\,(1-\mu)$	$1-2\,M_r^0$	$M_r^0\,(1+\mu)$
SBT	$S_{i,j}+2\,M_\varphi^+\,T_{IF}$		

Table D.28: Interface coefficients left j-sweep

j-sweep	$\boldsymbol{a_{J\,i,j}}$ / $\boldsymbol{\alpha_{J\,i,j}}$	$\boldsymbol{b_{J\,i,j}}$ / $\boldsymbol{\beta_{J\,i,j}}$	$\boldsymbol{c_{J\,i,j}}$ / $\boldsymbol{\gamma_{J\,i,j}}$
$\boldsymbol{n+1}$	$-M_r^+\,(1-\mu)$	$1+2\,M_r^+$	$-M_r^+\,(1+\mu)$
$\boldsymbol{n+1/2}$	0	$1-3\,M_\varphi^0$	M_φ^0
SBT	$S_{i,j}+2\,M_\varphi^0\,T_{IF}$		

- **Tangential right boundary $(i+1)$**

$$k_{i,j}\,\frac{T_{i,j}-T_{IF}}{r_j\,\Delta\varphi_{i,j}/2}=k_{i+1,j}\,\frac{T_{IF}-T_{i+1,j}}{r_j\,\Delta\varphi_{i+1,j}/2} \tag{D.42}$$

$$T_{IF}=\left(T_{i,j}+T_{i+1,j}\,\frac{k_{i+1,j}}{k_{i,j}}\,\frac{r_j\,\Delta\varphi_{i,j}}{r_j\,\Delta\varphi_{i+1,j}}\right)\Bigg/\left(1+\frac{k_{i+1,j}}{k_{i,j}}\,\frac{r_j\,\Delta\varphi_{i,j}}{r_j\,\Delta\varphi_{i+1,j}}\right) \tag{D.43}$$

$$k_{i,j}\,\frac{T_{i,j}-T_{IF}}{r_j\,\Delta\varphi_{i,j}/2}=k_{i,j}\,\frac{T_{i,j}-T_{i+1,j}}{r_j\,\Delta\varphi_{i,j}} \tag{D.44}$$

$$T_{i+1,j}=2\,T_{IF}-T_{i,j} \tag{D.45}$$

Table D.29: Interface coefficients right i-sweep

i-sweep	$\boldsymbol{a_{I\,i,j}}$ / $\boldsymbol{\alpha_{I\,i,j}}$	$\boldsymbol{b_{I\,i,j}}$ / $\boldsymbol{\beta_{I\,i,j}}$	$\boldsymbol{c_{I\,i,j}}$ / $\boldsymbol{\gamma_{I\,i,j}}$
$\boldsymbol{n+1/2}$	$-M_\varphi^+$	$1+3\,M_\varphi^+$	0
$\boldsymbol{n}$	$M_r^0\,(1-\mu)$	$1-2\,M_r^0$	$M_r^0\,(1+\mu)$
SBT	$S_{i,j}+2\,M_\varphi^+\,T_{IF}$		

Table D.30: Interface coefficients right j-sweep

j-sweep	$\boldsymbol{a_{J\,i,j}}$ / $\boldsymbol{\alpha_{J\,i,j}}$	$\boldsymbol{b_{J\,i,j}}$ / $\boldsymbol{\beta_{J\,i,j}}$	$\boldsymbol{c_{J\,i,j}}$ / $\boldsymbol{\gamma_{J\,i,j}}$
$\boldsymbol{n+1}$	$-M_r^+\,(1-\mu)$	$1+2\,M_r^+$	$-M_r^+\,(1+\mu)$
$\boldsymbol{n+1/2}$	M_φ^0	$1-3\,M_\varphi^0$	0
SBT	$S_{i,j}+2\,M_\varphi^0 T_{IF}$		

- **Radial inner boundary $(j-1)$**

$$k_{i,j}\,\frac{T_{i,j}-T_{IF}}{\Delta r_{i,j}/2}=k_{i,j-1}\,\frac{T_{IF}-T_{i,j-1}}{\Delta r_{i,j-1}/2} \tag{D.46}$$

$$T_{IF}=\left(T_{i,j}+T_{i,j-1}\,\frac{k_{i,j-1}}{k_{i,j}}\,\frac{\Delta r_{i,j}}{\Delta r_{i,j-1}}\right)\Bigg/\left(1+\frac{k_{i,j-1}}{k_{i,j}}\,\frac{\Delta r_{i,j}}{\Delta r_{i,j-1}}\right) \tag{D.47}$$

$$k_{i,j}\,\frac{T_{i,j}-T_{IF}}{\Delta r_{i,j}/2}=k_{i,j}\,\frac{T_{i,j}-T_{i-1,j}}{\Delta r_{i,j}} \tag{D.48}$$

$$T_{i,j-1}=2\,T_{IF}-T_{i,j} \tag{D.49}$$

Table D.31: Interface coefficients inner i-sweep

i-sweep	$\boldsymbol{a_{I\,i,j}}$ / $\boldsymbol{\alpha_{I\,i,j}}$	$\boldsymbol{b_{I\,i,j}}$ / $\boldsymbol{\beta_{I\,i,j}}$	$\boldsymbol{c_{I\,i,j}}$ / $\boldsymbol{\gamma_{I\,i,j}}$
$\boldsymbol{n+1/2}$	$-M_\varphi^+$	$1+2\,M_\varphi^+$	$-M_\varphi^+$
$\boldsymbol{n}$	0	$1-M_r^0\,(3-\mu)$	$M_r^0\,(1+\mu)$
SBT	$S_{i,j}+2\,M_r^0\,(1-\mu)\,T_{IF}$		

Table D.32: Interface coefficients inner j-sweep

j-sweep	$\boldsymbol{a_{J\,i,j}}$ / $\boldsymbol{\alpha_{J\,i,j}}$	$\boldsymbol{b_{J\,i,j}}$ / $\boldsymbol{\beta_{J\,i,j}}$	$\boldsymbol{c_{J\,i,j}}$ / $\boldsymbol{\gamma_{J\,i,j}}$
$\boldsymbol{n+1}$	0	$1+M_r^+\,(3-\mu)$	$-M_r^+\,(1+\mu)$
$\boldsymbol{n+1/2}$	M_φ^0	$1-2\,M_\varphi^0$	M_φ^0
SBT	$S_{i,j}+2\,M_r^+\,(1-\mu)\,T_{IF}$		

- **Radial outer boundary $(j+1)$**

$$k_{i,j}\,\frac{T_{i,j}-T_{IF}}{\Delta r_{i,j}/2}=k_{i,j+1}\,\frac{T_{IF}-T_{i,j+1}}{\Delta r_{i,j+1}/2} \tag{D.50}$$

$$T_{IF}=\left(T_{i,j}+T_{i,j+1}\,\frac{k_{i,j+1}}{k_{i,j}}\,\frac{\Delta r_{i,j}}{\Delta r_{i,j+1}}\right)\Bigg/\left(1+\frac{k_{i,j+1}}{k_{i,j}}\,\frac{\Delta r_{i,j}}{\Delta r_{i,j+1}}\right) \tag{D.51}$$

$$k_{i,j}\,\frac{T_{i,j}-T_{IF}}{\Delta r_{i,j}/2}=k_{i,j}\,\frac{T_{i,j}-T_{i-1,j}}{\Delta r_{i,j}} \tag{D.52}$$

$$T_{i,j-1}=2\,T_{IF}-T_{i,j} \tag{D.53}$$

Table D.33: Interface coefficients outer i-sweep

i-sweep	$\boldsymbol{a_{I\,i,j}\ /\ \alpha_{I\,i,j}}$	$\boldsymbol{b_{I\,i,j}\ /\ \beta_{I\,i,j}}$	$\boldsymbol{c_{I\,i,j}\ /\ \gamma_{I\,i,j}}$
$\boldsymbol{n+1/2}$	$-M_{\varphi}^{+}$	$1+2\,M_{\varphi}^{+}$	$-M_{\varphi}^{+}$
$\boldsymbol{n}$	$M_{r}^{0}\,(1-\mu)$	$1-M_{r}^{0}\,(3+\mu)$	0
SBT	$S_{i,j}+2\,M_{r}^{0}\,(1+\mu)\,T_{IF}$		

Table D.34: Interface coefficients outer j-sweep

j-sweep	$\boldsymbol{a_{J\,i,j}\ /\ \alpha_{J\,i,j}}$	$\boldsymbol{b_{J\,i,j}\ /\ \beta_{J\,i,j}}$	$\boldsymbol{c_{J\,i,j}\ /\ \gamma_{J\,i,j}}$
$\boldsymbol{n+1}$	$-M_{r}^{+}\,(1-\mu)$	$1+M_{r}^{+}\,(3+\mu)$	0
$\boldsymbol{n+1/2}$	M_{φ}^{0}	$1-2\,M_{\varphi}^{0}$	M_{φ}^{0}
SBT	$S_{i,j}+2\,M_{r}^{+}\,(1+\mu)\,T_{IF}$		

D.3.0.1 Interface temperatures at boundaries with different cell size and orientation

If only the steady-state temperature field shall be calculated, for two neighboured cells (1 and 2) of different size, shape and/or orientation two different interface temperatures can be calculated.

$$Q=A_{real}\,k_{real}\,\frac{T_1-T_2}{\Delta x_{real}}=A_1\,k_1\,\frac{T_1-T_{IF\,1}}{\Delta x_1}=A_2\,k_2\,\frac{T_{IF\,2}-T_2}{\Delta x_2} \tag{D.54}$$

$$T_{IF\,1}=T_1-\frac{A_{real}}{A_1}\,\frac{k_{real}}{k_1}\,\frac{\Delta x_1}{\Delta x_{real}}\,(T_1-T_2) \tag{D.55}$$

$$T_{IF\,2}=T_2+\frac{A_{real}}{A_2}\,\frac{k_{real}}{k_2}\,\frac{\Delta x_2}{\Delta x_{real}}\,(T_1-T_2) \tag{D.56}$$

D.4 Discretized heat conduction equation for Cartesian coordinates

The derivation of the coefficients for a Cartesian mesh is done analogously as demonstrated for the polar coordinates. The basic equations for cells in the middle of the meshed domain are illustrated in (D.57) and (D.58).

i-sweep:

$$\begin{aligned} &\underbrace{-M_x^+}_{a_{I\,i,j}} T_{i-1,j}^{n+1/2} + \underbrace{\left(1+2\,M_x^+\right)}_{b_{I\,i,j}} T_{i,j}^{n+1/2} \underbrace{-M_x^+}_{c_{I\,i,j}} T_{i+1,j}^{n+1/2} = \\ &= \underbrace{\overbrace{M_y^0}^{\alpha_{I\,i,j}} T_{i,j-1}^{n} + \overbrace{\left(1-2\,M_y^0\right)}^{\beta_{I\,i,j}} T_{i,j}^{n} + \overbrace{M_y^0}^{\gamma_{I\,i,j}} T_{i,j+1}^{n}}_{d_{I\,i,j}} + \overbrace{S_{i,j}\,(+\ldots)}^{\delta_{I\,i,j}} \end{aligned} \tag{D.57}$$

j-sweep:

$$\begin{aligned} &\underbrace{-M_y^+}_{a_{J\,i,j}} T_{i,j-1}^{n+1} + \underbrace{\left(1+2\,M_y^+\right)}_{b_{J\,i,j}} T_{i,j}^{n+1} \underbrace{-M_y^+}_{c_{J\,i,j}} T_{i,j+1}^{n+1} = \\ &= \underbrace{\overbrace{M_x^0}^{\alpha_{J\,i,j}} T_{i-1,j}^{n+1/2} + \overbrace{\left(1-2\,M_x^0\right)}^{\beta_{J\,i,j}} T_{i,j}^{n+1/2} + \overbrace{M_x^0}^{\gamma_{J\,i,j}} T_{i+1,j}^{n+1/2}}_{d_{J\,i,j}} + \overbrace{S_{i,j}\,(+\ldots)}^{\delta_{J\,i,j}} \end{aligned} \tag{D.58}$$

$$\begin{aligned} M_x^+ &= \frac{\Theta\,\Delta t\,k}{\rho\,c_p\,\Delta x^2} \\ M_x^0 &= \frac{(1-\Theta)\,\Delta t\,k}{\rho\,c_p\,\Delta x^2} \\ M_y^+ &= \frac{\Theta\,\Delta t\,k}{\rho\,c_p\,\Delta y^2} \\ M_y^0 &= \frac{(1-\Theta)\,\Delta t\,k}{\rho\,c_p\,\Delta y^2} \end{aligned}$$

E Symmetric Gauss-Seidel method with relaxation for the steady state heat conduction equation

The 2D beam screen model was generated as a mixture of cells described in Cartesian coordinates and in polar coordinates. The basic discretized steady-state heat (conduction) equations for cells in the middle of the meshed domain for Cartesian and polar coordinates are illustrated in (E.1) and (E.2). The indexing for the different coordinate system is shown in figure E.1.

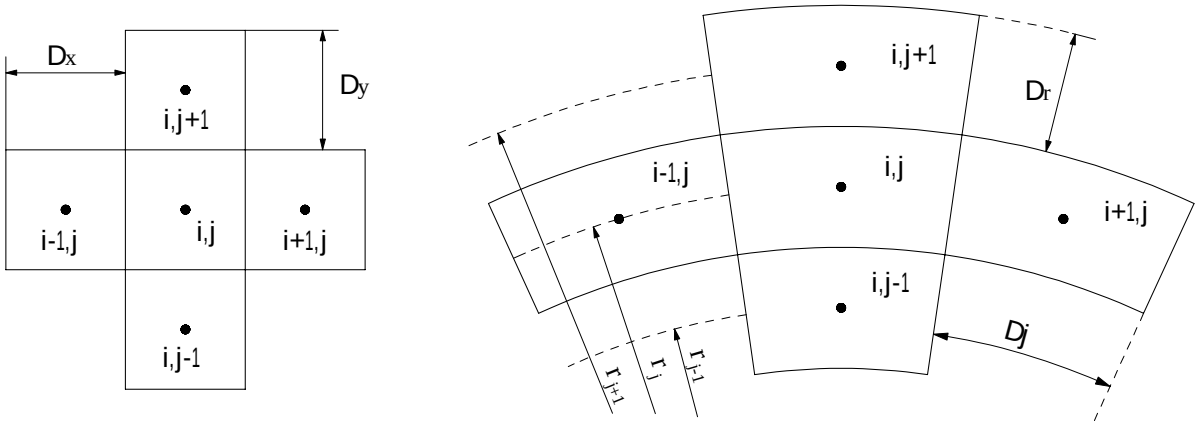

Figure E.1: Indexing of the grid in Cartesian coordinates (left-hand side) and polar coordinates (right-hand side).

Cartesian Coordinates:

$$T_{i,j} = \frac{T_{i+1,j} + T_{i-1,j}}{2\,(1 + \Delta x^2/\Delta y^2)} + \frac{T_{i,j+1} + T_{i,j-1}}{2\,(1 + \Delta y^2/\Delta x^2)} + \frac{\dot{q}_{Source}}{2k\,(1/\Delta x^2 + 1/\Delta y^2)} = \\ = \frac{T_{i+1,j} + T_{i-1,j}}{M_x} + \frac{T_{i,j+1} + T_{i,j-1}}{M_y} + \frac{\dot{q}_{Source}}{M_{xy}} \tag{E.1}$$

Polar Coordinates:

$$T_{i,j} = \frac{T_{i+1,j} + T_{i-1,j}}{2\left[1 + (r_j\,\Delta\varphi)^2/\Delta r^2\right]} + \frac{T_{i,j+1}\,(1+\mu) + T_{i,j-1}\,(1-\mu)}{2\left[1 + \Delta r^2/(r_j\,\Delta\varphi)^2\right]} + \frac{\dot{q}_{Source}}{2k\left[1/(r_j\,\Delta\varphi)^2 + 1/\Delta r^2\right]} =$$

$$= \frac{T_{i+1,j} + T_{i-1,j}}{M_t} + T_{i,j+1}\underbrace{\frac{(1+\mu)}{M_r}}_{1/M_{r+}} + T_{i,j-1}\underbrace{\frac{(1-\mu)}{M_r}}_{1/M_{r-}} + \frac{\dot{q}_{Source}}{M_{tr}} \tag{E.2}$$

$$\mu = \frac{\Delta r}{2r_j} \tag{E.3}$$

In each iteration step $n+1$ the temperature of a cell is solved with (E.4), where ω denotes the relaxation factor.

$$T_{i,j}^{n+1} = R_{i,j}^{n}\,\omega \tag{E.4}$$

The factor R is calculated with the temperature of the cell i,j and temperatures of its neighboured cells of the iteration steps n to $n+2$. To avoid asymmetry, the temperature information used of the different iteration steps are alternated with respect to the cell position. The equations below, two for Cartesian coordinates and two for polar coordinates, are solved alternatingly.

Cartesian Coordinates:

$$R_{i,j}^{n} = \frac{T_{i-1,j}^{n}}{M_x} + \frac{T_{i+1,j}^{n+1}}{M_x} + \frac{T_{i,j-1}^{n+1}}{M_y} + \frac{T_{i,j+1}^{n}}{M_y} + \frac{\dot{q}_{Source}}{M_{xy}} \tag{E.5}$$

$$R_{i,j}^{n} = \frac{T_{i-1,j}^{n+1}}{M_x} + \frac{T_{i+1,j}^{n}}{M_x} + \frac{T_{i,j-1}^{n}}{M_y} + \frac{T_{i,j+1}^{n+1}}{M_y} + \frac{\dot{q}_{Source}}{M_{xy}} \tag{E.6}$$

Polar Coordinates:

$$R_{i,j}^{n} = \frac{T_{i-1,j}^{n}}{M_t} + \frac{T_{i+1,j}^{n+1}}{M_t} + \frac{T_{i,j-1}^{n+1}}{M_{r-}} + \frac{T_{i,j+1}^{n}}{M_{r+}} + \frac{\dot{q}_{Source}}{M_{tr}} \tag{E.7}$$

$$R_{i,j}^{n} = \frac{T_{i-1,j}^{n+1}}{M_t} + \frac{T_{i+1,j}^{n}}{M_t} + \frac{T_{i,j-1}^{n}}{M_{r-}} + \frac{T_{i,j+1}^{n+1}}{M_{r+}} + \frac{\dot{q}_{Source}}{M_{tr}} \tag{E.8}$$

F Energy conservation of the FD method in polar coordinates for the radial derivative

The one-dimensional heat conduction equation in polar coordinates in radial direction reads

$$\underbrace{\frac{\partial T}{\partial t}}_{\text{time derivative}} = \underbrace{\frac{k}{\rho c_p}}_{a} \underbrace{\left(\frac{\partial^2 T}{\partial r^2} + \frac{1}{r}\frac{\partial T}{\partial r} \right)}_{\text{spatial derivative}} \tag{F.1}$$

Using the finite volume method, the discretized heat equation is conservative. The one-dimensional heat equation in radial direction now is discretized based on finite volumes and finite differences and the resulting formulas are compared. For cell-centered finite volumes (F.1) has to be integrated between the cell boundaries ($i+1/2$ and $i-1/2$) and the time step Δt [105].

$$\underbrace{\int_{i-1/2}^{i+1/2} \int_{t}^{t+\Delta t} \frac{\partial T}{\partial t}\, dt\, dr}_{\Delta r \left(T_i^{t+\Delta t} - T_i^t\right)} = \int_{t}^{t+\Delta t} \underbrace{\int_{i-1/2}^{i+1/2} a \left(\frac{\partial^2 T}{\partial r^2} + \frac{1}{r}\frac{\partial T}{\partial r} \right) dr}_{A}\, dt \tag{F.2}$$

The term A on the RHS of (F.2) can be rearranged to (F.3). By integrating (F.3) and combining it with the LHS of (F.2), (F.4) can be obtained.

$$\begin{aligned}
\int_{i-1/2}^{i+1/2} a \left(\frac{\partial^2 T}{\partial r^2} + \frac{1}{r}\frac{\partial T}{\partial r} \right) dr &= \int_{i-1/2}^{i+1/2} a \frac{1}{r}\frac{\partial}{\partial r}\left(r \frac{\partial T}{\partial r} \right) dr = \\
&= \frac{a}{r}\left(r \frac{dT}{dr} \right)_{i+1/2} - \frac{a}{r}\left(r \frac{dT}{dr} \right)_{i-1/2} = \\
&= a_{i+1/2} \frac{T_{i+1} - T_i}{r_i \Delta r} \left(r_i + \frac{\Delta r}{2} \right) - a_{i-1/2} \frac{T_i - T_{i-1}}{r_i \Delta r} \left(r_i + \frac{\Delta r}{2} \right) = \\
&= \frac{1}{\Delta r} \left[a_{i+1/2} \left(T_{i+1} - T_i \right) (1+\mu) - a_{i-1/2} \left(T_i - T_{i-1} \right) (1-\mu) \right] = \\
&= \frac{1}{\Delta r} \left[a_{i+1/2} T_{i+1} - \left(a_{i+1/2} + a_{i-1/2} \right) T_i + a_{i-1/2} T_{i-1} + \mu \left(a_{i+1/2} T_{i+1} - a_{i-1/2} T_{i-1} \right) \right]
\end{aligned} \tag{F.3}$$

$$T_i^{t+\Delta t} - T_i^t = T_i^{n+1} - T_i^n = \frac{\Delta t}{\Delta r^2} \left[\cdots \right] \tag{F.4}$$

F.1 Comparison with the FDM discretization

By assuming constant material properties ($a = const.$) the RHS of (F.4) can be simplified to obtain (F.5). Finally we compare the RHS of (F.5) with the RHS of the heat equation discretized with

the finite differences method.

$$T_i^{n+1} - T_i^n = \underbrace{a\frac{\Delta t}{\Delta r^2}}_{M} \left[T_{i-1} - 2T_i + T_{i+1} + \mu\left(T_{i+1} - T_{i-1}\right)\right] \tag{F.5}$$

Finite Differences (FD):

$$RHS_{FD} = M\left[T_{i-1} - 2T_i + T_{i+1} + \mu\left(T_{i+1} - T_{i-1}\right)\right] \tag{F.6}$$

Finite Volumes (FV):

$$RHS_{FV} = M\left[T_{i-1} - 2T_i + T_{i+1} + \mu\left(T_{i+1} - T_{i-1}\right)\right] \tag{F.7}$$

$$\rightarrow RHS_{FD} = RHS_{FV} \Rightarrow FDM = conservative \tag{F.8}$$

The discretizations performed with the finite difference method and with the finite volume method are equal, hence the finite difference discretization satisfies the energy conservation.

G Helium mass flow rates for the beam screen cooling without control valves

The purpose of the derivations illustrated in this section is to find a simple correlation between pressure drop and mass flow rates of the hydraulic scheme of the beam screen cooling without control valves for the counter flow scheme and the parallel flow scheme. The assumptions and simplifications are made with respect to the requirement to operate the beam screen cooling economically, i.e. to keep the additional mass flow rates to compensate the pressure losses in the headers small. Only the frictional pressure drop is taken into account, since the momentum pressure drop and the influence of the static head are negligible due to the header length of several kilometres.

G.1 Counter Flow

Rearranging (5.31) yields (G.1). By assuming the absolute pressure in the return header much higher than the sum of the occurring pressure losses (as indicated in (G.2)), the densities of the the single flows can be substituted by their mean values. The hydraulic impedances of supply and return header can be considered to be equal (G.3) due to their identical geometry.

$$\Delta p_{SH\,i} + \Delta p_{RH\,i} = \frac{L_{Mag}}{2} \underbrace{\frac{f_{SH}}{d_{SH}\,A_{SH}^2}}_{\hat{Z}_{SH}} \frac{\dot{m}_{SH\,i}^2}{\overline{\rho_{SH}}}\, n_{Mag} + \frac{L_{Mag}}{2} \underbrace{\frac{f_{RH}}{d_{RH}\,A_{RH}^2}}_{\hat{Z}_{RH}} \frac{\dot{m}_{RH\,i}^2}{\overline{\rho_{RH}}}\, n_{Mag} \tag{G.1}$$

$$p_{RH\,i} >> \Delta p_{BSU\,i+1} + \Delta p_{SH\,i} + \Delta p_{RH\,i} \rightarrow \frac{\overline{\rho_{SH}} + \overline{\rho_{RH}}}{2} \approx \overline{\rho_{BSU\,i}} \approx \overline{\rho_{BSU\,i+1}} \tag{G.2}$$

$$\hat{Z}_{SH} \approx \hat{Z}_{RH} = \hat{Z}_H \tag{G.3}$$

Based on the assumptions made, (G.1) can be simplified to (G.4)

$$\begin{aligned} &\overbrace{\frac{f_{BSU}}{d_{BSU}\,A_{BSU}^2}}^{\hat{Z}_{BSU}} \frac{L_{Mag}}{2} \frac{\left(\dot{m}_{Mag\,i+1} + \Delta\dot{m}_{Mag\,i}\right)^2}{\overline{\rho_{BSU\,i}}}\, n_{Mag}^3 = \\ &= 2\,\hat{Z}_H \frac{L_{Mag}}{2} \frac{\dot{m}_{H\,i}^2}{\overline{\rho_{BSU\,i}}}\, n_{Mag} + \hat{Z}_{BSU} \frac{L_{Mag}}{2} \frac{\dot{m}_{Mag\,i+1}^2}{\overline{\rho_{BSU\,i}}}\, n_{Mag}^3 \end{aligned} \tag{G.4}$$

where L_{Mag} denotes the length of a magnet, n_{Mag} denotes the number of magnets per parallel cooled BSU, $\dot{m}_{Mag\,i+1}$ denotes the mass flow rate per magnet in the parallel cooled BSU at position $i+1$ and $\Delta\dot{m}_{Mag\,i}$ denotes the additional mass flow rate per magnet for pressure drop compensation in

the parallel cooled BSU at the position i. To keep the total mass flow rate of reasonable size, the additional necessary mass flow rate $\Delta\dot{m}_{Mag\,i}$ to compensate the pressure drop in the headers, must be much smaller than the mass flow rate in the previous parallel cooled BSU $\dot{m}_{Mag\,i+1}$.

$$\frac{\dot{m}_{H\,i}^2}{n_{Mag}^2}\frac{\hat{Z}_H}{\hat{Z}_{BSU}} = \dot{m}_{Mag\,i+1}\,\Delta\dot{m}_{Mag\,i} + \underbrace{\frac{\Delta\dot{m}_{Mag\,i}^2}{2}}_{small} \tag{G.5}$$

$$\frac{\dot{m}_{H\,i}^2}{n_{Mag}^2}\frac{\hat{Z}_H}{\hat{Z}_{BSU}}\frac{1}{\dot{m}_{Mag\,i+1}} \approx \Delta\dot{m}_{Mag\,i} \tag{G.6}$$

$$\frac{\hat{Z}_H}{\hat{Z}_{BSU}}\underbrace{\frac{\dot{m}_{H\,i}^2}{n_{Mag}\dot{m}_{Mag\,i+1}}}_{\dot{m}_{BSU\,i+1}} \approx \underbrace{n_{Mag}\Delta\dot{m}_{Mag\,i}}_{\Delta\dot{m}_{BSU\,i}} \tag{G.7}$$

where $\dot{m}_{BSU\,i+1}$ denotes the mass flow rate in the parallel cooled BSU at the position $i+1$ and $\Delta\dot{m}_{BSU\,i}$ denotes the additional mass flow rate for pressure drop compensation in the parallel cooled BSU at the position i.

G.2 Parallel Flow

RHS and LHS of (5.36) yield (G.8) and (G.9). By assuming the absolute pressure in the manifold much higher than the sum of the occurring pressure losses (as indicated in (G.10)), the densities of the the single flows can be substituted by their mean values. The hydraulic impedances of supply header and manifold can be considered to be equal (G.11) due to their identical geometry.

$$\Delta p_{BSU\,i} + \Delta p_{MF\,i} = \underbrace{\frac{f_{BSU}}{d_{BSU}\,A_{BSU}^2}}_{\hat{z}_{BSU}}\frac{L_{Mag}}{2}\frac{\dot{m}_{Mag\,i}^2}{\overline{\rho_{BSU\,i}}}n_{Mag}^3 + \underbrace{\frac{f_{MF}}{d_{RH}\,A_{RH}^2}}_{\hat{z}_{RH}}\frac{L_{Mag}}{2}\frac{\dot{m}_{MF\,i}^2}{\overline{\rho_{MF\,i}}}n_{Mag} \tag{G.8}$$

$$\Delta p_{BSU\,i+1} + \Delta p_{SH\,i} = \underbrace{\frac{f_{BSU}}{d_{BSU}\,A_{BSU}^2}}_{\hat{z}_{BSU}}\frac{L_{Mag}}{2}\frac{\dot{m}_{Mag\,i+1}^2}{\overline{\rho_{BSU\,i+1}}}n_{Mag}^3 + \underbrace{\frac{f_{SH}}{d_{SH}\,A_{SH}^2}}_{\hat{z}_{SH}}\frac{L_{Mag}}{2}\frac{\dot{m}_{SH\,i}^2}{\overline{\rho_{SH\,i}}}n_{Mag} \tag{G.9}$$

$$p_{RH\,i} >> \Delta p_{BSU\,i+1} + \Delta p_{SH\,i} \rightarrow \frac{\overline{\rho_{SH}} + \overline{\rho_{MF}}}{2} \approx \overline{\rho_{BSU\,i}} \approx \overline{\rho_{BSU\,i+1}} \tag{G.10}$$

$$\hat{Z}_{SH} \approx \hat{Z}_{MF} = \hat{Z}_H \tag{G.11}$$

Based on the assumptions made, (G.8) and (G.9) can be simplified and then combined to obtain (G.12).

$$\begin{aligned}\hat{Z}_{BSU}\frac{L_{Mag}}{2}\frac{\dot{m}_{Mag\,i}^2}{\overline{\rho_{BSU\,i}}}n_{Mag}^3 + \hat{Z}_H\frac{L_{Mag}}{2}\frac{\dot{m}_{SH\,i}^2}{\overline{\rho_{SH\,i}}}n_{Mag} = \\ = \hat{Z}_{BSU}\frac{L_{Mag}}{2}\frac{\dot{m}_{Mag\,i+1}^2}{\overline{\rho_{BSU\,i}}}n_{Mag}^3 + \hat{Z}_H\frac{L_{Mag}}{2}\frac{\dot{m}_{MF\,i}^2}{\overline{\rho_{MF\,i}}}n_{Mag}\end{aligned} \tag{G.12}$$

where L_{Mag} denotes the length of a magnet, n_{Mag} denotes the number of magnets per parallel cooled BSU, $\dot{m}_{Mag\,i+1}$ denotes the mass flow rate per magnet in the parallel cooled BSU at position $i+1$ and $\dot{m}_{Mag\,i}$ denotes the mass flow rate per magnet in the parallel cooled BSU at the position i. After rearranging (G.14) is obtained.

$$\frac{1}{n_{Mag}^2}\frac{\hat{Z}_H}{\hat{Z}_{BSU}}\left(\frac{\dot{m}_{MF\,i}^2}{\overline{\rho_{MF\,i}}}-\frac{\dot{m}_{SH\,i}^2}{\overline{\rho_{SH\,i}}}\right)=\frac{\dot{m}_{Mag\,i+1}^2}{\overline{\rho_{BSU\,i}}}-\frac{\dot{m}_{Mag\,i}^2}{\overline{\rho_{BSU\,i}}} \tag{G.13}$$

$$\frac{1}{n_{Mag}^2}\frac{\hat{Z}_H}{\hat{Z}_{BSU}}\frac{\dot{m}_{MF\,i}^2-\dot{m}_{SH\,i}^2}{\overline{\rho_{BSU\,i}}}\approx\frac{\dot{m}_{Mag\,i}^2-\dot{m}_{Mag\,i+1}^2}{\overline{\rho_{BSU\,i}}} \tag{G.14}$$

The product of the mass flow rate per magnet $\dot{m}_{Mag}$ multiplied by the number of magnets per parallel cooled BSU n_{Mag} equals the mass flow rate per parallel cooled BSU $\dot{m}_{BSU}$.

$$\frac{\hat{Z}_H}{\hat{Z}_{BSU}}\approx\frac{\dot{m}_{Mag\,i}^2-\dot{m}_{Mag\,i+1}^2}{\dot{m}_{MF\,i}^2-\dot{m}_{SH\,i}^2}n_{Mag}^2=\frac{\dot{m}_{BSU\,i}^2-\dot{m}_{BSU\,i+1}^2}{\dot{m}_{MF\,i}^2-\dot{m}_{SH\,i}^2} \tag{G.15}$$

where $\dot{m}_{BSU\,i+1}$ denotes the mass flow rate in the parallel cooled BSU at the position $i+1$ and $\dot{m}_{BSU\,i}$ denotes the mass flow rate in the parallel cooled BSU at the position i. The manifold mass flow rate can be substituted with the difference of the total mass flow rate and the supply header mass flow rate. The mass flow rate in the parallel cooled BSU $i+1$ is the mass flow rate the parallel cooled BSU i plus the necessary mass flow rate difference to generate the additional pressure drop.

$$\dot{m}_{MF\,i}=\dot{m}_{tot}-\dot{m}_{SH\,i} \tag{G.16}$$

$$\dot{m}_{BSU\,i+1}=\dot{m}_{BSU\,i}+\Delta\dot{m}_{BSU\,i+1} \tag{G.17}$$

where $\Delta\dot{m}_{BSU\,i}$ denotes the additional mass flow rate for pressure drop compensation in the parallel cooled BSU at the position i. To keep the total mass flow rate reasonable, the additional necessary mass flow rate $\Delta\dot{m}_{BSU\,i}$ to generate the pressure drop in each previous parallel cooled BSU to compensate the pressure drop in the headers must be much smaller than the mass flow rate of the previous parallel cooled BSU $\dot{m}_{BSU\,i+1}$.

$$\frac{\hat{Z}_H}{\hat{Z}_{BSU}}\dot{m}_{tot}\left(\dot{m}_{MF\,i}-\dot{m}_{SH\,i}\right)\approx 2\,\dot{m}_{BSU\,i}\,\Delta\dot{m}_{BSU\,i+1}+\underbrace{\Delta\dot{m}_{BSU\,i+1}^2}_{small} \tag{G.18}$$

$$\frac{\hat{Z}_H}{\hat{Z}_{BSU}}\frac{\dot{m}_{tot}\left(\dot{m}_{MF\,i}-\dot{m}_{SH\,i}\right)}{2\,\dot{m}_{BSU\,i}}\approx\Delta\dot{m}_{BSU\,i+1} \tag{G.19}$$

H Current Lead Cooling

The current to feed the electromagnets to generate the magnetic field is produced and conducted to the FCC in cables at ambient temperature level. The transfer of the current to electric conductors at cryogenic temperature level occurs in so-called current leads. According to the Wiedemann-Franz law, good electrical conductors in general also are good thermal conductors [98]. The technical requirement to choose materials with a very low electrical resistivity to be able to conduct the large currents is accompanied by the necessity of an elaborate design to extract the resistive heat and thermally shield the cold mass against entering heat.

The dipoles and quadrupoles of the arcs require the major part of the supplied current. Since neither the magnetic pattern (including corrector magnets, sextupoles etc.), nor the current leads design are defined yet, an upscaling from the LHC requirements was performed to estimate the refrigeration power of the FCC [99]. The final number of electrical circuits per dipole yields the number of current leads, the transferred current and also the required cooling capacity.

Table H.1: Upscaled values for the FCC current lead cooling

			LHC	**FCC**		
Dipole current	I_{DP}	kA	12	16		
Number of arcs	n_{Arc}	-	8	10		
Number of circuits	n_{Ci}	-	1	1	2	3
Total current to conduct	I_{tot}	MA	3.4	6.8	13.6	20.4
Current to conduct per arc	I_{Arc}	MA	0.43	0.57	1.13	1.70
Total helium consumption	$\dot{m}_{CL\,tot}$	g/s	170	340	680	1020
Helium consumption per arc	$\dot{m}_{CL\,Arc}$	g/s	17	28	57	85

The current leads are located at the beginning and at the end of an arc (see figure 2.21). A schematic of the current leads design, proposed by Dresden University of Technology, is illustrated in figure H.1. Thermally it is separated into a cold part at the bottom and a warm part at the top. The current is entering/exiting at the top made from copper at ambient temperature level. The lower part consists of a stainless steel substrate on which a thin layer of superconductor is laminated. The bottom of the current leads is cooled isothermally by vaporization in a Joule-Thomson valve to the two-phase region. The helium vapour generated during the isenthalpic expansion and by absorbing heat is mixed with helium supplied by header D. The helium flow passes the outer surface of the current leads in upward direction and is warmed up close to ambient temperature at the top of the current leads. The helium then is discharged into the helium recovery line and conveyed back to the cryoplant. The length of the current leads is in the order of some meters. Considering the good thermal conduction, the resulting temperature gradient requires a sophisticated cryogenic design.

Figure H.1: Schematic of the current lead cooling.

$T_1 = 4.6$ K
$p_1 = 3$ bar

$T_2 = T_3 = 4.26$ K
$p_2 = p_3 = 1.3$ bar

$T_D = 40$ K
$p_D = 1.3$ bar

$p_4 \approx 1.3$ bar

$T_5 \approx T_a$
$p_5 = 1.05$ bar

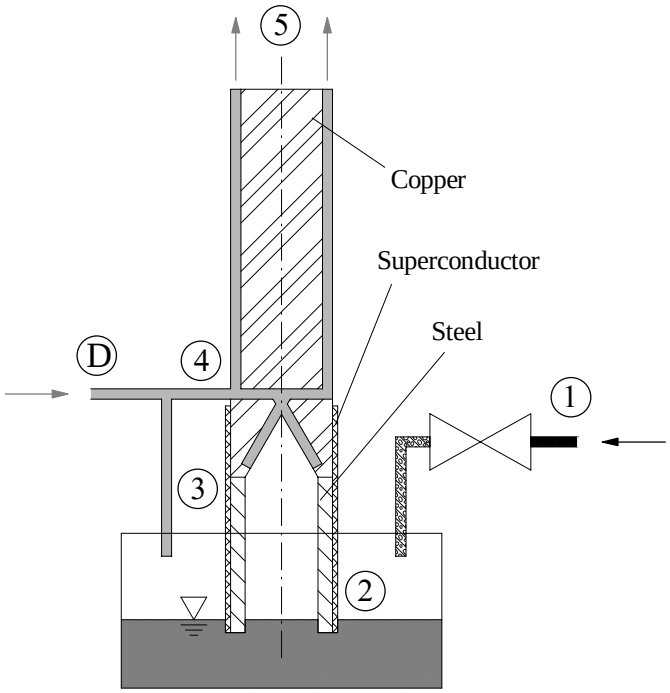

The lower, superconducting part has to extract a heat load of 0.1 W/kA by vaporization from the warm copper part the helium has to extract a heat load of 68.5 W/kA by a sensible temperature increase. Based on the assumed thermodynamic state variables shown in figure H.1 and an ideal heat transfer between the copper end the helium flow, table H.2 illustrates the exergetic efficiencies, the distribution of the relative exergy losses and the expected exergy consumption for one to three circuits per dipole and an assumed Carnot efficiency of the distribution system and the cryoplant of 29 %.

Table H.2: Results of the exergy analysis of the current lead cooling

			1	**2**	**3**
Mixing temperature	T_4	K		36	
Helium consumption per arc	$\dot{m}_{CL\,Arc}$	g/s	28.3	56.7	84.9
Exergy consumption per arc w/o cryoplant	$\dot{X}_{CLI}$	kW	69.53	139.06	208.59
Exergetic efficiency w/o cryoplant	ζ_{CLI}	-		0.842	
Exergy loss Joule-Thomson valve per arc	$\dot{B}_{JT}$	kW	0.283	0.567	0.850
Relative exergy loss Joule-Thomson valve	$\hat{b}_{JT}$	-		0.004	
Exergy loss mixing per arc	$\dot{B}_{Mix}$	kW	6.96	13.91	20.87
Relative exergy loss mixing	$\hat{b}_{Mix}$	-		0.1	
Exergy pressure drop per arc	$\dot{B}_{\Delta p}$	kW	3.77	7.54	11.31
Relative exergy loss pressure drop	$\hat{b}_{\Delta p}$	-		0.054	
Total exergy consumption per arc	$\dot{X}_{CLII}$	kW	239.8	479.5	719.3
Total exergetic efficiency	ζ_{CLII}	-		0.244	

Due to the high currents and the long sector lengths, the division of the cables in three parallel circuits by now seems to be the most probable option [55].

REFERENCES

References

[1] Wilson E 2001 *an introduction to Particle Accelerators*. Oxford University Press, Oxford (ISBN 0-19-850829-8)

[2] CERN 2013 *The European Strategy for Particle Physics Update 2013*. CERN-Council-S/106

[3] Rau H 1977 *Kurze Einführung in die Physikalische Chemie*. Friedr. Vieweg & Sohn Verlagsgesellschaft mbH, Braunschweig (ISBN 3-528-09208-4)

[4] Staguhn G 2012 *Quarks, Atome, Moleküle*. Anaconda Verlag GmbH, Cologne (ISBN 978-3-86647-824-4)

[5] Hauptmann J 2011 *Particle Physics Experiments at High Energy Colliders*. WILEY-VCH Verlag GmbH & Co. KGaA, Weinheim (ISBN 978-3-527-40825-2)

[6] Berger C 2006 *Elementarteilchenphysik*. Springer, Berlin (ISBN 978-3-540-23143-1)

[7] Halpern P 2009 *Collider*. John Wiley & Sons, Inc., Hoboken (ISBN 978-0-470-28260-3)

[8] Göbel H 2014 *Gravitation und Relativität*. Oldenbourg Wissenschaftsverlag, Munich (ISBN 978-3-11-034426-4)

[9] Chao AW, Tigner M (Editors) 1999 *Handbook of Accelerator Physics and Engineering*. World Scientific Publishing, Singapore (ISBN 9810235003)

[10] Dahl PF 1963 *Superconductivity, Its Historical Roots and Development from Mercury to the Ceramic Oxides*. American Institute of Physics, Melville (ISBN 978-0883188484)

[11] Shmidt VV 1963 *Critical current and critical magnetic field in hard superconductors*. Journal of Experimental and Theoretical Physics (USSR) Vol 45, pp. 1368 – 1376

[12] Baglin V, Bregliozzi G, Jimenez J M and Lanza G 2011 *Synchrotron Radiation in the LHC Vacuum System*. Proceedings of the 2nd International Particle Accelerator Conference (IPAC 2011), 4 – 9 Septemper 2011, San Sebastian, Spain, TUPS019 (ISBN 978-92-9083-366-6)

[13] Benedikt M et al. 2016 *Status of the Future Circular Collider Study*. Future Cirulcar Collider Study (CERN-ACC-2016-0331)

[14] Dominguez Sanchez de la Blanca CO 2014 *Electron cloud studies for the LHC and future proton colliders*. PhD thesis (N°6017), Ecole Polytechnique Federale de Lausanne, Lausanne, Switzerland

[15] Møller SP 1999 *Beam-residual gas interactions*. Proceedings of the CAS - CERN Accelerator School: Vacuum technology, 28 May – 3 June 1999, Snekersten, Denmark, pp. 155 – 164

[16] Brüning O, Collier P, Lebrun P, Myers S, Ostojic R, Poole J, Proudlock P (editors) 2004 *LHC Design Report Volume I: The LHC Main Ring* CERN, Geneva (ISBN 92-9083-224-0)

[17] Holzer BJ 2014 *Introduction to Particle Accelerators and their Limitations*. Proceedings of the CAS - CERN Accelerator School: Plasma Wake Acceleration, 23 – 29 November 2014, Geneva, Switzerland, pp. 29 – 50 (CERN-2016-001)

[18] Hatchadourian E, Lebrun P, Tavian L 1998 *Supercritical Helium Cooling of the LHC Beam Screens*. Proceedings of the 17$^{\text{th}}$ International Cryogenic Engineering Conference (ICEC 17), 14 – 17 July 1998, Bournemouth, UK, pp. 763 – 796 (ISBN 9780750305976)

[19] Lebedev V, Shiltsev V (Editors) 2014 *Accelerator Physics at the Tevatron Collider*. Springer, New York (ISBN 978-1-4939-0884-4)

[20] Rode CH, Ferry R, Lincicome T and Makara J 1983 *Operation of the Tevatron six-kilometer-long transfer line*. IEEE Transactions on Nuclear Science Vol NS-30, pp. 2769 – 2771

[21] Rode CH 1983 *Tevatron cryogenic system*. Proceedings of the 12$^{\text{th}}$ International Conference on High-Energy Accelerators (HEACC 1983), 11 - 16 August, Batavia, US, pp. 529 – 535

[22] Fowler WB 1990 *The Tevatron cryogenic system*. Particle Accelerators Vol 26, pp. 179 – 186

[23] Rode CH, Andrews RA, Ferry R, Gannon J, Makara J, Martin M, Mizicko D, Misek J, Peterson T and Theilacker J 1983 *Operation of the Tevatron satellite Refrigerators for 0.75-and 2.0-kilometer-long magnet strings*. IEEE Transactions on Nuclear Science Vol NS-30, pp. 2892 – 2894

[24] Brandt J, Feher S, Peterson TJ and Soyars WM 2002 *HTS Leads in the Tevatron*. AIP Conference Proceedings Vol 613, pp. 567 – 574

[25] Meinke R 1991 *Superconducting magnet system for HERA*. IEEE Transactions on Magnetics Vol 27, pp. 1728 – 1734

[26] Eschricht W, Horlitz G, Knopf U, Lange R, Lierl H, Moje J, Sellmann, D und Sindt H 1988 *Cryogenic test of helium transfer line modules for HERA*. Proceedings of the 12$^{\text{th}}$ International Cryogenic Engineering Conference (ICEC 12), 12 – 15 July 1988, Southampton, UK, pp. 505 – 510 (ISBN 40 80 125 95)

[27] Clausen M, Horlitz G, Knust G and Lierl H 1986 *The refrigeration system for the superconducting proton ring of the electron proton collider HERA*. Advances in Cryogenic Engineering Vol 31, pp. 635 – 645 (ISBN 978-1-4612-9299-9)

[28] Horlitz G, Clausen M, Lierl H and Lange R 1993 *The cryogenic operation of the superconducting magnet system in the HERA proton storage ring: cool down, staedy state operation, quench recovery processes*. Advances in Cryogenic Engineering Vol 39A, pp. 2319 – 2321 (ISBN 978-1-4613-6074-2)

[29] Barbier B, Bouillot A, Brodzinski K, Dupont M, Fathallah M, Fournel JL, Gitton E, Junker S, Moussavi H, Parnete C and Riddone G 2007 *Manufacturing and Installation of the Compound Cryogenic Distribution Line for the Large Hadron Collider*. Proceedings of the 21$^{\text{st}}$ International Cryogenic Engineering Conference (ICEC 21), 17 - 21 July, Prag, Czech Republic, CERN-LHC-PROJECT-REPORT-992 (ISBN 9788023988833)

[30] Stanyard J, Osborne J 2017 *FCC Civil Engineering Optimisation and Design Development*. Presented at the 3rd FCC Week, 29 May – 1 June 2017, Berlin, Germany (https://indico.cern.ch/event/556692/contributions/2496900/attachments/1468800/2271843/Civil_Engineering_Optimisation_and_Design_Development.pdf)

[31] Asner FM 1999 *High Field Superconducting Magnets*. Clarendon Press, Oxford (ISBN 0 19 851764 5)

[32] Edwards H 1985 *The Tevatron Energy Doubler: A Superconducting Accelerator*. Annual Revision Nuclear Particle Science 1985.35, pp. 605 – 660

[33] Hausen H, Linde H 1985 *Tieftemperaturtechnik*. Springer, Berlin (ISBN 978-3-662-10554-2)

[34] Wagner U 2002 *Refrigeration*. Proceedings of the CAS - CERN Accelerator School: Superconductivity and Cryogenics for Accelerators and Detectors, 8 – 17 May 2002, Erice, Italy, pp.295 – 345 (CERN-2004-008)

[35] Enss C and Hunklinger S 2000 *Tieftemperaturphysik*. Springer, Berlin (ISBN 3-540-67674-0)

[36] Balibar S 2003 *Looking back at superfluid helium*. Paper presented at the Conference "Bose Einstein Condensation", 29 March 2003, Paris, France (hal-00000262)

[37] Schäfer R and Fliessbach T 1994 *The two-fluid model with superfluid entropy*. Il nuovo cimento D Vol 16, pp. 373 – 390

[38] London F, Zilsel PR 1948 *Heat Transfer in Liquid Helium II by Internal Convection*. Physical Review Vol 75, pp. 1148 – 1156

[39] Chase CE 1962 *Thermal Conduction in Liquid Helium II. I. Temperature Dependence*. Physical Review Vol 127, pp. 361 – 370

[40] Vinen WF 1958 *Mutual Friction in a Heat Current in Liquid Helium II. IV. Critical Heat Currents in Wide Channels*. Proceedings of the Royal Society of London Series A, Mathematical and Physical Sciencez, Vol 243, pp 400 – 413

[41] Van Sciver S 2012 *Helium Cryogenics*. Springer, New York (ISBN 978-1-4419-9979-5)

[42] Sciacca M, Jou D, Mongiovu MS 2013 *Effective thermal conductivity of helium II: from Landau to Gorter-Mellink regimes*. Zeitschrift für angewandte Mathematik und Physik Vol 66, pp. 1835 – 1851

[43] Lebrun P and Tavian L 2013 *Cooling with Superfluid Helium*. Proceedings of the CAS-CERN Accelerator School: Superconductivity for Accelerators, 24 April – 4 May 2013, Erice, Italy, pp.453 – 476 (CERN-2014-005)

[44] Klöppel S, Quack H, Haberstroh C and Holdener F 2015 *Neon helium mixtures as a refrigerant for the FCC beam screen cooling: comparison of cycle design options*. IOP Conference Series: Materials Science and Engineering Vol 101, 012042

[45] Correia Rodrigues H 2016 *Cool-down and warm-up studies of a FCC sector*. Presented at the 2rd FCC Week, 11 – 15 April 2016, Rome, Italy (https://indico.cern.ch/event/438866/contributions/1085119/attachments/1257674/1857310/Hugo_Rodrigues_-_Presentation_-_Rome.pdf)

[46] Gemoll W 1908 *Gemoll - Griechisch-Deutsches Schul- und Handwörterbuch*. Oldenbourg Verlag, Berlin (ISBN 978-3-63700-2340)

[47] Gouy LG 1889 *Sur l énergie utilisable*. Journal de Physique Théorique et Appliquée Vol 8, pp. 501 - 518

[48] Rant Z 1956 *Exergie, ein Neues Wort für Technische Arbeitsfähigkeit*. Forschung auf dem Gebiete des Ingenieurwesens Vol 22, pp. 36 - 37

[49] Cerbe G, Wilhelms G 2013 *Technische Thermodynamik*. Carl Hanser Verlag, Munich (ISBN 978-3-446-43638-1)

[50] Baehr H D and Kabelac S 2012 *Thermodynamik*. Springer, Berlin (ISBN 978-3-642-24160-4)

[51] Millet F 2017 *Technical Specifications for industry studies on the FCC cryogenic system*. Presented at the 3rd FCC Week, 29 May – 1 June 2017, Berlin, Germany (`https://indico.cern.ch/event/556692/contributions/2488406/attachments/1469148/2272540/FCCWeek2017-Tech_Spec_Cryo_Industry_Study_Millet.pdf`)

[52] Claudet S, Lebrun P, Tavian L and Wagner U 2009 *Exergy Analysis of the Cryogenic Helium Distribution System for the Large Hadron Collider (LHC)*. AIP Conference Proceedings Vol 1218, pp. 1267 – 1274

[53] Grühagen H, Wagner U 2005 *Measured Performance of Four New 18 kW@4.5 K Helium Refrigerators for the LHC Cryogenic System*. Proceedings of the 20th International Cryogenic Engineering Conference (ICEC 20), Beijing, China, pp. 991 – 994

[54] van Nugteren J, Schoerling D, Kirby G, Murtomaki J, de Rijk G, Rossi L, Bottura L, Ten Kate H, Dhalle M 2016 *Layout Study for the Dipole Magnets of the Future Circular Collider Using Nb-Ti and Nb_3Sn*. IEEE Transactions on Applied Superconductivity Vol 26, 4003206

[55] Chorowski M, Correia Rodrigues H, Delikaris D, Duda P, Haberstroh C, Holdener F, Klöppel S, Kotnig C, Millet F, Polinski J, Quack H, Tavian L 2017 *Towards the conceptual design of the cryogenic system of the Future Circular Collider (FCC)*. IOP Conference Series: Materials Science and Engineering Vol 278, 012097

[56] Besana MI 2016 *Particle shower studies to tackle the FCC challenges*. Paper presented at the 2nd FCC Week 2016, April 11 - 15, Rome, Italy

[57] Alemany Fernandez R, Apollonio A, Bartmann W, Buffat X, Niemi A, Schulte D, Solfaroli M, Stoel L S 2016 *FCC-hh turn-around cycle*. Future Circular Collider Study (CERN-ACC-2016-0341)

[58] Sabbi G, Blomberg Ghini J, Gourlay SA, Marchevsky M, Ravaioli E, ten Kate H, Verweij A, Wang X 2016 *Design Study of a 16-T Block Dipole for FCC*. IEEE Transactions on Applied Superconductivity Vol 26, 4004705

[59] Sorbi M, Bellomo G, Caiffi B, Fabbricatore P, Farinon S, Marinozzi V, Volpini G 2017 *The EuroCirCol 16T Cosine-Theta Dipole Option for the FCC*. IEEE Transactions on Applied Superconductivity Vol 27, 4001205

[60] Toral F, Garcia-Tabares L, Martinez T, Munilla J, Ruuskanen J, Salmi T, Stenvall A 2017 *EuroCirCol 16 T Common-Coil Dipole Option for the FCC*. IEEE Transactions on Applied Superconductivity Vol 27, 4001105

[61] Bottura L 2013 *Magnet Quench 101.* Proceedings of the Workshop on Accelerator Magnet, Superconductor, Design and Optimization (WAMSDO), 15 – 16 January 2013, CERN, Geneva, Switzerland, pp. 1 – 9 (CERN-2013-006)

[62] Lebrun P 1997 *Superfluid helium as technical coolant.* Presented at the 15$^{\text{th}}$ UIT National Heat Transfer Conference, 19 – 20 June 1997, Torino, Italy (CERN-LHC-Project-Report-125)

[63] Lebrun P, Serio L, Tavian L and van Weelderen R 1997 *Cooling Strings of Superconducting Devices below 2 K: The Helium II Bayonet Heat Exchanger.* Advances in Cryogenic Engineering Vol 43, pp. 419 – 426 (ISBN 978-1-4757-9049-8)

[64] Taitel Y, Dukler AE 1976 *A Model for Predicting Flow Regime Transitions in Horizontal and Near Horizontal Gas-Liquid Flow.* AIChE Journal Vol 22, pp. 47 – 55

[65] Rousset B, Grimaud L and Gauthier A 1997 *Stratified two-phase superfluid helium flow: I**. Cryogenics Vol 37, pp. 733 – 737

[66] Rousset B, Gauthier A, Grimaud L and van Weelderen R 1997 *Latest Developments on He II CO-Current Two-Phase Flow Studies.* Advances in Cryogenic Engineering Vol 43, pp. 1441 – 1448 (ISBN 978-1-4757-9049-8)

[67] di Muoio E, Jager B, Puech L, Rousset B, Thibault P, van Weelderen R, Wolf PE 2002 *Optical investigations of He II two phase flow.* AIP Conference Proceedings Vol 613, pp. 1675 – 1682

[68] Brenn G 2017 *Analytical Solutions for Transport Processes.* Springer, Berlin (ISBN 978-3-662-51421-4)

[69] Andritsos N, Hanratty TJ 1987 *Influence of Interfacial Waves in Stratified Gas-Liquid Flows.* AIChE Journal Vol 3, pp. 444 – 454

[70] Grimaud L, Gauthier A, Rousset B and Delhaye JM 1997 *Stratified two-phase superfluid helium flow: II**. Cryogenics Vol 37, pp. 742 – 744

[71] Camacho D, Chevassus S, Policella C, Rieubland JM, Vandoni G, van Weelderen R 1998 *Thermal Characterization of the HeII LHC Heat Exchanger Tube.* Proceedings of the 17$^{\text{th}}$ International Cryogenic Engineering Conference (ICEC 17), 14 – 17 July 1998, Bournemouth, UK, pp.647 – 650 (CERN-LHC-Project-Report-232)

[72] Pollack GL 1969 *Kapitza Resistance.* Reviews of Modern Physics Vol 41, pp. 48 – 81

[73] Baehr HD and Stephan K 1993 *Wärme- und Stoffuebertragung.* Springer, Heidelberg (ISBN 978-3-642-05500-3)

[74] Baudouy B 2003 *Kapitza resistance and thermal conductivity of Kapton in superfluid helium.* Elsevier, Cryogenics. Vol 43, pp. 667 – 672

[75] Cheeke J 1970 *The Kapitza resistance and heat transfer at low temperatures.* Journal de Physique Colloques Vol 31, pp. C3-129 – C3-136

[76] Rane T, Chakravarty A, Singh RK and Singh T 2010 *Improved correlations for computations of liquid helium two phase flow in cryogenic transfer lines.* Cryogenics Vol 51, pp. 27 – 33

[77] Crowe CT (Editor) 2006 *Multiphase Flow Handbook.* Taylor & Francis Group, Boca Raton (ISBN 978-1-4200-4047-0)

[78] Huang X, Van Sciver SW 1995 *Pressure drop and void fraction of two-phase helium flowing in horizontal tubes*. Cryogenics Vol 35, pp. 467 – 474

[79] Tong LS, Yang YS 1997 *Boiling Heat Transfer and Two-Phase Flow*. Taylor & Francis, Washington (ISBN 1-56032-485-6)

[80] Tavian L 2016, private communication

[81] Roussel P, Bezaguet A, Bieri H, Devidal R, Jager B, Moracchioli R, Seyfert P, Tavian L 2002 *Performance tests of industrial prototype subcooling helium heat exchangers for the Large Hadron Collider*. AIP Conference Proceedings Vol 613, pp. 1429 – 1436

[82] Awad MM and Muzychka YS 2008 *Effective property models for homogeneous two-phase flows*. Experimental Thermal and Fluid Science Vol 3, pp. 106 – 113

[83] Papaevangelou G, Evangelides C and Tzimopoulos C 2010 *A new explicit relation for friction coefficient f in the Darcy Weisbach equation*. Paper presented at the International Conference on Protection and Restoration of the Environment X, July 5 - 9 2010, Korfu, Greece

[84] Jackson JD (Editor) 1986 *Conceptual Design of the Superconducting Super Collider*. SSC Central Design Group, Berkeley

[85] Lebrun P and Tavian L 2015 *Beyond the Large Hadron Collider: a first look at cryogenics for CERN future circular colliders*. Physics Procedia Vol 67, p. 768 – 775

[86] Baglin V, Lebrun P, Tavian L, van Weelderen R 2012 *Cryogenic Beam Screens for High-Energy Particle Accelerators*. Proceedings of the 24$^{\text{th}}$ International Cryogenic Engineering Conference (ICEC 24), May 14 - May 18 2012, Fukoaka, Japan (CERN-ATS-2013-006)

[87] Angerth B, Bertinelli F, Brunet J C, Calder R, Caspers F, Gröbner O, Mathewson A G, Poncet A, Reymermier C, Ruggiero F, Valbuena R 1994 *The LHC beam screen - specification and design*. Proceedings of 4$^{\text{th}}$ European Accelerator Conference (EPAC 1994), 27 June - 1 July 1994, London, UK, pp. 208 – 210 (CERN-LHC-Note-283)

[88] Mounet N 2012 *The LHC Transverse Coupled-Bunch Instability*. PhD thesis (N°5305), Ecole Polytechnique Federale de Lausanne, Lausanne, Switzerland

[89] Burg K, Haf H, Wille F, Meister A 2010 *Partielle Differentialgleichungen und funktionsanalytische Grundlagen*. Vieweg + Teubner Verlag, Wiesbaden (ISBN 978-3-8348-1294-0)

[90] Bestehorn M 2016 *Computational Physics*. Walter de Gruyter GmbH, Berlin (ISBN 978-3-11-037288-5)

[91] Deuflhard P, Hohmann A 2008 *Numerische Mathematik 1*. Walter de Gruyter GmbH, Berlin (ISBN 978-3-11-020354-7)

[92] Hanke-Bourgeois M 2009 *Grundlagen der Numerischen Mathematik und des Wissenschaftlichen Rechnens*. Vieweg + Teubner, Wiesbaden (ISBN 978-3-8348-0708-3)

[93] Garion C 2016 *FCC-hh beam screen studies and cooling scenario*. Presented at the 2$^{\text{nd}}$ FCC Week, 11 – 15 April 2016, Rome, Italy (`https://indico.cern.ch/event/438866/contributions/1084911/attachments/1257787/1857527/Beam_screen_studies.pdf#search=garion%20AND%20EventID%3A438866`)

[94] Topham J F, Garion C 2017 *FCC-hh beam screen design*. Presented at the 3rd FCC Week, 29 May – 1 June 2017, Berlin, Germany (`https://indico.cern.ch/event/556692/contributions/2487663/attachments/1468949/2272149/FCCweek_berlin_fdez_topham.pdf`)

[95] Tavian L 2015, private communication

[96] Grote K H, Feldhusen J (Editors) 2007 *Dubbel - Taschenbuch für den Maschinenbau*. Springer, Berlin (ISBN 978-3-540-49714-1)

[97] Correia Rodrigues H, Tavian L 2017 *Impact of large beam-induced heat loads on the transient operation of the beam screens and the cryogenic plants of the Future Circular Collider (FCC)*. IOP Conference Series: Materials Science and Engineering Vol 278, 012090

[98] Gottstein G 2007 *Physikalische Grundlagen der Materialkunde*. Springer, Heidelberg (ISBN 978-3-540-71104-9)

[99] Ballarino A 2000 *Application of high temperature superconductors to accelerators*. Proceedings of 7th European Accelerator Conference (EPAC 2000), 26 – 30 June 2000, Vienna, Austria, pp.227 – 234 (CERN-LHC-PROJECT-REPORT-420)

[100] Claudet S, Gayet P, Lebrun P, Tavian L, Wagner U 1999 *Economics of large helium cryogenic systems: Experience from recent projects at CERN*. Advances in Cryogenic Engineering Vol 45a, pp. 1301 – 1308

[101] Oertel jr. H, Böhle M, Dohrmann U 2006 *Strömungsmechanik*. Vieweg, Wiesbaden (ISBN-10 3-8348-0206-9)

[102] Fetzer A, Fränkel H 1999 *Mathematik 2*. VDI-Verlag, Düsseldorf (ISBN 978-3-540-65584-8)

[103] Lynch RL 2005 *Numerical Partial Differential Equations for Environmental Scientists and Engineers*. Springer, Science+Business Media, Inc. (ISBN 0-387-23619-8)

[104] Munz CD, Westermann T 2012 *Numerische Behandlung gewöhnlicher und partieller Differenzialgleichungen*. Springer, Berlin (ISBN 978-3-642-24335-6)

[105] Baumann WW, Bunge U, Frederich O, Schatz M, Thiele F 2006 *Finite-Volumen-Methode in der Numerischen Thermofluiddynamik*. Educational Script for Numerical Methods of Thermal-Fluid dynamics, Berlin University of Technology, Berlin, Germany